UNIVERSITY OF LEEDS

Carbonation Resistance of Alkali-activated Materials-Experimentation and Modelling

Zengliang Yue

Supervisor:

Professor Susan Bernal Lopez

Dr Yuvaraj Dhandapani

Submitted in accordance with the requirements for the degree of

Doctoral of Philosophy

The University of Leeds

Faculty of Engineering and Physical Science

School of Civil Engineering

June 2024

Intellectual Property and Publication statement

I confirm that the work submitted is my own, except where work which has formed part of jointly authored publications has been included. My contribution and that of the other authors of this work are explicitly indicated below. I confirm that appropriate credit has been given within the thesis where reference has been made to the work of others.

Chapter 4 is primarily based on the manuscript "*Phase evolution and performance of sodium sulfate-activated slag cement pastes"* by **Zengliang Yue**; Yuvaraj Dhandapani; Samuel Adu-Amankwah; Susan A. Bernal**,** CEMENTA (2024): 100117.

- Zengliang Yue is the leading author of this paper.
- Susan A. Bernal, Samuel Adu-Amankwah and Yuvaraj Dhandapani are supervisors/advisors of this PhD thesis.

Chapter 5 is based primarily on the paper "*Structural alterations in alkali-sulfate-activated slag cement pastes induced by natural and accelerated carbonation"* by **Zengliang Yue**; Yuvaraj Dhandapani; Susan A. Bernal**,** submitted and peer-reviewed by Cement and Concrete Research in April 2024.

- Zengliang Yue is the leading author of this paper
- Susan A. Bernal and Yuvaraj Dhandapani are supervisors of this PhD thesis.

Chapter 6 is primarily on the paper "3D crystalline phase and pore structure evolution upon CO_2 exposure in sodium sulfate-activated cement pastes" by **Zengliang Yue**, Zixian Su, Partha P. Paul, Alastair T.M. Marsh, Alice Macente, Marco DiMichiel, John L. Provis, Philip J. Withers, Susan A. Bernal, submitted and peer-reviewed by Cement and Concrete Research in July 2024.

- Zengliang Yue is the leading author of this paper.

- Zixian Su, Alastair T.M. Marsh and John L. Provis collaboratively conducted the synchrotron experiments at The European Synchrotron in Grenoble, France. John L. Provis also supported the interpretation of tomographic images and modelling from the perspective of cement science.

- Partha P. Paul is a beamline postdoctoral researcher and Marco DiMichiel is a beamline scientist at the European synchrotron in the ID15A beamline.

- Alice Macente, Philip J. Withers and Susan A. Bernal are the academic teams of this study. Susan A. Bernal is the main supervisor of this PhD thesis and PI of the proposal granted beamtime; Alice Macente supports the segmentation of tomographic images and Philip J. Withers is the co-I of the proposal granted beamtime, supported the interpretation of tomographic images and facilitated access to preliminary tomography experiments conducted at the Henry Royce Institute at the University of Manchester.

Acknowledgements

First and foremost, I would like to express my deepest gratitude to my supervisors, Prof. Susan Bernal Lopez and Prof. John Provis, for introducing me to this magic world of cement. My passion for studying the chemistry and modelling of cement and concrete was ignited by Prof. Provis's course, MAT4442, at the University of Sheffield. I am immensely thankful to Prof. Bernal for guiding me through this intriguing project, and for equipping me with skills and knowledge in multi-analytical techniques, the use of cutting-edge equipment, and providing an enriching academic environment.

I extend my sincere gratitude to my parents, Mr. Caili Yue and Mrs. Qin Liu, who have always encouraged me to embrace new challenges and taught me to balance career development with family life. I am also proud to acknowledge my grandparents, who, although they could not witness the culmination of my PhD journey, remain a significant inspiration in my life.

Special thanks to Dr. Dhandapani, who trained me to conduct various laboratory experiments, use sophisticated equipment, and discuss my research projects. I am also grateful to Stuart King and Duncan Hedges for their guidance in laboratory training.

I am thankful for the companionship, insightful discussions, and tremendous support of all my current and former colleagues in the School of Civil Engineering at the University of Leeds.

I acknowledge the Engineering and Physical Sciences Research Council (EPSRC) and the University of Leeds for sponsoring my PhD studies. Further, thanks to the UKCRIC National Centre for Infrastructure Materials at the University of Leeds for supporting my experiments. I am also grateful to the National X-Ray Computed Tomography Facility (NXCT) at the University of Manchester, the Henry Royce Institute, and the European Synchrotron for providing beamtime, training courses, and computational resources that supported this PhD the

Abstract

Alkali-activated cements, produced by reacting aluminosilicate precursors with alkaline solutions, offer a promising low-CO_2 alternative to Portland cement. This thesis introduces a multiphysics modelling framework to reduce the uncertainty in carbonation resistance, focusing on sodium sulfate (Na_2SO_4)-activated slag cements. Sodium sulfate, a near-neutral salt, is examined as a safer and more user-friendly alternative to traditional alkaline activators, offering reduced handling risks, easier on-site casting, and lower corrosion potential for steel reinforcement.

The developed modelling framework integrates thermodynamic and transport models to simulate chemical changes and pore structure evolution during carbonation. This novel approach helps to optimise mix design for durable, low-CO_2 concrete formulations. By capturing coupled carbonation and transport effects, the framework provides a comprehensive tool for predicting performance under varying conditions.

Experimental studies complement the modelling, exploring the impact of slag chemistry on sodium sulfate-activated slag cements, with a focus on reaction mechanisms, kinetics, and phase evolution. This with the aim to understand the CO_2 interactions with these materials. The study reveals fundamental physicochemical CO_2 interaction mechanisms taking place in the studied materials and highlights the critical role of selecting appropriate methodologies for studying their carbonation.

Additionally, this thesis advances the understanding of using time-resolved synchrotron X-ray diffraction computed tomography and X-ray microcomputed tomography to offer unique insights into microstructural changes induced by carbonation. This marks the first use of time-resolved 3D analysis to observe real-time microstructural evolution during CO_2 exposure, providing irrefutable evidence of carbonation mechanisms.

The integration of experimental data and modelling in this research offers a solid foundation for optimising alkali-activated cements, enhancing carbonation resistance, and supporting more sustainable concrete infrastructure. This framework is the first of its kind and enables the selection of optimal activators considering slag characteristics to design cements with lower CO_2 footprints and improved longevity, thereby enhancing the sustainability and durability of concrete infrastructure.

Content

Table of Figures

List of Tables

List of Abbreviations

AAC	Alkali-activated cement
AAS	Alkali-activated slag
PC	Portland cement
C-A-S-H	Calcium aluminosilicate hydrates $CaO-Al_2O_3-SiO-H_2O$
CLDH	Calcined hydrotalcite layer double hydroxide
N-A-S-(H)	Sodium aluminosilicate hydrates $Na_2O-Al_2O_3-SiO_2-H_2O$
BFS	Blast furnace slag
C-S-H	Calcium silicate hydrate $CaO-SiO-H_2O$
TRRP	Time to reach reaction peak
SEM-EDX	Scanning microscopy and energy dispersive X-ray spectroscopy
XRD	X-ray diffraction
TG-MS	Thermogravimetry-mass spectrometry
FTIR	Fourier-transform infrared spectroscopy
MAS NMR	Magic angle spinning nuclear magnetic resonance spectroscopy
MIP	Mercury Intrusion Porosimetry
R^3	Rapid, relevant and reliable
FEM	Finite element method
GEMs	Gibbs Energy Minimization
µCT	X-ray microtomography
XRD-CT	X-ray diffraction computed tomography
FBP	Filtered back projection
IR	Iterative reconstruction
DLR	Deep learning reconstruction

Chapter 1.

INTRODUCTION

Alkali-activated cements (AACs) are promising low-CO_2 alternatives to replace traditional Portland cement in the production of concrete and other construction products. AACs are produced by alkaline activation of aluminosilicate materials sourced from natural materials, industrial wastes, or by-products. Among the array of aluminosilicate sources utilised to produce AACs, blast furnace slag, originating from the iron-making process, stands as the most widely used precursor, for producing materials with desirable mechanical and durability properties.

Although alkali-activated slag (AAS) cements have been produced at industrial scales and applied in several countries, the main barrier restricting its broader industrial application is the use of conventional alkaline solutions, typically alkali hydroxide or silicates. These activators are viscous, corrosive and hazardous for handling; the production of these activators requires an energy-intensive process, causing CO_2 emissions. Consequently, the activator component of an AAC is deemed the most pollutant component of these materials. Natural salts, such as sodium sulfate (Na_2SO_4), can be obtained from natural resources or as by-products from different industries. They are promising activators due to their lower CO_2 footprint, competitive cost, and user-friendliness compared to conventional activators.

Despite the technical and environmental advantages offered by alkali-activated materials (AAMs) as alternative cementitious materials, the long-term stability and the factors influencing their performance remain largely unexplored. Interaction with CO_2—referred to as carbonation—is a critical area of uncertainty, which could compromise the long-term structural integrity of these materials and potentially lead to the degradation of steel-reinforced concrete under certain exposure conditions. Furthermore, the absence of modelling tools to predict the service life and enhance the durability of such materials underscores the need for development. There is an urgent need to develop a better understanding of the potential effects of carbonation

on these novel sustainable cements and to create modelling tools for their service life performance prediction. This knowledge gap can be addressed by developing a reactive-transport framework that incorporates complex chemical and physical interactions during carbonation, validated by experimental results. Such a framework can be used not only to predict the carbonation performance of clinker-free AAMs or other binders but also to determine their potential for CO_2 sequestration.

This PhD research centres on evaluating sodium sulfate-activated blast furnace slag cements, as a function of slag composition. This study conceptualises the reaction mechanism and investigates the long-term stability and properties of studied materials. The physicochemical alteration induced by the exposure to different CO_2 concentrations in sodium sulfate-activated slag cements, underpinned a novel understanding of the carbonation mechanism to provide recommendations for developing future carbonation resistance evaluation tests applicable to such materials. Ground knowledge then helped to develop a novel reactive-transport framework to predict the carbonation performance of sodium sulfate-activated slag cements and their CO_2 uptake potential at different CO_2 concentrations.

Chapter 2 presents a comprehensive literature review of the latest advancements in the reaction kinetics, phase assemblage, and mechanical properties of sodium sulfate-activated slag cements. It also explores the carbonation mechanisms in alkali-activated materials, focusing on phase evolution, alterations in pore structure, and mechanical development. Furthermore, the chapter summarises and discusses the progress in carbonation modelling within cementitious materials. The utilisation of 3D and 4D tomography characterisation techniques in studying the pore structure and reaction mechanisms of cementitious materials are also summarised and discussed.

Chapter 3 delineates the experimental methodology, detailing the physical and chemical properties of the anhydrous blast furnace slags as well as the grades and sources of the chemical agents used. It describes the procedures and steps involved in sample preparation. Additionally, this chapter provides a comprehensive overview of the multi-analytical techniques employed in this study for characterisation, along with the specific parameters used for each technique. Detailed discussions on thermodynamic modelling and image-based modelling methods are also included. Moreover, the chapter covers the workflows for processing X-ray diffraction and X-ray microtomography datasets.

Chapter 4 evaluates the reaction kinetics, phase assemblage, and microstructure evolution of Na_2SO_4-activated slag cements produced with three commercial slags. The main reaction

products identified are ettringite and calcium aluminosilicate hydrates, alongside a poorly crystalline SO_4^{2-} intercalated Mg-Al-layered double hydroxide (LDH) phase. Results revealed that the Al_2O_3 slag content alone does not correlate with the hardened cement performance. While pastes made with a higher Al_2O_3 content slag exhibit faster reaction kinetics, those made with a slag with a higher Mg/Al ratio developed superior compressive strength and reduced porosity over extended curing periods, which is comparable to that of blended Portland cement systems. Thermodynamic modelling simulations indicated that sulfate consumption occurs via ettringite and LDH phase formation, influencing the slag reaction degree, pH value, and porosity reduction in these cements. This chapter highlights the critical role of slag composition in controlling microstructure and, consequently, the mechanical properties of sodium sulfate-activated slag cements.

In Chapter 5, the impact of carbonation, induced at different CO_2 exposure concentrations (0.04 or 1%), in the phase assemblages and compressive strength of Na_2SO_4-activated slag materials was determined. The main carbonation reaction products forming are different $CaCO_3$ polymorphs, independent of the slag composition or carbonation conditions adopted. This is a consequence of the Ca-bearing phases' decalcification. In specimens exposed to 0.04% CO_2, a negligible carbonation front was observed, along with a continued phase assemblage evolution and compressive strength gain after 500 days of exposure. This was more noticeable in pastes produced with slags with a higher Mg/Al ratio. Conversely, exposure to 1 % CO_2 led to complete carbonation after 28 days, and a significant compressive strength reduction. Accelerated carbonation does not lead to the development of comparable microstructures to those observed in naturally carbonated pastes. Therefore, results derived from the accelerated tests are considered unsuitable for predicting the long-term carbonation performance of Na_2SO_4-activated slag cements.

Chapter 6 investigates the interaction of CO_2 with sodium sulfate-activated, by employing 3D microscale imaging techniques, specifically synchrotron X-ray diffraction computed tomography (XRD-CT) coupled with X-ray computed tomography (μCT), to analyse the pore structure and the spatial arrangement of crystalline phases in Portland clinker-free sodium sulfate-blast furnace slag cement pastes, before and after carbonation. Results reveal a discernible reduction in ettringite volumes and, notably, provide the first definitive evidence of Mg-Al-SO_4-layered double hydroxide (LDH) phase formation within the sodium sulfate-activated slag cement system, highlighting its critical role in CO_2 sequestration. The process of accelerated carbonation was observed to increase porosity while reducing the tortuosity across the studied alkali-activated slag pastes, yielding a pore network that rivals conventional blended Portland cements in terms of lower porosity and enhanced tortuosity. Remarkably, the

paste produced using slag with the highest Mg/Al ratio (0.8) demonstrated superior carbonation resistance. Additionally, a correlation was established between simulated tortuosity and 3D porosity in accordance with Archie's law. This represents a significant step forward enabling a rapid and reliable estimation of carbonation resistance and CO_2 binding capacity of alkali-activated slag cements.

Chapter 7 introduces a novel reactive transport framework tailored for hardened cementitious materials. This framework integrates key processes, including slag hydration, carbonation reactions, ionic transport and moisture transport, while accounting for variations in microstructure and transport properties over time and reacted CO_2. The framework was applied to simulate both accelerated carbonation (1% CO_2 v/v over one year) and natural carbonation (0.04% CO_2 v/v over ten years) in clinker-free alkali-sulfate blast furnace slag for a case study, under controlled temperature and humidity conditions. The simulation results showed strong alignment with experimental data and existing literature, demonstrating the model's robustness. The novelty of this framework lies in its ability to predict phase evolution, transport properties such as diffusivity, permeability, saturation, liquid volume fraction, capillary pressure, pore solution pH, the composition of aluminium-substituted calcium silicate hydrate gel (C-A-S-H), and CO_2 sequestration profiles across different depths. The model is designed to be adaptable, supporting the development of simulation tools that can assess the durability performance and CO_2 uptake capacity of more complex cement systems, including those containing supplementary cementitious materials (SCMs) or based on alkali-activated cements.

Chapter 8 presents the conclusions and outlines recommendations for future research in the development of near-neutral salt activation technology. It addresses the challenges and identifies potential directions for advancing 3D tomographic analysis in cementitious materials. Furthermore, this chapter proposes future directions for refining the reactive-transport framework developed in this study, aimed at enhancing the reliability and service life of alkali-activated slag (AAS) concrete.

Chapter 2.

LITERATURE REVIEW

2.1 Alkali-activated blast furnace slag

Rapid population growth and urbanisation have led to an exponential increase in the demand for cement and concrete for many applications including housing, transportation and energy infrastructures [1]. Portland cement is the most widely used binder in concrete production, and it is a major contributor of anthropogenic CO_2, with its production responsible for ~8 % of global total CO_2 emissions [2, 3] and about 19 % of industrial emissions, which refers to various pollutants, including gases, particles and other harmful substances, as a result of industrial processes and activities [4]. Alkali-activated cements are alternative low-carbon materials, with the potential to provide 30-80 % CO_2 emissions savings compared to Portland cement, depending on their mix design and curing conditions adopted [5]. Alkali-activated cements are considered a suitable and technically feasible solution for achieving low-carbon and implementing sustainable construction practices [6, 7].

AACs are cementitious materials formed by reacting aluminosilicate precursors with an alkaline solution. Blast furnace slag (BFS) is an iron industry vitreous by-product quenched from the melted iron slag into glassy products, then dried and grounded into a fine powder [8]. It has been reported that ~200-400 kg of melted blast furnace slag is produced per ton of pig iron [9], and a considerable amount of BFS is produced from metallurgical industries in China [10], Japan [11] and the USA [12]. Despite the extensive use of BFS in Europe for producing blended Portland cements, this is not the case in other geographical locations, which motivates the continued development of cements with ultra-high contents of blast furnace slags such as AACs. These cements can be designed to achieve similar or better properties than ordinary Portland cement by modifying the activation conditions (e.g. type and amount of activator) [7]. Consequently, there is significant interest in identifying the optimal activation conditions for a given BFS source and activator type to produce materials with targeted performance.

The main components of BFS are CaO (35-40 %), SiO_2 (25-35 %), MgO (5-10 %) and Al_2O_3 (5 -15 %) [13]. Both the chemical composition and physical properties of BFS, such as particle size distribution, specific surface area, fineness, oxide chemical composition and silicon and aluminium coordination conditions, vary depending on the iron ore, location of extraction and its processing [14-16]. Such differences affect rheology [16, 17], reaction kinetics [18, 19], phase assemblage [20-22] and transport properties [23-25] of alkali-activated materials produced with them.

Alkali-activated materials have been recognised as an alternative binder since 1895 [26]. Significant advancements have been achieved in recent decades using locally sourced BFS, activated by sodium hydroxide and/or sodium silicate solutions, in local applications and infrastructure development [27-29]. In 2018, the standard PAS 8820 [30], was introduced, facilitating the broad adoption of alkali-activated cementitious materials and concrete for fit-for-purpose applications in the United Kingdom.

The performance of alkali-activated slag cements has demonstrated comparable performance to blended ordinary Portland cements (OPC). Extensive work has been reported showcasing that alkali-activated material can achieve comparable or even better performance in terms of mechanical properties [31-33], workability [34-36], durability [37-39], such as carbonation [40-42], chloride [43-46] and sulfate attacks [47-49], compared to OPC-based materials by tailoring the mix design.

The major difference between PC and AAS is the nanostructure of the main reaction products calcium silicate hydrates (C-S-H). Aluminium-substituted calcium silicate hydrates (C-A-S-H) are the main reaction products forming in AAS, and play an important role in the mechanical and durability performance of these cements [50]. Contrary to PC, where C-S-H is dominant by Q^1 and Q^2 silicate tetrahedra [51], in C-A-S-H, aluminium tetrahedra tend to substitute for silicon at the bridging site forming $Q^2(1Al)$ tetrahedra [52]; the practical maximum aluminium substitution appears at ~0.2 of Al/Si ratios in alkali-activated slag cements with increased mean chain length [53]. Increased Al substitution in C-S-H changes its morphology from a fibrillar-like to a fine foil-like structure, and this more impermeable nanostructure contributes durability improvement of these cements [54, 55].

2.2 Environmental considerations in alkali-activated cements

Alkali-activated cements represent a promising alternative to Portland cement for concrete production; however, the manufacturing processes and CO_2 footprint associated with the

production of activators limit their widespread adoption at an industrial scale [56]. The most commonly used activators in alkali-activated cements, alkali hydroxide or alkali silicate, are chosen for their effective activation capabilities, which promote the formation of high-strength materials with other superior properties. Nonetheless, these substances are viscous, corrosive, and hazardous to handle [56]. Moreover, although the principal CO_2 reductions in alkali-activated cement are attributed to the use of industrial waste or by-products as precursors, the production of sodium silicate and sodium hydroxide is energy-intensive, leading to significant CO_2 emissions and secondary pollution [57].

Specifically, sodium silicate production involves melting silica and carbonate salt at approximately 1400°C, followed by dissolution in water in an autoclave at temperatures between 140-160°C [58]. Sodium hydroxide production relies on the electrolytic decomposition of NaCl in brine solution [59]. Heath et al. [60] noted that producing 1 kg of sodium silicate results in 300 g of CO_2 emissions, while the emissions from sodium hydroxide production are half of this amount. According to Habert et al. [61], the goal of reducing the environmental impact of conventional PC by utilising alkali-activated cement systems is currently unachievable when sodium silicate or hydroxide activators produced by conventional methods are used. Consequently, the use of these highly alkaline solutions appears to be suboptimal.

2.3 Near natural salt-sodium sulfate

Natural salts, such as sodium sulfate (Na_2SO_4) and sodium carbonate (Na_2CO_3), which can be obtained in nature or as by-products from different industrial activities, can also activate BFS [62-64]. Sodium carbonate (Na_2CO_3) is sourced from mined trona or via the Solvay process [65]. Also, sodium sulfate (Na_2SO_4) can be obtained from mined mirabilite, sodium-bearing brines or by-products during HCl production, or silica pigments [57, 66]. Using neutral salts as activators represents a significant advantage in reducing the hazards linked to the handling of highly alkaline solutions, while potentially minimising the environmental impact of the cements produced with them. Besides, these neutral salts' costs are very competitive compared to sodium silicate and sodium hydroxide [57]. However, the general perception is that both the early and later strength of these neutral salts-activated slag systems is limited, compared with using silicate activators, and the products take a longer time to harden than commercially required in the construction industry [67].

Studies from the past eight years have proved that sodium carbonate-activated slag binders show excellent mechanical properties and durability [18, 68-73]. It is important to analyse

whether the strategies used to optimise the sodium carbonate-activated slag can be replicated in sodium sulfate-activated slag cements. The reaction of sodium carbonate-activated slag proceeds in a similar way to that of sodium hydroxide-activated slag after the carbonate ions supplied by the activator are exhausted in the solution. These materials present high compressive strength and decreased porosity after 4 days of curing, and can be used as a building material [74]. Furthermore, the long setting time and delayed development of compressive strength challenges can be solved by using high MgO content of slag and/or incorporating nano-admixtures such as calcined layered double hydroxides (CLDH), where pastes set within 24 h [18]. The addition of CLDH quickly removes the CO_3^{2-} ion and increases the pH value in the pore solution, thus increasing the degree of BFS reaction. Also, the use of high MgO content of slag controls the formation of hydrotalcite-type phases, which also promotes the removal of CO_3^{2-} ions in the pore solution, accelerating the kinetics of the reaction [18]. The chloride and carbonation resistance of sodium carbonate-activated slag is optimised by incorporating CLDHs. Ke et al. [75] reported that 5 % CLDH addition significantly densifies the microstructure, showing a lower chloride migration coefficient and higher compressive strength. Besides, the incorporation of CLDH increases the amount of hydrotalcite-type phases and these phases release OH^- to the pore solution under carbonation, which slows down the drop in pH value [76], so it increases the CO_2 uptake in the sodium carbonate-activated slag without damaging the C-A-S-H gels or lowering its mechanical strength [68].

On the other hand, sodium sulfate-activated cements have been less studied, and are considered suitable for nuclear waste cementation [77-79], due to their unique properties including reduced free water, lower pH value, and less released heat during hydration compared with PC. The early strength of neutral salts activated slag cement has been overcome by adequate selection of the slag source, as it is clear that not all slags will react in the same manner when activated with different alkali activators [18]. Other strategies include adding some fractions of $Ca(OH)_2$ [80], OPC clinker [81], or blending with sodium silicate or hydroxide [82] or applying high-temperature curing [83]. These methods could satisfy construction requirements, but they may again increase the embodied energy consumption and carbon footprint associated with the production of these cements. Therefore, in order to move forward to produce a "green" alkali-activated slag system, it is necessary to understand the chemical and properties of the cements produced with slag from different sources and different activator types and dosages. It is impossible to make a type of alkali-activated slag cement for all applications, and the versatility of these materials calls for the adoption of a fit-for-purpose design approach.

2.4 Sodium sulfate-activated slag

Alkali-activated cements produced by using a sodium sulfate activator have not been extensively explored, because early reports identified that the early and later strength of these systems were not as high as those obtained when using hydroxide or silicate activators, and in some cases, extended setting times limited their potential application to pre-casting. For example, Wang et al. [81] reported that the sodium sulfate-activated slag mortar with a 2M concentration only developed 20 MPa at 28 days. Rashad et al. [66] found that the setting time of sodium sulfate-activated slag takes over 50 h when using 3 % (Na_2O equivalent) Na_2SO_4. Mobasher et al. [63] reported that the induction period of Na_2SO_4-activated slag using 25 wt.% activator is 80 h, and the time can rise to 110 h by using 5 wt.% solutions.

The low heat of the reaction released in the sodium sulfate-activated slag is considered advantageous for application in nuclear waste cementation [77-79], but the setting time for this material might take several days [63, 84]. The slag fineness and curing temperature used accelerate the slag reaction in Na_2SO_4-activated slag cements [66, 85]. Tan et al. [86] used wet grinding to reduce the average slag particle size of BFS from 18.12 μm to 3.87 μm and found that the reaction kinetics of alkali-activated slag cements is effectively accelerated. Promising results also demonstrated that the replacement of blast furnace slag with 10 wt.% limestone can accelerate the reaction kinetics, independently of the chemical composition of the slag [84]. Limestone addition improved the compressive strength due to the refinement of the pore structure and better space filling. A similar observation was also found in the substitution of 5 wt.% limestone in this system [87]. The filler effect of limestone increases the nucleation of binding gel phases and accelerates the reaction kinetics without modifying the phase assemblage of the cements produced [88, 89].

The chemical composition of the slag used also has a significant influence on the reaction kinetics of sodium sulfate-activated slag cements [57]. It has been reported that slag with higher Al_2O_3 content is more reactive [84]. Similar results have been reported for supersulfated cements whose main secondary reaction product is also ettringite [90]. This is also consistent with results evaluating 16 industrial slags using the R^3 (rapid, relevant and reliable) test [91, 92] shows that the slag with higher Al_2O_3 contents shows higher kinetics of the reaction in the first 7 days [19]. However, the trend observed in the sodium sulfate-activated slag cements [93] differs from what has been reported for sodium hydroxide and sodium silicate systems, where a higher Al_2O_3 and reduced MgO contents can lead to a lower degree of slag reaction. This has been attributed to the formation of secondary reaction products such as hydrotalcite-type phases [21]. The local chemical environments of Al coordination and the nature of the glassy

phase are also important factors affecting the reactivity of the slag [84, 94]. More detailed work is needed to understand to what extent the slag reactivity is affected as a function of the Al coordination, regardless of other factors (e.g. chemical composition and/or fineness).

The majority of studies in sodium sulfate-activated slag cements have centred on determining the phase assemblage evolution of a single slag source. It has been reported [63, 66, 84] that the main reaction product formed in these cements is an aluminium-substituted calcium silicate hydrate phase, with a tobermorite-type structure, with a low Ca/Si ratio. The main secondary reaction product, ettringite ($3CaO{\cdot}Al_2O_3{\cdot}3CaSO_4{\cdot}32H_2O$), is often reported. It has been hypothesised that a layer double hydroxide (LDH) phase is also forming the Na_2SO_4-activated slag cements, as a low-intensity shoulder at δ_{iso} =~9 ppm is reported when samples are analysed by ^{27}Al MAS NMR [63, 84], although no reflection associated with this phase is identifiable when analysed by X-ray diffraction. It has been reported that sulfate-intercalated LDHs are poorly crystalline [95], which might explain these findings.

As a means of increasing slag reactivity and compressive strength development of sodium sulfate-activated slag cements, the effect of different additives has been evaluated. Wang et al. [81] reported that the compressive strength of sodium sulfate-activated slag increases significantly by adding 5-10 wt% Ca $(OH)_2$. He et al. [96] observed addition of 6 % reactive MgO in sodium sulfate-activated slag results in the pH value of the cements to 12, along with an improvement of compressive strength. Besides, the addition of 6-8 % reactive MgO also reduces the drying shrinkage of this material due to the increased degree of slag reaction with more formation of ettringite [96, 97]. Additionally, Yuan et al. [98] used a blended activator comprising Na_2CO_3 and Na_2SO_4 with the 28-compressive strength slightly increasing with higher contents of Na_2CO_3 in the activator.

Sodium sulfate solutions can be effectively used to activate various supplementary cementitious materials (SCMs). Adding 4 wt. % Na_2SO_4 (relative to the mass of the cements) to the fly ash/slag blended system enhances the early-stage reactive kinetics and mechanical properties. This is associated with a more compact pore structure and reduced drying shrinkage [98]. In 70 % slag blended cements, 8 wt. % Na_2SO_4 (relative to the total mass of BFS and clinker) significantly accelerates the reaction kinetics within the first two days and increases the degree of slag reaction within 28 days [99]. Similar effects have been observed in sulfate-activated materials with a high volume of fly ash in both mortar [100] and concrete [101]. In the 70 % calcined clay/ 30% calcium hydroxide system, the use of a 5 % Na_2SO_4 activator significantly promotes the early strength of the paste specimens reaching 13 MPa at 3 days of curing, linked to the formation of ettringite. Furthermore, it has also been reported [102] that

sodium sulfate can activate construction demolition wastes, releasing ten times less heat than Portland cement and achieving comparable strengths of approximately 31 MPa at 28 days and sustained performance at 180 days of curing.

2.5 The carbonation mechanism of cementitious materials

The general effects of carbonation are associated with decreased pH value in the pore solution with the decalcification of reaction products, leading to the instabilities of mechanical properties and variation of transport properties, depending on the analysed cements system and exposure condition [37, 103, 104]. This section summarises the carbonation mechanism of PC and alkali-activated slag cements. The different carbonation mechanisms (PC vs AAMs) are attributed to the difference in phase assemblage, pore solution, pore structure and transport properties. Moisture is an important transport medium. Carbonation does not happen in either dry conditions or saturated conditions within the pore structure (RH=100 %). The optimum carbonation conditions appear to be around 50 % relative humidity [58].

2.5.1 The carbonation of Portland cement

The carbonation of Portland cement systems is well understood, and it has been extensively researched. In Portland cement, CO_2 diffuses into the material through pores and reacts with pore solution forming carbonic acid, followed by the decalcification of the hydration products, including portlandite, C-S-H gel, and other secondary reaction products [105].

Figure 2-1 presents the thermodynamic modelling simulations showing the phase assemblage (type and amount of reaction products forming) and pH value of the pore solution in OPC as a function of reacted CO_2 [106]. The carbonation proceeds according to the following steps: Firstly, AFm phases are carbonated into monocarbonate [107]. After the consumption of portlandite with the formation of $CaCO_3$ until 12.5 pH value, the C-A-S-H gel starts to be decalcified. When the Ca/Si ratio of C-S-H gel decreases to 0.75 and monocarboante is consumed, the pH value rapidly drops to 11 [106]. With further carbonation, the ettringite starts to decompose at pH 10. The released aluminium and sulphur tend to form aluminosilicate and gypsum, respectively [107].

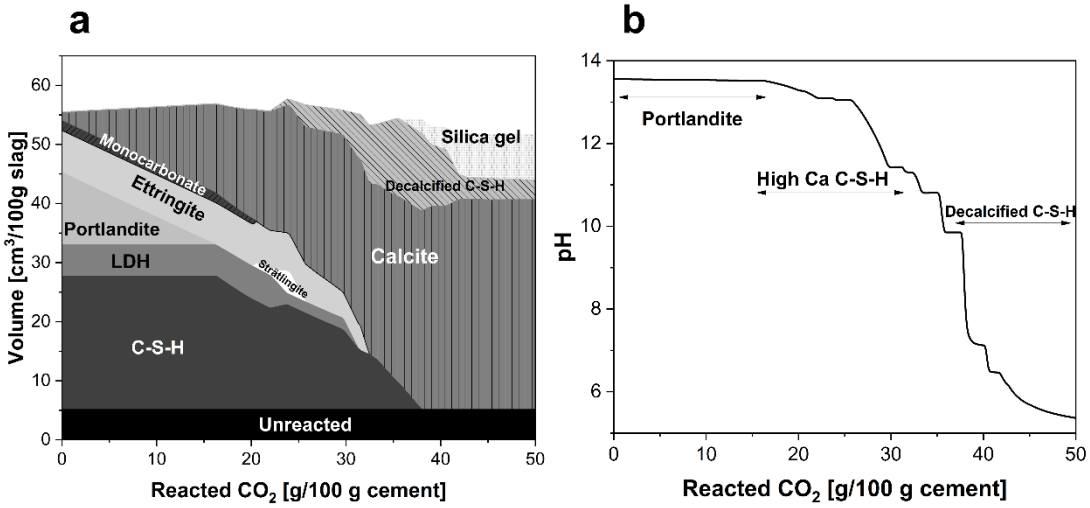

Figure 2-1. Thermodynamics modelling of phase assemblage (a) and pH value in the pore solution as a function of reacted CO_2 in a white OPC with 0.5 of w/b ratio and 90 % degree of hydration, replotted from [106]

The decomposition of ettringite leads to the formation of calcite, gypsum and Al $(OH)_4^-$ [108]. Subsequently, the $Al(OH)_4^-$ interacts with aluminium and silicon species from the decalcified C-A-S-H gel, resulting in the formation of aluminosilicate gels [68]. In thermodynamic modelling of cementitious materials' carbonation, Na-based and K-based zeolites are commonly employed to represent alkali aluminosilicate gels with varying Al/Si ratios, as the bulk chemical composition, particularly the Al/Si ratio, significantly influences the Gibbs energy of formation for these minerals [109-112]. However, it is important to note that zeolites are rarely observed in the carbonation of PC-based systems. This is attributed to the slow transition from amorphous to crystalline forms under ambient conditions and the typically low water content, both of which depend on the material's service environment [113].

It should also be noted that while carbonation steps may be concurrently identified during experimental evaluation, the fundamental processes remain consistent with those predicted by thermodynamic modelling. Shah et al. [114] reported that both portlandite and C-S-H gel undergo carbonation simultaneously, although thermodynamic principles suggest that portlandite should be decalcified first.

The properties of the primary calcium-bearing C-S-H gel phase in hardened cements provide the cementitious properties to concrete, and play a crucial role in determining the progression of carbonation. The decalcification of C-S-H gel due to carbonation occurs in two distinct stages, and the rate of decalcification decreases as the Ca/Si ratio increases [115]. The initial

stage involves the removal of calcium from interlayer spaces and defect sites within the silicate chain until the Ca/Si ratio reaches 0.67; the subsequent stage entails the consumption of chemically bound calcium from the principal layers, leading to the formation of silica gel, including Q^3 and Q^4 tetrahedral structures [76, 115]. The overall loss of calcium in the regions of the inner product C-S-H gel may lead to carbonation shrinkage, as evidenced by TEM-EDX observations [116]. Chen et al. [117] observed that carbonation shrinkage becomes more pronounced when the Ca/Si ratio falls below 1.3. Furthermore, Swenson and Sereda [118] reported that carbonation shrinkage increases with higher CO_2 concentrations, concurrent with a decrease in the Ca/Si ratio.

The understanding of phase assemblage during carbonation is crucial but not sufficient to predict the long-term behaviour of cementitious materials under exposure to elevated CO_2 conditions. This limitation arises because chemical transformations can modify the volume of each phase, impacting both the microstructure and the pore structure of the material. Specifically, alterations in pore structure due to the reaction of the binder with CO_2 significantly affect the transport dynamics of CO_2 diffusivity and water permeability within the system. For instance, the formation of microcrystal $CaCO_3$ on the surface of portlandite and inter-fibrillar voids of the outer C-S-H gel can potentially inhibit the transport of these molecules [116, 119]. Additionally, the carbonation process of portlandite and C-S-H gel, among other hydrates, produces water. This water generation can have varying effects: it can increase the porosity of the binder, potentially causing shrinkage under dry conditions and facilitating faster CO_2 transport, or it can enhance the degree of saturation within the pore structure, thus impeding CO_2 diffusion. The optimal carbonation rate occurs in conditions of intermediate moisture, which supports both the solvation of CO_2 into carbonic acid and the diffusion of CO_2 [120]. The variability in water content within the binder's pore structure further complicates the modelling of carbonation. Therefore, a comprehensive approach that incorporates both chemical reactions and transport phenomena is essential for developing a more accurate predictive long-term carbonation model in cementitious materials.

2.5.2 The carbonation of alkali activated-slag system

The carbonation mechanism of alkali-activated slag differs significantly from that of PC due to variations in the chemical composition, type, and quantity of reaction products [76, 121, 122], as well as differences in pore structure development influenced by slag composition [21, 23] and the type of activators used [123-125]. Studies [126-128] reported that AAS materials, activated by sodium hydroxide and sodium silicate, are more susceptible to carbonation than PC. This increased susceptibility is primarily due to the absence of portlandite and a lower

Ca/Si ratio in the C-A-S-H gel of AAS compared to the C-S-H gel in PC, which results in faster decalcification [76, 115]. However, these conclusions often assume the same carbonation reaction products and adherence to Fick's law under both elevated and ambient CO_2 concentrations [129, 130], assumptions which may not hold true for alkali-activated materials. Instead, several studies have suggested that accelerated carbonation tests may not accurately reflect the actual service conditions [42, 68, 131, 132]. A recent study [40] revealed that alkali-activated concretes produced with slag and/or fly ash exhibit similar carbonation coefficients to those of modern blended Portland concretes with high levels of supplementary cementitious materials, under natural carbonation conditions. Therefore, natural carbonation testing is recommended for a more accurate assessment of the carbonation performance in AAS systems [133].

2.5.3 The carbonation of sodium sulfate-activated slag

Most importantly, the carbonation mechanism of the Na_2SO_4-activated slag remains largely unknown. Studies analysing the carbonation of alkali-activated cement products with sodium hydroxide [126, 134, 135], silicate [126, 134-137] or carbonate [68, 105] have been reported, however, to the best of the authors' knowledge, there are few reports available evaluating the carbonation of sodium sulfate-activated slag cements.

Modelling results from Bernal S.A. et al. [138] evaluating the carbonation of sodium carbonate-activate slag cements showed that natron is the main sodium carbonate phase at ambient CO_2 conditions, whereas nahcolite is dominant at 4 % CO_2. The bicarbonates prefer to form at high CO_2 concentration rather than carbonate, resulting in a greater drop in pH value and more damage to embedded steel in accelerated carbonation (CO_2 concentration >1 %) [138].

Ye and Radlińska [139] stated that structural alterations in calcium-aluminium-silicate-hydrate (C-A-S-H) gels lead to a more porous microstructure, reducing both cohesion and strength in cement pastes. However, Bernal et al. [136] identified that the presence of MgO plays a crucial role in enhancing the carbonation resistance of alkali-activated slag, primarily through the formation of magnesium-aluminium layered double hydroxide (Mg-Al-LDH). This secondary product can mitigate acid attack by facilitating the exchange of intercalated anions in the LDH with carbonates in the pore solution, thereby moderating the pH drop through the release of OH^- ions [76]. The addition of calcined layered double hydroxide (CLDH) has proven effective in increasing the carbonation resistance of various cement systems. This approach has been successfully applied to different cements system, including fly ash blended cements [140-142],

sulfoaluminate cements [143], sulfate-activated fly ash-slag-dredged blended cements [144] and sodium carbonate-activated slag cements [68].

The majority of studies on the carbonation of alkali-activated slag have centred on the effect of sodium hydroxide and sodium silicate with various dosages and silica modulus. There is consensus that the high alkali dosage increases the carbonation resistance of alkali-activated slag since the high pH value in the pore solution can neutralise more carbonate acid [139, 145]. However, the results vary in the effect of silica modulus. Shi et al. [135] reported that increasing silica modulus results in a decrease of carbonation depth, showing a higher degree of reaction and refinement of microstructure. On the other hand, Puertas F et al. [126] stated that the decreased Ca/Si ratio of C-A-S-H due to increased silica modulus reduces the carbonation resistance and strength. However, little attention has been focused on comparing accelerated carbonation and atmospheric carbonation of alkali-activated slag using near-neutral activators such as sodium sulfate and sodium carbonate. Besides, there is little knowledge of the phase assemblage and the effect of the chemical composition of sodium sulfate-activated slag cements.

A recent study indicated that the compressive strength decreases by about 30 % after 8 weeks of accelerated carbonation (induced using 5 % CO_2) compared to the uncarbonated Na_2SO_4-activated slag mortar, and the decomposition of the main reaction product ettringite led to the formation of gypsum and calcite [146]. Rashad et al. [147] investigated the impact of slag fineness and activator concentration on the carbonation resistance of sodium sulfate-activated cements when exposed to 5% CO_2. Their findings indicate that finer slag and higher concentrations of the activator enhance the material's resistance to carbonation. However, it should be noted that a CO_2 concentration over 1 % could falsely predict the service life of the materials in the alkali-activated slag cement system [138], so the results reported in such studies cannot be considered as a true reflection of the carbonation performance of a Na_2SO_4-activated slag cement.

Ye et al. [105] analysed the phase assemblage of carbonated sodium sulfate-activated slag (2 M Na_2SO_4) using X-ray diffraction (XRD), after exposing the sample to natural carbonation conditions of 20°C and 60% humidity for four months. They observed the disappearance of ettringite, indicating its decomposition during carbonation, while the Mg-Al-LDH was preserved [105]. Additionally, they noted the formation of calcite and aragonite, the latter of which could contribute to volumetric instability [105, 145]. Figure 2-2 presents the phase assemblage of carbonated sodium sulfate-activated slag based on thermodynamic modelling [105]. However, the model shows the decomposition of the Mg-Al-LDH phase, contrary to

their experimental findings [105]. This discrepancy is primarily due to the omission of databases for Mg-Al-SO_4-LDH and Mg-Al-CO_3-LDH in the modelling. It is also suggested that minerals such as gibbsite and dolomite, which require specific temperatures and pressures to form, are unlikely to form under these conditions. The inclusion of the Na-based zeolite database [112] is proposed to better represent the formation of aluminosilicate as carbonation reaction products. Therefore, a more comprehensive database will be integrated into this PhD thesis to accurately reflect the true carbonation process in sodium sulfate-activated slag cements.

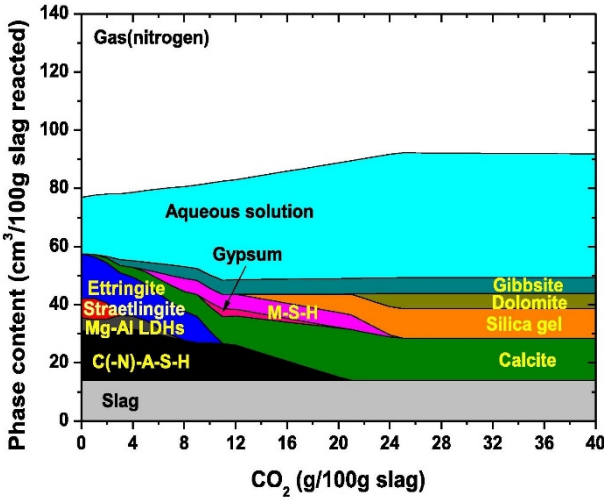

Figure 2-2. Thermodynamic modelling of phase evolution as a function of reacted CO_2 in sodium sulfate-activated slag [105]

2.6 Carbonation modelling of cementitious materials

The deterioration of concrete due to carbonation is associated to the intrinsic properties of the material and the exposure conditions during its service life. In a practical situation, several factors, such as temperature, CO_2 concentration, external loading, relative humidity, water-to-cement (w/c) ratio and chemical composition of raw materials (and consequently the binder) contribute to the carbonation performance [76, 103, 104, 132, 135]. However, it is challenging in a laboratory setting to simulate and combine those variables with long-term conditions.

2.6.1 Significance in building a life service model for alkali-activated slag cements

Carbonation of Portland cement (PC) has been simulated by thermodynamics [106] and multiphysics modelling [148], as it is well-understood what the carbonation mechanism is,

which enables the use of empirical equations to determine the change of pore structure and phase assemblages as a function of carbonation progress. However, as modern cements include high contents of a variety of SCMs, the carbonation mechanisms taking place in such materials are more complex and not completely understood [121, 149]. In the carbonated regions, usually identified by using a pH indicator [150], the chemical reaction occurs between dissolved carbonic acid and reaction products. This process is accompanied by drying due to the relative humidity gradient between the pore structure and the exposure surface [151]. The water released during the decomposition of hydrates alters the saturation degree within the pore structure [103]. In the uncarbonated region, the hydration reaction continues over time, resulting in a more compacted microstructure compared to the regions more closely exposed to CO_2 [135, 152]. Across these two regions, CO_2 diffusivity and liquid permeability vary significantly at different CO_2 exposure depths [153, 154]. This variation is influenced by the porosity [155, 156], tortuosity [23, 25], degree of saturation [157, 158] and CO_2 uptake [138, 159].

The reaction mechanism of CO_2 with clinker-free alkali-activated materials differs from that of PC due to the absence of portlandite as a reaction product. In such cases, carbonation directly causes the decalcification of the main binding phase, an aluminium-substituted calcium silicate hydrate (C-(A)-S-H type gel) and the decomposition of secondary reaction products [76, 160, 161]. The differences in reaction mechanism, reaction products forming, and the interaction of such products with CO_2 make carbonation in alkali-activated materials challenging to understand. By experimentation alone, it is challenging to isolate each of the potential reactions and phenomena taking place during carbonation, and therefore modelling tools are required to better understand the factors governing the carbonation process in those materials.

For developing novel low-carbon cement, the carbonation performance is one of the most important durability indicators that need to be assessed, considering the increased levels of CO_2 in the atmosphere and the catastrophic effect that this can have on the longevity of the material. Although accelerated carbonation is adopted for evaluating carbonation resistance in short periods of time, it has been questioned if using an elevated CO_2 concentration to induce carbonation will be suitable to simulate what could be expected to occur in real service conditions of alkali-activated materials [42, 132]. Nature carbonation is a slow process that unfolds over decades [41, 162]. To assess the carbonation resistance of new mix designs utilising various SCMs, accelerated carbonation tests with elevated CO_2 concentrations (ranging from 1% to 20%) are employed to shorten the testing period. It is assuming that the carbonation reaction in cementitious materials is mainly a diffusion-controlled mechanism, and therefore the carbonation depth can be considered to be proportional to the square root of time

[130], $x = k\sqrt{t}$, where x is the carbonation depth determined by phenolphthalein, k is the rate coefficient and t is the time. For two carbonation exposure conditions, it is often assumed that the ratio of k equals the square root of CO_2 concentration, based on Fick's law [163]. This simplified approach only uses CO_2 concentrations and carbonation depth as input to estimate the corresponding natural carbonation depth based on results from accelerated carbonation and shows a good agreement with experimental results in PC [164]. However, this approach overlooks the chemical changes occurring during the carbonation reaction and assumes that CO_2 diffusion is a steady-state process, implying that the pore structure is not changing over time [130]. Those two factors are generally true for 28 days of cured-PC, however, when adding SCMs in blended cements and clinker-free alkali-activated materials, published studies report that elevated CO_2 concentrations can no longer predict the natural carbonation performance in high-volume blended cement [132, 163, 165-167] or alkali-activated materials [42, 168-170]. With the widespread adoption of novel SCMs in sustainable cements, and interest in determining how carbonation might influence the longevity of such materials, there is an urgent need to develop a comprehensive modelling framework, that can account for the chemical reaction taking place due to the continued hydration reaction, as well as CO_2 exposure, with changes in internal saturation and pore structure throughout the service life of the materials.

2.6.2 Controlled factors in the reactive-transport model

In a cementitious material reactive-transport model, the reaction rate and the degree of reaction (DoR), are critical inputs. It governs the evolution of the pore network, which in turn influences transport properties. Numerous reaction models have been proposed, each employing different assumptions to describe the rate-controlling mechanisms [171, 172]. The modified Parrot and Kiloh (MPK) method has been successfully applied in the modelling hydration of Portland cements [173], but it is uncertain whether input parameters adopted in such a model are physicochemically reasonable to be applied in other cement systems. In the sodium hydroxide/silicate-activated slag system, the Jander equation was used to calculate the degree of slag reaction in a few days of reaction [174]. It has been emphasised importance of considering particle surface curvature by using the Ginstling-Brounshtein equation [175]. This equation was then adopted to model heat release from slag dissolution in the first 7 days activated by sodium silicate solution [176]. However, modelling DoR at an extended curing age is needed for service life service predictions. Additionally, sodium sulfate-activated slag cements have attracted attention due to health and safety benefits, lower CO_2 footprint and lower prices compared to conventional activators [177]. These materials react slowly in the first 28 days but then show increased strength development and reduced porosity after 56 days of reaction [63, 68, 84]. There is no reaction kinetics model for sodium sulfate-activated slag

cements, and this will be addressed in the current study as an example of the applicability of the developed framework as a tool for simulating the carbonation life service of this material.

In 1990, it was proposed that storing a numerical image of an entire porous sample's structure in a computer would allow for the numerical resolution of appropriate transport equations [178]. Regrettably, this method has not obtained substantial attention in cements research, despite the significant advancements in computational technologies in the 21st century. The experimental measurement of transport properties such as diffusivity and permeability are constrained by two major factors: (a) the drying process significantly alters the microstructure [179-181]; b) diffusion and permeability tests require weeks to reach steady-state conditions, during which the raw materials continue to react and alter the microstructure [182-184]. Although increased pressure has been applied to expedite testing [185], this approach may risk damaging the pore structure and causing water leakage from interfaces [181]. This then explains that the simulated water permeability by using the Lattice Boltzmann method in 3D uCT images [186] and the pore size distribution model shows 2-3 orders of magnitude lower than experimentally determined values [187, 188]. A similar observation is found in image-based diffusivity modelling [189-191]. Workflow for using tomography images in finite element method (FEM)-based simulation is provided in a recent study [192]. In this study, diffusivity and permeability are simulated based on uCT images using a random walker and finite volume method as model input in sodium sulfate-activated slag cements, respectively.

2.6.3 Current achievement in reactive-transport models in carbonation of cementitious materials

A state-of-the-art review of numerical modelling methods for hardened cements can be found in recent review papers [193, 194]. The subsequent section will discuss the current advancements in reactive-transport models specifically applied to simulate the carbonation of cementitious materials.

As discussed in Section 2.5, carbonation is a physiochemical process. Chemically, the modification of phase assemblage and pore solution chemistry results from both time-evolved raw materials reaction within uncarbonated regions, as well as from CO_2 interactions with reaction products formed in the carbonated regions. Collectively, these chemical reactions influence the pore structure of the hardened cements, affecting parameters such as saturation degree, pore size distribution, and tortuosity, which in turn impact transport properties like CO_2 diffusivity and pore solution permeability. This suggests that solely using a thermodynamic model to elucidate the carbonation mechanism of the cement system, or applying a diffusion

model to describe the CO_2 transport profile and penetration depth, may not suffice for accurately predicting the service life of the cements analysed.

Significant advancements in building reactive-transport models for the carbonation behaviour of cementitious materials have been made over the past decade. Table 2-1 summarises the published reactive-transport models simulating carbonation in these materials. It is noted that a) the coupling of thermodynamic and diffusion models has garnered some attention in constructing reactive-transport models; b) while computationally intensive, the finite element method (FEM) is considered for use in the diffusion model to achieve precise calculations. However, these models as shown in Table 2-1 are predominantly based on Portland cement chemistry, assuming a static degree of clinker reaction over time. More complex 3D models have typically only considered main reaction products like C-S-H gel, portlandite, and calcite, which is generally valid for PC cured for 28 days. Nonetheless, moisture transport due to atmospheric relative humidity changes and water release during carbonation reactions, which affect saturation conditions and transport properties, should also be considered.

Although natural carbonation provides more valuable information for evaluating the carbonation performance of cementitious materials, the carbonation test at ambient conditions (~0.04 % CO_2) is a slow process and takes decades to collect sufficient results for longevity prediction. For the rapid widespread adoption of novel low-carbon cements, it is then imperative to develop a suitable modelling tool for predicting their service life particularly when exposed to detrimental conditions, such as CO_2 present in the atmosphere. As a physicochemical process, the carbonation process can be simulated by coupling chemical reactions between CO_2 and cement paste, and mass transport. The chemical reaction can be simulated using thermodynamic modelling with the help of geochemical software such as GEMs (Gibbs Energy Minimization Software) [195]. Modelling phase assemblage and carbonation process of alkali-activated slag cements using this platform has been successfully achieved and results correlate well with experimental observations [76, 121, 122], with the support of additional databases [109, 111, 112], depending on analysed cement systems. The mass transport of carbonate ions in the pore structure of unsaturated cementitious materials is based on the extended Nernst-Planck equation [196]. The dissolution of CO_2 from gas to the aqueous state is normally ignored in the simplified mathematical models; Henry's law [197] could be a potential option to describe this process. Pioneer works have been conducted by coupling these two methods in a blended cement system by assuming the isotropic porosity of the cementitious material [198, 199]. That seminal work provides a roadmap for developing a multiphysics framework for predicting the life service of cementitious materials.

With the ongoing shift towards low-carbon cement technologies, which includes the use of local supplementary cementitious materials (SCMs) or clinker-free alkali-activated materials, the degree of cement reaction is reduced [200, 201], indicating that assumptions based on mature hardened cements focusing solely on carbonation are no longer valid. Most critically, the carbonation mechanisms of these newly developed low-carbon cements remain largely unexplored. Therefore, this study will incorporate previously overlooked parameters in the existing reactive-transport models, establish research trajectories, and develop a novel service life 3D model for the carbonation of sodium sulfate-activated materials. This framework is expected to be applicable to other SCM-related systems and alkali-activated materials.

Table 2-1. Summary of different reactive-transport models in carbonation of cementitious materials

Modelling method	Considered parameters	Exposure condition	Scale	Cement systems	Refs
Simulator ReactMiCP: numerical iteration and thermodynamic modelling	Chemical composition of raw materials and mix design; phase assemblage; moisture transport; ionic diffusion; constant porosity values in uncarbonated and carbonated regions; permeability(saturation); diffusivity(saturation)	3 % CO_2, 25℃ and 50 % RH for 28 days	1D	Portland cement pastes	[202, 203]
Simulator Dynaflow^{TM}: Finite element model and thermodynamic modelling	Chemical composition of raw materials and mix design; phase assemblage; ionic diffusion; constant porosity values in defined four zones; diffusivity (porosity)	CO_2-saturated water for 30 days	1D	Portland cement pastes	[204]

Finite element method	Gaseous CO_2 concentration and dissolution; moisture transport; constant porosity; diffusivity (CO_2 partial pressure) and permeability(CO_2 partial pressure)	500, 000 Pa (5bar) CO_2; 25 ℃; 65 % RH for 28 days	1D	Portland cement pastes	[153]
Pseudo-analytic approach	Dissolution of gaseous CO_2; carbonation of portlandite and C-S-H with precipitation of $CaCO_3$; constant porosity; carbonation front	Sheltered outdoor exposure for 40.5 months	1D	Portland cement pastes	[205]
Finite element method	Dissolution of gaseous CO_2; reactivity rate of clicker and C-S-H gel, precipitation rate of $CaCO_3$ and decalcification rate of C-S-H gel; aggregate spatial distribution	Atmospheric, 10 % and 75 % CO_2 carbonation for 300 days	1D and 3D	Portland cement mortar	[206]
Thermodynamic modelling and numerical modelling package	Dissolution of gaseous CO_2; phase assemblage; Porosity(t, CO_2); saturation(CO_2); diffusivity (saturation, porosity); permeability (saturation)	Atmospheric conditions, 0.4 porosity and 0.3 saturation in the pore for 2 years	1D	C_3S pastes	[207, 208]

Numerical calculation	Dissolution of gaseous CO_2; reaction rate of portlandite, C-S-H and $CaCO_3$; Porosity; porosity (CO_2), diffusivity (saturation, porosity); permeability (saturation)	0.038% and 0.15 % CO_2; 60 % and 90 % RH; 25 ℃; 100 years	1D	Portland cement pastes; 20 % fly ash/slag blended pastes	[209]
Finite element method	Reaction rate portlandite, C-S-H gel and $CaCO_3$; ionic diffusion; porosity (CO_2); permeability (porosity); Diffusivity (porosity)	CO_2-saturated water; 20 ℃; 30 days	1D	Portland cement paste	[210]
Thermodynamic modelling and numerical calculation	Phase assemblage; constant porosity; constant diffusivity and saturaiton	0.038 % CO_2; 12℃; 70 % RH; 50 years	1D	Sulphate-resistant Portland cement pastes	[211]
Lattice Boltzmann method and thermodynamic modelling	Phase assemblage only consider clinker, C-S-H gel, Portlandite and calcite; diffusivity (time, porosity); porosity(time)	CO_2-saturated water;120 hours,	2D and 3D	Portland cement pastes	[212]

Thermodynamic modelling and numerical calculation	Phase assemblage; ionic diffusion; particle size distribution (time)	CO_2 contained solution (0.1 mol/kg); 2 years	1D	Portland cement pastes	[213]
Thermodynamic modelling and finite element method	Phase assemblage; ionic diffusion; porosity (CO_2); diffusiovity (porosity)	CO_2 saturated water; 85 ℃; 0.1 MPa; 42 days	1D	Portland cement pastes	[198, 199]

2.7 Tomographic approach for understanding properties of cementitious materials

X-ray computed tomography (CT) enables the visualization of three-dimensional internal structures in materials, ranging from meters down to tens of nanometres in scale [214, 215]. By penetrating an object, X-rays capture a series of two-dimensional (2D) radiographs from multiple projections [215, 216]. These 2D projection data are then transformed into three-dimensional images through computed reconstruction algorithms [216, 217]. Various reconstruction methods are employed, including filtered back projection (FBP) [218], iterative reconstruction (IR) [219], and the more recent deep learning reconstruction (DLR) [220]. FBP has been widely utilised for over 40 years due to its lower computational demands and numerical stability [221]. While this thesis does not delve into the differences between reconstruction algorithms, a thorough review of contemporary methods can be found in a recent study [222]. The computational reconstruction processes yield a 3D greyscale representation of the object's internal structure, which can be quantitatively analysed, colour-rendered, and virtually sliced in any orientation to suit various research objectives.

Hardened cements are multi-phase porous materials whose pore size varies from mm to nm scale [223-225]. The long-term performance of the cementitious materials is determined by the ionic transport of species via advection and/or diffusion through the pore structure [196, 198, 226], which in turn affects the rate of degradation mechanisms such as carbonation [103, 227], sulfate attack [48, 228], or chloride-induced corrosion [229, 230]. Assessing the durability of a novel AASC is important for its widespread uptake in different applications. This is strongly dependent on its microstructure features including the pore network [25].

Techniques currently used to investigate porosity in cementitious systems include nitrogen adsorption/desorption (NAD) [231], mercury intrusion porosimetry (MIP) [232], ^{1}H NMR relaxometry [233], small-angle X-ray/neutron scattering (SAX/SANS) [234] and micro-CT (micron-scale computed tomography) [235]. X-ray micro-CT is the reconstruction of a 3D image of the object on the basis of many projections (radiographs) collected as the specimen is rotated, usually through 180° or 360° [215]. This allows the 3D visualisation of the pore structure, a capability absent in bulk measurement techniques like MIP, NAD, SAXS/SANS and ^{1}H NMR relaxometry, as they provide only averaged measurements across the entire sample and require drying the sample prior to testing. In this way, the three-dimensional (3D) network from micropores to macropores can be characterised non-destructively. From this, the connectivity, tortuosity, and porosity can be quantified [23, 25, 236]. However, there is a trade-off between spatial resolution and specimen size.

The application of microtomography (μCT) in the study of cementitious materials has garnered some attention in recent decades. μCT analysis in cementitious materials has been discussed in review papers. [235, 237]. Previously, uCT has been conducted on AASCs with a voxel size of around 1.5 μm [238] and in Portland cement as fine as 0.5 μm [239]. These voxel sizes are characteristic of uCT and mean that identification and quantification of the nanometre-size pores is not possible by uCT. Pixel size is calculated by dividing the field of view (FOV) by the matrix size, while spatial resolution refers to the system's ability to distinguish between closely spaced structures, typically assessed in terms of spatial or contrast resolution [240]. In addition to pixel size and matrix size, spatial resolution is heavily influenced by various technical factors of the CT system, such as detector technology [241], X-ray characteristics [242] and reconstruction algorithms [222]. Nevertheless, the pore size larger than 10 um [243] can be observed, which are the most relevant types of pore in terms of ionic movement and hence durability of cementitious materials [244]. In addition, nano-sized pores predominantly appear in the calcium silicate hydrate (C-S-H) or aluminium-substituted calcium silicate hydrate (C-A-S-H), which although responsible for the strength properties of the cement, might be less critical in defining the durability of these materials, depending on the main mechanism of attack [245]. Therefore, the resolution achievable by uCT is deemed sufficient to characterise the pore structure and provide meaningful insights into the transport properties of cementitious systems.

Carbonation causes changes in the phase assemblage and pore structure of cementitious materials, but there is very limited understanding of how phase assemblage alterations modify the pore structure, or vice versa. Although scanning electron microscopy coupled with energy-dispersive X-ray spectroscopy provides elemental distribution information and enables visualisation of the phase assemblage (including porosity), it is limited to two dimensions [246] and is destructive, meaning that it is difficult to conduct repeat analysis of the same point(s) on a specimen. Phase contrast tomography (PCT) [247] has been used to provide more contrast between the constituents, while nanotomography has been used to achieve greater spatial resolutions [248, 249].

There are, however, very few techniques able to collect 3D structural and mineralogy data simultaneously, and most of them are rarely applied to the study of cementitious materials. One such technique is X-ray diffraction computed tomography (XRD-CT) [250] which provides spatially resolved XRD patterns. There have been a few studies using XRD-CT to understand the phase changes that occur in cement and concrete [251, 252]. Seminal studies have focused on evaluating the hydration of ordinary Portland cement [253, 254] and blended Portland cements [255], mainly to identify the distribution of portlandite or ettringite and C-S-H gel in

the material. However, to date, the technique has not been used to study alkali-activated cements, or for delineating the effects of carbonation in such systems.

In this study, the effects of CO_2 exposure on the microstructure of sodium sulfate-activated slag cements produced with three types of blast furnace slag are investigated. In order to simultaneously elucidate the changes in phase assemblage and changes in pore structure resulting from carbonation, synchrotron XRD-CT imaging and higher resolution synchrotron μCT results are presented and discussed. This is the first study to visualise the reaction products forming in sodium sulfate-activated slag cements and to determine how they change as a consequence of accelerated carbonation. Changes in pore structure, diffusion tortuosity and formation factor of the assessed material are also examined by using three commercial European blast furnace slag precursors. More broadly, this study also demonstrates the potential of combining XRD-CT and μCT to study complex multi-component composite materials such as alkali-activated cements, providing unique novel insight into their microstructural features as a function of mix design and chemical interaction with CO_2.

2.8 General remark and conclusions

Depending on the chemical composition of the slag and the dosage of sodium sulfate, carbonation in alkali-activated slag might induce significant changes in the physical and chemical properties of reaction products, phase assemblage, matrix pore structure, water fraction, and pH of the pore solution [126, 155, 256]. The effect of the slag chemistry on Na_2SO_4-activated slag cements microstructure remains relatively unexplored, with few studies examining the carbonation mechanisms of these materials. Therefore, their potential resilience under in-service conditions is largely unknown.

Generally, CO_2 ingress leads to decalcification of C-(A)-S-H gel and a reduction in pH within the pore solution in alkali-activated slag systems, particularly those activated with sodium hydroxide or silicate solutions, resulting in a coarser microstructure and diminished mechanical properties [126]. Nevertheless, secondary phases such as Mg-Al-LDH, M-S-H gel, and ettringite may buffer the pH under carbonation [76, 257]. This thesis will address four primary research questions to leverage the near-neutral pH characteristic of sodium sulfate with activation of blast furnaces slags: (a) the long-term phase assemblage, microstructure, chemical composition of C-(A)-S-H gel and Mg-Al-LDH phase, mechanical properties, and stability in sodium sulfate-activated slag cements as a function of time and slag chemistry; (b) the interaction of CO_2 with sodium sulfate-activated slag cements affecting phase assemblage evolution, microstructural changes, carbonation rate, and mechanical properties under 0.04%

(natural) and 1% (accelerated) carbonation conditions at controlled temperatures and humidity, as a function of time and slag composition; (c) 3D phase spatial distribution and pore structure evolution as a function of CO_2 uptake and slag composition; (d) the development of a novel 3D reactive-transport model by integrating thermodynamic modelling, CO_2 transport, and moisture transport models based on reacted CO_2, slag composition, exposure time, and relative humidity. This model aims to predict outcomes from the first three research topics and, upon validation with experimental results, will provide a realistic 3D multiphysics framework. This framework is crucial for understanding carbonation mechanisms and performance under more complex exposure conditions and can be extended to other low-carbon cement systems, such as wet and drying cycles, varying slag compositions, mix designs, gradually increasing atmospheric CO_2 levels, or supercritical CO_2 conditions with thermal transport in geothermal systems.

Chapter 3.

MATERIALS AND METHODS

3.1 Materials characterisation

The oxide composition of the three slags used in this study, determined by X-ray fluorescence (XRF) using a fused bead preparation method in a Rigaku ZSX Primus II, is shown in Table 3-1. The selection of those three slags is based on different Mg/Al ratios, which are 0.8, 0.7 and 0.5 for S1, S2 and S3, respectively In this study, LOI (Loss on ignition) was determined by thermogravimetric analysis with coupled mass spectra (TG-MS) under nitrogen gas flow until 700 ℃ to avoid the mass gain due to oxidation of sulphur; detailed setting is referred to in section 3.3.2. LOI can be used to assess the pre-hydration and/or weathering of slags, which affects the reactivity and performance of hardened cementitious materials [258]. Thermogravimetry coupled with mass spectrometry for three anhydrous slags is shown in Figure 3-1. The mass loss between 30 °C and 400 °C corresponds to free water and chemically bound water, as indicated by the mass spectra of H_2O (m/z = 18). This observation is related to the pre-hydration of blast furnace slag [259]. The mass loss of CO_2 (m/z = 44) between 500 °C and 700 °C is attributed to minor weathering of the slag, forming $CaCO_3$ during storage, which is also evident in the XRD patterns of the three raw slags shown in Figure 6. Above 700 °C, the mass spectra of SO_2 (m/z = 64) indicate the formation of sulfates consistent with oxidation of sulfides typically present in blast furnace slag [260]. Nevertheless, the extent of pre-hydration and slag weathering, as reflected in the loss on ignition (LoI) in Table 1, is negligible and comparable across all three slags.

Table 3-1. The chemical oxide composition of the raw slags

Precursors	Oxides (wt.%)										
	CaO	SiO_2	Al_2O_3	MgO	SO_3	Fe_2O_3	TiO_2	Na_2O	K_2O	Others	LOI
Slag 1 (S1)	42.7	35.8	9.6	7.2	2.0	0.7	0.7	0.3	0.5	0.5	0.7
Slag 2 (S2)	40.3	35.6	11.5	8.0	2.4	0.3	0.6	0.3	0.5	0.5	1.1
Slag 3 (S3)	42.2	34.4	12.0	5.6	2.9	0.5	1.1	0.3	0.6	0.4	1.1

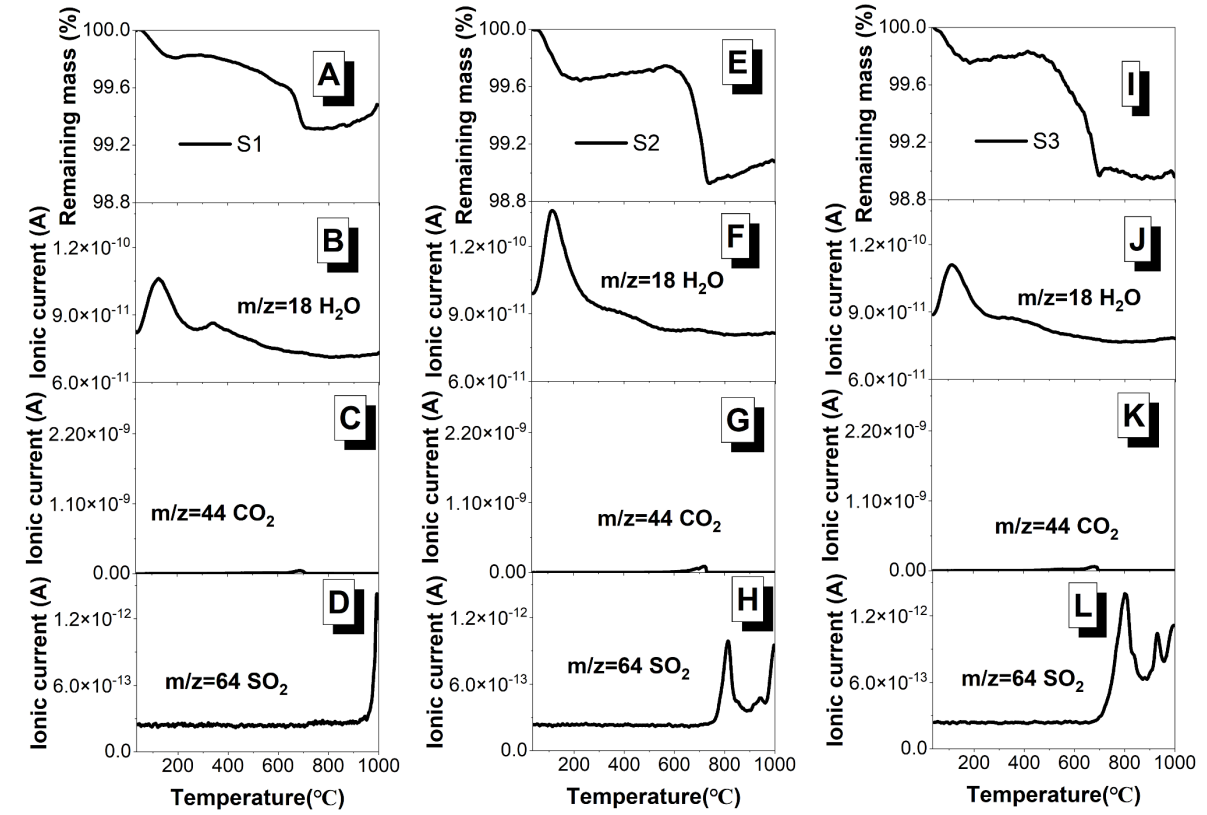

Figure 3-1. Differential derivative thermogravimetry curve of three anhydrous slags used (A) S1, (E) S2 and (I) S3. Mass spectra of (B, F and J) H_2O, (C, G and K) CO_2 and (D, H and L) SO_2 are presented for S1, S2 and S3, respectively. m/z = mass/charge ratio for each ion

The particle size distribution of three slags was measured with a Malvern Mastersizer 2000 laser diffractometer, using isopropanol as dispersion liquid. Nitrogen adsorption-desorption measurements were conducted at 77 K using a Micromeritics Tristar 3000 to ascertain the Brunauer-Emmett-Teller (BET) surface area. Prior to the measurements, the three slag samples were stored in a desiccator. The samples were subsequently cooled with liquid nitrogen, and the N_2 adsorption volume at specific pressures was quantified during the analysis. The particle

size distribution of the three anhydrous slags is shown in Figure 3-2. Table 3-2 shows the D_{10}, D_{50}, D_{90} and BET-specific surface area of three precursors slags.

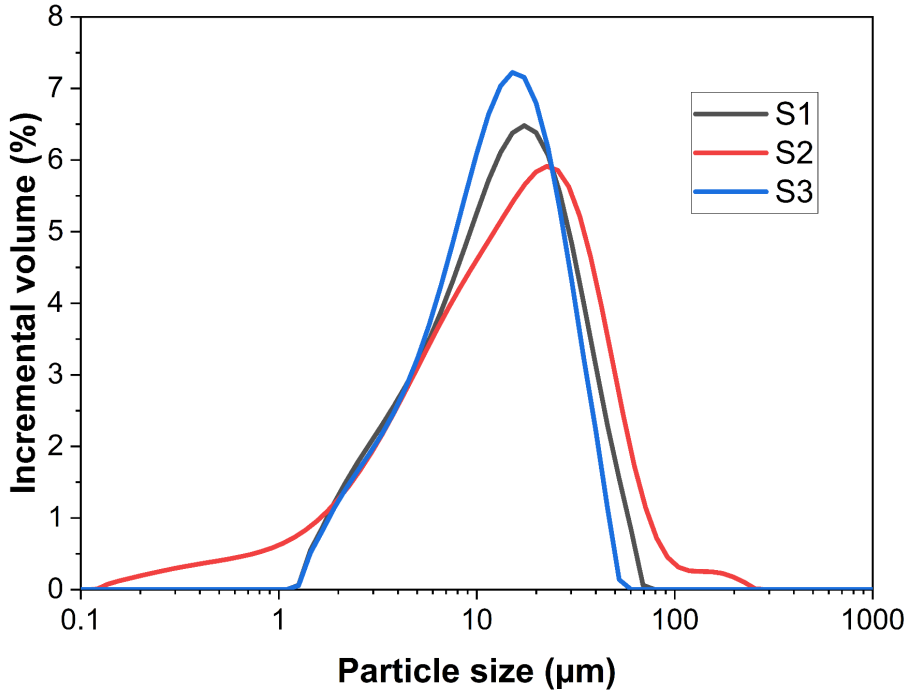

Figure 3-2. Particle size distribution curves for the unreacted blast furnace slags studied

Table 3-2. Laser diffraction and BET-specific surface area of the underacted slags. Error bars correspond to the standard deviation of three measurements

	D_{10} (µm)	**D_{50}(µm)**	**D_{90}(µm)**	**BET specific surface area (m^2/g)**
S1	3.30±0.2	12.5±0.2	32.3±0.3	1.48±0.17
S2	2.2±0.1	13.4±0.4	41.8±0.5	1.38±0.11
S3	3.4±0.1	11.7±0.1	27.2±0.2	1.53±0.18

3.2 Mix design and sample preparations

Alkali-activator anhydrous sodium sulfate (Acros Organics, Na_2SO_4>99 %) was used. Sodium sulfate powder was dissolved in deionised water at 40°C and cooled down to room temperature (20 °C) prior to use. The selection of 40 °C is based on the sodium sulfate solubility curve as a function of temperature [261]. Below 32.4 °C, the decahydrate form (also known as mirabilite

or Glauber's salt) is more stable and has a higher solubility than the anhydrous form of sodium sulfate. At 32.4 °C, a eutectic point is reached where the solubilities of mirabilite and anhydrous sodium sulfate are equal. Above this temperature, the anhydrous form becomes more soluble than mirabilite. Therefore, selecting 40 °C ensures the complete dissolution of any potentially formed sodium sulfate decahydrate in the solution. The Na_2SO_4-activated slags were prepared with an activator dose of 6 g Na_2SO_4 per 100 g precursors and a water-to-solids (slag + sodium sulfate) ratio of 0.4.

To generate homogeneous mixtures of the Na_2SO_4-activated slag pastes, a high-shear mixer Heidolph was used to mix the paste samples for 10 minutes. A mixing speed of 200 rpm is used for the first 3 minutes, increased to 400 rpm for the next 3 minutes, and further increased to 800 rpm for the final 3 minutes. Between speed changes, the mixer was stopped for 30 seconds to remove the paste adhered to the container wall and placed back into the middle of the container for homogeneous mixing. The produced pastes were cast in 15 ml centrifuge tubes and then sealed cured in a water bath at 20 ℃ until the age of testing. For synchrotron XRD-CT and μCT measurements in Chapter 6, the same batch of paste samples was then cast in homemade 2 mm moulds (inner diameter: 2 mm and height: 4 mm) and then sealed for curing at 20 ℃ for 28 days.

Na_2SO_4-activated slag mortars were produced using the Hobart mixer, using standardised sand with a sand/slag mass ratio = 3:1 following the BS EN: 191-1:2005 [262]. To produce a homogeneous mortar mixture, the sand and slag were first added into the mixer and blended at low speed (140 ± 5 rpm) for 3 minutes. Then, the Na_2SO_4 solution was added without stopping the mixer keeping mixing for an additional 2 minutes at low speed. This was followed by 5 minutes of high-speed (285 ± 10 rpm) mixing. All the specimens were cast in 50 mm x 50 mm x 50 mm cubic moulds, sealed in plastic bags and cured in a fog room at a constant 20 ℃ and high relative humidity (> 95 %) avoiding carbonation during curing.

3.3 Determining reactivity of blast furnace slags used

The ASTM C1897-20 reactivity test was adopted to assess the reactivity of three blast furnace slags (S1, S2 and S3) used in this study [91]. The cumulative heat of the reaction was monitored using a TAM Air Calorimeter over 16 days at 40 °C; detailed experimental setups are referred to next section 3.4.1. All the raw materials, i.e., the mixture of slag, calcium hydroxide, calcite and water, were stored overnight at 40 °C, following the procedures recommended in the literature [91, 92, 263]. Figure 3-3 shows the cumulative heat of three slags used in this study based on the R^3 test. At the early-stage reaction (first 50 hours), slag S3 with the higher Al_2O_3

content (lower Mg/Al ratio) produced more heat compared to the other two slags, which is consistent with the previous R^3 test of 16 industrial slag that slag with higher Al_2O_3 content is more reactive in the first 25 hours [19]. However, cumulative heat indicates higher reactivity S1, i.e., slag with the highest Mg/Al ratio from ~50 to 400 hours of reaction, compared to slag S2 and S3. All three slags had cumulative heat in the range of 550-600 J/g of SCM consistent with the previous reports [263].

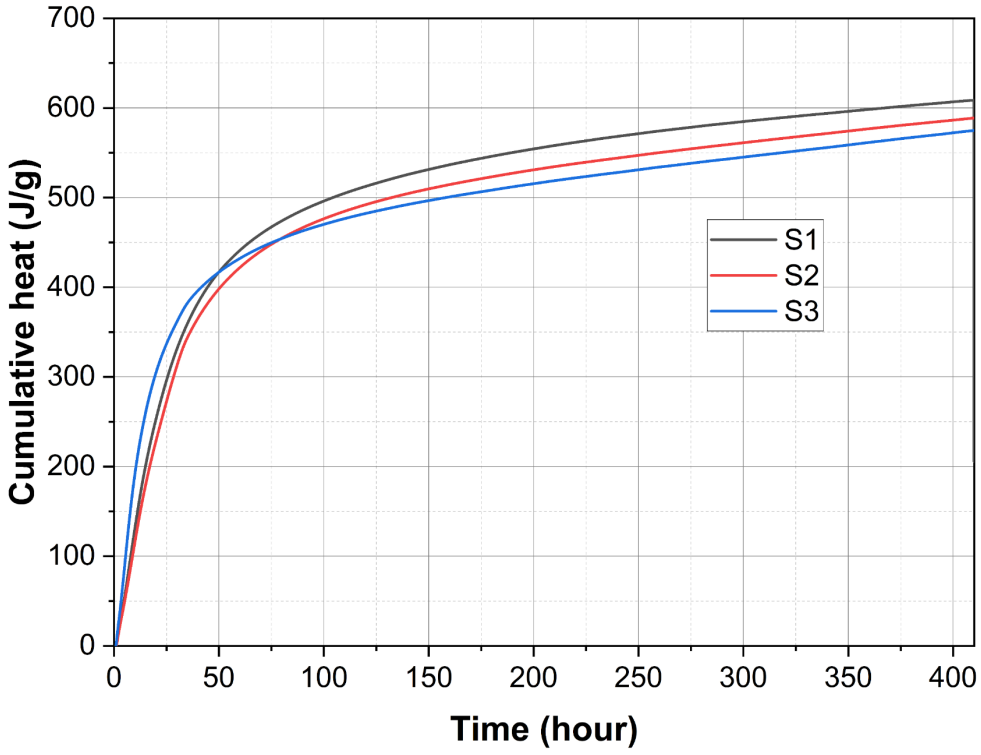

Figure 3-3. The cumulative heat of three blast furnace slags used in this study based on R^3 test

3.4 Testing methods

3.4.1 Reaction kinetics study using isothermal calorimetry

Figure 3-4 depicts the isothermal calorimetry setup using the TAM Air Calorimeter employed in this study. Each calorimetric channel is designed with a twin configuration, comprising one side for the sample and the other for the reference. Within each channel, two heat flow sensors are positioned under the sample and reference, respectively. This dual configuration enables direct comparison of the heat flow from the sample, resulting from chemical reactions, with that from the inert reference [264]. The temperature gradient across the sensor generates a

voltage signal proportional to the heat flow [264]. Isothermal calorimetry experiments in this thesis were conducted on fresh pastes at 20 ± 0.02 °C for studying the reason kinetics and at 40 ± 0.02 °C for the R^3 test. The pastes were prepared by using a vortex mixer for 5 minutes. 9 g of paste was weighed into an ampoule and immediately placed in the calorimeter to record heat flow up over 16 days. Reference samples containing quartz and distilled water (9 g in total) were used, and all heat flow and cumulative heat measurements were normalised by the total mass of the paste.

Figure 3-4. Photograph of the TAM Air Calorimeter used in this PhD thesis

3.4.2 Phase assemblage characterisation

After specific curing durations, cylinder-shaped specimens (15 mm diameter and 95 mm height) were cut using an ISOMET low-speed saw into 2 mm slices. The cut slices were then ground and immediately characterised without any solvent exchange treatment to arrest the reaction. Hydration stopping was not performed in this study to minimise modifications to reaction products, as ettringite is one of the main secondary reaction products in these cementitious matrices, and this phase is known to be sensitive upon solvent exchange treatment [265, 266]. Structural characterisation of these samples was conducted via:

Powder X-ray diffraction (XRD) was conducted using a Bruker D8 with Cu-Kα radiation and a nickel filter, as shown in Figure 3-5. When X-rays interact with the crystalline structures within the sample, they are diffracted in specific directions according to Bragg's Law [267], which correlates the wavelength of the X-rays and the lattice spacing of the crystal to the diffraction angle. Data acquisition was conducted in a continuous scan model from 8° to 60° 2θ with a step size of 0.03° and a counting time of 3 s/step. X'pert Highscore plus V5.1 was used for phase identification based on the PDF-4+ 2023 ICDD database. The American Mineralogist Crystal Structure Database was also used to check the formation of bloedite, which was not found in the ICDD database.

Figure 3-5. Photograph of the XRD Bruker D8 with Cu-Kα radiation used in this thesis

Thermogravimetry coupled with mass spectrometry (TG-MS), using a Netzsch STA 449 F5 coupled with a Netzsch QMS 403D mass spectrometry unit shown in Figure 3-6, was used in this thesis. TG-MS enables the continuous measurement of the sample's mass as a function of temperature in the TG. The gaseous products evolved during the heating process are ionised, and the resulting ions are separated by mass-to-charge ratio (m/z) in the MS, providing detailed information about the composition of the evolved gases [268]. In each case, 30 mg of sample was tested from 35 to 1000 ℃ at a heating rate of 10 ℃/min under nitrogen flowing at 60 mL/min. The selection of 60 mL/min of nitrogen flow is referred to a previous study to eliminate oxygen gas and then the mass gain due to oxidation of sulphur [269]. A 10-minute isotherm at 30 ℃ and 1000 ℃ under nitrogen flow was performed before and after the heating ramp.

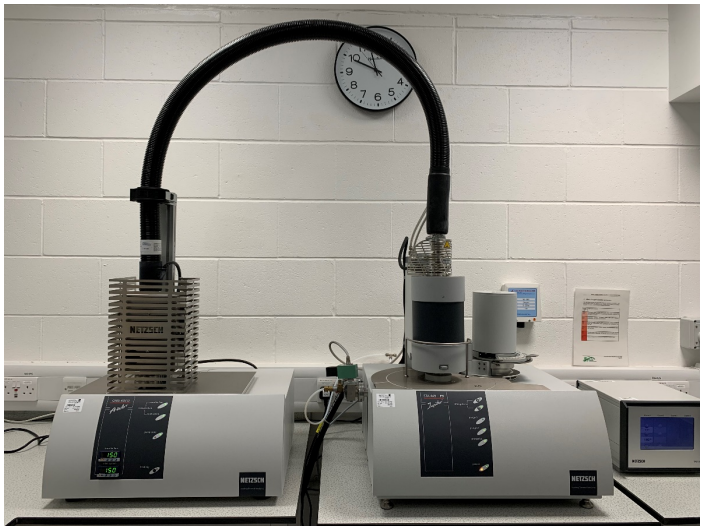

Figure 3-6. Photograph of the STA equipment, coupled with mass spectrometry, used in this thesis

Solid-state magic angle spinning (MAS) nuclear magnetic resonance (NMR) spectra were collected using Bruker Avance III HD spectrometer a 400 MHz wide bore magnet (magnetic field 9.4 T), shown in Figure 3-7. NMR spectroscopy exploits the magnetic properties of certain atomic nuclei. Under a strong magnetic field, these nuclei resonate at characteristic frequencies upon exposure to a radiofrequency pulse [270]. The resulting NMR signal provides detailed information about the local chemical environment of the nuclei. By rapidly spinning the sample at an angle of 54.74° (the magic angle) relative to the magnetic field, magic Angle Spinning (MAS) minimises anisotropic interactions, yielding narrower and clearer NMR signals [270]. MAS NMR provides detailed information about the atomic-level structure of the studied materials. In this thesis, solid-state ^{27}Al MAS NMR spectra were collected at an operating frequency of 104.3 MHz, using a zirconia rotor and spun at 12 kHz in a 2.5 mm solid-state MAS probe, and employed a 90° pulse of duration 0.23 μs, a relaxation delay of 0.5 s and a minimum of 16000 scans. ^{27}Al chemical shifts were referenced to external samples of Yttrium Aluminium Garnet (YAG) with the hexa-coordinated site referenced to 0.7 ppm. Signals were normalised by area under the curve before plotting [271].

Figure 3-7. Photograph of the solid-state magic angle spinning nuclear magnetic resonance spectrometer used in this thesis

Scanning electron microscopy and energy dispersive X-ray spectroscopy (SEM-EDX), using a Zeiss EVO MA15 scanning electron microscope at a working distance of 8.5 mm and accelerating voltage of 20 KeV, as shown in Figure 3-8. SEM is an imaging technique that a focused beam of high-energy electron to scan the surface of a sample. When electrons interact with the atoms in a sample, they produce signals that can be detected and used to generate high-resolution images [272]. Backscattered Electron (BSE) imaging, a mode of SEM, is commonly used to study the microstructure of cementitious materials [273]. The backscattered electrons, which are primary beam electrons reflected back out of the specimen, are detected [272]. The intensity of BSE is dependent on the atomic number of the elements; heavier elements with higher atomic numbers scatter more electrons back towards the detector, resulting in brighter regions in the BSE images [272]. When the electron beam interacts with the sample, it generates characteristic X-rays, which are detected by the EDX detector that measures their energy and intensity [274]. This information helps to identify and quantify the elements within the sample [274]. In this thesis, about 2 mm cut disc along the transverse section from the cylinders demoulded from centrifuged tubes were epoxy impregnated, polished and carbon coated for both backscattered electron imaging and EDX analysis. The specimen was preparing

a similar procedure described in [246]. At each curing age assessed, at least 35 images were taken at 2000 x magnification for image analysis. A global thresholding method was used to segment the unreacted slags and pores [275]; the in-house Macros script was then used to do the batch calculation, achieving automated calculation of the two-dimensional volume fraction of unreacted slag and porosity in Fiji [276]. The degree of slag reaction (DoR) was calculated using equation 3.1; the volume fraction of slag before reacting was calculated using equation 3.2 based on the mix design and the density of Na_2SO_4 solution is referred to as molality of the activator at 20 ℃ [277].

$$\partial_{slag}(\%) = \left[\frac{V_{slag}(0) - V_{slag}(t)}{V_{slag}(0)}\right] \times 100\ \% \tag{3.1}$$

$$V_{slag}(0) = \frac{\frac{m_{slag}}{\rho_{slag}}}{\frac{m_{slag}}{\rho_{slag}} + \frac{m_{Na2SO4\ solution}}{\rho_{Na2SO4\ solution}}} \tag{3.2}$$

Figure 3-8. Photograph of the scanning electron microscope and energy dispersive X-ray spectrometer used in this thesis

When infrared (IR) radiation interacts with a sample, the absorption of specific wavelengths corresponds to the vibrational modes of the molecules within the sample [278]. The resulting IR spectrum serves as a fingerprint of the molecular structure [278]. Attenuated Total Reflectance (ATR) is a sampling technique used in IR spectroscopy; the sample is placed in contact with a crystal made of an IR-transparent material, such as the diamond used in this study [279]. IR beams are directed into the ATR crystal at an angle greater than the critical angle, causing total internal reflection within the crystal [279]. This reflection generates an evanescent wave that extends a few micrometres beyond the crystal surface. The sample

absorbs the evanescent wave's energy at specific wavelengths, corresponding to its molecular vibrations, which can then be related to different reaction products in cementitious materials [280]. In this thesis, attenuated total reflectance Fourier transform infrared spectroscopy (ATR-FTIR) was conducted using a Thermo Scientific Nicolet Is10 Spectrometer equipped with a Thermo Scientific Smart Diamond ATR sampling, as shown in Figure 3-9. A consistent pressure of the swivel tower was applied for all the powder samples using the diamond crystal with a refractive index of 2.4, and a 45° of the incident refractive infrared beam. Spectra in the wavenumber range between 400 to 4000 cm^{-1} with 2 cm^{-1} resolution were collected for all samples. Before each scan, a background scan was taken and corrected in the spectrum of the analysed powder samples, a total of 32 scans per sample were collected. Considering the heterogeneity of the carbonated samples, each sample was tested 3 times for the same batch. The Thermo Scientific software was used for conducting the baseline corrections as well as the detection of the peak positions.

Figure 3-9. Photograph of the attenuated total reflectance Fourier transform infrared spectrometer used in this thesis

3.4.3 Compressive strength

Figure 3-10 presents the steps for determining the compressive strength of sodium sulfate-activated slag cements. 25 x 25 x 25 mm^3 paste cubes were used for compressive strength measurement at 7, 14, 28, 56, 365 and 600 days. The specimens were kept sealed at 20 ℃ for a period of 6 days and demoulded after the sealed curing period. This is because some of the cubic paste specimens (depending on the slag reactivity) took a longer duration to harden after sealed curing. The Instron 3382 was used to test the compressive strength with a loading speed

of 500 N/s, an initial touched load of 1 N and a sensitivity of 40 %. Triplicate specimens were measured per curing condition at each time.

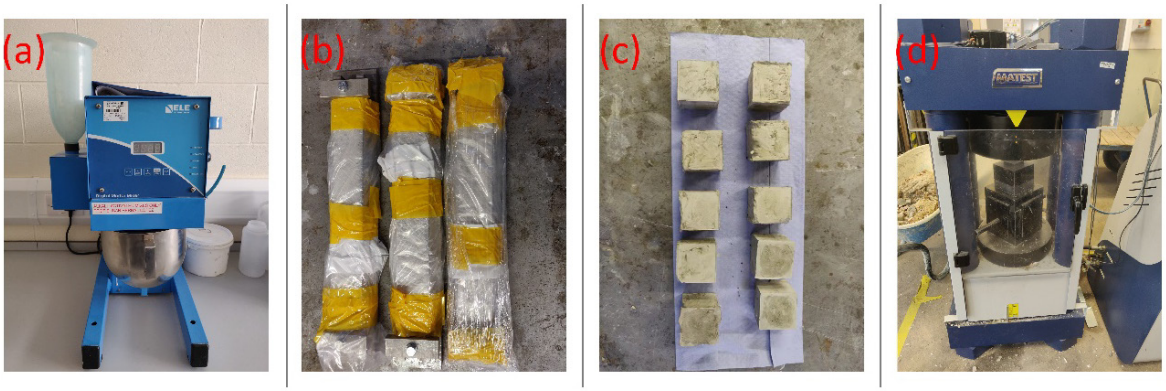

Figure 3-10. Photographs showing the steps for determination of compressive strength of Na_2SO_4-activated slag using 25 x 25 mm cubes. (a) Use the Hobart mixer to mix Na_2SO_4-activated slag paste for 10 minutes. (b) Cast the paste into steel moulds; the parafilm and cling film were used to achieve seal curing. (c) A batch of mould produces 10 cubes with 25 x 25 mm. (d) The Instron 3382 was used to measure the compressive strength

3.4.4 Carbonation depth measurement

After exposing paste cylinders and mortar cubes to natural and accelerated carbonation, the carbonation depth was determined using 1 wt % phenolphthalein indicator solution prepared in 100% isopropanol on a fresh split surface. Detailed information about the carbonation exposure protocols and analysis of carbonated samples are given in Chapter 5.

3.5 Thermodynamic modelling

The open-source GEM-Selektor v.3 [195, 281] was used to conduct thermodynamic modelling. Gibbs Energy Minimization (GEMs) is a thermodynamic modelling algorithm that can provide the molar amount of ions and molecules, their activities and the chemical potential of the system [282]. The thermodynamic modelling programme was used to predict the equilibrium phases in sodium sulfate-activated slag based on the composition used in this experimental study. The Cemdata18 was used as the primary database [108]. An extended Debye-Hűckel equation was used to calculate the activity coefficients of aqueous species shown in equations 3.3 and 3.4. This equation has been proven to work successfully in alkali-activated materials [76, 110, 283, 284].

$$log_{10}\gamma_i = \frac{-Az_i^2\sqrt{I}}{1+Ba\sqrt{I}} + bI + log_{10}\frac{x_{iw}}{X_w} \quad (3.3)$$

Where $'\gamma_i'$ is the activity coefficient, $'z_i'$ is the charge of the ith aqueous species. 'A' (kg$^{0.5}$mol$^{-0.5}$) and 'B' (kg$^{0.5}$mol$^{-0.5}$) are the temperature and pressure-dependent electrostatic parameters. It was assumed that the NaOH is dominant in the aqueous phases, so the average ion size 'a' is 3.31 Å and the parameter for common short-range interactions of charges species 'b' is 0.098 kg/mol. The $'x_{iw}'$ is the molar quantity of water and $'X_w'$ is the total molar amount of aqueous phase. 'I' is the total ionic strength of the aqueous solution, which was calculated using equation 4.

$$I = \frac{1}{2}\sum c_i z_i^2 \quad (3.4)$$

Where $'c_i'$ is the concentration of the ith ionic species and $'z_i'$ is its charge.

The solid solution models for sodium-substituted calcium aluminate silicate hydrate gels (CNASH_ss) and hydroxylated hydrotalcite (MgAl-OH-LDH_ss) were used, and thermodynamics properties of these end members can be found in detail in [121, 285]. Due to the lack of data in Cemdata 18, the thermodynamic data for SO_4^{2-} intercalated MgAl-LDH, a MgAl-s-LDH phase is used based on experimental results reported in [284]. The chemical composition of the end member for these three solid phases is presented in Table 3-3. Furthermore, the zeolites 2020 database was added to the model to represent the alkali aluminosilicate gel (N-A-S-H) formed in alkali-activated materials with different Al/Si ratios. The thermodynamic properties of these zeolites can be found in [112, 286]. The mordenite zeolites are excluded due to their slow formation kinetics under ambient temperature. The degree of slag reaction is selected by increasing the reaction degree from 10 % to 80 % with a step of 5 % to simulate the phase evolution. All simulations were conducted at 20 °C under standard atmospheric pressure. An additional database was also added to accurately predict the phase assemblage resembling the experimental results obtained in this study, and recent studies, including SO_4^{2-} and CO_3^{2-} intercalated double-layer hydroxide (LDH), various magnesium sulfate and sodium carbonate [284, 287]. The selection of this database is primarily because their work is based on experimental results [284], and the Mg/Al ratio of the synthesised Mg-Al-SO_4-LDH closely matches the Mg-Al-LDH phase formed in currently studied systems (1.5-1.9), as determined by SEM-EDX in the inner reaction product regions shown in Chapter 4 Figure 4-14.

Table 3-3. Chemical composition of end member in CNASH_ss solid solution and MgAl-OH-LDH_ss solid solution. Their end members are consistent with thermodynamic data in the Cemdata18 database [108]

C-N-A-S-H_ss			
End member	Chemical formula	Bulk Ca/Si	Bulk Al/Si
	With interlayer Na^+ and Ca^{2+}		
5CNA	$(CaO)_{1.25}(SiO_2)_1(Al_2O_3)_{0.125}(Na_2O)_{0.25}(H_2O)_{1.375}$	1.25	0.25
	With only interlayer Ca^{2+}		
5CA	$(CaO)_{1.25}(SiO_2)_1(Al_2O_3)_{0.125}(H_2O)_{1.625}$	1.25	0.25
T2C	$(CaO)_{1.5}(SiO_2)_1(H_2O)_{2.5}$	1.50	0
T5C	$(CaO)_{1.25}(SiO_2)_{1.25}(H_2O)_{2.5}$	1.00	0
	With only interlayer Na^+		
INFCN	$(CaO)_1(SiO_2)_{1.5}(Na_2O)_{0.3125}(H_2O)_{1.1875}$	0.67	0
INFCNA	$(CaO)_1(SiO_2)_{1.1875}(Al_2O_3)_{0.15625}(Na_2O)_{0.34375}(H_2O)_{1.3125}$	0.84	0.26
	Without interlayer Na^+ and Ca^{2+}		
INFCA	$(CaO)_1(SiO_2)_{1.1875}(Al_2O_3)_{0.15625}(H_2O)_{1.65625}$	0.84	0.26
TobH	$(CaO)_1(SiO_2)_{1.15}(H_2O)_{2.5}$	0.67	0
MgAl-OH-LDH_ss			
End member	Chemical formula	Bulk Mg/Al	
M4A-OH-LDH	$Mg_4Al_2(OH)_{14}\cdot 3H_2O$	2.0	
M6A-OH-LDH	$Mg_6Al_2(OH)_{18}\cdot 3H_2O$	3.0	
M8A-OH-LHD	$Mg_8Al_2(OH)_{22}\cdot 3H_2O$	4.0	
MgAl-s-LDH_ss			
End member	Chemical formula	Bulk Mg/Al	
M4A-s-LDH	$Mg_{3.85}Al_{2.05}(OH)_{12.09}(SO_4)_{0.88}\cdot 3.14H_2O$	1.88	
M6A-s-LDH	$Mg_{5.79}Al_{2.13}(OH)_{16.08}(SO_4)_{0.94}\cdot 5.04H2O$	2.72	

In Chapter 5, the simulation of accelerated carbonation conditions involved a stepwise addition of CO_2. In each step, reacted 0.3 g of pure CO_2 gas (density 1.98 kg/m^3) was added alongside 18.6 g of air (density 1.22 kg/m^3), resulting in an equivalent of 1 vol% CO_2. Using 0.3 g CO_2 per step was identified as sufficient for accurately predicting the phase evolution changes associated with the carbonation of alkali-activated slag cements [76]. In the simulations, air was introduced to consider the oxidation of samples during carbonation exposure. Cemdata 18

[108] and zeolite 2020 [112, 286] with additional Mg-Al-LDH phases [284] from experimental results, as presented in Table 3-3, were used in Chapter 5. For a given type and concentration of activator, changes in the slag chemical composition will lead to different reaction kinetics and degree of reaction (DoR). In Chapter 5, a 40 % slag reaction was assumed, which has been reported as the DoR at 28 days of curing of sodium sulfate-activated slag cements [161]. The simulations reported in Chapter 5 focus on the phase evolution as a function of reacted CO_2 (g) using three different slags.

3.6 Synchrotron μCT and XRD-CT measurement

The μCT and XRD-CT experiments were conducted at The European Synchrotron (ESRF) on Beamline ID15A [288]. Figure 3-11 shows the synchrotron experiment uCT and XRD-CT setup for sodium sulfate-activated slag cements, studied in this thesis. A monochromatic 50 keV X-ray beam was used for the scan. After precise positioning and alignment, the specimen was rotated through 360° during data acquisition. A total of 7201 projections were captured with an exposure time of 0.04 seconds per projection, resulting in an overall scan time of 7201 projection*0.04 seconds/projection = 288 seconds (approximately 5 minutes) per sample. A CMOS detector (PCO-edgeHS 5.5, 2560 x 2160 px) with a 10X optic magnification was used to obtain the pixel size of 0.7 μm. The nabu pipeline [289] was used to perform filter-back projections and reconstruct the volume of the sample.

For the XRD-CT, a monochromatic X-ray beam with an incident energy of 50 keV (wavelength λ = 0.2480 Å) with a Dectris Pilatus3 X CdTe 2M area detector at a distance of 2m from the sample was used to collect diffractograms. The measured *d*-space ranged from 3.7 Å to 27.3 Å. A silver behenate standard was used for the detector geometry corrections. Compound refractive lenses were used to focus the beam to a ~10 x 10 μm^2 spot size on the sample. To obtain spatially resolved phase information, XRD patterns were collected at 300 different angular orientations, with an angular step size of 1.2° and a step size of 10 μm in both the horizontal and vertical directions. Each vertical stack, with a height of 10 μm, required approximately 15 minutes for the line scan, and a total of 31 line scans were performed for each sample. The 2D diffractograms were azimuthally integrated using the PyFAI module [290]. Subsequently, the integrated diffractions were tomographically reconstructed with the filter back projections using in-house Matlab scripts, to obtain 3D spatial distributions of diffractograms. All diffractograms were converted to equivalent 2θ based on Cu-Kα radiation (λ = 1.5406 Å) for comparison with results collected from the lab-based XRD.

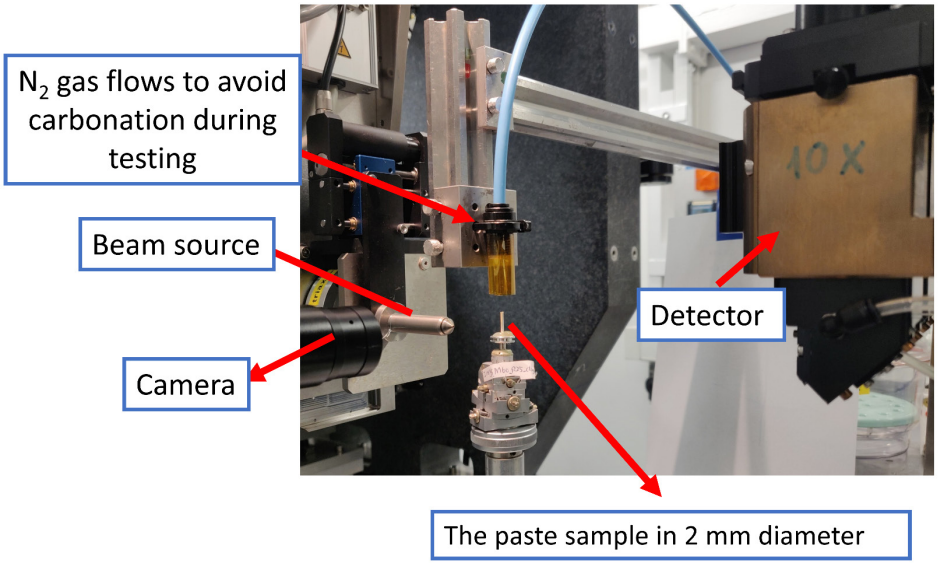

Figure 3-11. Photograph illustrating the synchrotron specimen setup of sodium sulfate-activated slag pastes for synchrotron experiments conducted in ID15 A, at the European synchrotron

3.7 Data analysis in µCT and XRD-CT datasets

3.7.1 Workflow for processing synchrotron XRD-CT results

Figure 3-12 shows the workflow adopted for mapping the spatial distribution of ettringite using in-house Matlab and Python scripts [288, 291]. The XRD-CT technique involves the sequential collection of diffraction data as the specimen is translated and rotated while being irradiated by a pencil beam. For each rotation angle, a two-dimensional diffraction pattern is recorded. These patterns are subjected to azimuthal integration, transforming them into one-dimensional diffraction profiles (intensity vs. 2θ), as shown in Fig. 3-12B. The integration across all rotation angles results in a global sinogram for the entire dataset (Fig. 3-12C). To map the spatial distribution of a specific phase (e.g., ettringite), a sinogram corresponding to that phase is selected by integrating the diffraction data within a defined 2θ range, characteristic of the phase. Finally, the tomogram is reconstructed by applying a Radon transform to the sinogram, producing a spatially resolved map of the phase distribution, with intensity corresponding to phase concentration (Fig. 3-12E).

The 2θ range corresponding to d-spacings from 17.63 to 3.73 Å (equivalent to an angle range from 5°-23.82° 2θ when recalculated to the wavelength of Cu-Kα radiation) was selected to generate the sinogram of the ettringite intensity and spatial distribution of ettringite in each slice. Every 10-pixel (0.1 mm) thick layer was cropped from the outside to the core of the specimen shown in Figure 3-13 in XRD-CT and μCT data using in-house Python code. The XRD-CT results at each layer were normalised for comparison [271].

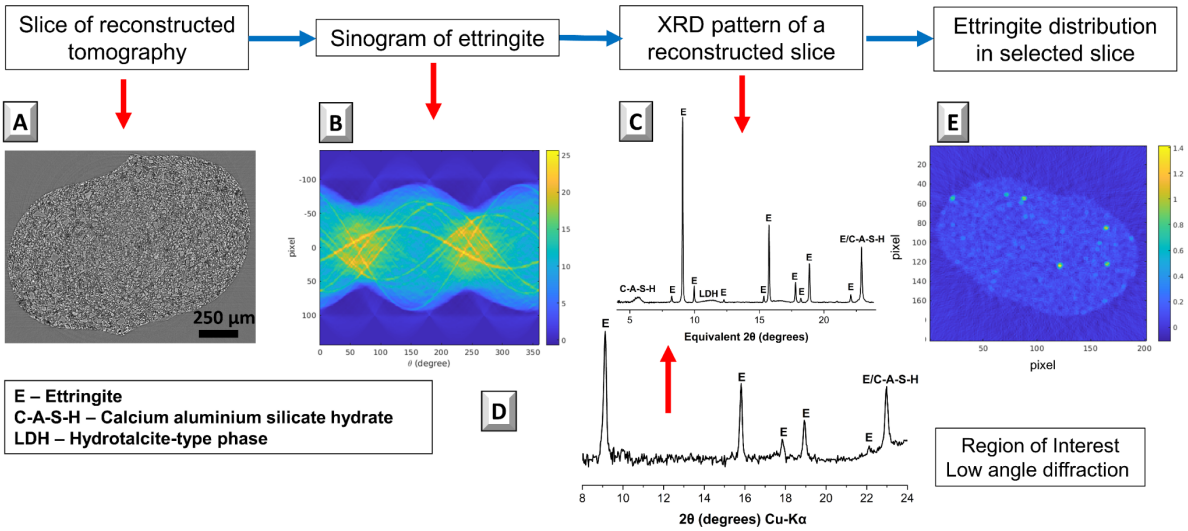

Figure 3-12. Schematic of the workflow used for data analysis showing (A) Slice of reconstructed μCT; (B) Sinogram of ettringite; (C) XRD pattern of a reconstructed slice; (D) Lab-based Cu-Kα XRD pattern of Na_2SO_4-activated slag; (E) Ettringite distribution in selected slice

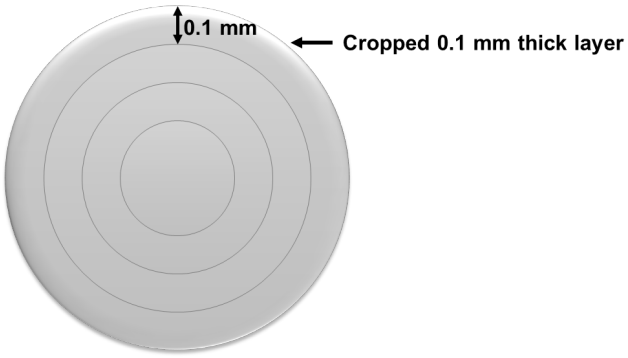

Figure 3-13. Illustration showing the cropped layer of carbonated material assumed in a cylindrical sulfate-activated slag cement for analysis of the XRD-CT results

3.7.2 Workflow adopted for processing of the μCT results

3.7.2.1 Volume of interest

The volume of interest (VOI) for reconstructed tomography, as a proportion of the full data set, was selected large enough to reduce the computation time without introducing statistical errors [25]. In this study, 500 x 500 x 500 voxels (cubes with 350 μm length) were cropped from the entire data set as the VOI. Previous studies suggest that the VOI should be larger than 100 μm^3, or at least 3 times larger than the largest feature in Portland cement paste [292]. Thus, the cropped VOI is deemed sufficient for quantification analysis.

3.7.2.2 Segmentation in uCT datasets and validation

Segmentation involves selecting certain threshold values to distinguish the pore space, unreacted slag, and reaction products. Figure 3-14A shows the histogram of the cropped region from μCT tomographs, where it is clearly seen that the three main types of features are intermixed. The most widely used segmentation methods are local and global grayscale thresholding [293, 294]. Those methods depend on histogram evaluation and ignore the spatial distribution of pixels [295]. Also, these methods rely on the accuracy and robustness of the image quality [296]. Due to the formation of Ca-bearing type-gel phases expected in the cements evaluated with fine pores, the low X-ray attenuation coefficient of the reaction products leads to intermixing with the pores generated by the consumption of the precursors [25]. Therefore, machine learning-based Trainable WeKa Segmentation (TWS) in Fiji was used in this study, and this algorithm classifies each phase based on its feature shape rather than just on the greyscale values [297]. This method has been successfully applied in the segmentation of images of cementitious materials [236]. Three phases (slag, reaction products and pores) were manually identified by sketching the respective regions in 40 randomly selected data slices. A representative example of one segmented slice is presented in Figure 3-14B. The segmented results were compared with the original images. Then, the sketching step is repeated until satisfactory results are obtained by checking the value for the out-of-bags error, which is the percentage of misclassification of predicted pixels by the random forest classifier [298]. The lowest out-of-bag error is the one suited for the classification. The satisfied classifier is then applied to the cropped VOI. Figure 3-15 presents the 3-dimensional rendering of the reconstructed tomography of sodium sulfate-activated slag cements using S2 and segmented phases with corresponding volume fractions.

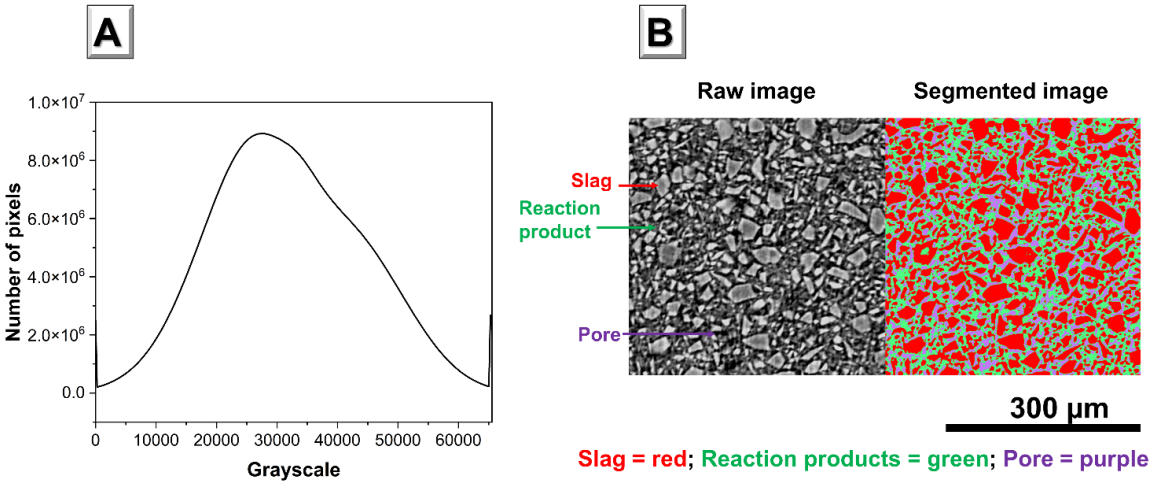

Figure 3-14. (A) The histogram of VOI; (B) One slice of µCT image using WeKa segmentation

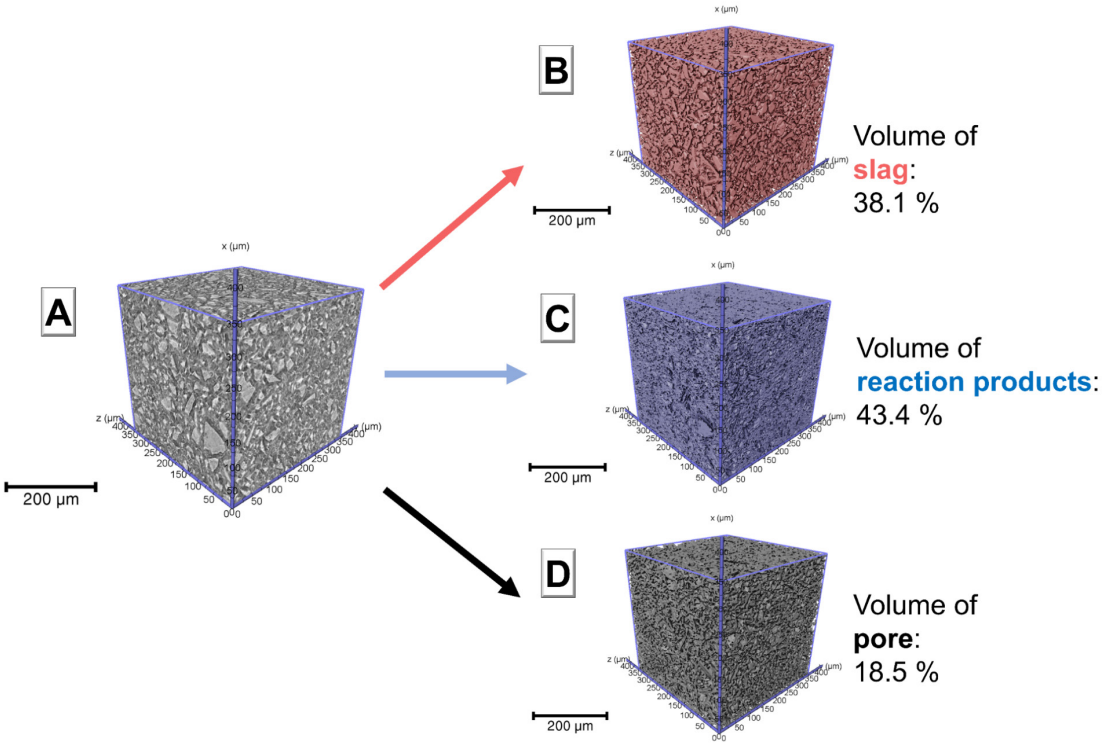

Figure 3-15. (A) 3D rendering of reconstructed tomography of sodium sulfate-activated slag cements using slag S2 before accelerated carbonation; (B) segmented slag; (C) reaction products; (D) pore

In order to validate the accuracy of segmentation in uCT datasets, electron microscopy image analysis was used to cross-check the volume fraction of the slag and then the DoR of slag in sodium sulfate-activated slag cements, based on equations 3.1 and 3.2. Figure 3-16 shows examples of SEM images for sodium sulfate-activated slag using three slags studied. DoR determined by SEM image analysis is applied to validate the segmentation of μCT images. At each curing age of the sample, at least 40 images were taken at 2000 x magnification for image analysis. The global thresholding method was used to segment the unreacted slags and pores, which has been proven to successfully segment phases in SEM images [275]. Table 3-3 presents the range of threshold values for pore, reaction products and unreacted slag, respectively.

Table 3-3. The threshold value range of sodium sulfate-activated slag after 28 days of curing

	Pore	Reaction products	Slag
S1	**0-124**	**125-186**	**187-255**
S2	**0-106**	**107-156**	**157-255**
S3	**0-111**	**112-193**	**194-255**

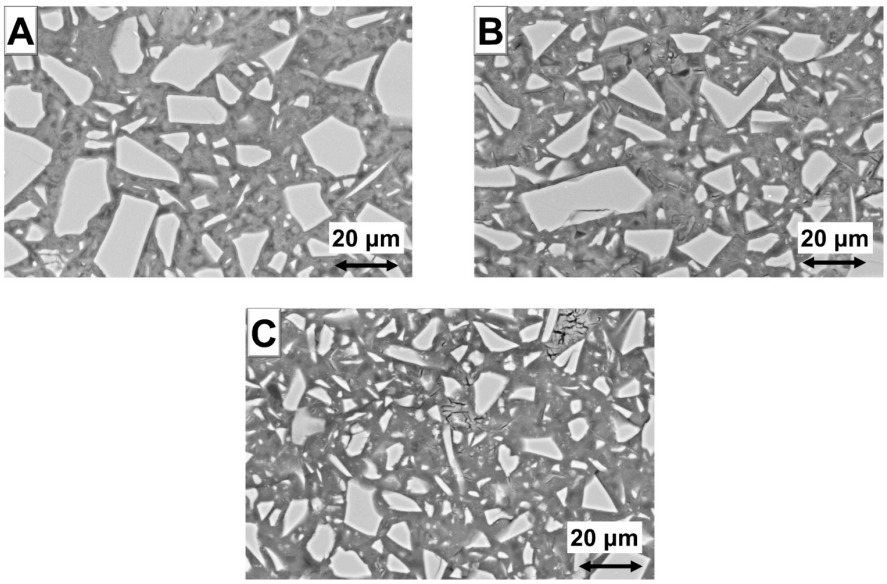

Figure 3-16. SEM images of sodium sulfate-activated slag using slag S1(A), S2(B) and S3 (C), after 28 days of curing

Different techniques and methods can be adopted for determining the DoR of slag in cementitious materials, such as selective dissolution [299], electron microscopy image analysis [300] and ^{29}Si nuclear magnetic resonance (NMR) [301]. It has been suggested that BSE image analysis and ^{29}Si MAS NMR can provide a reasonable precision of DoR of slags [300, 302]. To the best knowledge, there are no reported results in image analysis either using BSE and μCT of sodium sulfate-activated slag cements. Comparable DoR was observed (Figure 3-17) within one σ standard deviation, using image analysis in 2D (SEM) and 3D image (μCT) in this study, independently of the slag used. The values reported here are also comparable to the DoR based on the deconvolution of ^{29}Si MAS NMR using a similar mix design [161], which reveals the accuracy of segmentation and ground knowledge of this material. The cements produced with the S1-slag with the higher Mg/Al ratio present a higher degree of slag reaction, consistent with other studies where it has been reported that a high Mg/Al ratio favours the formation of a higher amount of products C-A-S-H type gel and secondary reaction products ettringite and LDH phases [63, 84].

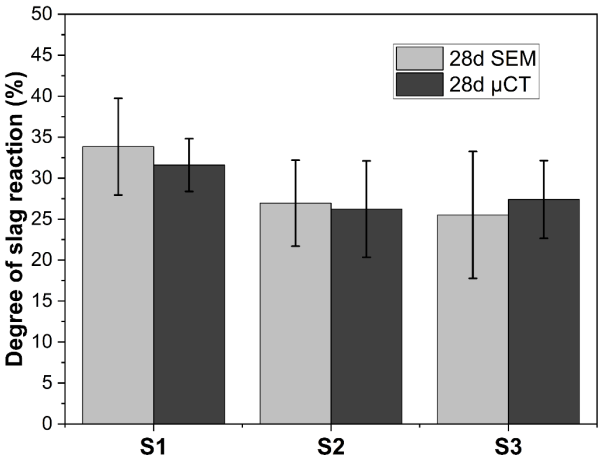

Figure 3-17. Calculated degree of slag reaction (DoR) comparison using SEM and μCT of sodium sulfate-activated slag cements using slag S1, S2 and S3 after 28 days of seal curing

3.7.2.3 Characterisation of the pore network

The 3D pore size distribution determination of the evaluated cement pastes was conducted using Label Analysis in Avizo. To avoid noise and reduce statistical errors in μCT measurements, the segmented pore larger than 3 times voxels, which is estimated to the spatial resolution, was considered. Voxel size is calculated by dividing the field of view (FOV) by the matrix size, while resolution refers to the system's ability to distinguish between closely spaced structures, typically assessed in terms of spatial or contrast resolution [240]. In addition to pixel

size and matrix size, resolution is heavily influenced by various technical factors of the CT system, such as detector technology [241], X-ray characteristics [242] and reconstruction algorithms [222]. The spatial resolution ranges from 2.5 to 10 times the voxel size, depending on the noise level. The 4th generation synchrotron source at ESRF provides a high flux of X-rays and coherence, enabling the generation of high-resolution images. Therefore, a spatial resolution of 3 times the voxel size is sufficient for analysis and segmentation. In addition, the segmented slag and degree of slag reaction are validated using SEM analysis, as shown in Fig. 3-17. All point-adjacent pores (only 1 pixel) were separated using the Separate Object algorithm. The pore size was calculated as a function of the equivalent sphere diameter. Similar approaches have been used to characterise the pore size distribution of other cement systems [236, 303].

Porosity was calculated as a percentage of the segmented pores in the volume of interest (VOI), using the Volume Fraction algorithm in Avizo. The error bar for the porosity value is calculated based on the probability map collected from the segmented pore using trainable WeKa segmentation. The range from the lower to the upper bar is based on the σ value of a Gaussian distribution. The probability maps of porosity for cements based on all three slags before and after carbonation are shown in Figure 3-18. The probability map of porosity for each 0.1 mm layer from the exposure surface to the core of the specimen, as depicted in Figure 3-13, is presented in Figure 3-19.

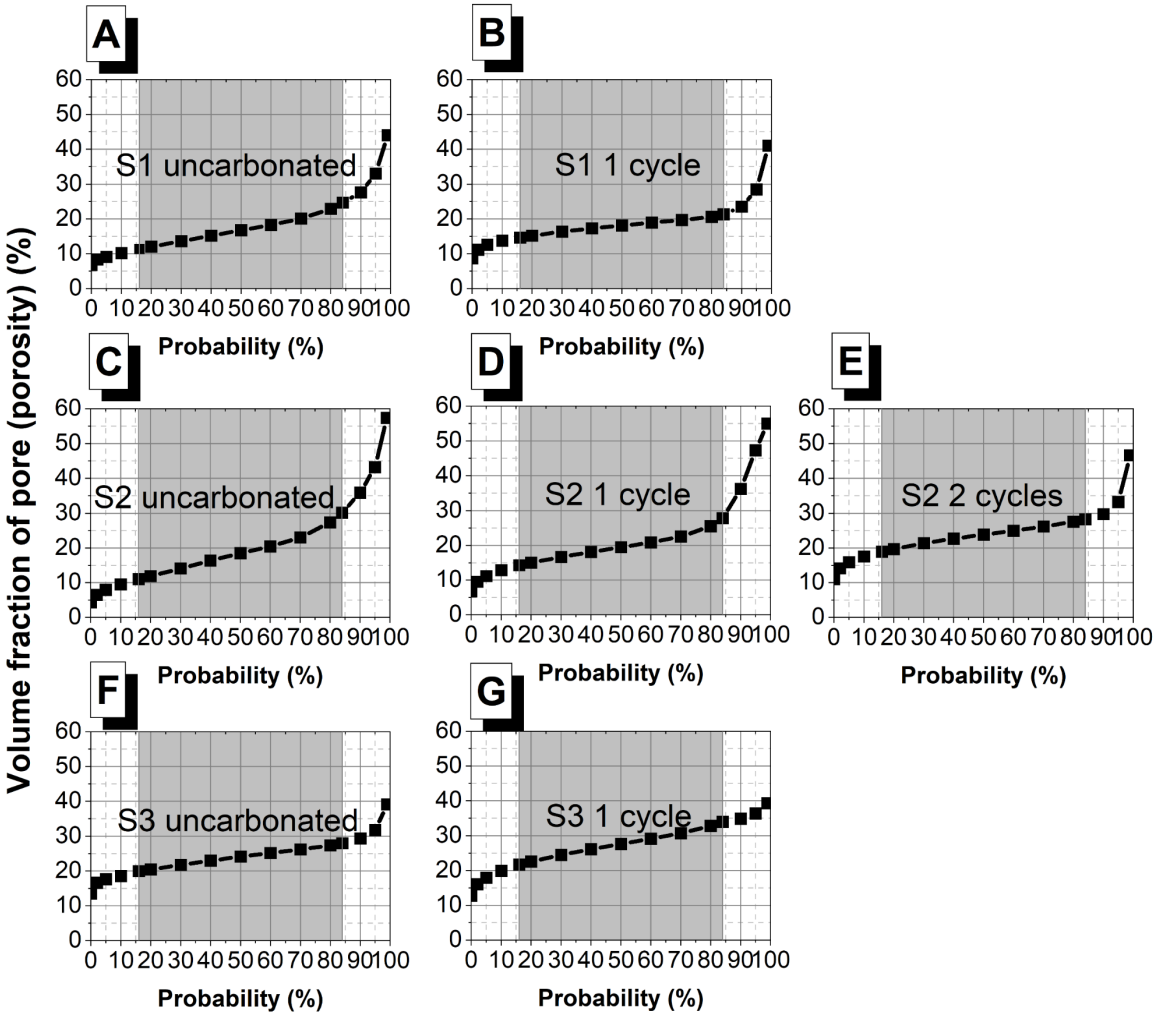

Figure 3-18. Probability of porosity for sodium sulfate-activated slag cements using slag S1, S2 and S3, before and after 1 cycle and 2 cycles of carbonation (slag S2 only)

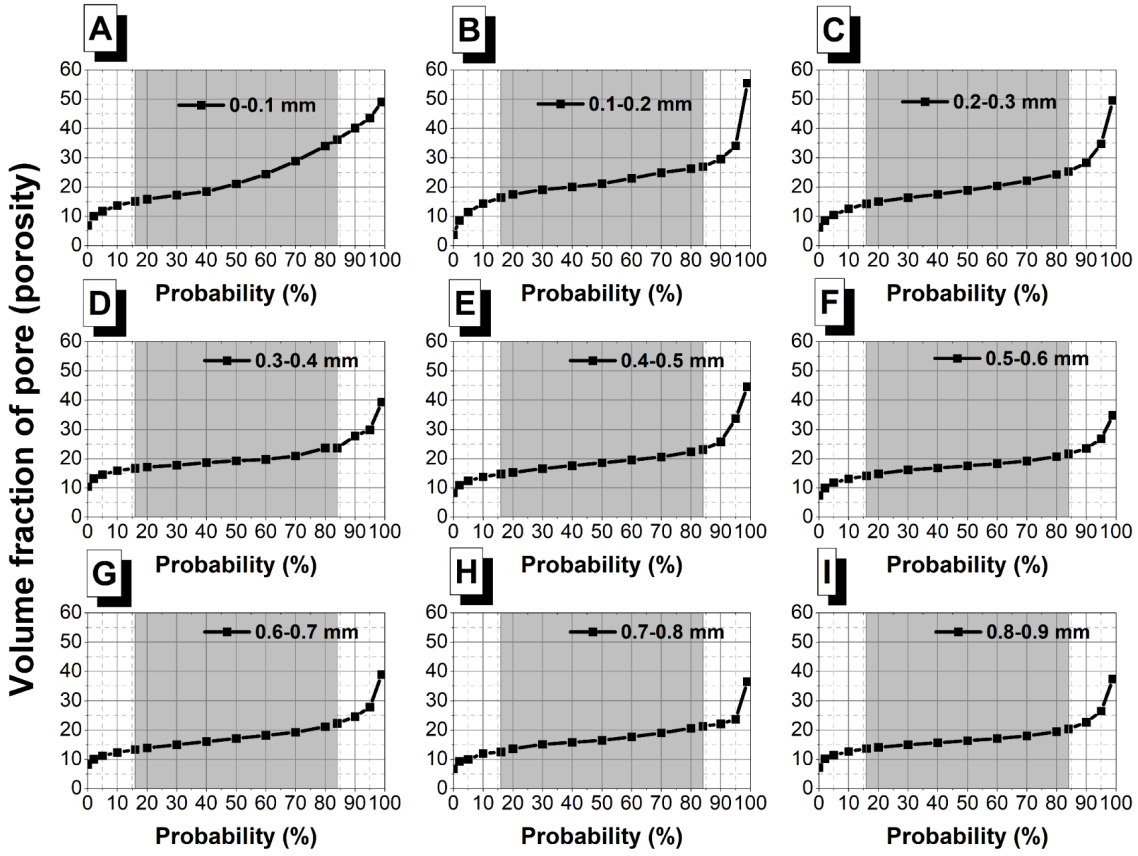

Figure 3-19. Probability distributions of porosity values resulting from segmentation, in cropped layers of sodium sulfate-activated slag cements using slag S2 after 2 cycles of carbonation

3D pore network information is important as a means to infer the likely performance of cementitious materials. The ionic transport only happens in the connected capillary pores of cementitious materials [25, 244], so the ability of deleterious substances to enter the material and influence its durability, is controlled by the interconnected pore structure. The statistical analysis of the 3D pore network was conducted based on the images of the segmented pore phase (binary). As the connected pores mainly influence the durability of cementitious materials, only face-adjacent pores were considered for pore connectivity. This was done by using the axis connectivity algorithm within Avizo in the type of 6-connectivity, so voxels sharing a vertex or edge were not defined to be connected. Then, this cluster of pores is used to characterise diffusion tortuosity and formation factor.

3.7.3 Determination of diffusion tortuosity and formation factor

Diffusion tortuosity is an essential parameter for predicting mass transport in porous media [304]. The diffusion tortuosity is defined as the mean free distance divided by the Euclidean distance from the start to the endpoint [305]. Then, this parameter is calculated by dividing the effective diffusion coefficient by the bulk diffusion coefficient through free space [306]. This value was determined using the pytrax Python module [307]. Similar to diffusive flow, this algorithm intends to simulate Brownian motion, and the tortuosity mathematically relates diffusivity in the pore network to diffusivity in free space [308]. Each walker has an equal and unbiased probability of movement in any direction allowed by the geometry of the pores (i.e. not moving through voxels defined as being solid), following a Gaussian distribution. Tests were conducted for 10^6 time steps and 20,000 random walkers for each sample. These parameters were based on previous studies in alkali-activated slag cements that showed no significant change in the diffusion tortuosity with minimised uncertainty [23, 25].

The simulation of the formation factor was conducted in the Avizo package Formation Factor Effective Simulation in XLab. Ohm's law defines the transportation of electrical charges within a fully saturated pore solution (electrolyte) under applied constant electrical potential difference in a segmented 3D pore structure. The formation factor was calculated based on Archie's law as a ratio of the resistivity of cement paste ρ_c (Ω m) to the resistivity of the water ρ_{water} (Ω m) [309, 310].

$$F_F = \frac{\rho_c}{\rho_{water}} \qquad \text{(Equation 3.5)}$$

It was assumed that the pore space was fully saturated so that all the segmented pore structure was considered in the simulation. The conductivity of the electrolyte (pore solution) is based on thermodynamic modelling in pore solution chemistry of sodium sulfate-activated slag cements, as a function of slag composition. It is expected that different slag compositions lead to different pore solutions with corresponding resistivity values. Detailed thermodynamic modelling has been discussed in section 3.3.5.

The input potential is 1 V, and the output potential is defined as 0 V. The electrical conductivity is independent of boundary conditions, and the formation factor is intrinsic to the segmented porous network [311]. This modelling approach calculated the electrical conductivity of the porous media, and the electrical resistivity is reciprocal of the conductivity value. The formation factor simulation was conducted along the X, Y and Z axes separately, so the standard deviation was based on the formation factor along those 3 axes.

3.7.3.1 Calculation of pore solution resistivity using thermodynamic modelling

The pore solution resistivity was calculated based on the ionic composition of the pore solution at a given DoR in Figure 3-17 and slag composition as shown in Table 3-1. The resistivity of the pore solution is then calculated using equation 3.6 and 3.7:

$$\rho_s = (\sum_i z_i c_i \lambda_i)^{-1} \quad \text{(equation 3.6)}$$

Where the ρ_s [S/m] is the resistivity of the pore solution, z_i and c_i are the valence and molar concentration for each ionic species. λ_i is the equivalent conductivity of each ionic species, which can be calculated using equation 3:

$$\lambda_i = \frac{\lambda_i^0}{1+G_i I_M^{0.5}} \quad \text{(equation 3.7)}$$

where λ_i^0 is the equivalent conductivity of the ionic species at infinite dilution, Gi $(mol/L)^{-0.5}$ is the empirical coefficient for each and I_M (mol/L) is the molar ionic strength of the solution. Properties of these ionic species at 25 °C are obtained from [198]. Pore solution resistivity of sodium sulfate-activated slag cements using slag S1, S2 and S3 after 28 days of curing is shown in Figure 3-20. The calculated results are comparable to experimental results for alkali-activated slag cements [24] and modelling results for blended slag cements with 40 % Portland cement replacement [198].

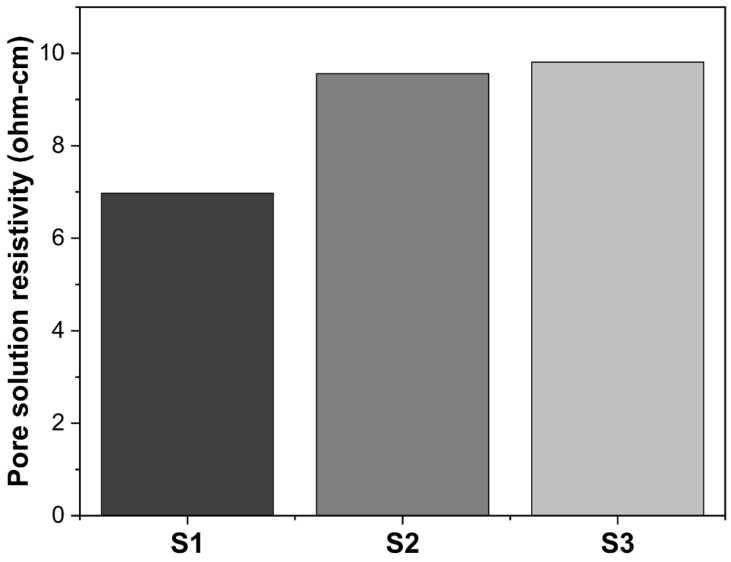

Figure 3-20. Pore solution resistivity of sodium sulfate-activated slag cements using slag S1, S2 and S3 after 28 days of curing

3.8 Troubleshooting in XRD-CT measurement

Figure 3-21A shows the ideal scenario for XRD-CT results presenting powder-like diffraction rings, as the particle size of crystals is smaller than the beam size. However, the main issue with the synchrotron XRD-CT of analysed samples in this study is unreacted crystalline particles, whose particle size is comparable to or larger than the beam size, as shown in Figure 3-21B. These unreacted crystalline particles are impurities in the slag [19] and do not contribute to overall chemical reactions, such as calcite and quartz. However, their presence and Bragg diffraction then lead to a few high-intensity spots in the diffractograms. A similar observation was also reported in the previous XRD-CT measurement of Portland cement (PC) paste and mortar samples that the larger crystallite size of clinker phases, such as alite, and natural aggregates causes diffraction spots in the detector [253]. In the current study, the quartz diffraction spot is one order of magnitude higher than the threshold of the detector, using 50 keV X-rays. The detector will then automatically shut down as a means of self-protection. This then causes failure of experiments such that even the XRD pattern before the main peak of quartz (the most troublesome point) cannot be collected (Cu Kα equivalent 2θ angle of 26.65°).

In order to collect the results before the main peak of quartz, the detector was moved further away from the sample so that troublesome diffraction spots were excluded from the detector, as shown in Figure 3-22A. However, the detector has a square shape, so troublesome reflections still appear in the corners of the detector. A lead mask was then used to block out troublesome

reflections, leaving a 142 mm diameter hole, as shown in Figure 3-22B. The XRD-CT was then successfully run for S2-based samples, due to the lower amount of quartz in slag S2 compared to slag S1 and S3. Note that in all slags, the amount of quartz present, which caused these severe issues in the XRD-CT experiments, was barely detectable by conventional laboratory XRD.

Future work should therefore bear in mind the size of unreacted crystalline phases in the samples. To produce smooth powder-like diffraction rings with high-quality XRD-CT results, it is important to control the size of crystallite size one order magnitude smaller than the beam size [253]. It is not problematic for analysing the reaction products in cementitious materials, such as aluminium-substituted calcium silicate hydrate, ettringite and hydrotalcite, as those reaction products are intermixed below the micro-scale [312]. This technique is more sensitive to raw or unreacted crystalline materials compared to reaction products.

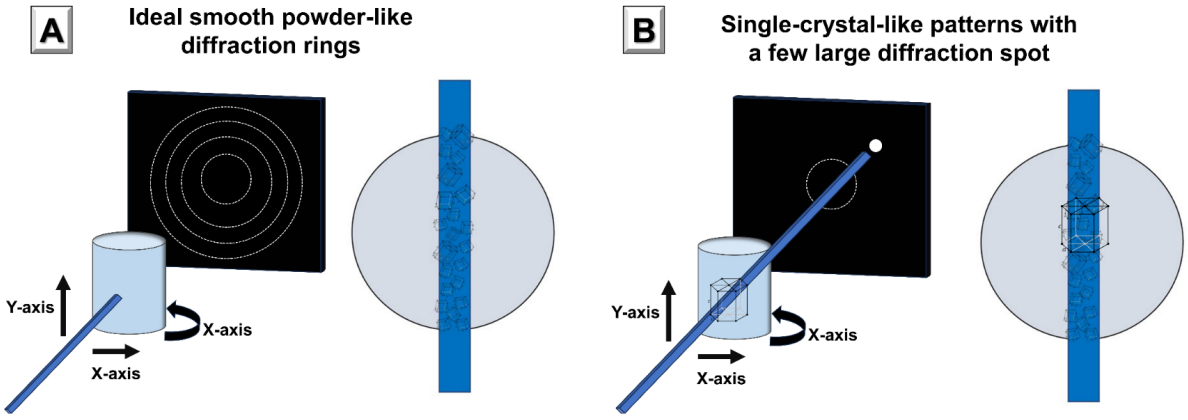

Figure 3-21. (A) The ideal scenario showing smooth powder-like diffraction rings; (B) The current scenario showing single-crystal-like diffraction spots

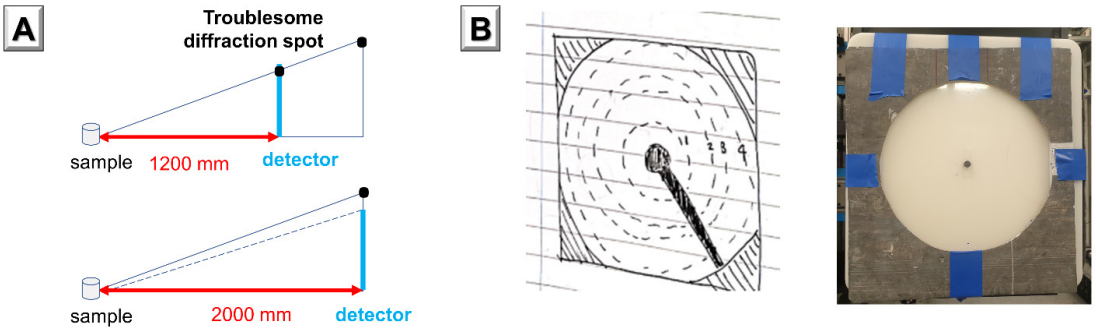

Figure 3-22. (A) Method 1: Moving the detector further away so that higher reflection angles were not included in the detector. (B) Method 2: Use a lead mask to block out troublesome reflection at higher reflection angle

Chapter 4

PHASE EVOLUTION AND PERFORMANCE OF SODIUM SULFATE-ACTIVATED SLAG CEMENTS PASTE

Note: This chapter is primarily based on the paper "*Phase evolution and performance of sodium sulfate-activated slag cement pastes"* by **Z. Yue**, Y. Dhandapani, S. A. Amankwah; S. A. Bernal**,** CEMENT (2024): 100117.

4.1 Introduction

This chapter evaluated the reaction kinetics, phase assemblage, and microstructure evolution of Na_2SO_4-activated slag cements produced with three commercial slags. This was achieved by following a multi-technique approach using different materials characterisation analytical techniques for analysing paste samples for up to 1 year of curing. Additionally, thermodynamics modelling was used to validate the experimental results and elucidate the reaction mechanisms leading to the differences identified in the materials evaluated.

Results revealed that the main reaction products forming in these cements are ettringite and calcium aluminosilicate hydrates, alongside a poorly crystalline SO_4^{2-} intercalated Mg-Al-layered double hydroxide (LDH) phase. The Al_2O_3 slag content alone does not correlate with the cement performance. While pastes made with a higher Al_2O_3 content slag exhibit faster reaction kinetics, those made with a slag with a higher Mg/Al ratio developed superior compressive strength and reduced porosity over extended curing periods. Thermodynamic modelling simulations indicate that sulfate consumption occurs via ettringite and LDH phase formation, influencing the slag reaction degree, pH value, and porosity reduction in these cements. This research highlights the critical role of slag composition in controlling microstructure and, consequently, cement performance.

4.2. Experimental methodology

Raw materials characterisation, mix design, sample preparation and materials characterisation are reported in Chapter 3.

4.3 Results and Discussion

4.3.1 Reaction kinetics determined by isothermal calorimetry

Figure 4-1 presents the heat flow and cumulative heat of Na_2SO_4-activated slag pastes produced with the three different slags studied. The shape of the curve is consistent with what has been reported for other alkali-activated slag systems, such as sodium silicate and sodium carbonate [18, 136, 174]. A pre-induction period is observed in the first few hours, followed by an extended induction period. Depending on the type of activator, the induction period could last a few hours or days [18, 21, 84]. The high-intensity acceleration and deceleration periods are then observed, which are related to the formation of reaction products [136]. A significant difference was identified in the kinetics of reaction between slag S1, and the other two slags evaluated. Although the glassy fraction of the slag has a significant effect on the slag reactivity [94], the three types of slag used in this study are highly amorphous, based on the XRD patterns of three raw slags shown in Figure 4-2. The difference in the reaction kinetics is likely due to the differences in the chemical composition of the slag, and slight differences in particle size distribution and specific surface area, depicted in Figure 3-2 and Table 3-2 in Chapter 3.

The S2 and S3-based pastes have similar induction periods (about 150 h) despite slight compositional differences. A longer induction period was observed in S1-based paste (about 300 h). Previous studies on NaOH-activated slag, super sulfate slag cement and Na_2SO_4-activated slag cement have reported that the higher amount of Al_2O_3 content in the slag accelerates the reaction kinetics [21, 84, 90]. This observation agrees well with the R^3 test for three slags used in this study (Fig. 3-3) that higher Al_2O_3 content is more reactive with improved reaction kinetics in the first 50 hours of reaction.

The intensity of the acceleration peak in S3 is similar to that of S2, however, a smaller heat peak is observed in S2 during the induction period suggesting some preferential dissolution of the slag, showing accelerated reaction kinetics and a minor increase in cumulative heat before first 180 hours of reaction. However, after 400 hours of reaction, the cumulative heat is comparable for both S2 and S3-based pastes.

Additionally, it is observed that the tail of the deceleration period (Figure 4-1A) seems more pronounced for the S1-based binder. This is the slag that showed slightly higher chemical reactivity according to R^3 test results (Fig. 3-3, chapter 3) and also presents the highest Mg/Al of the slags used in the study. Given the negligible differences in the specific surface area of the slags evaluated (Table 3-2, chapter 3), it is reasonable to suggest that the composition of the slag is influencing the reaction kinetics of these cements, as it has been observed in other studies [84]. The cumulative reaction heat (Fig 4-1B) is an indication of the degree of slag reaction [263]. Despite the extended induction period observed in S1-based pastes, the cumulative heat is comparable to that of S2 and S3-based pastes after 400 hours of reaction.

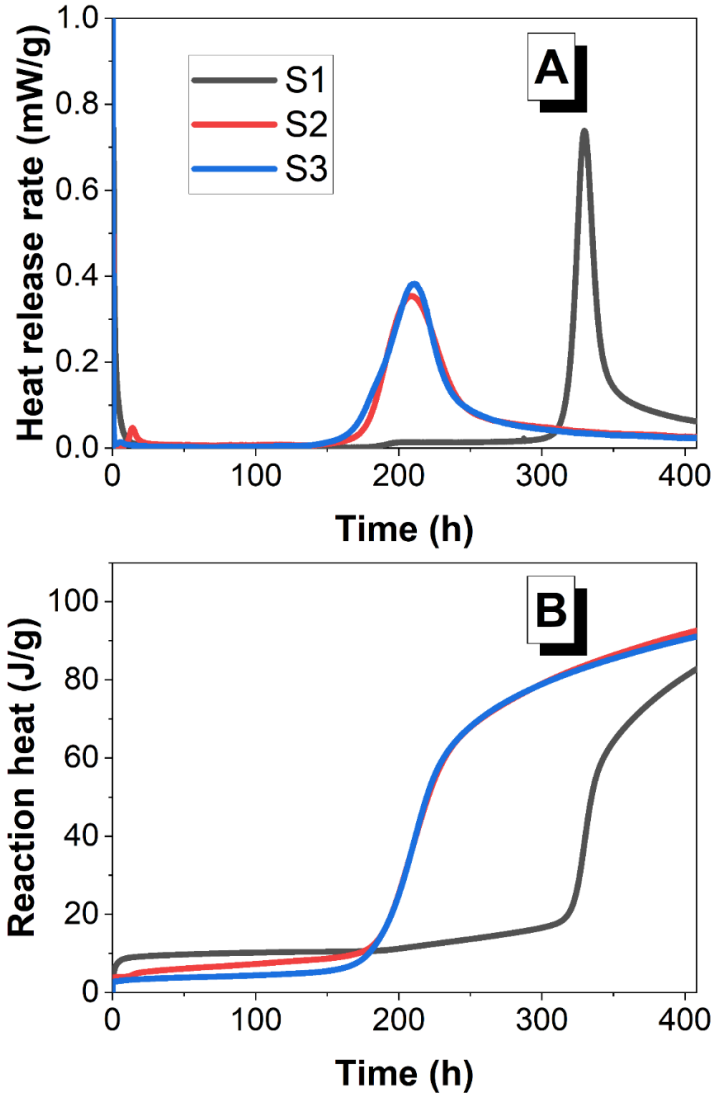

Figure 4-1. Isothermal calorimetry results of Na_2SO_4-activated slag as a function of slag source. Heat flow and cumulative heat curves correspond to A and B, respectively

4.3.2 Phase assemblage determined by X-ray diffraction

Figures 4-2 (A-C) show the X-ray diffraction patterns of the Na_2SO_4-activated S1, S2 and S3 cement pastes, respectively. Traces of calcite (powder diffraction file (PDF) #01-083-0578), gehlenite (PDF#01-079-1726), akermanite (PDF#98-008-0391) and quartz (PDF#01-081-0069) are identified in the anhydrous slags (S1 and S3). Independent of the slag chemistry, the main crystalline reaction products identified in this study are ettringite (E) ($Ca_6Al_2(SO_4)_3(OH)_{12}\cdot 26H_2O$, PDF# 00-013-0350) and a tobermorite-type C-(A)-S-H (PDF# 00-019-0052). These results are consistent with previous studies [63, 66, 84, 161]. A hydrated sodium magnesium sulfate mineral bloedite ($Na_2Mg(SO_4)_2\cdot 4H_2O$) was observed in S1-based pastes.

The reflections of ettringite, especially its main plane (100) at about 9.14° 2θ°, were more intense in the S3-based paste than S1 and S2, arguably related to higher aluminium content in the slag S3. A similar observation was also reported for other sodium sulfate-activated slag cements and super sulfate slag cement systems [84, 90]. The XRD patterns show that the intensity of the main ettringite peak decreases at longer curing times in all three slags. In the Portland cement system, the continuously released $Al(OH)_4^-$ causes the dissolution of the ettringite with the formation of monosulfate [313]. Thermodynamic modelling of Na_2SO_4-activated slag had shown that higher Al could favour the conversion of ettringite to AFm phases [284]. However, a peak associated with monosulfate between 10-15 2θ° was not observed in the current study. This may be due to the small quantities and less crystalline nature of this phase, which if present, is highly intermixed [314].

Mg-Al LDH-type phases were not observed in the diffractograms of the three slags evaluated, independently of the curing duration. The main peak of Mg-Al-LDH phases (intercalated with CO_3^{2-}, OH^- or SO_4^{2-}) is in the (003) plane at about 11.40° 2θ° [95]. The absence of this phase in XRD results is either related to the low MgO content within the slag hindering the formation of such phases, [18] or the poorly crystalline structure of the Mg-Al-SO_4-LDH phase [95].

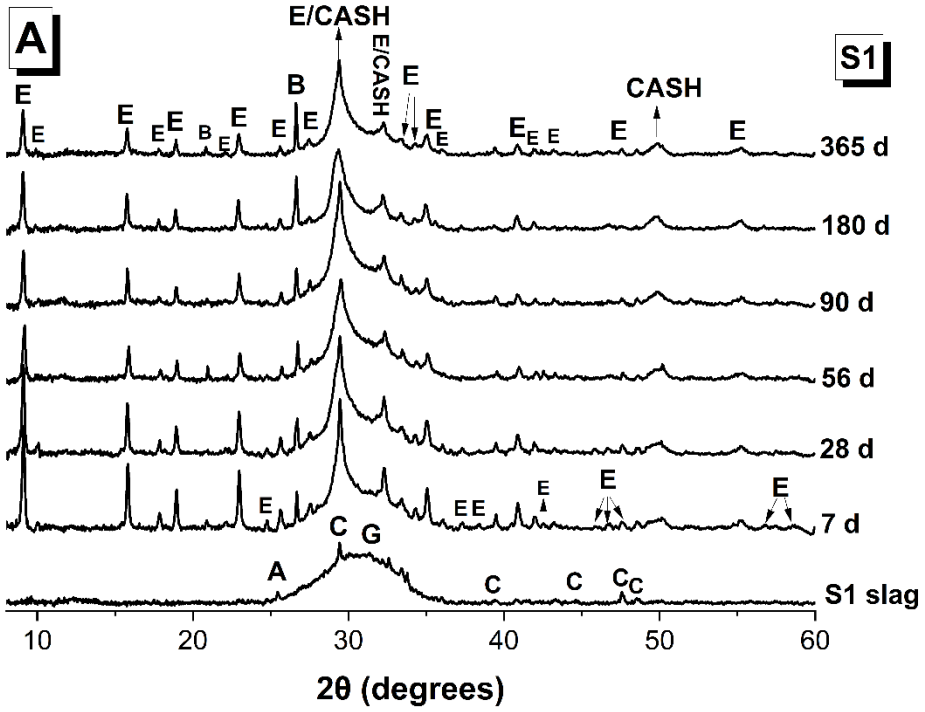
A
S1
E/CASH
E/CASH
B
CASH
365 d
180 d
90 d
56 d
28 d
7 d
S1 slag
C G
A
10
20
30
40
50
60
2θ (degrees)

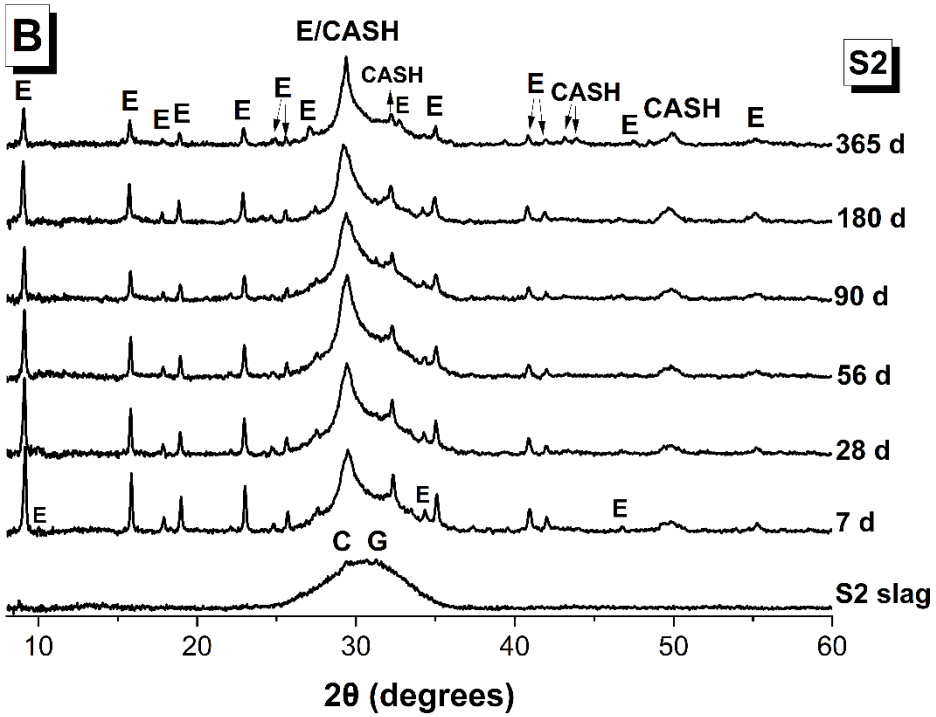
B
S2
E/CASH
CASH
365 d
180 d
90 d
56 d
28 d
7 d
S2 slag
C G
10
20
30
40
50
60
2θ (degrees)

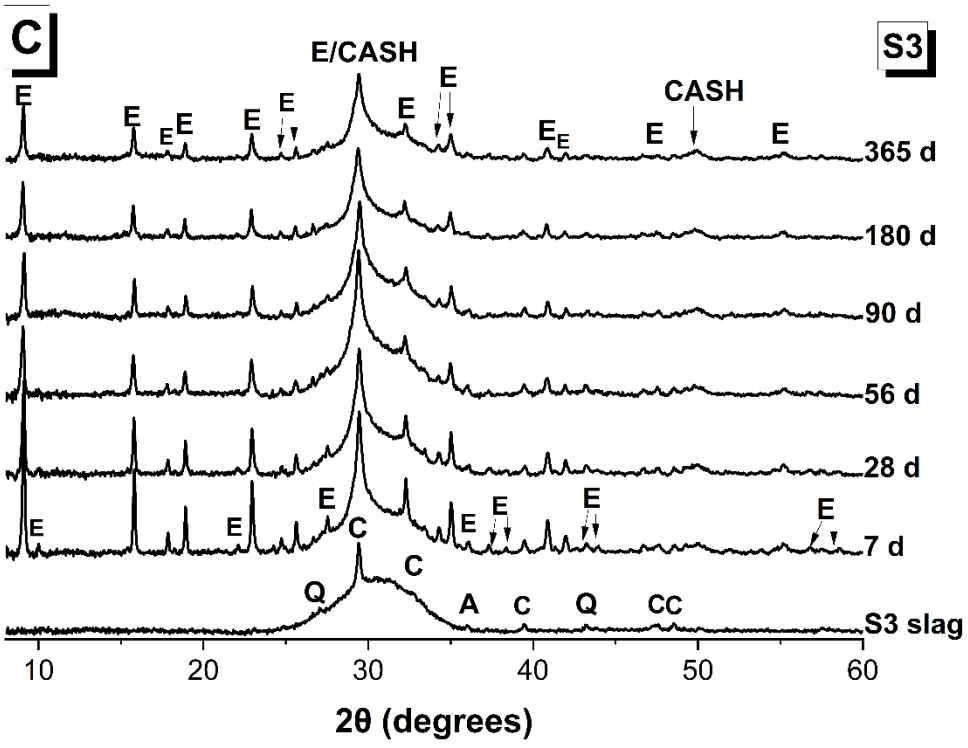

Figure 4-2. X-ray diffraction patterns of Na_2SO_4-activated slag by using slag S1, S2 and S3 with time. Notes: Phase marked are E-ettringite, C-A-S-H-calcium aluminate silicate hydrate, B-bloedite (American Mineralogist Crystal Structure Database), c-calcite, A-akermanite, G-gehlenite and Q-SiO_2

4.3.3 ^{27}Al MAS NMR spectroscopy

Apart from the main Al-bearing reaction products ettringite and C-(A)-S-H type gels, secondary Al-bearing reaction products that might be forming in the assessed binders, since AFm and/or Mg-Al-SO_4-LDH-type phase were not identified by XRD. Therefore, ^{27}Al MAS NMR spectroscopy was applied to potentially identify poorly crystalline Al-bearing phases that might be forming in these cements. The spectra of the unreacted slag (Fig. 4-3) exhibited an asymmetric and broad resonance of 58-59 ppm associated with Al^{IV} sites, consistent with the highly disordered nature of blast furnace slags [315].

Figure 4-3 presents the ^{27}Al MAS NMR spectra of Na_2SO_4-activated slag produced with slag S1, S2 and S3. The Al^{VI} region is assigned to range between δ_{iso}= 0 and 20 ppm [316] of all spectra. The resonance centred at δ_{iso} = 13 ppm is attributed to ettringite [317]. This resonance is sharper in S3 containing the highest Al content (12.01 wt.%, Table 3-1, Chapter 3) compared to other slags used. The intensity of the ettringite peak increases for all three slags with time

evolved from 28 d to 180 d. However, the band intensity decreases at 365 d. This observation in single pulse ^{27}Al MAS NMR is consistent with the XRD results that show a reduction in the ettringite peak intensity at later ages. Therefore, both the XRD pattern and ^{27}Al MAS NMR results indicate a decreased amount of ettringite in these cements at extended curing age.

Unlike XRD results, the Mg-bearing phase Mg-Al-LDH was observed in this system via ^{27}Al MAS NMR spectra. The low-intensity shoulder centred at δ_{iso}= ~ 9 ppm is attributed to the hydrotalcite-type phase containing Al^{VI} sites [318, 319]. However, both the XRD pattern (Fig. 4-2) and ^{27}Al MAS NMR (Fig. 4-3) cannot indicate the type of anionic groups intercalated within the interlayer of the LDH phase such as carbonate, hydroxide or sulfate that might present in sodium sulfate activated slag cements. For the three slags, the band intensity of the LDH-type phase (δ_{iso}= ~ 9 ppm) increases following a sequence of S2 > S1 > S3 at all the curing ages evaluated. This is consistent with the MgO content in the slag (8.0 > 7.2 > 5.6 wt.%). Thus, a higher MgO content within the slag seems to be yielding to Mg-Al-LDH phases forming in Na_2SO_4-activated slag cements.

In addition, the intensity of the band attributed to the ettringite decreases at extended curing ages, which indicates that another SO_4-bearing phase could be forming from ettringite. Monosulfate exhibits a single resonance between 10 -12 ppm, depending on the field strength of the NMR experiment [320]. By comparing the 28 d results with those of later curing ages, such as 180 d and 365 d, the resonance in this range becomes broader, which could indicate the formation of minor amounts of monosulfate in all sulfate-activated slag systems, however, this cannot be confirmed using this technique.

A third resonance was also identified at δ_{iso} =4 ppm, which is hydrated cements and is often attributed to the third aluminate hydrate (TAH) [321]. This phase was thought to be an amorphous nanoscale aluminate hydrate phase precipitated at the surface of the C-(N)-A-S-H type gels. However, it has been demonstrated by Mohamed et al. [322] that this resonance is most likely silicate-bridging $[AlO_2(OH)_4]^{5-}$ sites in C-(A)-S-H type gels and therefore the TAH does not exist. Negligible changes in the intensity of this site were identified for all three slags at different curing times.

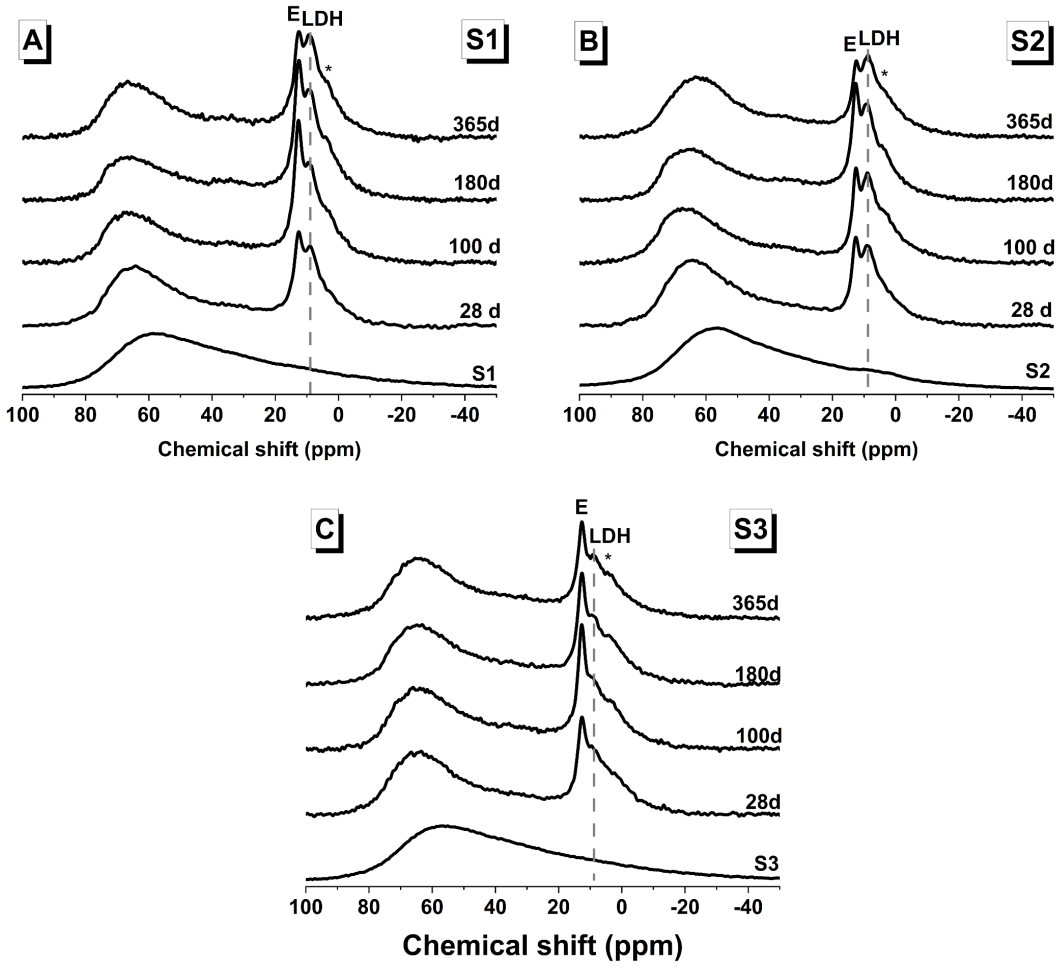

Figure 4-3. Solid state ^{27}Al MAS NMR results of Na_2SO_4-activated slag produced with slag S1, S2 and S3 as a function of the curing time

4.3.4 Thermogravimetric analysis

Thermogravimetry curves of Na_2SO_4-activated slag cements produced using S1, S2 and S3 are shown in Figure 4-4, and a summary of the total mass loss up to 1000 °C is presented in Table 1. All the paste samples exhibited a higher total mass loss at a longer curing time (Table 4-1), consistent with the increase in the reaction products forming with time due to the continued slag reaction. At 28 d of curing, the mass loss of S3 is higher than that of S1 and S2-based pastes samples, consistent with the faster reaction kinetics at early age identified for the S3-based pastes (Fig. 4-1) and higher amount of ettringite formed in samples produced with this material (Fig. 4-2 and 4-3). On the other hand, the S1 with the highest Mg/Al ratio shows a higher mass loss than other hardened pastes at 365 days of curing, meaning that a higher degree of reaction has been achieved at extended curing times.

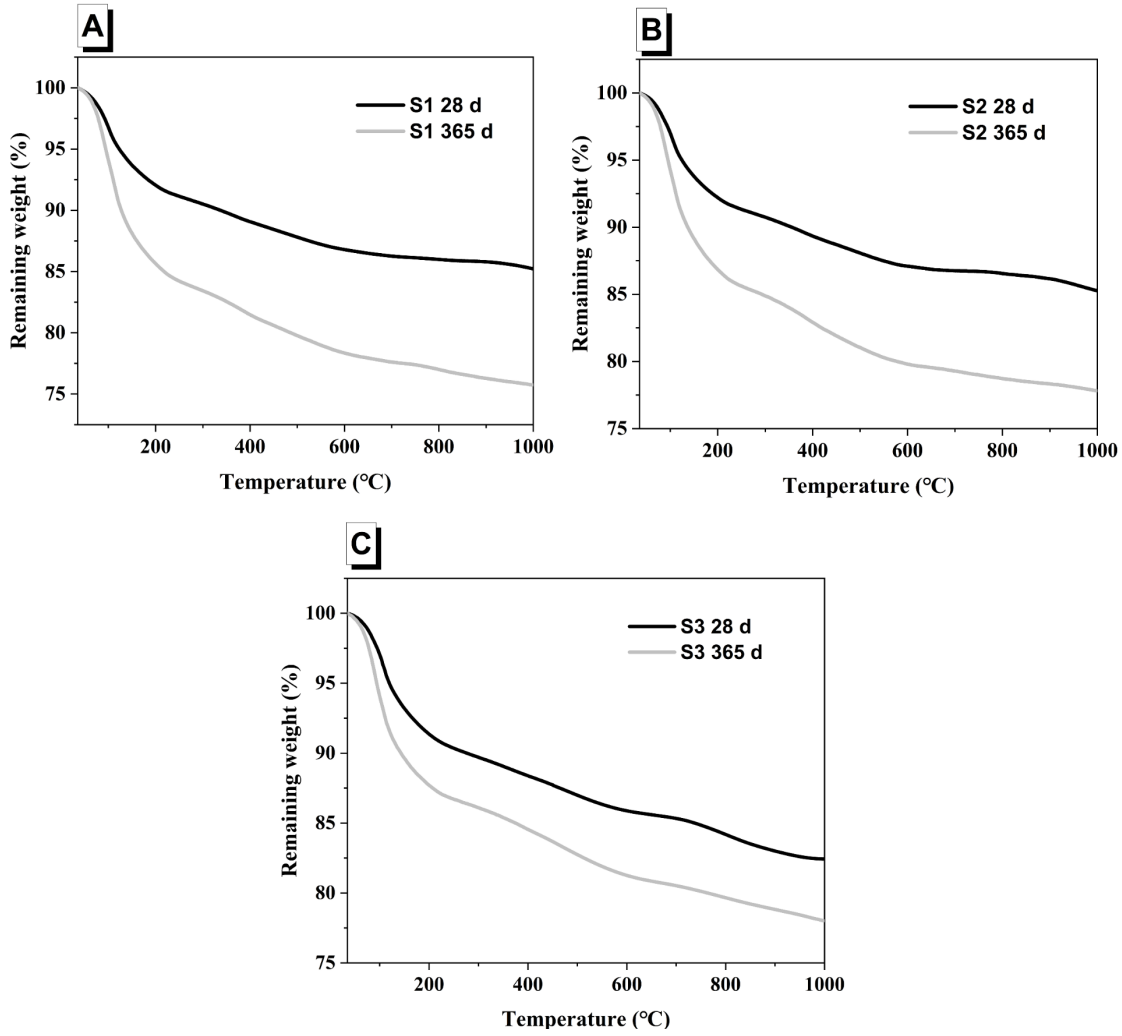

Figure 4-4. Thermogravimetry curves of Na_2SO_4-activated slag cements produced with (A) slag S1, (B) slag S2 and (C) slag S3, as function of curing time

Table 4-1. Total mass loss at 1000 °C determined by thermogravimetry of Na_2SO_4-activated slag cements (±1%)

Curing time (days)	Slag type		
	S1	S2	S3
28	14.8	14.7	17.6
365	24.3	22.2	22.0

Differential thermogravimetry (DTG) curves of Na_2SO_4-activated slag cements for S1, S2 and S3-based cements with corresponding gas mass spectra of H_2O (m/z=18), CO_2 (m/z=44) and SO_2 (m/z=64) are presented in Figure 4-5. The mass loss below 200 ℃ is related to dehydration of the C-(A)-S-H type gel [323] and the decomposition of the ettringite, which is normally observed at about 114 ℃ [324]. All three slags-paste samples showed pronounced ettringite peaks (around 114 ℃) at 28 days of curing, whereas there is a decrease in the ettringite peak at 365 d of curing, as seen from the decreased ionic current of H_2O (g) (m/z=18) shown on Figure 4-5. This further confirms the reduction in the amount of ettringite at the later age of curing as observed in XRD (Fig. 4-2) and ^{27}Al MAS NMR (Fig. 4-3). The release of SO_2 observed between 700 ℃ and 1000 ℃ is attributed to the sulfur decomposition, as H_2S from the unreacted slag is reducing under N_2 environment [258, 269] and also confirmed by TG-MS of three anhydrous slags used in this study (Fig. 3-1, Chapter 3). The ionic current of SO_2 was higher in the 28-day samples compared to the later age, meaning the lower degree of slag reaction at an early age.

A low-intensity mass loss peak between 300 ℃ and 600 ℃ accompanied by the release of H_2O can be observed for all three slags studied (Fig 4-5A, E and I). This may indicate the formation of the Mg-Al-LDH phases [95]. Mg-Al-LDH phases have been reported to show two mass loss ranges at 30-320 ℃ and 320-600 ℃ [95, 284]. The first weight loss is related to water loss, corresponding to the physically bound water and interlayer water; the second peak is related to the main layer water and water-associated intercalated anions [95]. However, it is impossible to confirm the type of intercalated anions in the Mg-Al-LDH phases form in these systems based on the techniques used in this study. It is reasonable to consider the poorly crystalline sulfate-LDHs might form, based on the sodium sulfate activator in this study [84].

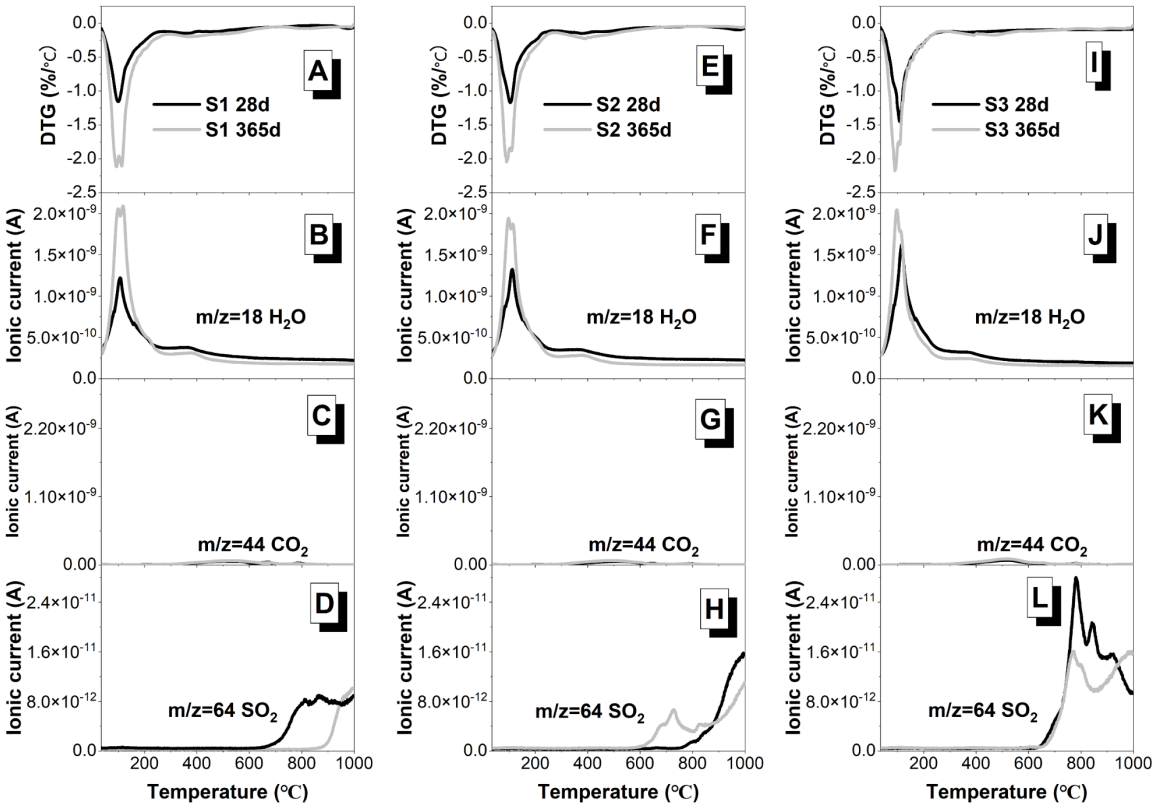

Figure 4-5. Differential derivative thermogravimetry curve of Na_2SO_4-activated slag cement using (A) S1, (E) S2 and (I) S3, as a function of curing time. Mass spectra of (B, F and J) H_2O, (C, G and K) CO_2 and (D, H and L) SO_2 are presented for S1, S2 and S3, respectively. m/z = mass/charge ratio for each ion

4.3.5 Microstructure analysis of Na_2SO_4-activated slag

Figure 4-6 shows backscattered electron images of Na_2SO_4-activated slag pastes for S1, S2 and S3 cured for 28, 56 and 365 days. The bright grey particles in the micrographs correspond to unreacted slag; the grey regions between slag particles are the reaction products i.e., mainly composed of C-(A)-S-H type gel and ettringite as indicated by XRD (Fig. 4-2). The dark regions correspond to pores in the cementitious matrix [325]. For all three slag-based pastes, the microstructures became denser and more homogeneous as the reaction progressed from 28 days to 365 days, due to an increased degree of slag reaction.

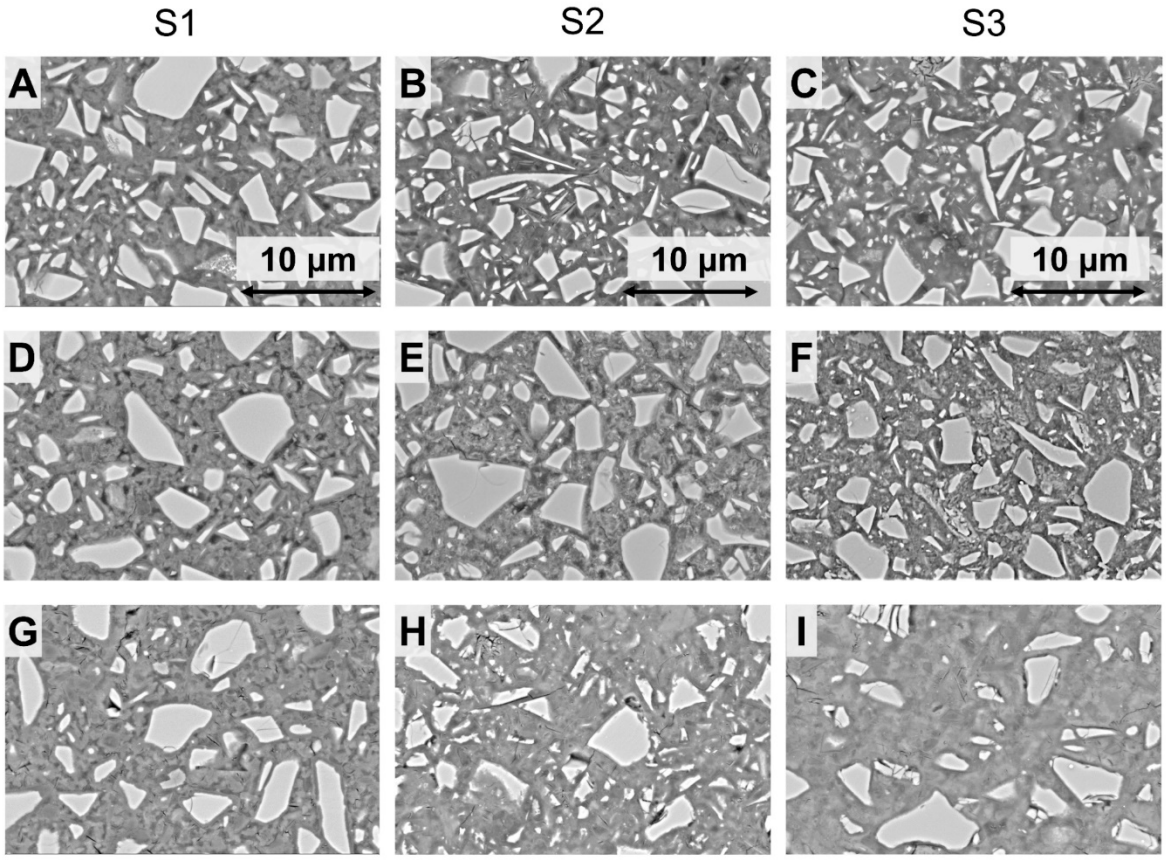

Figure 4-6. BSE images of Na_2SO_4-activated slag pastes at 2000 magnification using slags S1 (A, D, G), S2 (B, E, H) and S3 (C, F. I) cured for 28, 56 and 365 days, respectively

Figure 4-7 shows the calculated degree of slag reaction (DoR) and porosity of the studied sodium sulfate-activated slag cements, determined via image analysis. S1-based cement pastes attained the highest degree of slag reaction with the lowest porosity, consistent with the thermogravimetry results (Table 4-1). This finding is strengthened based on the R^3 test (Fig. 3-3, chapter 3) of three slags used in this study, which showed that the S1 slag has the highest reactivity over 400 hours of reaction. Similar observations have been reported for Na_2CO_3-activated slag cements [18], NaOH and Na_2SiO_3-activated slag cements when using slags with an increased Mg/Al ratio [20, 136]. Although the S3 slag-based pastes show the highest reaction kinetics in the first 14 days (Fig 4-1), it presents minor changes in the DoR and porosity from 28 to 56 days (Fig. 4-7A and 4-7B).

The results suggest that the initial chemical reactivity is not a determining factor of the longer-term DoR that can be achieved in sodium sulfate-activated slag cements. S1-based pastes with the higher Mg/Al ratio of the slags used show lower porosity at all the evaluated ages, compared

to S2 and S3-based paste samples. Independent of the slag composition, Na_2SO_4-activated slag cements can reach ~20-28 % of porosity at 28 days, ~20 % at 56 days and 15 % at 365 days.

The S1-based pastes show the highest DoR from 28 to 365 days among the three slags used in this study (Fig 4-7A). Independently of the slag composition, Na_2SO_4-activated slag cements achieve 30 % DoR at 28 days and continuously increase with age reaching at least ~55 % DoR after 1 year of curing. The range of DoR for Na_2SO_4-activated slag cements calculated in this study using BSE image analysis agrees with the report [161] which indicated that a 30 % DoR can be achieved when using a higher activator dosage (10 g Na_2SO_4 per 100 g of slag) that was used in this study at about 50 days of curing. The Na_2SO_4-activated slag cements normally show lower DoR at early age (56 days) compared to using NaOH, Na_2SiO_3 and Na_2CO_3 activators [122, 161]. Nevertheless, after 56 days of curing, the DoR of slag material between 30-50 % is comparable to the blended slag cements with 30-50 % of clinker substitution [200].

Although techniques used to determine the porosity, such as SEM, MIP (mercury intrusion porosimetry) and micro-computed tomography (uCT) detect different pore size distribution with a certain overlapping range, statistically the porosity determined by segmentation of BSE images, by using at least 35 images per age, generally agrees with the porosity measured by MIP in Na_2SO_4-activated slag cements using similar mix design and slag compositions, reaching 20-25 % of porosity after 28 days of curing [84]. A ~15 % of porosity observed after 365 days of curing is comparable to that reported for alkali-activated slag cements using conventional activators (NaOH and Na_2SiO_3) determined by MIP, image analysis of BSE images and uCT images [20, 23, 25]. The porosity values identified in Na_2SO_4-activated slag cement pastes, especially ~20 % at 56 days and 15 % at 365 days, are comparable to or even lower than metakaolin blended cements [326], fly ash blended cements [327] and slag blended cements [328], produced with 30-70 % of clinker replacement.

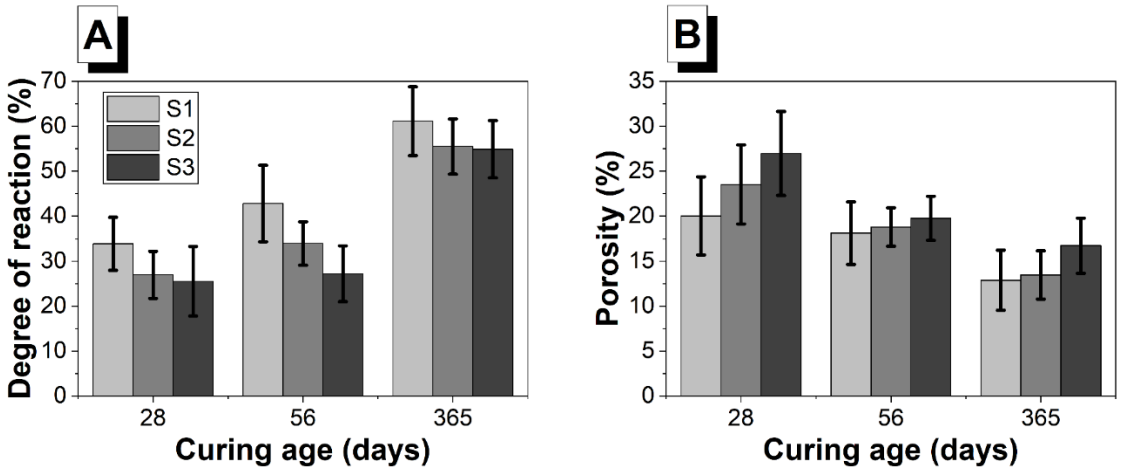

Figure 4-7. The degree of slag reaction (%) (A) and porosity (%) (B) of Na_2SO_4-activated slag cements using S1, S2 and S3 for 28, 56 and 365 days of curing based on image analysis of BSE images

Figure 4-8 shows the correlation between the degree of reaction and the porosity developed in the sodium sulfate-activated slag cements evaluated. Consistent with the OPC-based cements system, an increased degree of slag reaction led to a reduction of porosity in sodium sulfate-activated slag cements from 28 to 365 days, irrespective of the slag used.

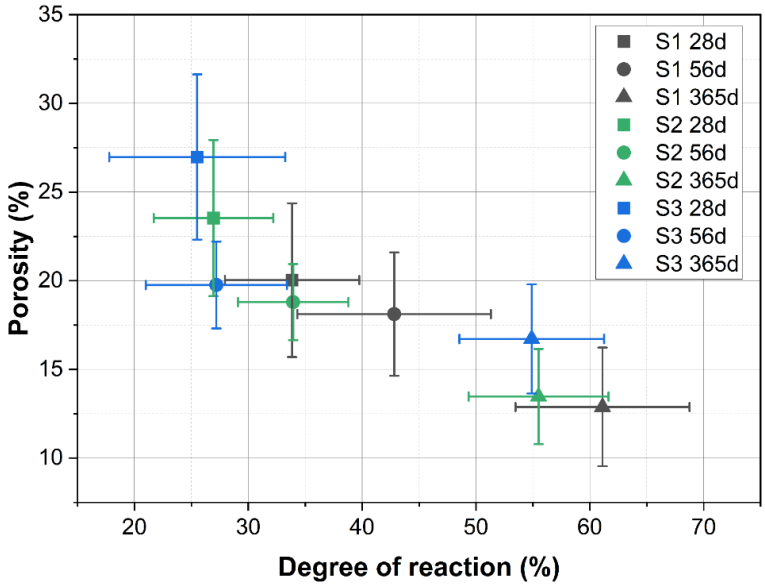

Figure 4-8. Relationship between porosity and degree of slag reaction in sodium sulfate activated slag cement pastes

Figure 4-9 presents backscattered electron imaging (BSE) and EDX elemental mapping of the Na_2SO_4-activated slag produced using S1 slag for 28 days of curing. A locally precipitated phase was observed in the region of outer reaction products. EDX mapping shows that this phase has pronounced S and Na concentrations, and depleted Ca and Si signals. Minor concentrations of Mg and Al were observed in this region. This corresponds to a sodium sulfate-rich mineral present in the sample, most likely bloedite as it is the only sodium-sulfate bearing phase observed in the XRD results (Fig. 4-2), or to a form of Na_2SO_4 precipitate from the pore solution. It is worth noting that neither thenardite (Na_2SO_4) nor mirabilite ($Na_2SO_4 \cdot 10H_2O$) were observed by XRD (Fig. 4-2)

Although the formation of ettringite has been confirmed by the different techniques applied in this study, it is still unclear how this phase spatially distributes in the microstructure of the hardened pastes evaluated. Figure 4-10 clearly shows ettringite present in the S1-cement paste in the microstructure. The locally concentrated ettringite crystals form a pocket-shaped cluster. A possible explanation for the ettringite pocket can be the precipitation of ettringite in the large pores and voids due to higher supersaturation of the ettringite phase as alumina from the slag becomes available in the presence of Na_2SO_4, which contributes to the progressive refinement of microstructure.

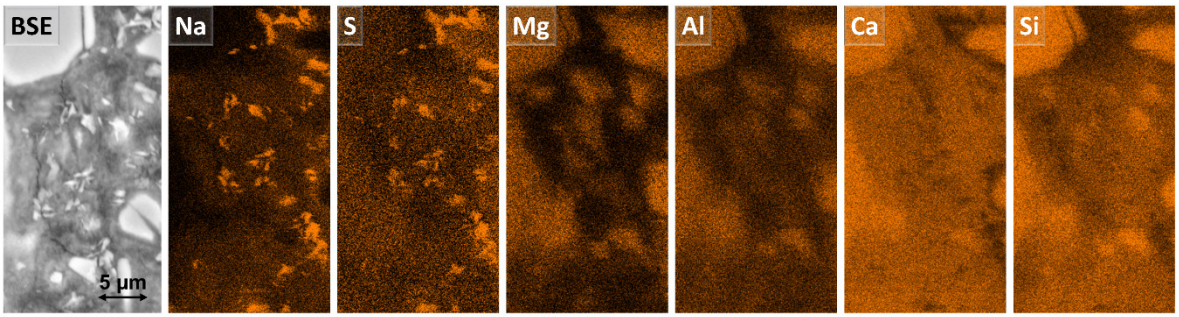

Figure 4-9. Backscattered electron image of Na_2SO_4-activated slag produced using S1 for 28 d of curing. The elemental map shows the same region as the backscattered electron image

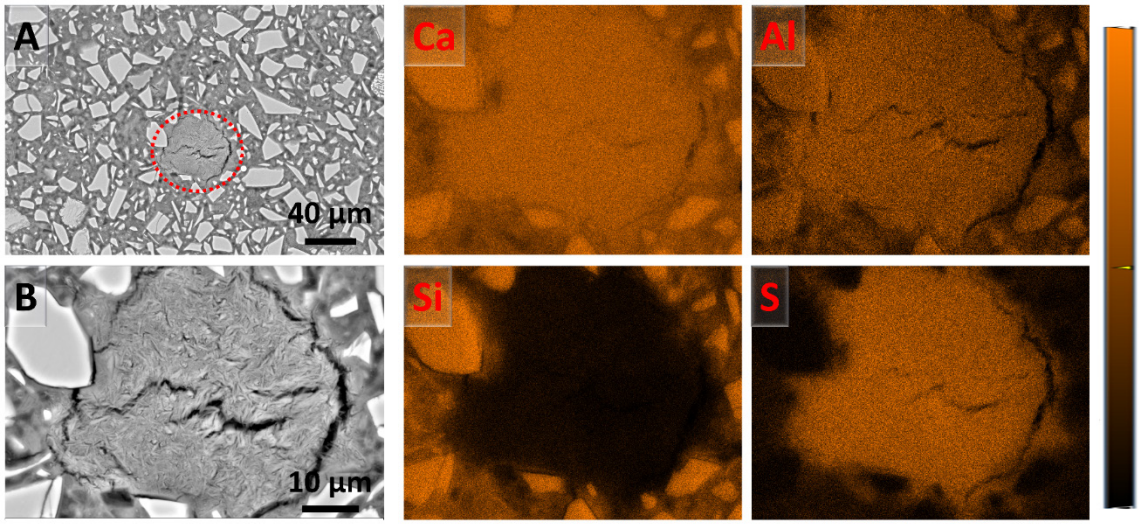

Figure 4-10. The precipitation of ettringite in Na_2SO_4-activated slag using S1 cured for 28 days at 1000 magnification (A); (B) 4000 magnifications with elemental mapping of the same region for Ca, Al, Si and S

Figure 4-11 shows the ternary diagram of CaO-Al_2O_3-SiO_2 in Na_2SO_4-activated slag cements reporting the EDX results of the cements produced with the slags used after 28 and 365 days of curing. Superimposing the EDX points collected in this study shows that the C-(A)-S-H gel forming in the sodium sulfate-activated slag cements has additional calcium, aluminium or silicon, compared to theoretical C-(A)-S-H gel models [50, 52]. It has been reported that outer reaction products in alkali-activated slag cement systems are a mixture of C-A-S-H gel and other secondary reaction products [63].

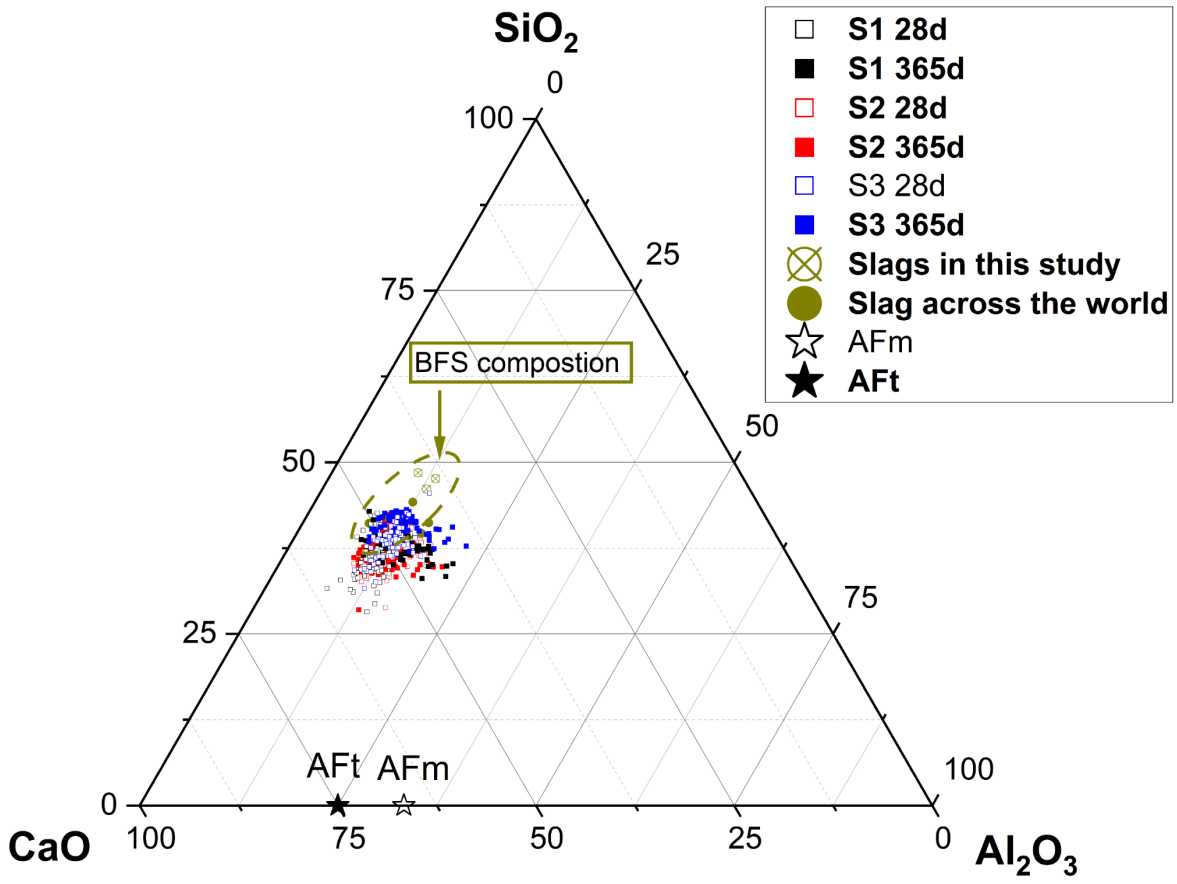

Figure 4-11. The ternary CaO-SiO_2-Al_2O_3 diagram of the Na_2SO_4-activated slag cements using the three slags in this study after 28 and 365 days; the EDX points (at least 90 points per sample per age) were taken in the region of outer reaction products. The chemical composition of blast furnace slag across the world refers to [58]

Independent of the slag composition, the Ca/Si ratio and Ca/(Al+Si) ratio of C-(A)-S-H gel in the outer region are listed in Table 4-2. It can be seen that the Ca/Si and Al/Si atomic ratio of C-(A)-S-H gel barely change from 28 to 365 days, where the Ca/Si is in the range of 1.1-1.3 and the Al/Si ratio is around 0.3. The relatively high deviation (>0.05) is due to the intermixing of C-(A)-S-H gel and ettringite in the outer reaction products regions. Ca/Si ratios quantified here ratio are similar to those reported for Na_2CO_3-activated slag cements [18, 74] and hydroxide-activated slag cements produced with slags with comparable compositions to the ones used in this study [301]. Al substitution in the C-S-H gels seems to be similar to that identified in Na_2CO_3-activated slag cements [18, 74], but higher than what has been reported for NaOH-activated slag cements [20]. A high Al substitution tends to form a more foil-like morphology of C-(A)-S-H gel with lower permeability compared to C-S-H gel, when

Ca/(Si+Al) ratio < 1.3 and Al/Si ratio >0.15 [312, 329]. This result potentially suggests the promising durability of this material due to the compacted morphology of the C-(A)-S-H gel.

Table 4-2. Ca/Si and Ca/(Al+Si) average atomic ratios of C-A-S-H gel for Na_2SO_4-activated slag cements using 3 slags at 28 and 365 days. Error corresponds to the standard deviation of 100 measurements per sample per age

	S1 28 d	S1 365 d	S2 28 d	S2 365 d	S3 28 d	S3 365 d
Ca/Si	1.30±0.08	1.27±0.07	1.25±0.07	1.32±0.08	1.26±0.10	1.13±0.06
Ca/(Al+Si)	1.00±0.06	0.91±0.08	0.92±0.07	1.00±0.07	0.94±0.07	0.86±0.08
Al/Si	0.31±0.05	0.35±0.08	0.33±0.04	0.31±0.04	0.32±0.03	0.29±0.04

Figure 4-12 shows the BSE-EDX mapping of a slag grain at 10, 000 magnification. The selection of regions corresponding to the inner reaction products is based on its grayscale and EDX mapping. The darker regions surrounding the unreacted slag are mainly the mixture of C-(A)-S-H gel and Mg-Al-LDH phase, this colouration is due to lower atomic number [330] and reduced density [331]. The dark rim around unreacted slags was also reported in the previous study in alkali-activated slag cements, composing C-A-S-H gel and LDH phases as characterised by nanoindentation [332] and TEM-EDX [53]. Elemental maps confirm the regions rich in Mg and Al with reduced signals from Ca and Si that may correspond to Mg-Al-LDH formation around slag particles.

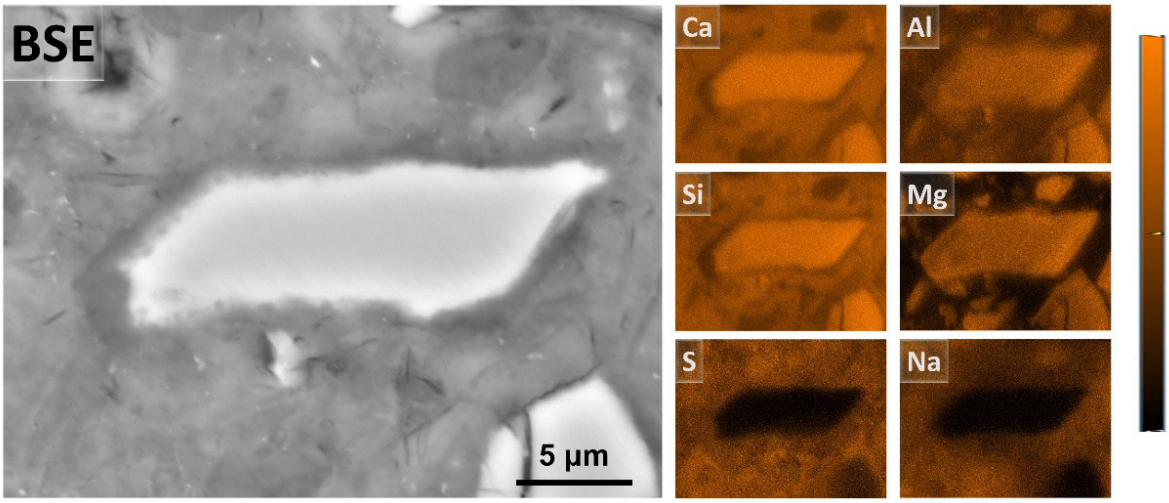

Figure 4-12. Backscattered electron image of Na_2SO_4-activated slag produced using S3 after 365 days of curing at 10, 000 magnification. The elemental map shows the same region as the backscattered electron image

Figure 4-13 shows the EDX line scan crossing the unreacted slag, covering the outer reaction products, and inner reaction products (grey rim area) around unreacted slag. Two Mg and Al peaks with pronounced reduction of Ca and Si signals in the rim area confirm the formation of the Mg-Al-LDH phase. A plateau of the S signal in this region suggests that the interlayer of the LDH phase is the SO_4^{2-} anion group, which agrees with the hypothesis from a previous study that the interlayer of the Mg-Al-LDH phase is the SO_4^{2-} group [84].

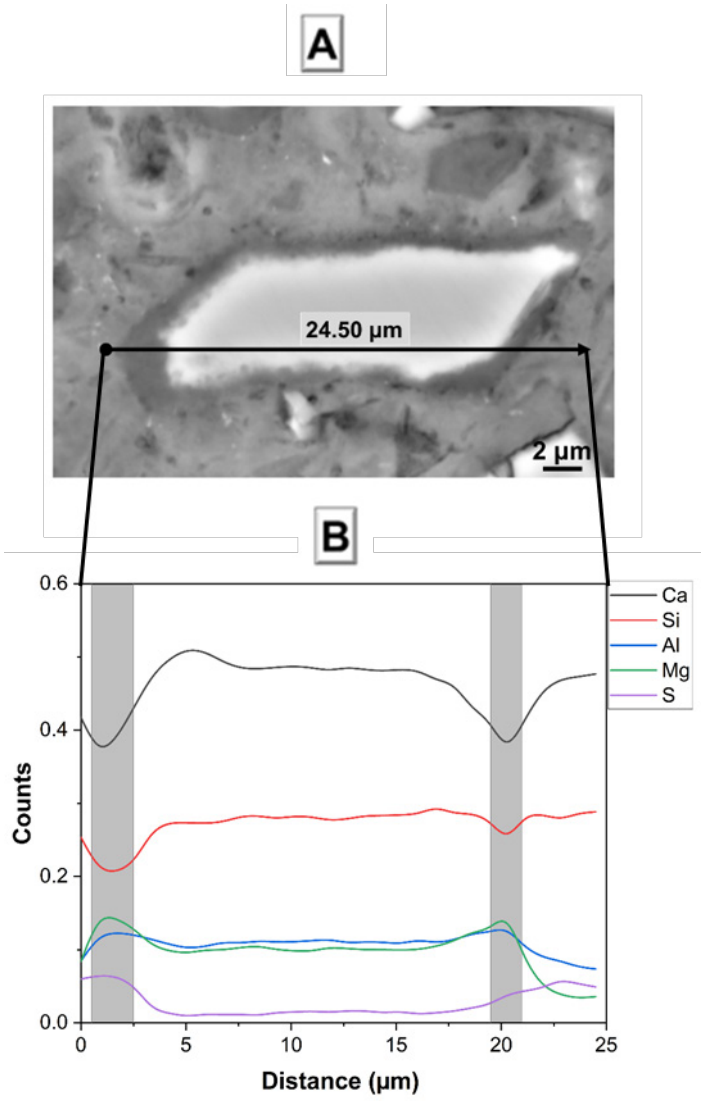

Figure 4-13. Line scan of Na_2SO_4-activated slag cements using S3 for 365 days of curing at 10, 000 magnification. (A) one line was selected for EDX line scan analysis; the filled circle means the starting point and the arrow is the endpoint. The plot of normalized Ca, Si, Al, Mg, and S elemental distribution for three lines (B, C and D), normalised to a scale between 0 and 1. The grey area indicates the inner reaction products

Figure 4-14 shows the scatter of Mg/Si against Al/Si atomic ratios from EDX analysis of inner reaction product regions at 365 days of curing for the three slags used. The equations shown in the figure are based on the regression analysis of EDX data points. As Mg-Al-LDH phases mainly precipitate in the regions of inner reaction products for slag-based cements [18, 53, 300, 331], EDX analysis of this region provides information about the Mg/Al ratio of LDH phases in the different mixes. Results reveal that S1-based cement with high Mg/Al in the anhydrous slag presents a higher Mg/Al ratio of LDH phases compared to S3-based cements despite

presenting a similar Ca content. The lowest Mg/Al ratio of the Mg-Al-LDH phase is observed in S2-based pastes. This suggests that in addition to the Mg and Al content in raw slag, the formation of the Mg-Al-LDH phase is significantly influenced by the chemical composition of the pore solution, as suggested in [333]. Different dissolution rates of Ca, Si, Mg and Al under different activation conditions (pH value) are likely affecting the chemical composition of Mg-Al-LDH phases.

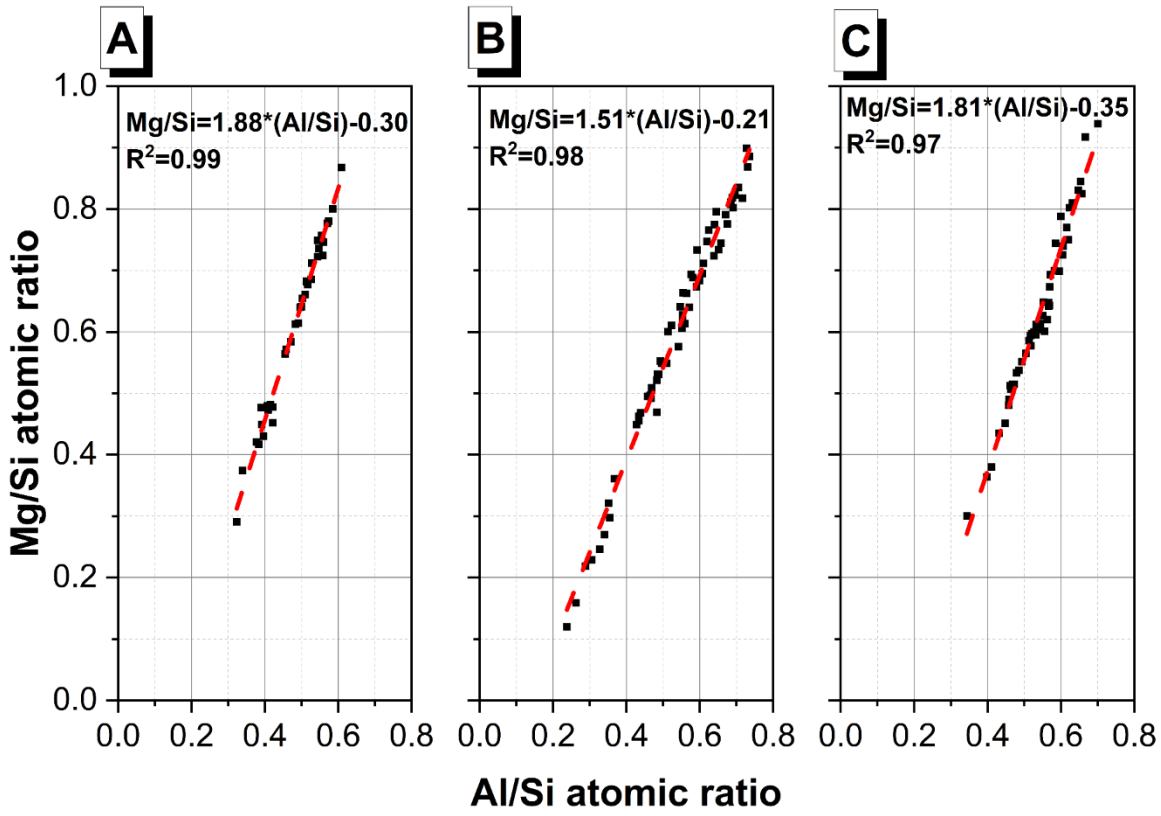

Figure 4-14. Mg/Si vs Al/Si atomic ratio for EDX point analysis of inner reaction products in the SEM for Na_2SO_4-activated slag cements using S1 (A), S2 (B) and S3 (C) cured for 365 days. The equation is based on the regression analysis of the EDX points. The solid points are the EDX points and the red dash lines are fitted lines

4.3.6 Thermodynamic modelling

Figure 4-15 shows the simulated volume change of the phase assemblages as a function of reacted slag from 10 % to 80 % in Na_2SO_4-activated slag cements considering the oxide compositions of slag S1, S2 and S3. The predicted phases agree with previous thermodynamic modelling simulations reported for Na_2SO_4-activated slag cements elsewhere [122, 257, 284].

In line with the experimental observations reported in this study, the thermodynamic modelling predicts the formation of C-(A)-S-H, ettringite and SO_4-intercalated Mg-Al-LDH phases (MgAl-OH-s-LDH) as the major reaction products for the three types of slags used in this study. The formation of this type of LDH phase has also been confirmed by its thermodynamic preference for Na_2SO_4-activated slag cements in other studies [257, 284]. Although bloedite was observed in the XRD pattern (Fig. 4-2), this mineral was not predicted in the thermodynamic modelling due to a lack of thermodynamic data in the existing database.

The Ca/(Al+Si) ratio simulated based on thermodynamic modelling generally agrees with EDX results within the standard deviation (Table 4-2). For all three slag-based cements, the porosity values decrease with an increased DoR indicating the potential for porosity reduction as the reaction progresses in these systems, consistent with the relationship between the degree of reaction and porosity as quantified by SEM image analysis (Fig 4-8). The simulated porosity values are larger than those determined from the BSE image analysis. This is mainly because total porosity determined by thermodynamic modelling considers the full range of pore size distribution and the chemical shrinkage due to the formation of the reaction product [334], which cannot be captured by BSE.

The reduction of ettringite was predicted at a higher degree of slag reaction, consistent with the XRD (Fig 4-2), ^{27}Al MAS NMR (Fig. 4-3) and TG-MS (Fig. 4-4) results in this study. The model predicted monosulfoaluminate ($Ca_4Al_2(SO_4)(OH)_{12}\bullet 6H_2O$) formation, as this phase is more stable than ettringite at ambient temperature based on solubility measurements [335]. However, no experimental evidence of this phase was found in the present study. The modelling simulations only predicted the formation of monosulfoaluminate at a higher DoR (~70 %) of the slag than those achieved in the pastes experimentally evaluated.

On the other hand, strätlingite ($Ca_2Al(Si, Al)_2O_2(OH)_{10}\bullet 2.25H_2O$) was predicted in slag-cements with a higher amount of Al content (e.g. S2 and S3). The formation of hydrotalcite-type phases consumes the Al in pore solution and this leads to the stabilisation of the strätlingite phase [110]. This AFm-type phase has been identified in a minor amount in NaOH and Na_2SiO_3-activated slag cements by experiments and thermodynamic modelling [76, 336]. However, the formation of this phase cannot be confirmed in the current study due to its small quantities and poorly crystalline structure, which is difficult to identify in the XRD [335]. Also, two Al^{IV} and Al^{VI} sites at around 61 ppm and 11.3 ppm of strätlingite in ^{27}Al MAS NMR overlap with the bands attributed to C-(A)-S-H type gel, ettringite and monosulfoaluminate, respectively [337, 338]. This phase has also been predicted in previous studies reporting thermodynamic modelling simulations for Na_2SO_4-activated slag cements with a comparable

slag composition to the one used in this study [122, 257]. Thus, although strätlingite is thermodynamically favoured to form, more detailed studies especially for long-age Na_2SO_4-activated slag cements are needed to validate the modelling results.

A minor amount of the zeolite phase SOH(OH) ($Na_8Al_6Si_6O_{24}(OH)_2 \bullet 2H_2O$) was predicted to form in S2 and S3-based slags with higher Al content than S1. However, the crystalline zeolite phases are unlikely to form in ambient curing conditions. The zeolites phase to represent the sodium aluminosilicate hydrate (N-A-S-H) type gel that might form in alkali-activated cements, due to their similar Al/Si ratio [76, 110]. Previous studies found that less extent of crosslinking of C-(A)-S-H type gel is observed using sodium carbonate activator compared to more polymerised N-A-S-H type gel in the presence of soluble silicates solution [124]. This indicates that it is likely that the structure of the C-(A)-S-H type gels forming sodium sulfate-activated slag cements, with Q^2 and $Q^2(1Al)$ tetrahedral coordination [84, 257], is comparable to those identified in sodium carbonate-activated systems.

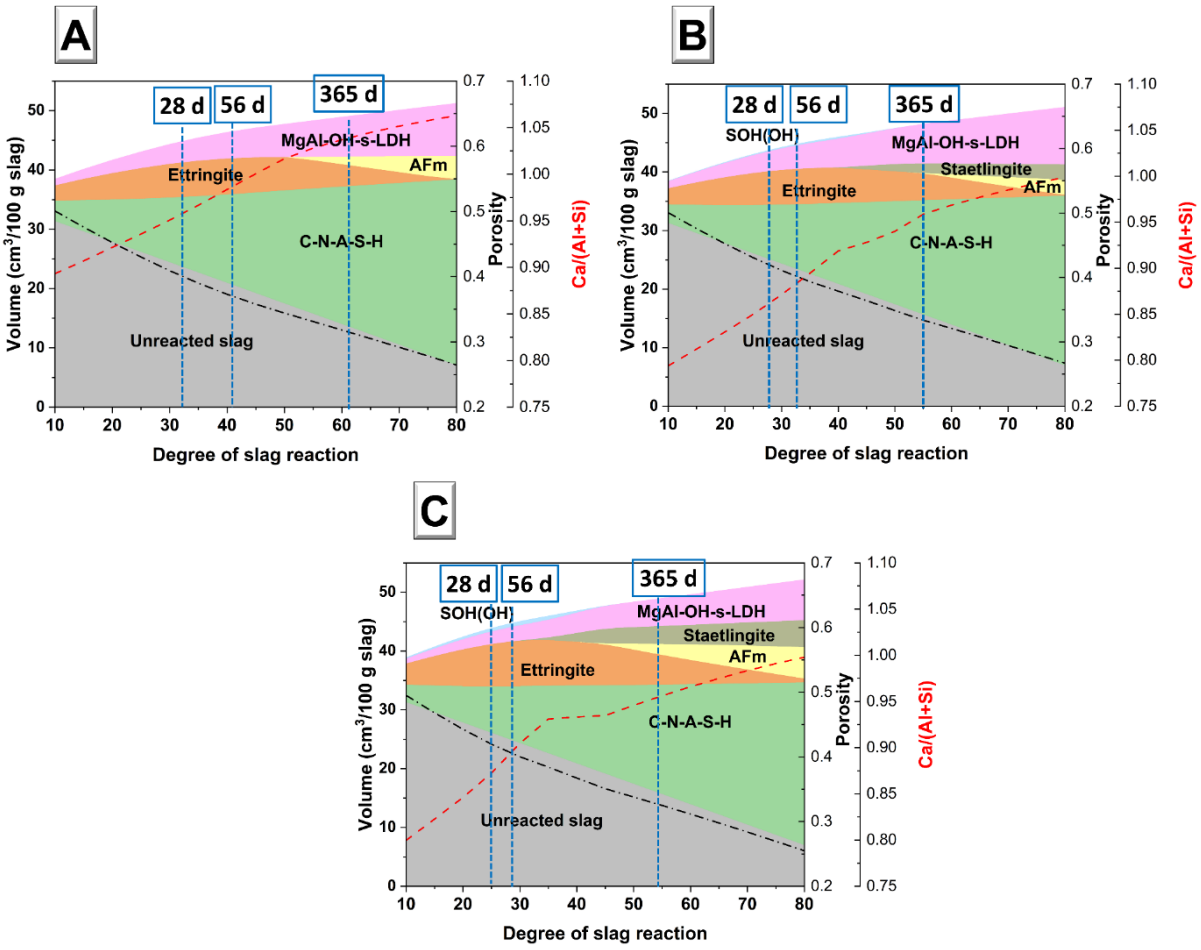

Figure 4-15. The calculated volume change of phase assemblage, porosity and the molar ratio of Ca/(Si+Al) of C-A-S-H gel as a function of reacted slag from 10 % to 80 % in Na_2SO_4-activated slag cements using (A) S1, (B) S2 and (C) S3. The black dashed line represents the change of porosity, and the red dashed line represents the change of Ca/(Al+Si) of C-A-S-H gel. The light blue dashed line indicates DoR experimentally calculated for the three slags used at 28, 56 and 365 days, respectively

Figures 4-16 show simulated ionic concentration in the pore solution of Na_2SO_4-activated slag cements using S1, S2 and S3, as a function of the degree of slag reaction. The Si concentration as an important ion to stabilise the formation of C-(A)-S-H type gel shows an opposite trend to the Ca concentration as more C-(A)-S-H type gel forms. The Na, mainly originating from the activator, decreases with increased reaction which could be due to its sorption in the C-(A)-S-H type gel [339, 340]. The initial decrease of S concentration is associated with the precipitation of ettringite, while S concentration increases when the decomposition of the ettringite happens, leading to the drop in pH value. A similar observation has been reported in thermodynamic modelling simulations of NaOH-activated slag cements [341]. As the pH value

in the pore solution mainly affects the reactivity of the slag in the alkali-activated slag system [336], the availability of S in the system is depleted causing an increased pH value, due to the precipitation sulfur-bearing phases, such as the LDH phase and ettringite. This plays a key role in maintaining/increasing the pH value in the pore solution as more slag is reacting and consequently favours the dissolution of slag to progress. A similar reaction mechanism has been proposed for Na_2CO_3-activated slag cements, where the gradual consumption of the anion contributed by the activator as the reaction progresses leads to an increase of the pH value of the pore solution and the system tends to react like NaOH-activated slag cements thereafter [18]. Over 13 of the simulated pH values observed in the thermodynamic modelling agree with the experimental observation that after two days of reaction, the pH value of the pore solution reached ~13.2 in sodium sulfate-activated slag cements [342].

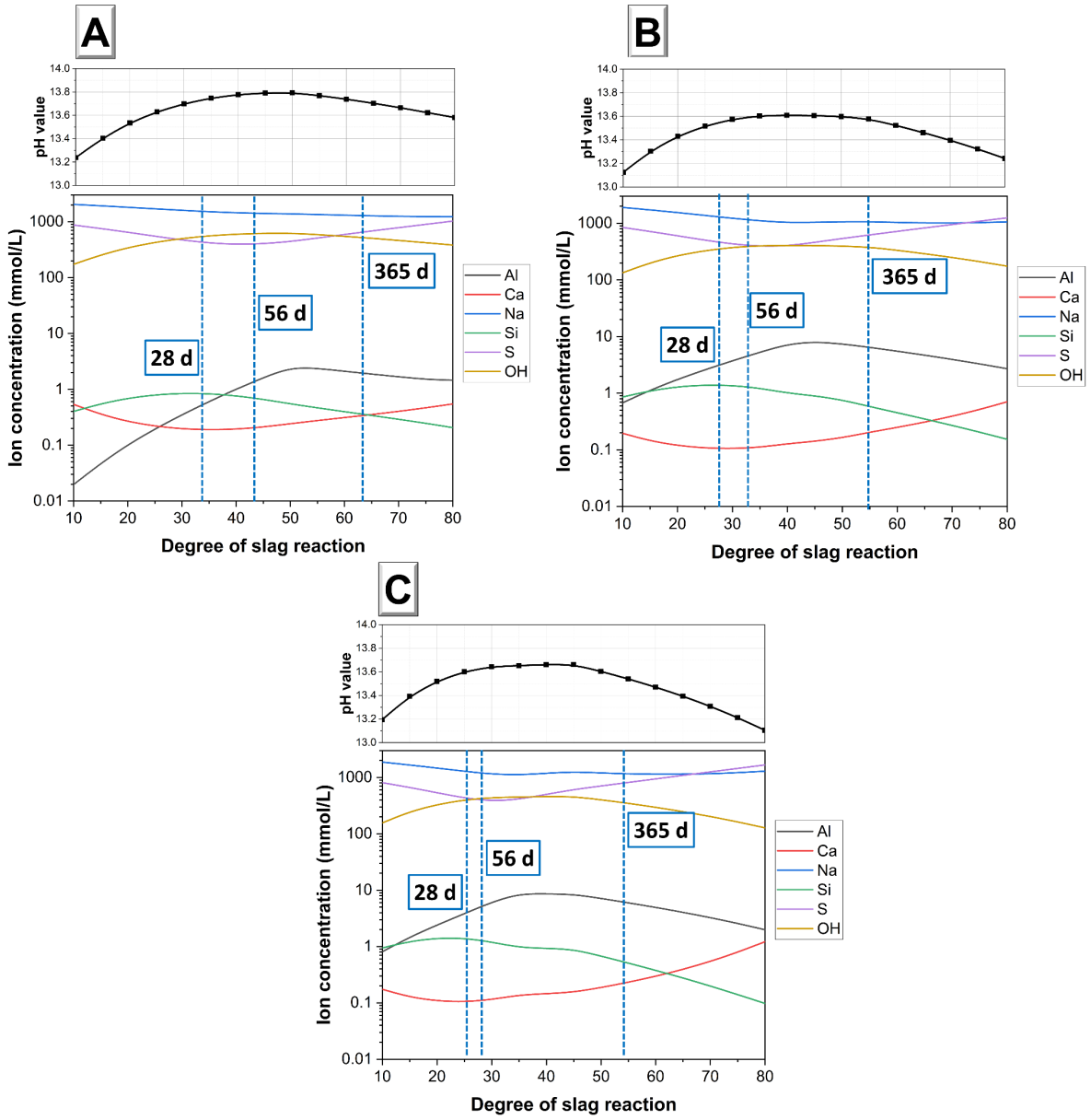

Figure 4-16. The ion concentration of Al, Ca, Na, Si, S, OH and pH value in the pore solution of Na_2SO_4-activated slag cements as a function of reacted slag using (A) S1, (B) S2 and (C) S3. The concentration of hydroxide ion is the free concentration based on the pH value in the pore solution [336]. The light blue dashed line indicates DoR using three slags at 28, 56 and 365 days, respectively

4.3.7 Compressive strength

Figure 4-17 shows the compressive strength development for Na_2SO_4-activated evaluated up to 600 days. All three slag pastes showed increased compressive strength with age due to a

continuous increase in DoR of slag that leads to a reduction in porosity as discussed in previous sections (Fig. 4-7). All three activated slag pastes developed a strength between 13-17 MPa after 7d of seal curing. For S1 and S2, a significant strength increase from 7 to 56 days was observed, reaching values of up to 45-50 MPa at 56d of curing. S1-based cements show negligible strength gain between 56 and 90 days and reach the highest strength of ~68 MPa at 365 days, while the S2 presents a marginally slower strength development compared to S1 achieving about 60 MPa at extended curing ages.

S3-based samples reached ~17 MPa at 7d and developed the lowest strength gain from 14 days to 365 days. Reactivity results from the R^3 test also showed similar lower heat release at a later period for S3. One of the reasons could be the TiO_2 content (1.1 %) in S3, which may lead to reduced strength development in slag systems. The amount of TiO_2 has been shown to have a detrimental effect on the reactivity of blast furnace slag [343, 344] and compressive strength development [345]. The TiO_2 amount for the slags used here is between 0.5-1%. Previous studies have reported that TiO_2 of 2.5 could cause over 50 % compressive strength loss at 2 days and over 40 % loss at 28 days in 75 % substitution of blended slag cement compared to without TiO_2 content of the slag [345]. Nevertheless, the effect of TiO_2 content, if any, does not seem significant at longer curing age. S3-based pastes exhibited a higher porosity (Fig. 4-7) compared to the other specimens evaluated, consistent with their lower strength.

There are only very limited studies that discuss factors influencing the strength development of near-neutral salts-activated slag cements. A previous study reveals that the slag with higher Al_2O_3 content (11.5 vs 7.7 wt.%) showed higher reactivity with corresponding higher strength, but the monitoring of the strength development was only carried out for 28d in super sulphated slag cement [90]. Another study also confirmed that the slag with higher Al_2O_3 content presents a higher initial slag dissolution rate, however, the degree of slag reaction can also influenced by the pore structure formed at a later stage [90, 346]. Thus, the faster dissolution of slag with higher Al content (lower Mg/Al ratio) led to the increased amount of ettringite surrounding the slag surface, and this may be correlated with the highest strength of S3 at 7d, but dense microstructure formed may limit the space available at the later age for precipitation, thereby causing slower strength development [90, 346].

On the other hand, slag with a higher Mg/Al ratio contributes to strength development rapidly after 28 days of curing, which agrees with previous findings in Na_2CO_3-activated slag cements [18, 68], NaOH and Na_2SiO_3-activated slag cements [20]. A slag with a higher Mg/Al ratio has a slower dissolution, leading to gradual precipitations of ettringite and C-(A)-S-H in the free

pore space that contributes to pore refinement and strength development as observed in the experimental finding in this study and elsewhere [90, 346].

After 600 days of hydration, the compressive strength of sodium sulfate-activated slag cements stabilises around 65 MPa, regardless of slag composition. Due to the lack of published data on the long-term compressive strength of near-neutral salt slag cements, it is likely that the Mg and Al content predominantly influences reaction kinetics (Fig. 4-1). After a degree of reaction (DoR) of 60% is achieved in all three paste samples (Fig. 4-7), the similar Ca/Si ratio of the anhydrous slag (Table 3-1), as the primary source for C-(A)-S-H gel precipitation, appears to play a more critical role in determining long-term mechanical properties. Future studies should focus on investigating the long-term mechanical properties and microstructural evolution of sodium sulfate-activated slag cements to gain a comprehensive understanding of their long-term performance.

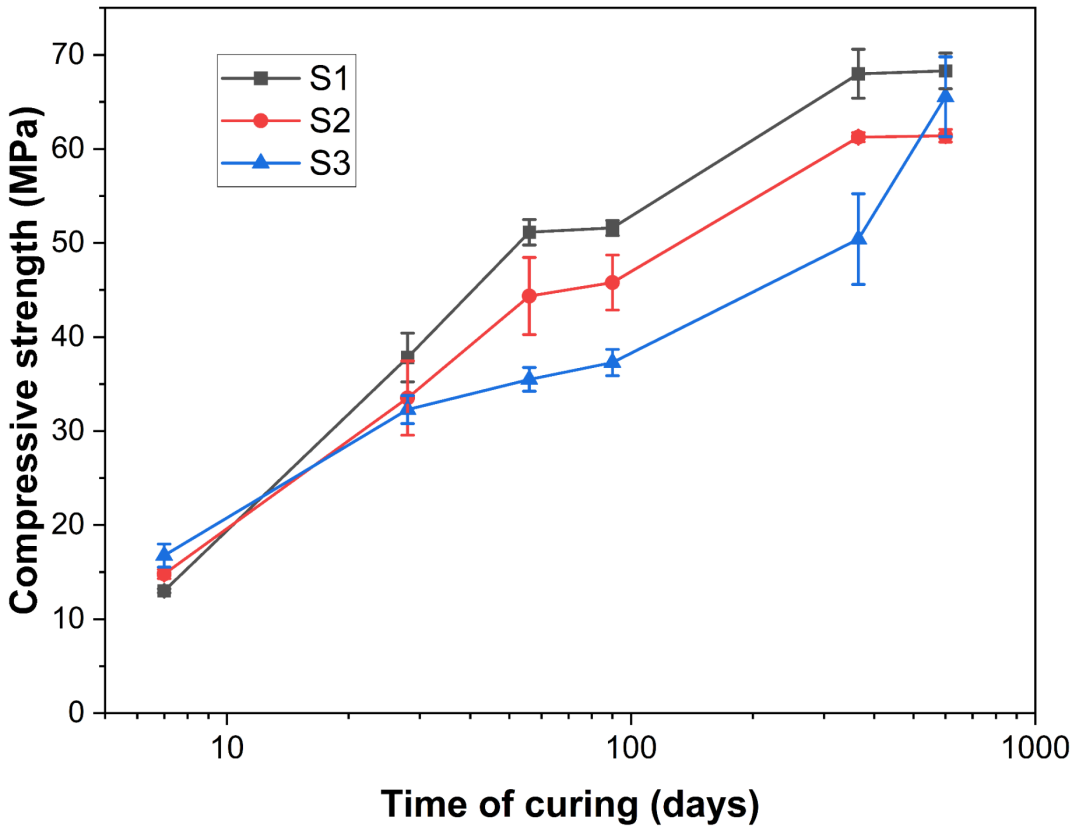

Figure 4-17. The compressive strength development of Na_2SO_4-activated slag binders using S1, S2 and S3 as a function of time

4.4 Conclusions

The slag source has a significant effect on the phase assemblage evolution and properties developed in sodium sulfate-activated slag cements. A slag with a higher Al_2O_3 seems more reactive when using Na_2SO_4 solution, as an activator, in the first 14 days. Independent of the slag properties, the main crystalline reaction products identified in Na_2SO_4-activated slag pastes are C-(A)-S-H-type gels and ettringite. The amount of ettringite decreases at extended curing ages, which was confirmed by XRD, ^{27}Al MAS NMR and TG-MS analysis, and further validated by thermodynamic modelling simulation. The formation of a poorly crystalline Mg-Al-SO_4-LDH phase was confirmed by ^{27}Al MAS NMR and BSE-EDX analysis.

The Ca/(Al+Si) ratio of C-(A)-S-H type gels forming in sodium sulfate-activated slag cement is ~1, which is comparable to that reported for Na_2CO_3 and NaOH-activated slag cements. This indicates that sodium sulfate-activated slag cements have the potential to develop comparable performance to other alkali-activated slag cements. The Mg/Al ratio of the LDH phase identified in these cements is between 1.5 and 1.8 depending on the slag composition. A higher ratio is observed when using slag with a higher Mg/Al ratio, which is also consistent with a higher degree of slag reaction achieved by such slag under the activation conditions evaluated in this study. Thermodynamic modelling simulations revealed that the consumption of sulfates in the pore solution via the formation of ettringite and LDH phase leads to an increased degree of slag reaction, pH value and reduced porosity of the cements. This implies the kinetics of the reaction potentially can be accelerated adding rapid consumption of sulfates in the pore solution.

Independent of the slag composition, the microstructure of Na_2SO_4-activated slag cements densifies at extended curing ages, and the degree of reaction of the slag reached can be of up to 50-60 % with a rough porosity of 15% after 365 days of curing, which is comparable to that reported for slag blended cements systems. The compressive strength of Na_2SO_4-activated slag cements varies depending on the chemical composition of the slag used for their production. Pastes based on the slag with the highest Mg/Al ratio showed excellent strength development after 28 days of curing. This reveals that the mix design for each slag source should be tailored to optimise mechanical properties.

While the slag with the highest Al content exhibited the fastest reaction kinetics in the first 14 days, this did not result in greater compressive strength, reduced porosity, or a higher degree of slag reaction at later stages, compared with other slag used in this study. Conversely, the slag with higher Mg and lower Al contents, than other slags in this study, developed the highest compressive strength, with the corresponding highest chemical reactivity as confirmed by the

R^3 test over 400 hours of measurement. This observation raises questions about whether the slag's reaction kinetics characterised by isothermal calorimetry, can be used as an indicative of the mechanical and durability performance of sodium sulfate-activated slag cements. Calorimetry results alone should not be used for mixed design optimisation to formulate these materials.

The findings in this study confirm the long-term stability of sodium sulfate-activated slag cements phase assemblage, continuous slag reaction at advanced curing ages leading to densification of the pastes and increased mechanical performance. Given the global diversity of slag compositions, desirable properties can be achieved when producing alkali sulfate-activated slag cement by tailoring its mix design.

Chapter 5.

STRUCTURAL ALTERATIONS IN ALKALI-SULFATE-ACTIVATED SLAG CEMENTS PASTES INDUCED BY NATURAL AND ACCELERATED CARBONATION

Noted: This chapter is primarily based on the paper "*Structural alterations in alkali-sulfate-activated slag cement pastes induced by natural and accelerated carbonation"* by **Z. Yue**, Y. Dhandapani; S. A. Bernal**,** submitted to the journal *Cement and Concrete Research* (accepted).

5.1 Introduction

The present chapter centres on evaluating the carbonation performance of sodium sulfate-activated slag cement pasted assessing the effect of CO_2 concentration exposure (0.04% vs. 1%), in specimens exposed to controlled environmental conditions. Changes in phase assemblages were evaluated by X-ray diffraction (XRD), Attenuated Total Reflectance Fourier Transform Infrared (ATR-FTIR) spectroscopy and Scanning Electron Microscopy (SEM). Experimental results were then complemented by thermodynamic modelling simulations for a better understanding of the carbonation mechanism of the evaluated binders. Carbonation depths and changes in the compressive strength due to carbonation were also determined.

Results indicated that the main carbonation reaction products forming are different $CaCO_3$ polymorphs, independent of the slag composition or carbonation conditions adopted. This is a consequence of the Ca-bearing phases' decalcification. In specimens exposed to 0.04% CO_2, a negligible carbonation front was observed, along with a continued phase assemblage evolution and compressive strength gain after 500 days of exposure. This was more noticeable in pastes produced with slags with a higher Mg/Al ratio. Conversely, exposure to 1 % CO_2 led to complete carbonation after 28 days, and a significant compressive strength reduction. Accelerated carbonation does not lead to the development of comparable microstructures to

those observed in naturally carbonated pastes. Therefore, results derived from the accelerated tests are considered unsuitable for predicting the long-term carbonation performance of Na_2SO_4-activated slag cements.

5.2 Experimental methodology

Raw materials characterisation, mix design, sample preparation and materials characterisation were reported in Chapter 3. Similar samples to those evaluated in Chapter 4 were exposed to carbonation.

5.2.1 Carbonation exposure

After a sealed curing period of 28 days, slag paste specimens with dimensions of 25 mm in diameter and 95 mm in height, along with mortar specimens measuring 50 x 50 mm, were subjected to carbonation exposure under two distinct conditions. The first condition involved natural carbonation in a JTS environmental chamber, where the CO_2 concentration was set to 0.04% to mirror the average CO_2 levels commonly found in atmospheric air. The second condition employed accelerated carbonation in a TFB Carbonator C5 chamber, with a CO_2 concentration of 1%, as specified by the EN 13295:2004 standard [347]. This standard represents the most widely recognised methodology for assessing the carbonation of alkali-activated materials.

Both the JTS and TFB environmental chambers were controlled to maintain a temperature of 20 ± 2°C and a relative humidity of 55 ± 5%, based on the guidelines outlined in BSI 1881-210:2013 [348]. This stringent control of environmental conditions was designed to ensure that variations in CO_2 concentration were the sole variable during the carbonation testing process.

To mitigate the effect of moisture and CO_2 ingress, both the top and bottom surfaces of the paste cylinders were sealed with aluminium foil. While pre-conditioning of samples is adopted in most carbonation testing standards, such a procedure was intentionally omitted in this study. This decision is grounded in findings from prior research [349], which suggests that pre-conditioning steps might adversely affect the microstructure of paste samples. Specifically, these steps have been linked to the premature formation of carbonation products, thereby potentially skewing the carbonation assessment results. This approach allows for a more direct evaluation of the carbonation process, focusing on the inherent behaviour of the material under study without the potential confounding effects introduced by pre-conditioning.

5.2.2 Analysis of paste specimens

The carbonated cylinders were cut into 5 mm discs along the transverse section using a Sectom with 3200 rpm of the rotation speed and 0.02 mm/s of feed speed after 7, 14, 21 and 28 days of 1 % CO_2 exposure; and 60, 250, 365 and 500 days of 0.04% CO_2 exposure. The cutting process was conducted with distilled water continuously sprayed to the diamond blade to remove the dust, avoiding the contamination of the test surface. The cut discs were then sprayed with a 1 % phenolphthalein indicator prepared by dissolving 1 gram of solid indicator in 100 mL of isopropanol solution. A Jiusion 2K HD digital microscope was used to take images of the transverse section of the specimens before and after spraying with the indicator. The average carbonation depth values reported correspond to the average of 20 measurements per sample.

After the carbonation depth was determined, a Cordless mini rotary tool was used to drill holes in the carbonated, partially carbonated and uncarbonated parts of the fresh-cut specimen. Figure 5-1 shows an example of the typical positions of the drilled holes in the tested specimens. The diameter of the drill was ~4 mm, and the lowest 3000 rpm spin rate of the drill was used. The rotary tool was stopped every 5 minutes until the drill reached ambient temperature to avoid localised high temperatures during the drilling. The collected samples were then ground using a mortar and pestle and immediately analysed by X-ray diffraction (XRD) and attenuated total reflectance Fourier transform infrared (ATR-FTIR).

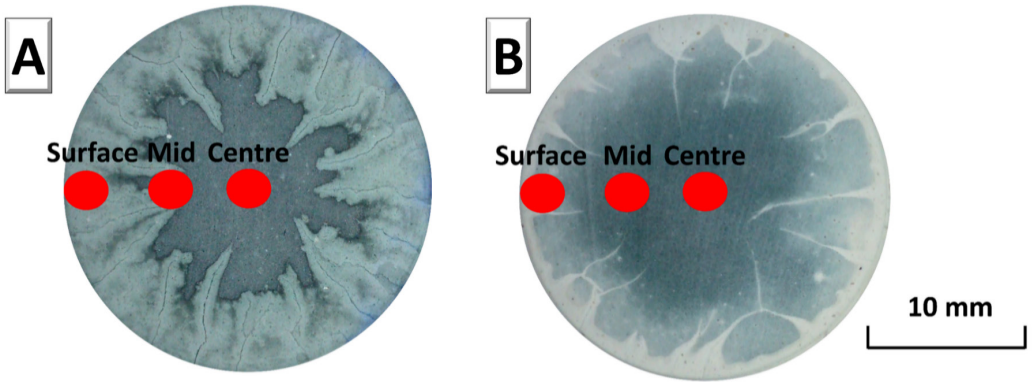

Figure 5-1. Photographs showing the position of drilled holes (red circles) in the transverse section of Na_2SO_4-activated slag cement after exposure to 1% CO_2 for 14 days (Fig. 5-1A) and 0.04% CO_2 for 365 days (Fig. 5-1B). The surface, middle and centre represent the fully carbonated, partially carbonated and uncarbonated regions

5.3 Results and discussion

5.3.1 Phase assemblage alterations induced by CO_2 exposure

Figure 5-2 presents the XRD pattern of sodium sulfate-activated slag cements exposed to 1% CO_2 for 14 days. Independently of the slag used, the main crystalline reaction products identified in the Na_2SO_4-activated slag cements were an aluminium-substituted calcium silicate hydrate (C-(A)-S-H) gel (powder diffraction file (PDF) # 00-020-0452) and ettringite (PDF#00-013-0350). Upon accelerated or natural carbonation, calcite (PDF#01-083-1762), aragonite (PDF# 01-075-9987) or vaterite (PDF#00-060-0483) were identified as the main carbonation reaction products. The formation of different calcium carbonate polymorphs is consistent with the carbonation of the Ca-rich phases identified in other alkali-activated slag cements [136, 137]. The type and amount of $CaCO_3$ polymorphs vary depending on the slag type slag and CO_2 concentration.

Upon exposure to 1% CO_2 (Fig. 5-2), the reflections associated with ettringite are no longer observed in the diffractograms of the surface regions, particularly its main peak at 9.138°(2θ) corresponding to the (200) plane has completely disappeared. Instead, the formation of gypsum ($CaSO_4 \cdot 2H_2O$) (PDF#00-001-0385) was identified independently of the slag used. This is consistent with what has been reported [350] about the decomposition of ettringite under accelerated carbonation conditions, where the formation of calcium carbonate polymorphs (vaterite and aragonite), gypsum and alumina gel are typically observed. Additionally, no carbonation reaction products were observed in the centre (dark lines in Fig. 5-2) in the three slags-based cements evaluated, which verifies that no carbonation occurred in this region, consistent with the phenolphthalein testing results (Fig. 5-10). In the middle regions (red lines in Fig. 5-2), different $CaCO_3$ polymorphs and gypsum were observed in S2 and S3-based pastes, whereas comparable diffraction patterns were observed in samples obtained from the middle and centre regions in the S1-based pastes.

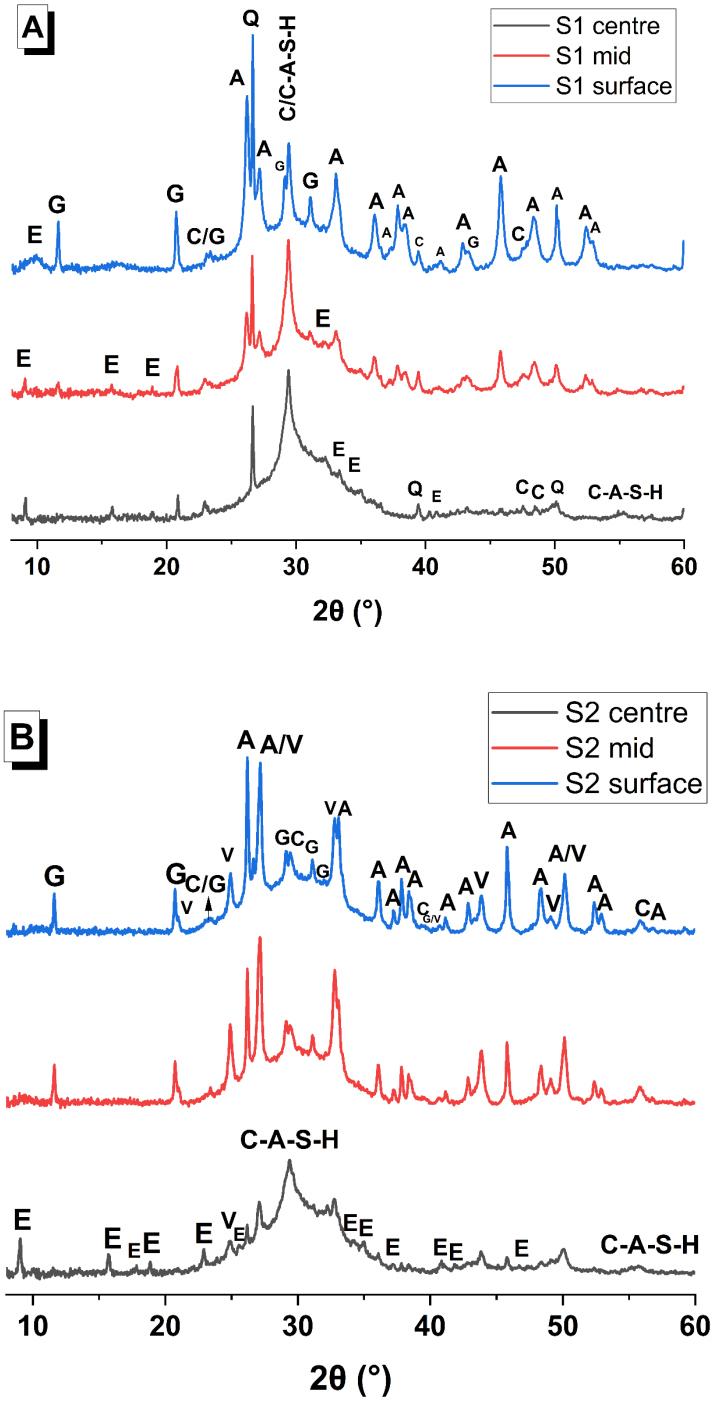
A
S1 centre
S1 mid
S1 surface
C/C-A-S-H
C/G
C-A-S-H
2θ (°)
B
S2 centre
S2 mid
S2 surface
A/V
C-A-S-H
2θ (°)

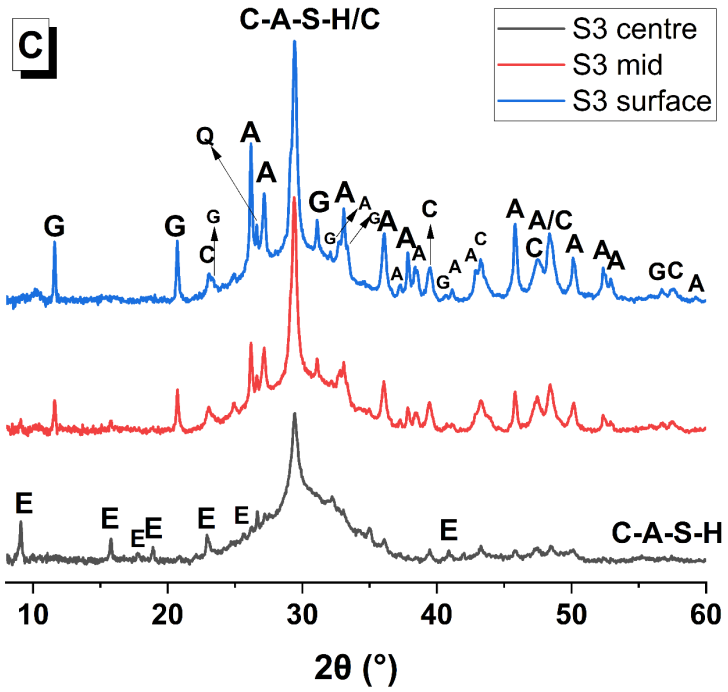

Figure 5-2. XRD patterns of Na_2SO_4-activated slag cements produced with slag (A) S1, (B)S2, (C) S3, exposed to accelerated carbonation for 14 days. Noted: C-A-S-H: aluminium-substituted calcium silicate hydrate; E-ettringite; G-gypsum; Q-Quartz (PDF#01-081-0069); C-calcite; A-aragonite and V-vaterite

In contrast, exposing the specimens to natural carbonation for 365 days did not lead to the complete decomposition of ettringite in the surface region (Fig. 5-3). The type of $CaCO_3$ polymorphs formed under natural carbonation is similar to those observed under accelerated carbonation conditions. However, instead of gypsum, bassanite ($CaSO_4 \cdot 0.5H_2O$) (PDF#00-014-0453) was identified as the main sulfate-rich carbonation product associated with the decomposition of ettringite. This is consistent with the results reported in [257], where bassanite and aragonite were the main carbonation products observed in powdered Na_2SO_4-activated slag cements. The severe carbonation at 1 % CO_2 is leading to a rapid decalcification of C-A-S-H gel and ettringite, which might be causing an increased saturation in the pore structure, as a consequence of the water released as part of the carbonation reaction [76, 103]. This might lead to differences in the degree of saturation in the carbonated regions of the samples exposed to the two CO_2 concentrations evaluated. Bassanite has been reported as the sulfate-bearing phase along with $CaCO_3$ particles upon carbonation at a moderated RH (40-80%), while gypsum formed at high RH (80-100 %) [351]. This is consistent with thermodynamic modelling simulations predicting the formation of carbonated saturated specimens [257].

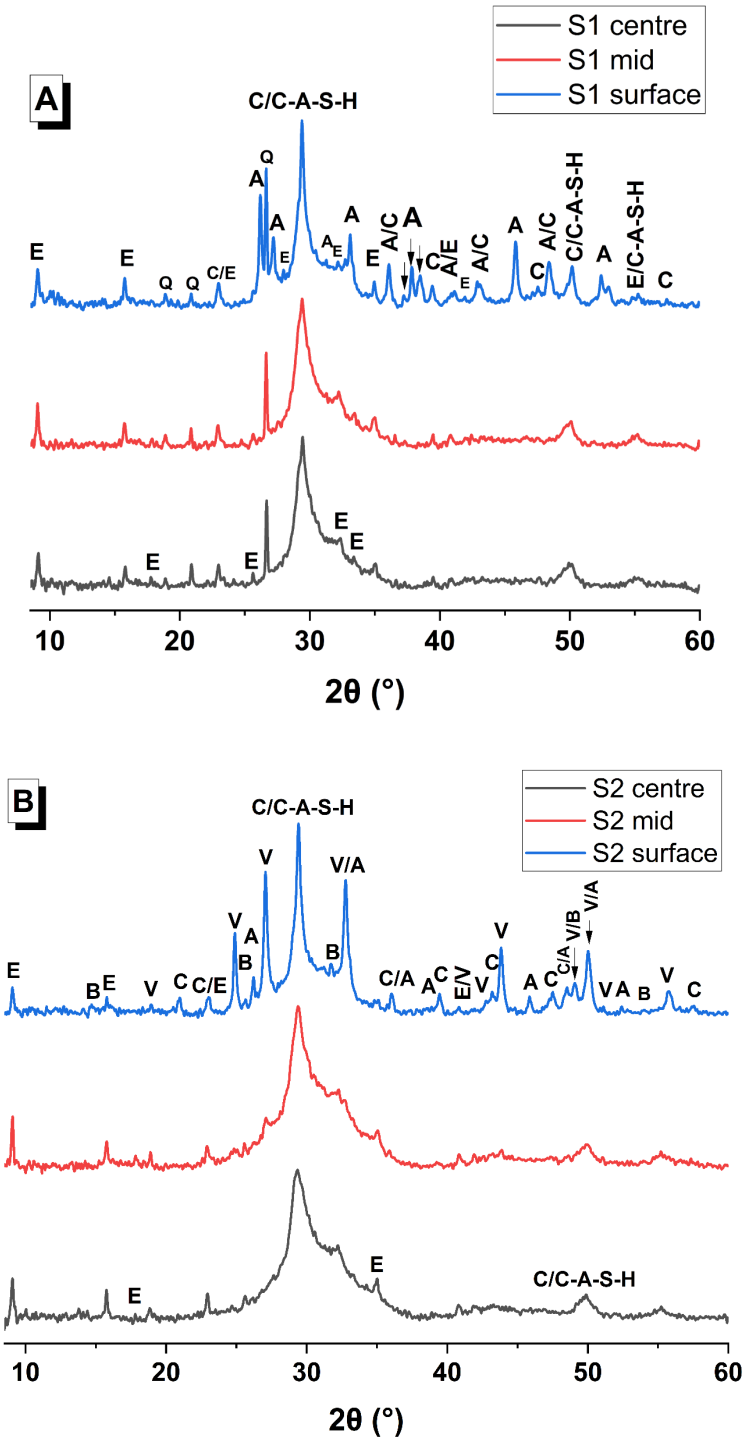
A
S1 centre
S1 mid
S1 surface
C/C-A-S-H
E/C-A-S-H
2θ (°)
B
S2 centre
S2 mid
S2 surface
C/C-A-S-H
2θ (°)

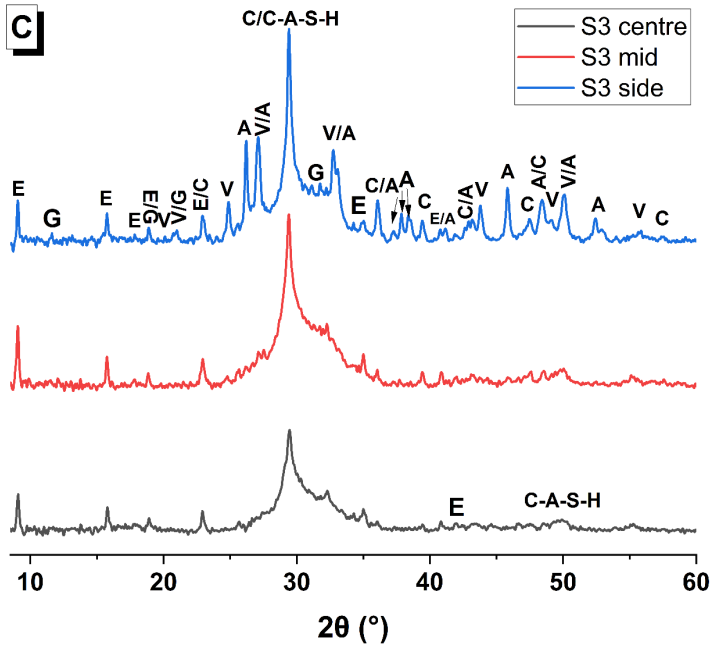

Figure 5-3. XRD pattern of Na_2SO_4-activated slag cements produced with slag (A) S1, (B) S2 and (C) S3, exposed to natural carbonation for 365 days. Noted: C-A-S-H: aluminium-substituted calcium silicate hydrate; E-ettringite; G-gypsum; B-bassanite; Q-Quartz (PDF#01-081-0069); C-calcite; A-aragonite and V-vaterite

For the three slag-based cements exposed to different CO_2 concentrations, the formation of aragonite intermixed with a minor amount of vaterite and calcite, was identified independent of the level of carbonation, CO_2 concentration or slag type used in this study. Vaterite formation was mainly observed in the S2-based cements exposed to 0.04 % or 1 % CO_2. The precipitation of different $CaCO_3$ polymorphs is influenced by the pH and saturation levels of Ca^{2+} and CO_3^{2-} in the pore solution [12], as well as the relative humidity or degree of saturation reached within the pore structure at different depths [130, 352]. Auroy et al. [132] reported that in addition to the gypsum, the carbonation of the pure ettringite mainly leads to aragonite formation. Similarly, Steiner et al. [158] identified aragonite with a minor amount of vaterite during the carbonation of the ettringite under both 57 % and 91 % RH at 1 vol % CO_2 and 20 °C. The results in this study further indicate that the carbonation of ettringite, and therefore the molar ratio of SO_4^{2-}/CO_3^{2-} within the pore solution of the system, influences the type of $CaCO_3$ polymorphs formed, as suggested by [353], governing the phase assemblages of carbonated sodium sulfate-activated slag specimens.

5.3.2 Calcium carbonate polymorphs and changes in the C-A-S-H phase

Figure 5-4 shows the infrared spectra of Na_2SO_4-activated slag cements exposed to accelerated carbonation for 14 days and natural carbonation for 365 days. The band between 1590 and 1300 cm^{-1} is assigned to the asymmetric O-C-O stretching mode (ν_3), which is related to the overlapping stretching vibration band of $CaCO_3$ polymorphs, including calcite (1430 cm^{-1}), vaterite (1490 cm^{-1} and 1440 cm^{-1}) and aragonite (1490 cm^{-1}) [135, 354, 355] and amorphous $CaCO_3$ (1475 cm^{-1} and 1418 cm^{-1}) [355].

As observed in the XRD results (Fig.5-2), 14 days of accelerated carbonation induce a higher extent of carbonation than exposure for 365 days (Fig. 5-3) to natural carbonation, with the formation of three types of $CaCO_3$ polymorphs, mainly on the specimen's surface and mid-region. The formation of the amorphous $CaCO_3$ phase normally shows split peaks with two maxima at ~1410 cm^{-1} and ~1480 cm^{-1} [356], while the crystalline carbonate phases typically show a shaper band at this region. The split peaks corresponding to the amorphous carbonate phase were observed in the mid and centre regions of 365 d natural carbonated samples for all three slags (Fig 5-4B, 4D and 4F) used in this study, which suggests a lower extent of carbonation in these regions compared to the surface regions. The amorphous $CaCO_3$ is not a stable phase and tends to transform to aragonite in the presence of Mg ions [355]. This observation also agrees with early-stage carbonation of blended cements (30 % and 60 % slag replacement) that amorphous $CaCO_3$ was found with spilt ν_3 bands [357]. Long-term exposure to carbonation leads to a shaper band of the carbonate ν_3 bands with the formation of crystalline $CaCO_3$ phases, and it is pronounced in the surface region for the three slag-based samples consistent with the XRD results (Fig 5-2 and 5-3).

The type of $CaCO_3$ polymorphs can be identified by carbonate groups in the out-of-plane deformation band (ν_2) between ~850 and 880 cm^{-1} [354] [165] and the in-plane band (ν_4) between ~700 and 750 cm^{-1}[355]. Both calcite and vaterite show similar ν_2 bond vibrations at ~877 cm^{-1} [356], whereas aragonite exhibits a band at ~854 cm^{-1}. The carbonate group ν_4 bond at ~750 cm^{-1} is related to vaterite, and ~713 cm^{-1} is aragonite [355]. Results reveal that calcite and aragonite are the main carbonation products irrespective of the slag used or CO_2 concentration of exposure in the surface regions, consistent with the observed in the XRD results (Fig. 5-2 and 5-3).

After 14 days of accelerated carbonation, a high intensity was observed in the regions assigned to the $CaCO_3$ phases (1590 - 1300 cm^{-1}) in mid and surface regions for all three slag-based pastes (Fig. 5-4A, 4C and 4E). On the other hand, under natural carbonation exposure, a higher

extent of carbonation was only observed in surface regions (Fig. 5-4B, 4D and 4F), compared to the mid and centre regions. This observation is consistent with the XRD results (Fig. 5-3). Thus, it suggests that the elevated CO_2 concentration (1 %) leads to a much higher extent of carbonation than the specimen placed under the ambient condition for all three slag-based pastes.

The C-(A)-S-H gel formed in the Na_2SO_4-activated slag cements presents an asymmetric stretching vibration of Si-O-T bands at ~959 cm^{-1} [358]. The T means either the tetrahedral silicate or aluminium, in Q^2 and Q^2 (1Al) sites, confirmed by ^{29}Si MAS NMR when analysing Na_2SO_4-activated slag cements [63, 84]. Small peaks at ~668 cm^{-1} and ~448 cm^{-1} are associated with symmetrical stretching vibration of Si-O-T bands [359]. The increased wavenumber of the C-(A)-S-H gel at asymmetric stretching vibration (~959 cm^{-1}) suggests the higher degree of polymerisation in silicates with a low concentration of calcium, attributed to C-(A)-S-H gel decalcification [126]. After 14 days of accelerated carbonation, significant wavenumber shifts in peaks corresponding to C-(A)-S-H were detected in the surface compared to the mid and centre regions for all three slags used, and the greater extent of decalcification in the surface area is related to the fully carbonated area, which will be further discussed in the following section. On the other hand, 365 days of natural carbonation only cause a modest shift in the wavenumber corresponding to the C-(A)-S-H in surface regions for all three slags, indicating limited carbonation of this phase. A similar observation was found in a blended slag cement system comparing the carbonation results using 2 % CO_2 accelerated condition and ambient exposure [165]. These observations raise questions about whether the carbonation mechanism is similar in exposing the material to these two CO_2 concentrations (1 % vs 0.04 %) and whether the experimental results are comparable or directly transferable for long-term prediction of carbonation performance in Na_2SO_4-activated slag cements. It is known that varying degrees of polymerisation with corresponding changes in the morphology of C-A-S-H gel, may in turn affect the pore structure of cements, accelerating the CO_2 diffusivity [63, 115, 329].

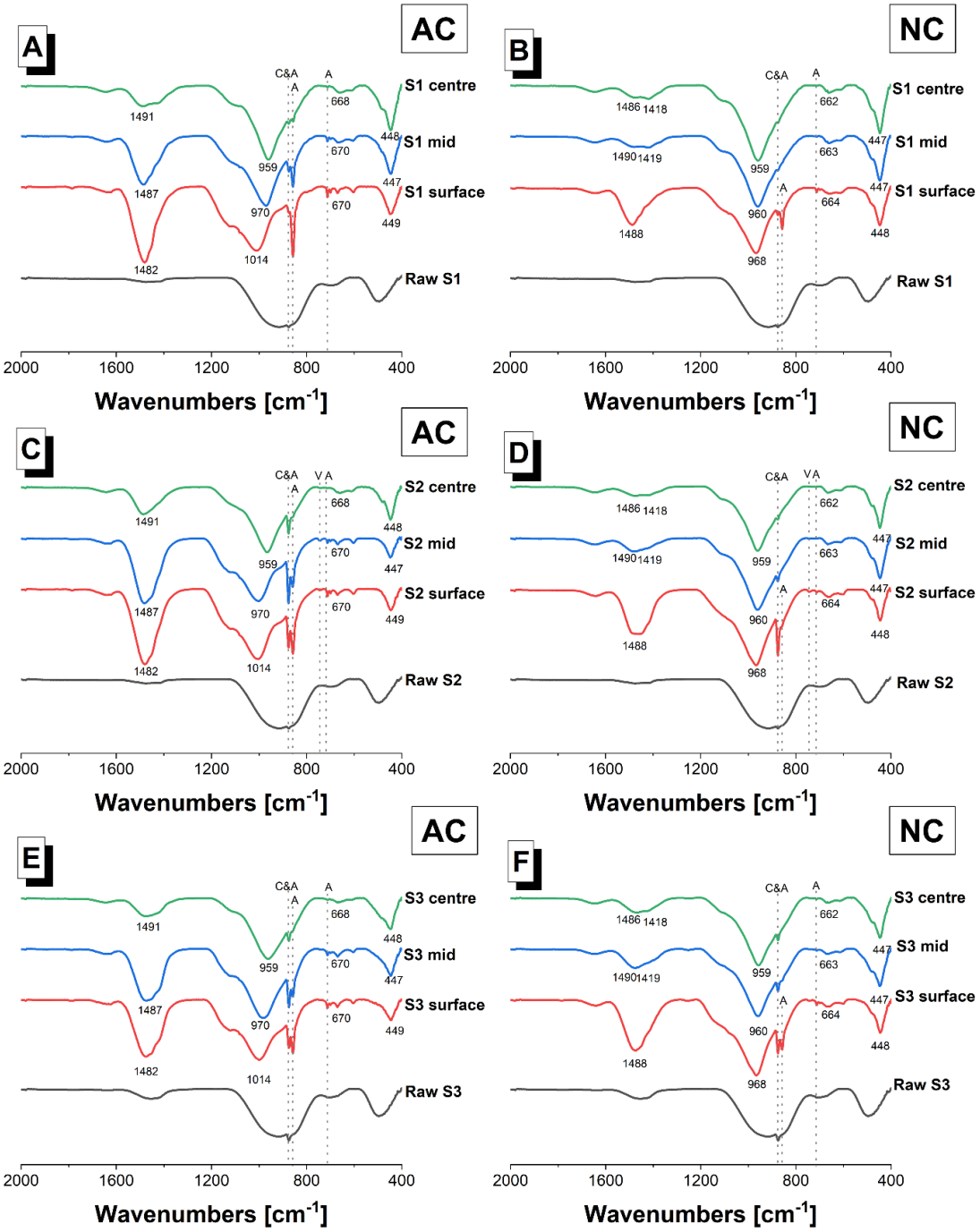

Figure 5-4. Fourier transform infrared spectra of Na_2SO_4-activated slag cements exposed to accelerated carbonation (AC) conditions for 14 days using slag (A) S1, (C) S2 and (E) S3; and exposed to natural carbonation (NC) conditions for 365 days using slag (B) S1, (D) S2 and (F) S3. The NC and AC mean natural and accelerated carbonations, respectively. The C, V and A indicate three types of $CaCO_3$ polymorphs: calcite, vaterite and aragonite

5.3.3 Microstructural changes

Figure 5-5 shows backscattered electron (BSE) images at the interfacial regions of the carbonation front identified from pH indicator measurement after 14 days of accelerated carbonation and 500 days of natural carbonation. The brightness of phases in BSE images is a function of atomic number. Phases with higher atomic numbers have more electrons, so higher possibility of interacting with incident electrons with brighter images [360, 361]. The bright grey particles in the micrographs correspond to unreacted slag; the less bright grey regions between the remnant slag particles correspond to the previously identified reaction products i.e., C-A-S-H gel, $CaCO_3$ polymorphs and ettringite, which has been confirmed in the XRD (Fig. 5-2 and 5-3) and ATR-FTIR (Fig. 5-4). The darker black regions correspond to pores of different sizes within the cementitious matrix.

The regions affected by carbonation can be identified based on the difference in greyscale observed on the BSE images (Fig. 5-5). The uncarbonated region (lighter grey matrix) shows a more compact and denser microstructure than the carbonated regions. This indicates that a more porous microstructure was formed in the carbonated regions being more visible under accelerated conditions compared to ambient conditions (Fig. 5-5). A similar observation has been reported in blended Portland slag and other alkali-activated slag cements [68, 114, 135].

Under accelerated carbonation microcracks along with an increase in porosity are observed and likely associated with the formation of $CaCO_3$ polymorphs and low-density reaction products causing localised strains within the microstructure, often referred to as carbonation shrinkage [117], or loss of moisture at exposure RH causing capillary pressure and correspondingly leading to volume changes [362]. On the contrary, the specimen exposed to atmospheric CO_2 conditions shows (Figures 5-5D, 5-5E and 5-5F) no microcracks. This behaviour highlights the difference in carbonation mechanisms using different CO_2 concentrations. As the exposure temperature and RH are similar under natural or accelerated carbonation, an intact microstructure in natural carbonation after 500 days indicates that the elevated CO_2 concentration is the main reason leading to the microcracking. Studies related to carbonation shrinkage of alkali-activated slag cements are very limited [139, 363], and there is no published research focusing on carbonation-induced shrinkage of Na_2SO_4-activated slag cements.

The microcracking is likely induced by drying and carbonation shrinkage occurring simultaneously. Under accelerated carbonation conditions rapid decalcification of C-A-S-H gel and secondary reaction products takes place, leading to internal RH changes due to the simultaneous consumption of carbonic acid and formation of water [103]. The local moisture

gradient between the pore structure and the environmental chamber can also lead to the desiccation of the paste sample and the consequent formation of cracks [118, 363]. The carbonation shrinkage is induced by the decalcification of the C-(A)-S-H gel and ettringite.

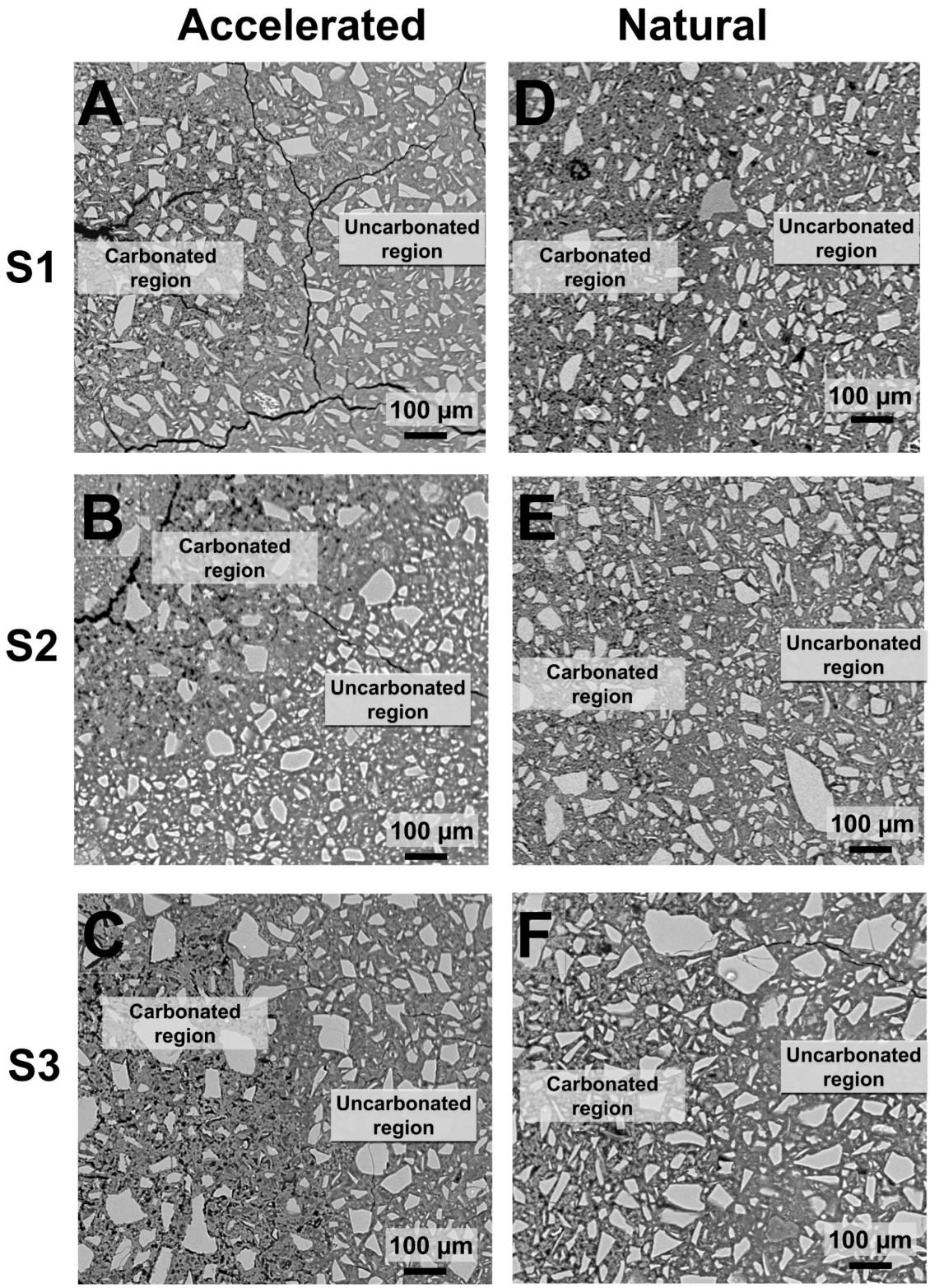

Figure 5-5. BSE images of Na_2SO_4-activated slag cements at 200 magnifications in the regions of carbonation front, determined by using 1 % phenolphthalein, after 14 days of accelerated carbonation (A, B, C) and 500 days of natural carbonation (D, E, F), as a function of the slag used

In BSE-EDX maps of Na_2SO_4-activated slag cements exposed to accelerated carbonation (Figure 5-6) for 14 days or natural carbonation (Figure 5-7) for 500 days is observed that although the CO_2 concentration leads to a different microstructure development, sulfur is significantly depleted in the fully and partially carbonated region. This is due to the decomposition of the main sulfur-bearing phase ettringite, as confirmed by XRD (Fig. 5-2 and 5-3), while Na is concentrated mainly in the carbonated region. This indicates that potential ionic migration might happen between Na^+ and S^{2-} due to the decomposition of C-(A)-S-H gel and ettringite during carbonation. Similar observations were also reported in the carbonation of Portland cements pastes [114], 30 % fly ash blended mortars [364] and calcined clay blended cements [365].

Diffusion within the pore solution is primarily governed by the gradient of ionic concentrations, exhibiting an inverse relationship with the intensity of solid elements detected via EDX analysis [196, 341]. Considering Na_2SO_4 is serving as an activator, it is anticipated that the sodium (Na) and sulfur (S) concentrations from any residual unreacted activator would be evenly distributed throughout the sample. Sulfur, when incorporated into ettringite, is mainly present as an anionic sulfate group [63, 84]. A discernible decline in the EDX detected sulfur signal within carbonated regions indicates that sulfate is released because of ettringite decomposition. Moreover, the relatively smaller crystal sizes of sulfur-bearing carbonation products (gypsum and bassanite) as identified by XRD (Fig. 5-3) compared to those of ettringite, are likely favouring a more homogeneous distribution of sulfate-containing phases within carbonated areas [366, 367]. In contrast, ettringite typically forms clusters that appear with greater brightness in SEM images.

Beyond the conversion of ettringite into gypsum or bassanite, previous studies have underscored gypsum's high solubility in contributing to the diffusion of sulfate [VI] ions from carbonated to non-carbonated zones [203, 364]. Within sodium sulfate-activated slag cements, this gypsum or bassanite formation promotes the movement of sulfate ions, driven by the sulfur concentration gradient. Such a migration pattern has similarly been observed in the carbonation processes of blended cements that include sulfur-rich phases like ettringite and monosulfoaluminate [364, 368].

The higher sodium signal detected in the carbonated region via EDX mapping suggests differences in sodium concentration between carbonated and uncarbonated regions. This discrepancy may stem from moisture transport, known as wick action, wherein ions migrate from the core of uncarbonated regions to the surface [369]. Then, the decrease in relative humidity within the pore structure may lead to the precipitation of pore solution near the exposed surface. Similar phenomena of alkali leaching have been observed in the carbonation of blended cement systems through various techniques and thermodynamic modelling [114, 364, 368].

As mirabilite ($Na_2SO_4 \cdot 10H_2O$) and thenardite (Na_2SO_4) were not identified by XRD (Fig 5-2 and 5-3), the high sodium in solid phases (Fig. 5-6 and 5-7) is likely sorbed for charge-balancing in the decalcified C-(A)-S-H gel. It has been reported for alkali-activated slag cements that Na^+ is expected to be present in the C-(N)-A-S-H gel, both intercalated within interlayer and sorbed on the surface sites and the high alkali content tends to stabilise the C-(N)-A-S-H gel when the Ca/Si ratio is below 1 [339, 340]. Therefore, irrespective of the CO_2 concentration, the ionic transport of sulfur and sodium is similar in both natural and accelerated carbonation with different intensities, consistent with the corresponding change of pore solution and phase assemblage between carbonated and uncarbonated regions.

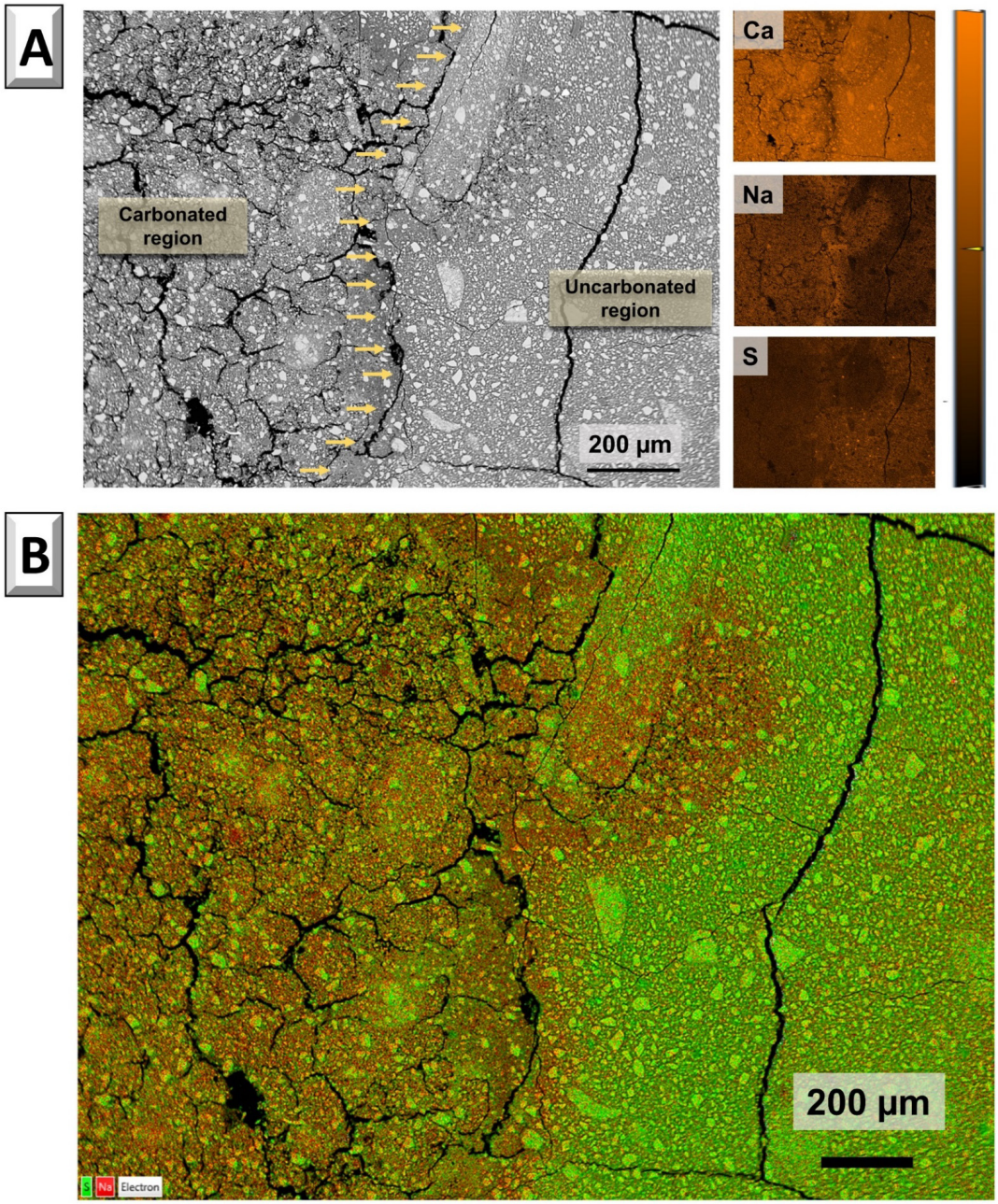

Figure 5-6. (A) Backscattered electron image and elemental maps of a Na_2SO_4-activated slag using slag S2 in the boundary between carbonated and uncarbonated regions after 14 days of accelerated carbonation exposure. The yellow arrows indicate the carbonation front, determined by phenolphthalein measurement and CO_2 diffused direction; a higher intensity of orange means more corresponding elements precited. (B) The combined maps of S (green) and Na (red) are overlapped on the top of BSE images

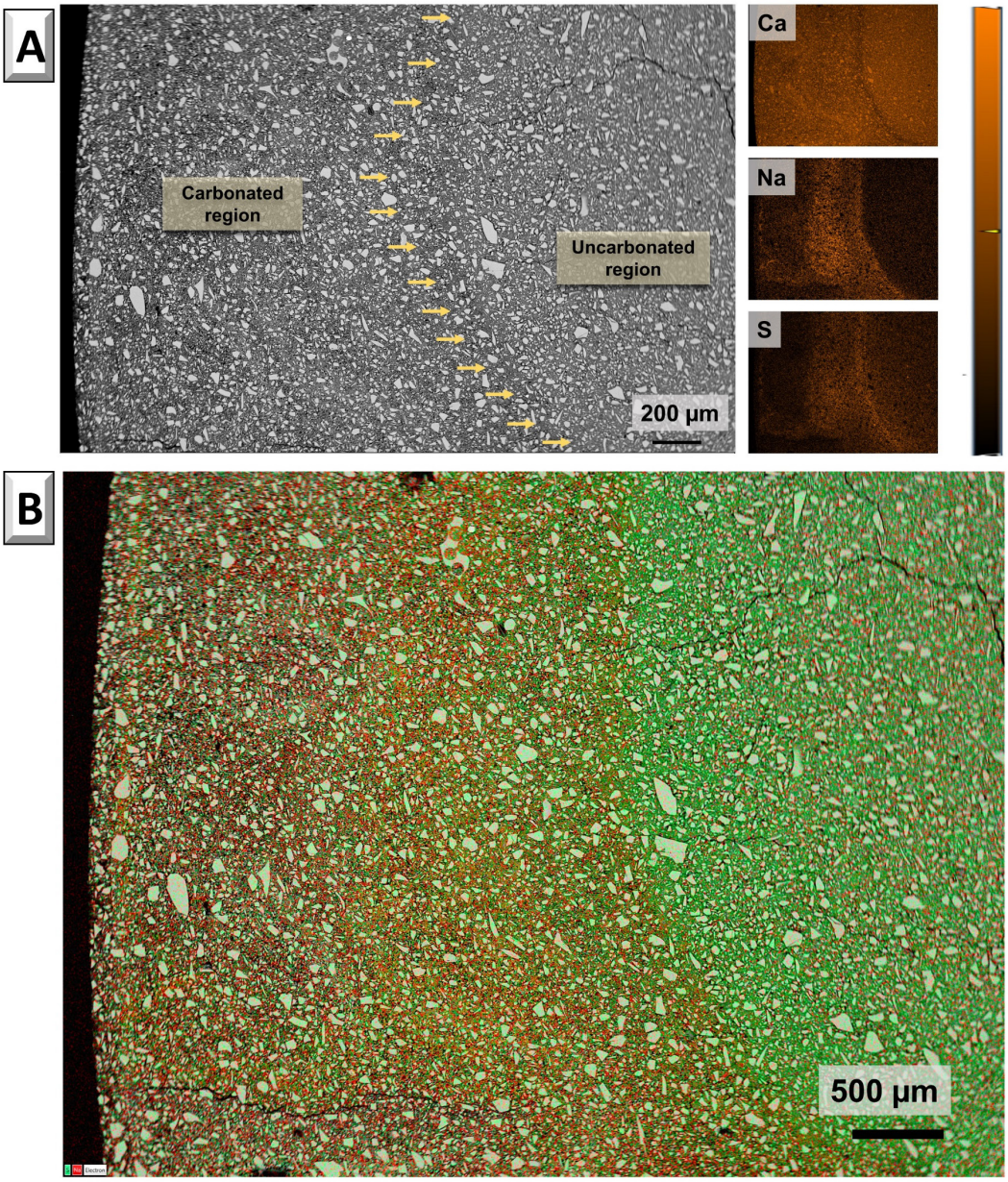

Figure 5-7. (A) BSE images and elemental maps of a Na_2SO_4-activated slag produced with slag S2, showing the boundary between carbonated and uncarbonated regions after 500 days of natural carbonation. The yellow arrows indicate the CO_2 diffused direction; a higher intensity of orange means more corresponding elements are identified. (B) BSE image with superposition of the S (green) and Na (red) elemental maps

Figure 5-8 shows the ternary diagram of CaO-Al_2O_3-SiO_2 in Na_2SO_4-activated slag cements for all three slags of this study in carbonated and uncarbonated regions after 14 days of accelerated carbonation (Fig. 5-8A) and 500 days of nature carbonation (Fig. 5-8B). The data collected through EDX shows a large scatter for accelerated carbonation (Fig. 5-8A) compared

to natural carbonation (Fig. 5-8B), which is related to a higher degree of carbonation. The composition of the carbonated points is significantly different from that of the uncarbonated region clusters. This is consistent with decalcified C-(A)-S-H gel with reduced Ca/Si ratio and the formation of an aluminosilicate type gel upon carbonation [68, 76]. The scatter of points collected in the carbonated regions towards higher calcium contents is related to the formation of $CaCO_3$ polymorphs and gypsum or bassanite, as confirmed earlier from XRD results (Fig. 5-2 and 5-3). It is not possible to directly distinguish the intermixing of $CaCO_3$ and aluminosilicate gels in the BSE images due to limitations in resolution. Groves et al. [116] found that the overall morphology of the C-S-H gel tends to be retained upon carbonation, and also identified that vaterite is intermixing with decalcified C-S-H gel at outer reaction products regions at the nanoscale characterising by TEM-EDX. This might explain the similar Al content in both carbonated and uncarbonated regions, with the intermixing of $CaCO_3$ polymorphs and decalcified C-(A)-S-H gel.

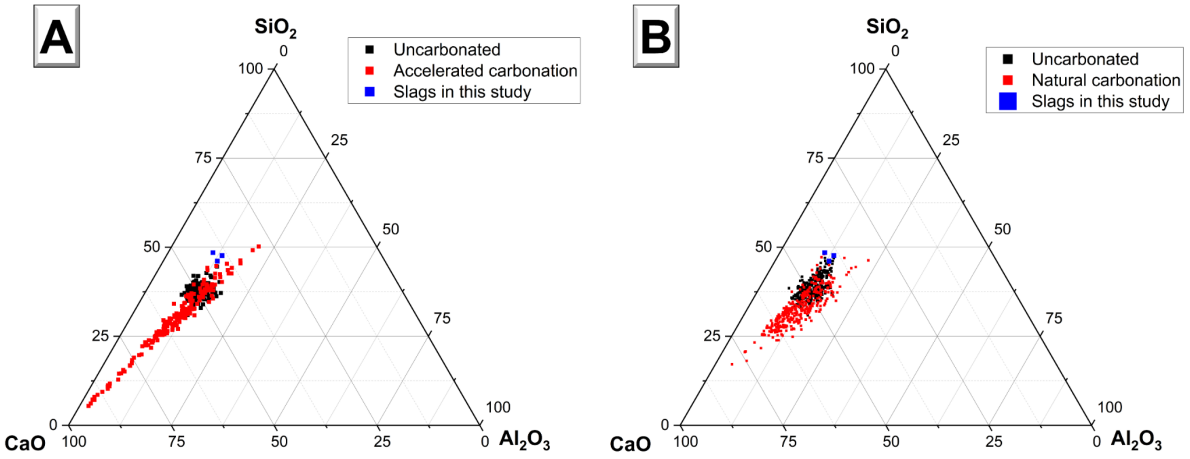

Figure 5-8. The ternary CaO-SiO_2-Al_2O_3 system in Na_2SO_4-activated slag cements using three slags after (A) 14 days of accelerated carbonation and (B) 500 days of nature carbonation.; the EDX points (at least 80 points per sample) were taken in both uncarbonated and carbonated regions. The chemical composition of the blast furnace slag is based on XRF results of three anhydrous slags

5.3.4 Carbonation depth of paste specimens

Figure 5-9 shows photographs of the specimen cross-sections before and after spraying 1 % phenolphthalein indicator on three slag-based pastes after accelerated carbonation for different exposure duration. The dark green area, which has not been exposed to oxygen and/or CO_2, presents a bright fuchsia colour after spraying the phenolphthalein indicator, associated with

the uncarbonated region of the paste. Green colouration originates from sulfur within the slag and oxidation causes the formation of polysulfides that vanish green colour [370]. In the accelerated carboned samples, the beige regions were most likely due to the oxidation of sulfur [136], which closely matched the carbonated regions as they were colourless after spraying phenolphthalein, indicating the pH value in this region was lower than 8.5 [103]. For all three slag-cements assessed, the oxidation front matches the carbonation front in accelerated carbonation conditions, and both the oxidation front and carbonation depth increase at higher exposure time (Fig. 5-9). S1-based paste showed less carbonation depth in the first 14 days under 1 % CO_2 exposure, and all three slags were fully carbonated by 28 days of accelerated carbonation.

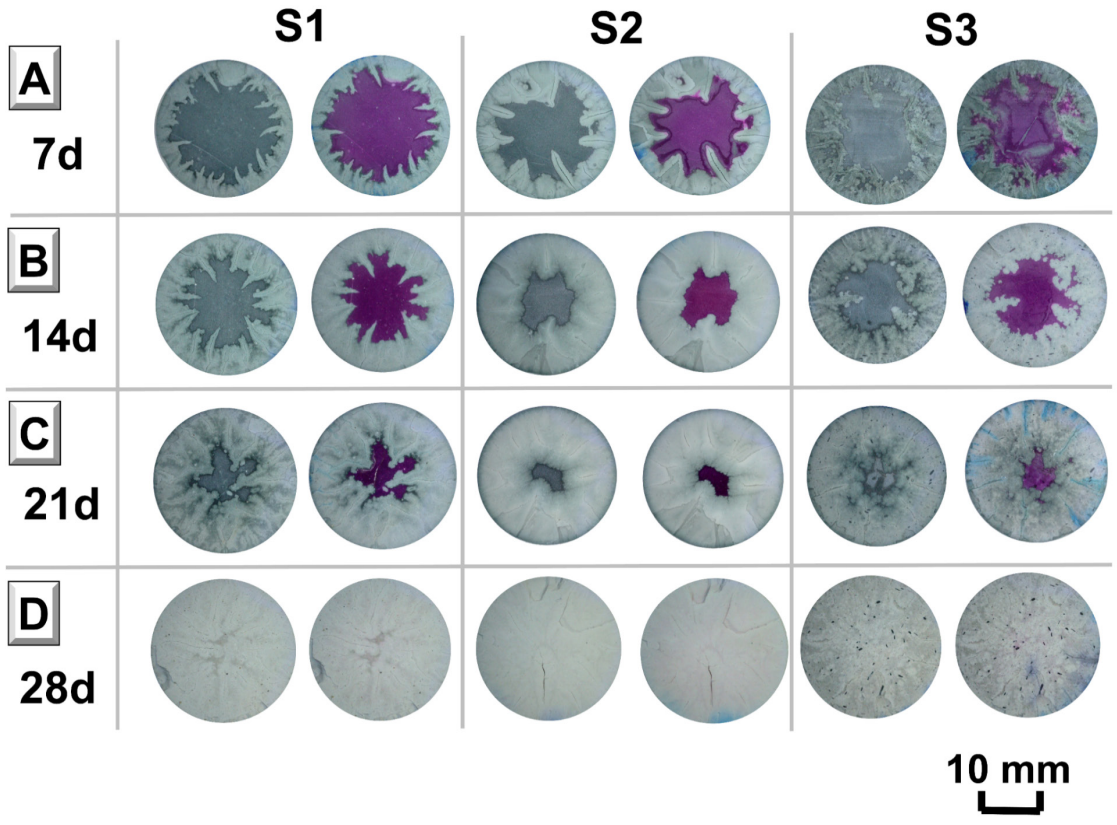

Figure 5-9. Photographs of transverse sections of Na_2SO_4-activated slag cements produced with S1, S2 and S3 slags before (left) and after (right) spraying with the 1 % phenolphthalein indicator, after 7 days (A), 14 days (B). 21 days (C) and 28 days (D) of accelerated carbonation

Figure 5-10 shows that the carbonation depth is not necessarily consistent with oxidation depth in natural CO_2 exposure, contrary to the observations under 1 % accelerated carbonation condition. A gradual increase in the oxidation front was observed over time, especially in S2 and S3-based pastes. The oxidation front was higher in S2>S3>S1, indicating a reduced diffusivity of O_2/CO_2 in the S1 paste compared with the other cement pastes evaluated. Unlike the observed in samples exposed to accelerated carbonation, under natural exposure conditions, a homogeneous and clear oxidation front retained a higher pH and fuchsia colour after spraying the phenolphthalein indicator, confirming the lack of carbonation in that region. After 500 days of natural carbonation (0.04 % CO_2) under the same temperature and RH only ~1.5 mm carbonation depth was observed (Fig. 5-11). This further confirms differences in the carbonation mechanisms when samples are exposed to 1 % and 0.04 % CO_2 concentrations.

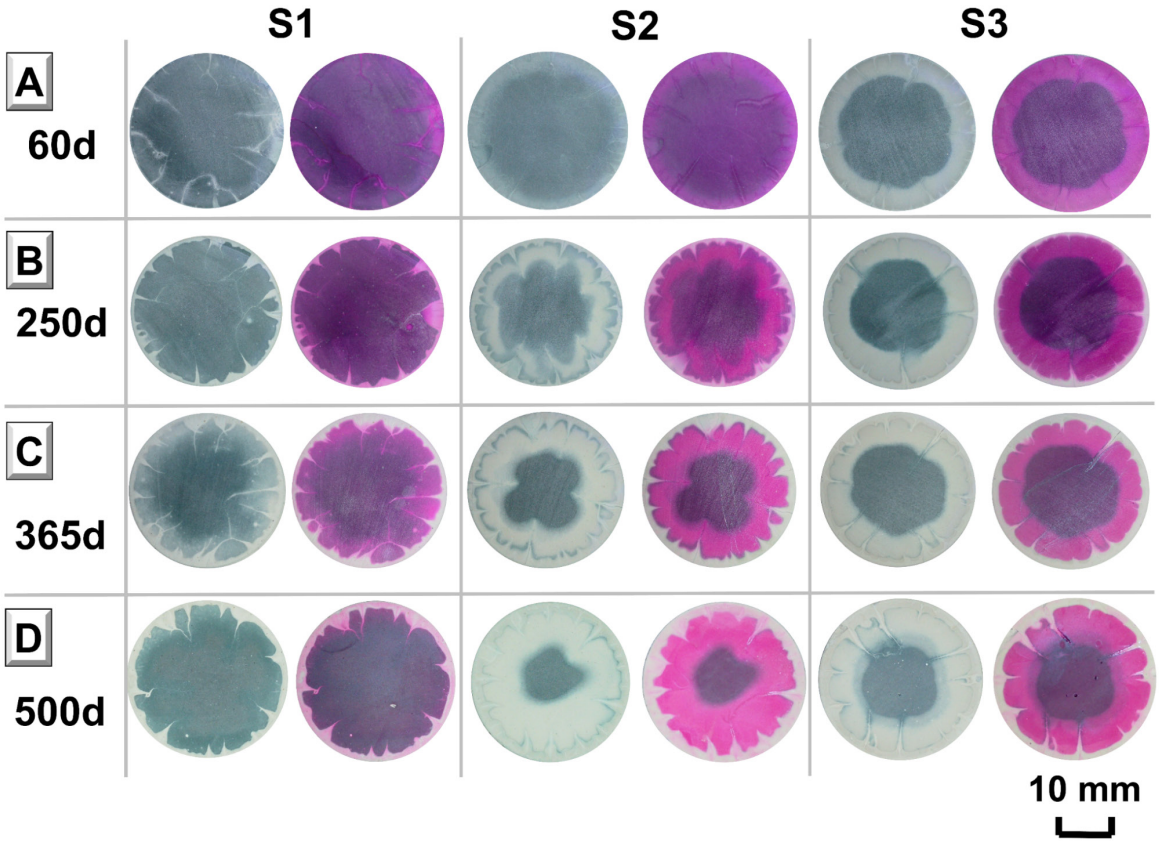

Figure 5-10. Photographs of transverse sections of Na_2SO_4-activated slag cements produced with S1, S2 and S3 slags, before (left) and after (right) spraying with the 1 % phenolphthalein indicator, after 60 days (A,), 250 days (B), 365 days (C) and 500 days (D) of nature carbonation

Under accelerated carbonation conditions the S1 slag with a higher Mg/Al ratio showed the lowest carbonation depth compared to S2 and S3 (Fig. 5-11), consistent with the observed oxidation depth under natural carbonation exposure (Fig. 5-10). This is likely associated with potentially lower diffusivity or the potential formation of a higher amount of layered double hydroxides in the S1 slag paste system compared to S2 and S3. Although this was not identified by XRD (Fig. 5-2), its formation has been observed by NMR spectroscopy in other studies [18, 63, 84] in near-neutral salt slag cements. Previous studies demonstrated that this phase increases the CO_2 capacity of the alkali-activated slag cements [68].

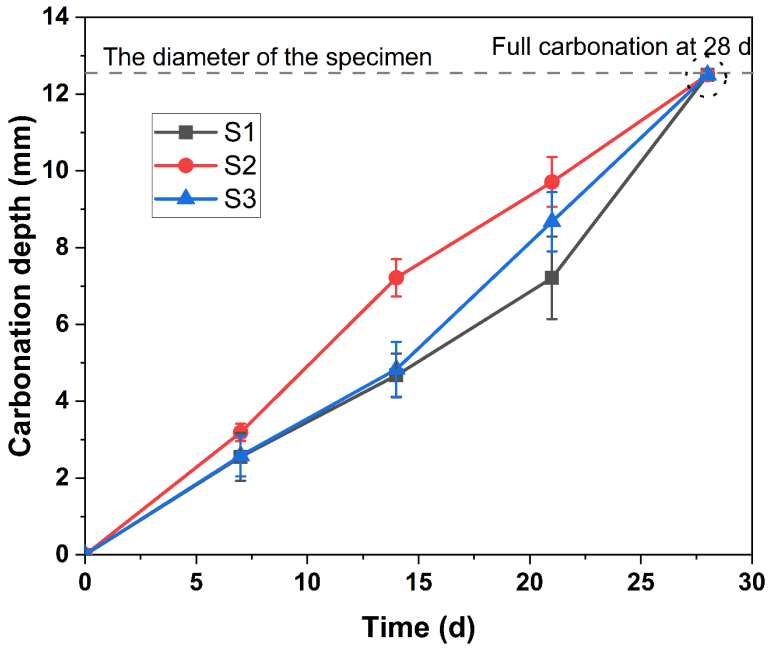

Figure 5-11. The evolution of carbonation depth for the Na_2SO_4-activated slag cements exposed to accelerated carbonation condition (1%) from 7 to 28 days as a function of the slag type used; the carbonation depth was determined by a phenolphthalein indicator using three mortar specimen per sample per age

5.3.5 Carbonation coefficient of pastes

Figure 5-12A shows the measured carbonation depth using the phenolphthalein colour indicator as a function of the square root of the exposed time (days) to determine of carbonation rate coefficient, based on Equation 5.1 [163]. This equation assumes that the carbonation progress in these samples is a diffusion-controlled mechanism that can be described by the square root of exposure time [163]. Irrespective of the slag composition, ~2 mm/√days of accelerated carbonation coefficient was observed in Na_2SO_4-activated slag pastes, and this result is comparable to the carbonation coefficient of alkali-activated slag mortar and concrete

using conventional activators (sodium hydroxide and sodium silicate) exposed to 1 % CO_2 [40]. A significant difference was observed in the carbonation rate coefficient (slope of the fitted line) between natural and accelerated carbonation for all three slag-based cement, based on the regression analysis of the scatter points.

$$x = k\sqrt{t} \quad \text{(Equation 5.1)}$$

x is the carbonation depth [mm]; t is the exposure time [days] and k is the carbonation rate coefficient.

Accelerated carbonation is typically applied to determine carbonation resistance within a short testing period, from several years under ambient conditions to a few weeks. However, natural carbonation provides more realistic information that reflects the in-service life. To correlate the results from accelerated carbonation with the prediction of the carbonation depth under the ambient condition, the relation was derived by Fick's law shown in Equation 5.2 [163].

$$\frac{k_{acc}}{k_{nat}} = \frac{\sqrt{c_{acc}}}{\sqrt{c_{nat}}} \quad \text{(Equation 5.2)}$$

c is the CO_2 concentration [g/m^3]. Subscript *acc* and *nat* mean the accelerated and natural carbonation, respectively.

Considering in this study the only variable is the CO_2 concentration, theoretically the accelerated carbonation (1% CO_2) rate should be 5 times faster than the natural carbonation (0.04%). However, considering the carbonation coefficients calculated for the pastes produced with the three slags used in this study and reported in Figure 5-12A, it was calculated (Fig. 5-12B) that the average accelerated carbonation coefficient is 32.78 times the average natural carbonation coefficient. This suggests that inducing accelerated carbonation using 1 % CO_2 concentration significantly overestimates the carbonation rate of these cements, compared with what is observed at ambient conditions, leading to an underestimation of the potential service life of these materials.

Besides, it should be noted that the square root-of-time law assumes the CO_2 diffusivity is a constant value for samples exposed to different CO_2 concentrations as a function of time [163]. However, this study has found that the two carbonation conditions lead to a different amount of carbonated products which might cause a gradient in the degree of saturation and degree of slag reaction at different depths of the specimen, consistent with what has been reported in

other studies [148, 161, 198, 257]. Those factors change the pore network of the material, causing a dynamic value of the CO_2 diffusivity as a function of reacted CO_2, degree of saturation and curing time at each layer from exposure surface to the core of the specimen [148, 199].

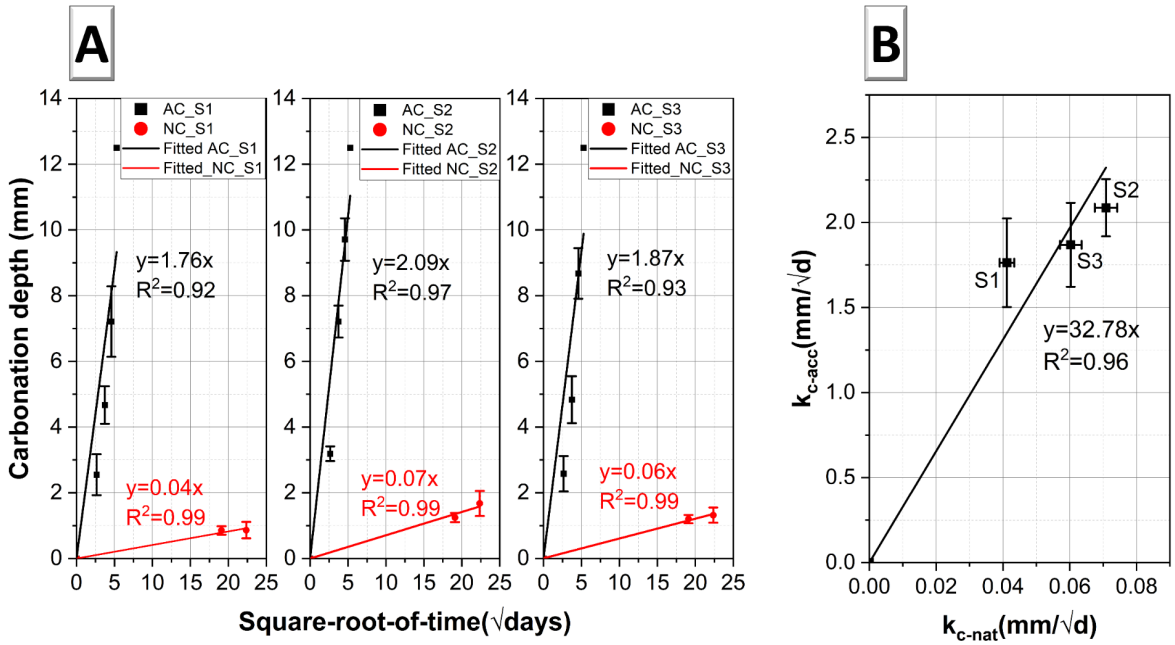

Figure 5-12. (A) The effect of CO_2 concentration (AC: 1 % vs NC: 0.04 %) on the carbonation rate for S1, S2, and S3-based sodium sulfate-activated slag pastes. AC and NC mean accelerated and natural carbonation, respectively. The slope of the curve represents the carbonation rate; (B) correlation of the carbonation rate obtained under accelerated carbonation condition (c_{CO2}, acc= 1 %) vs carbonation rate obtained under natural condition (cco_2, nat= 0.04 %)

5.3.6 Thermodynamic modelling of Na_2SO_4-activated slag exposed to CO_2

Figure 5-13 shows the phase evolution of sodium sulfate-activated slag predicted under accelerated carbonation (1% v/v). With the increased addition of CO_2 and air into the system to mimic 1 % CO_2 condition, the C-(N)-A-S-H, ettringite and Mg-Al-SO_4-LDH were predicted to decompose leading to the formation of calcite, gypsum and Mg-Al-CO_3-LDH phase, which is consistent with the carbonation modelling of the similar system reported elsewhere [257]. This result indicates a decrease in both paste sample volume and pH value with an increase in CO_2 uptake, attributed to the decomposition of reaction products. This is the major cause for the dimensional instability of the cement matrix consistent with the formation of microcracking

as observed by BSE (Fig. 5-5). Similar findings have also been reported in the carbonation of calcium sulfoaluminate blended slag cement, known to be an ettringite-rich cementitious matrix [371]. The formation of calcite and gypsum agrees with experimental observations obtained using XRD (Fig. 5-2). Except, for calcite, aragonite and vaterite have also been identified using XRD (Fig. 5-2) and ATR-FTIR (Fig. 5-4) in this study, in good agreement with results reported in the literature for this material and other alkali-activated slag cements system [68, 76, 136, 257]. However, in thermodynamic modelling, the standard Gibbs free energy of the formation of calcite is lower than aragonite and vaterite [76, 372], and GEMs predict the equilibrium state of the pore solution with formed phases [373], so thermodynamic modelling tends to predict the calcite among $CaCO_3$ polymorphs preferentially. Therefore, the experimental observation of other $CaCO_3$ polymorphs that form in the intermediate state is due to the kinetics involved in the formation of $CaCO_3$ polymorphs (metastable state) rather than the phase composition reaching an equilibrium state rapidly upon carbonation.

The NAT phase ($Na_2Al_2Si_3O_{10}{\cdot}2H_2O$) and silica gel were merged to represent the formation of aluminosilicate gel with varying compositions. The progressive carbonation leads to an increased amount of this aluminosilicate gel. Although these zeolites have different crystalline structures from aluminosilicate gels, the bulk chemical composition is similar, especially the Al/Si ratio. This value then determines the standard Gibbs free energy of formation [374]. Despite crystalline zeolites cannot form under ambient temperature and pressure due to the limited kinetics [375], the thermodynamic database of crystalline zeolites and disordered aluminosilicate phases are similar [109, 374]. It is considered reasonable to use zeolites to represent the disordered aluminosilicate gels during carbonation. Modelling results in this study (Fig. 5-14) align with experimental studies that carbonation of Na_2SO_4-activated slag cements causing increased resonance in the Q^3 and Q^4 sites using ^{29}Si MAS NMR are related to the formation of aluminosilicate gel [257]. A similar observation has also been found in the Na_2CO_3-activated slag cements [68].

As the degree of carbonation increases with higher amounts of CO_2 reactions, the pH value and Ca/(Al+Si) ratio decrease, as shown in Figure 5-13. Two stages in the decalcification process of C-(N)-A-S-H are reported in the alkali-activated slag cements, including the loss of interlayer charge balanced Na^+ and Ca^{2+}, and loss of structural Ca^{2+} [76, 115, 257]. These observations are consistent with the carbonation of Na_2SO_4-activated slag cements for the three slags used in this study. Although the equivalent DoR was kept constant for these simulations, the S1-based sample (Fig. 5-13A) still shows a relatively higher initial pH value and Ca/(Al+Si) ratio. It further confirms the experimental observation that the slag with a higher Mg/Al ratio shows higher carbonation resistance. The total CO_2 reacted for complete carbonation of C-(N)-

A-S-H and ettringite were found to be 13 g per 100 g of slag in S1 which is also higher than 12 g and 11.8 g in S2 and S3, respectively.

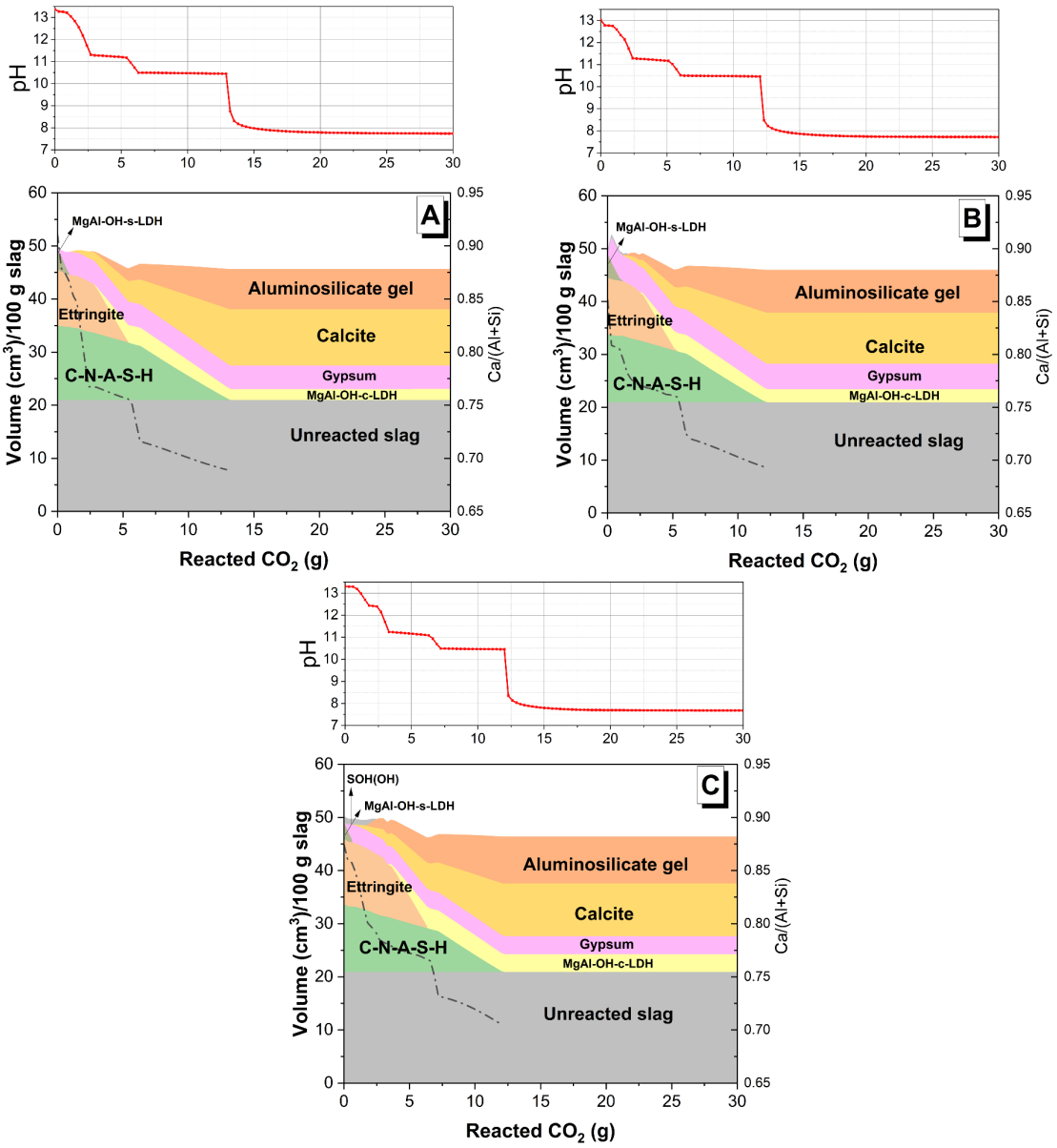

Figure 5-13. The predicted phase assemblage of Na_2SO_4-activated slag pastes (40 % degree of slag reaction) under stepwise accelerated carbonation (1 %). Diagrams correspond to simulations of Na_2SO_4-activated slag cements using the slag (A) S1, (B) S2 and (C) S3 slag, respectively. The red dashed line represents the pH value of the pore solution; the black dashed line represents the Ca/(Al+Si) ratio of C-(N)-A-S-H gel

5.3.7 Compressive strength development and carbonation depth of Na_2SO_4-activated slag mortar

The specimen exposed to 0.04 % CO_2 concentration (Fig. 5-14) showed a significantly higher compressive strength compared to those sealed cured, with an increase of ~28 MPa from 28 to 180 days under natural carbonation exposure. Although 180 days of accelerated carbonation caused complete carbonation, the specimens presented 30 MPa of compressive strength, demonstrating robust load-bearing capabilities of these materials, consistent with what has been observed in sodium carbonate-activated slag cements [376]. Considering the RH was similar between accelerated or natural carbonation, the difference between the two exposure conditions can be attributed to chemical alteration in the microstructure induced by differences in CO_2 concentrations.

Carbonation depth in mortar increased rapidly between 60 to 140 days and the specimens were fully carbonated after 100 days of accelerated carbonation. However, only ~2 mm carbonation depth was observed after 180 days of natural carbonation. Loss of strength is ~ 25 % relative to 28 days of curing, after complete carbonation in accelerated conditions. Rashad [146] also found that 5 % CO_2 leads to a ~25 % decrease in compressive strength after 56 days of exposure to Na_2SO_4-activated slag mortar. These observations in mortar specimens further confirm the complex chemical alterations under different CO_2 concentrations leading to the formation of varying carbonation reaction products as discussed earlier (Fig. 5-2 and 5-3). The results may imply that the 1 % CO_2 concentration is too aggressive for these cements, and it may significantly underestimate its carbonation performance.

As highlighted in section 5.3.3, the severe microcracking observed in the accelerated carbonation might be due to shrinkage. It has been reported that the dry shrinkage of the alkali-activated mortar is two times lower than the corresponding paste samples [377], and 28 days of sealed curing can further minimise the drying shrinkage reaching comparable performance as Portland cement in alkali-activated slag and fly ash concrete [378]. It is reasonable to assume that the effect of dry shrinkage in Na_2SO_4-activated slag mortar could have been minimal. No physical signs of cracking were observed on the surfaces of the mortar specimens. Carbonation-related pore coarsening and shrinkage are the dominant factors that cause instability of the cement pastes, resulting in degraded mechanical properties and porous microstructure at accelerated conditions.

Given the slow rates of carbonation observed under natural exposure conditions, reductions in compressive strength due to elevated CO_2 concentrations might only become apparent after

extended periods of natural exposure. However, the sustained increase in compressive strength under natural carbonation conditions and the limited carbonation depth suggest a continuous increase in the degree of slag reaction over time. This ongoing reaction under natural carbonation may ensure sufficient alkalinity in the pore solution to further activate the slag, progressively refining the pore structure and thereby enhancing resistance to CO_2 ingress [379]. Additionally, the reduced water content under ambient conditions is potentially another contributing factor to the higher compressive strength observed, compared to the nearly saturated sealed-cured specimens[380].

The reduced compressive strength induced by carbonation in sodium silicate-activated slag cements [41, 135] is not observed in Na_2SO_4-activated slag cements. Consistent with what has been reported for Na_2CO_3-activated slag cements in [68] where 0.04 % CO_2 concentration led to decreased overall intrudable porosity from precipitation of $CaCO_3$ polymorphs blocking the percolating pores [68], which is similar to the carbonation of Portland cement [103] and supersulfated cement [381]. Therefore, the result of this study reveals that the Na_2SO_4-activated slag cements can present extended service performance without compromising its structure integrity, potentially due to some extent to carbon absorbance. This characteristic might not adequately be captured by current standardised accelerated carbonation testing developed for Portland or blended Portland cements.

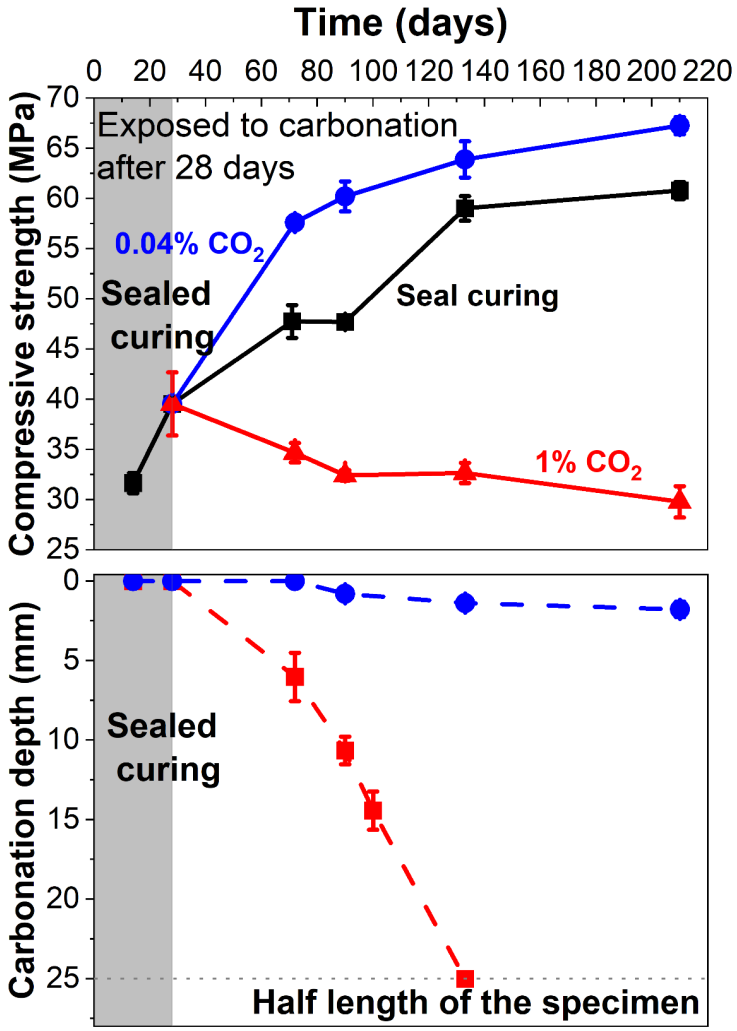

Figure 5-14. Change in compressive strength and carbonation depth of Na_2SO_4-activated slag cement mortar using slag S2 under different CO_2 concentrations. All the specimens were sealed curing for 28 days before carbonation exposure

5.4 Conclusion

This Chapter presents the structural alterations in Na_2SO_4-activated slag cements as a function of the CO_2 exposure concentration. Under accelerated carbonation (1 % CO_2) decomposition of ettringite is the major alteration identified in the cements assessed, resulting in the formation of aragonite and gypsum as dominated carbonation reaction products, intermixed with calcite and vaterite. Conversely, after 1 year of natural carbonation, ettringite was still observed in the exposed surface of the specimen. The partial decomposition of ettringite led to the formation of bassanite instead. Decalcification of the main reaction products a C-(A)-S-H gel leads to the formation of a more crosslinked aluminosilicate structure under accelerated carbonation

conditions, whereas natural carbonation barely affects the structure of C-(A)-S-H gel. Carbonation seems to induce ionic transport as high concentrations of sodium precipitate in the carbonated region, whereas sulfur is concentrated in the uncarbonated region.

Accelerated carbonation induces severe microcracking in Na_2SO_4-activated slag cements consistent with the rapid decomposition of reaction products and potential shrinkage. The decalcification of C-(A)-S-H gel happened rapidly, leading to a reduction of the Ca/Si ratio as determined by BSE-EDX analysis, and confirmed by thermodynamic modelling simulations. On the other hand, microcracking was not observed in specimens exposed to ambient conditions at controlled temperature and RH after 500 days of exposure.

Na_2SO_4-activated slag pastes were fully carbonated after 28 days under accelerated carbonation (1% CO_2), while only ~1.5 mm carbonation depth was noted under ambient conditions (0.04% CO_2) after 500 days, irrespective of the slag used in this investigation. The carbonation rate under a 1% CO_2 concentration is significantly higher compared to that determined under natural carbonation exposure, indicating that the conventional equation based on Fick's law, typically applied to Portland or blended Portland cements, does not enable to predict the carbonation potential of Na_2SO_4-activated slag cements accurately.

The compressive strength of Na_2SO_4-activated mortar continues to rise beyond 180 days of natural carbonation exposure, with a minor carbonation depth of approximately 2 mm, reaching up to ~68 MPa. Even with complete carbonation after 100 days of accelerated exposure, the mortar specimens maintained a compressive strength of about ~30 MPa. This outcome suggests that, unlike other alkali-activated slag cements, sodium sulfate-activated slag materials retain their load-bearing capacity post-carbonation, exhibiting compressive strengths and carbonation resistance akin to blended Portland cements.

Chapter 6

3D CRYSTALLINE PHASE AND PORE STRUCTURE EVOLUTION UPON CO_2 EXPOSURE IN SODIUM SULFATE-ACTIVATED CEMENTS PASTES

Note: This chapter is primarily based on the paper "3D crystalline phase and pore structure evolution upon CO_2 exposure in sodium sulfate-activated cement pastes" by **Z. Yue**, Z. Su, P. P. Paul, A.T.M. Marsh, A.Macente, M. D. Michiel, J. L. Provis, P. J. Withers, S. A. Bernal, submitted to the journal *Cement and Concrete Research* (accepted).

6.1. Introduction

In this Chapter, the effects of CO_2 exposure on the microstructure of sodium sulfate-activated slag cements produced with three types of blast furnace slag are investigated. To elucidate the simultaneous changes in phase assemblage and pore structure resulting from carbonation in a non-destructive manner, 3D microscale imaging techniques were employed. Specifically, synchrotron X-ray diffraction computed tomography (XRD-CT) was coupled with X-ray computed tomography (μCT) to analyse the pore structure and spatial arrangement of crystalline phases in Portland clinker-free sodium sulfate-activated blast furnace slag cement pastes, both before and after carbonation.

This is the first study using these techniques to visualise the reaction products forming in sodium sulfate-activated slag cements and to determine how they change as a consequence of accelerated carbonation. Changes in pore structure, diffusion tortuosity and formation factor of the assessed material are also examined by using three commercial European blast furnace slag precursors. Results reveal a discernible reduction in ettringite volumes and, notably, provide the first definitive spatial evidence of Mg-Al-SO_4-layered double hydroxide (LDH) phase

formation within the sodium sulfate-activated slag cement system, highlighting its critical role in CO_2 sequestration. The process of accelerated carbonation was observed to increase porosity while reducing the tortuosity across the studied alkali-activated slag pastes, yielding a pore network that rivals conventional blended Portland cements in terms of lower porosity and enhanced tortuosity. Remarkably, the paste produced using slag with the highest Mg/Al ratio (0.8) demonstrated superior carbonation resistance. Additionally, a correlation was established between simulated tortuosity and 3D porosity in accordance with Archie's law. This represents a significant step forward enabling a rapid and reliable estimation of carbonation resistance and CO_2 binding capacity of alkali-activated slag cements.

More broadly, this study also demonstrates the potential of combining XRD-CT and μCT to study complex multi-component composite materials such as alkali-activated cements, providing unique novel insight into their microstructural features as a function of mix design and chemical interaction with CO_2.

6.2 Experimental methodology

The sodium sulfate-activated slag pastes were prepared using an activator dose of 6 g sodium sulfate powder per 100 g of slag and a water-to-solids (slag + sodium sulfate) mass ratio of 0.40, as detailed in Chapter 3.2. To achieve homogeneous mixtures, a high-shear mixer (Heidolph) was employed to mix the pastes for 10 minutes. The mixing speed was set at 200 rpm for the initial 3 minutes, increased to 400 rpm for the subsequent 3 minutes, and further increased to 800 rpm for the final 3 minutes. During speed transitions, the mixer was paused for 30 seconds to scrape off any paste adhering to the container walls, ensuring it was returned to the centre of the container to maintain uniform mixing. The pastes were then cast into custom-made 2 mm moulds and sealed for curing at 20°C for 28 days.

After the curing period, the specimens were demoulded and subjected to synchrotron uCT and XRD-CT testing both before and after carbonation. Detailed synchrotron experimental setting and image processing workflow are referred to in sections 3.6 and 3.7.

6.2.1 Onsite CO_2 exposure

Each specimen was mounted on a rotation stage and scanned by uCT and XRD-CT (described in Section 3.3.6) in the pristine state. Subsequently, the specimen was placed into a desiccator under vacuum. Figure 6-1 shows on-site carbonation in sodium sulfate-activated slag pastes to achieve a 5 % CO_2 atmosphere at ambient pressure.

A 5 % CO_2 / 95% N_2 (v/v) gas mix was then injected until atmospheric pressure was reached. One cycle of CO_2 exposure corresponded to 18 minutes of exposure. After completing the first cycle of CO_2 exposure (cycle 1), the mounted specimen was placed back on the stage. Similar steps were repeated for cycle 2 of carbonation (i.e., an additional 18 min of CO_2 exposure). The CO_2 concentration used is quite high for evaluating the carbonation of alkali-activated slag cements for predicting performance under environmental conditions [42], mainly because exposure beyond 1% CO_2 induces changes in the type of sodium and calcium carbonates forming. However, this study aimed to validate the applicability of the XRD-CT technique to determine different microstructural features induced by accelerated carbonation of these materials, and therefore this CO_2 concentration was selected to induce severe and rapid changes in the paste within the experimental synchrotron beamtime constraints.

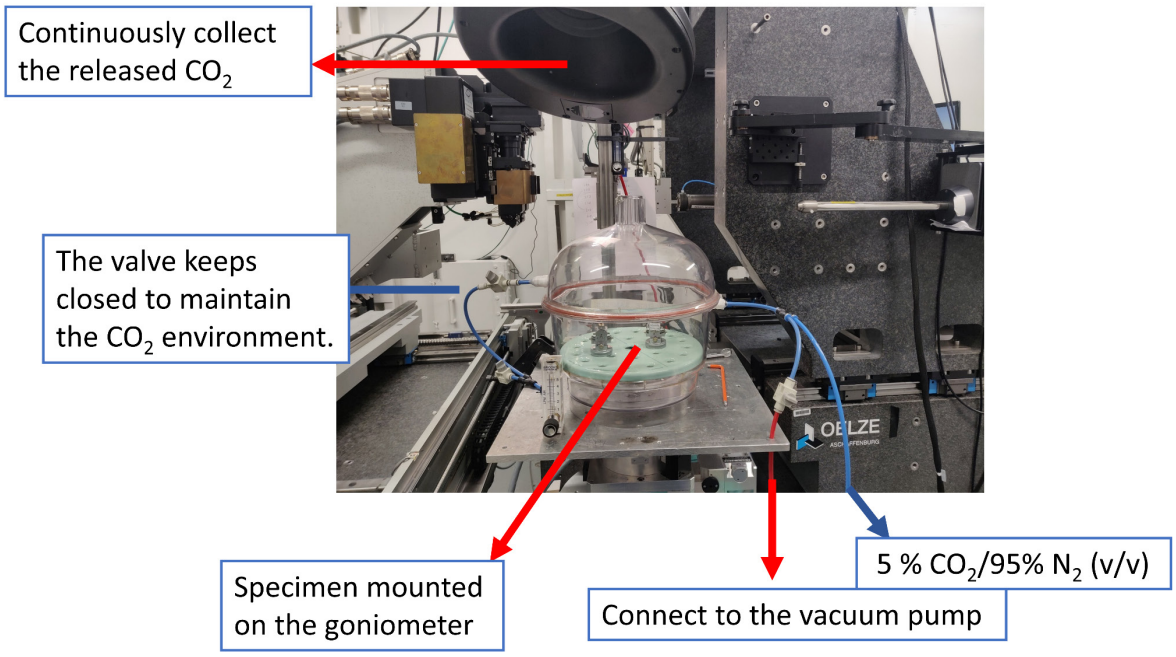

Figure 6-1. On-site carbonation setup for synchrotron uCT and XRD-CT testing

6.3 Results and discussion

6.3.1 Effect of secondary reaction products on carbonation performance

The reaction products of sodium sulfate slag cements are well-known, but their exact relationship with the evolving porosity under carbonation is still not fully understood. The XRD-CT measurements were limited to angles less than 26° Cu-Kα equivalent 2θ, where the

main diffraction peaks of ettringite and Mg-Al layered double hydroxide (LDH) type phases are identifiable in alkali-activated cements [84]. These are the main crystalline secondary reaction products forming in sodium sulfate-activated slag cements, and consequently, this section will mainly focus on analysing the effect of carbonation exposure on changes in their crystallinity. Figures 6-2 a, b and c present the equivalent XRD patterns (recalculated to give angles equivalent to Cu-Kα radiation) shown layer-by-layer (i.e. data integrated over the volume at each specific depth) from the surface to the core of a specimen, before and after exposure to carbonation in the S2-based pastes. The main crystalline product identified is ettringite (powder diffraction file (PDF)# 01-072-0646). As CO_2 tends to diffuse from the surface to the core, creating a concentration gradient, the bound amount of CO_2 decreases as the distance from the surface increases.

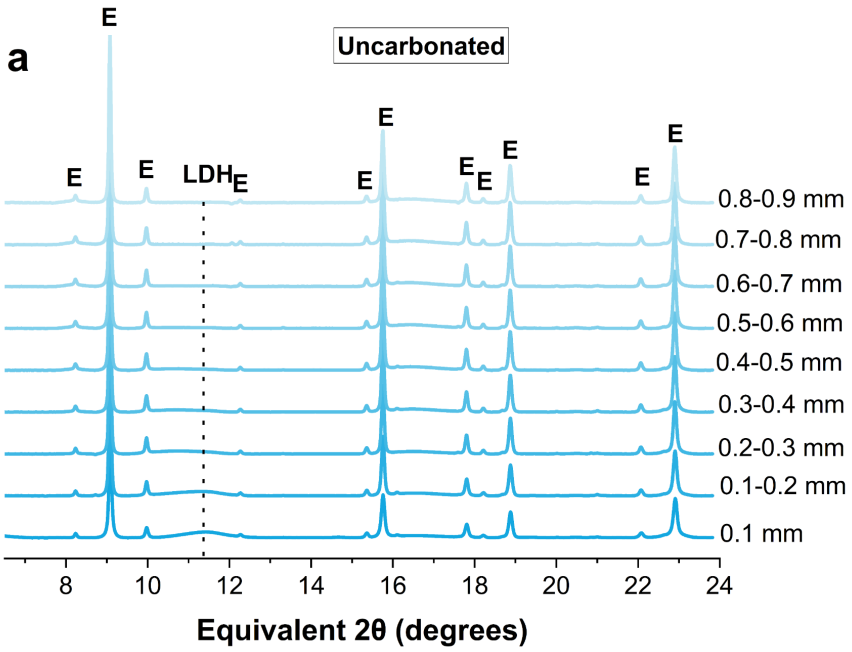

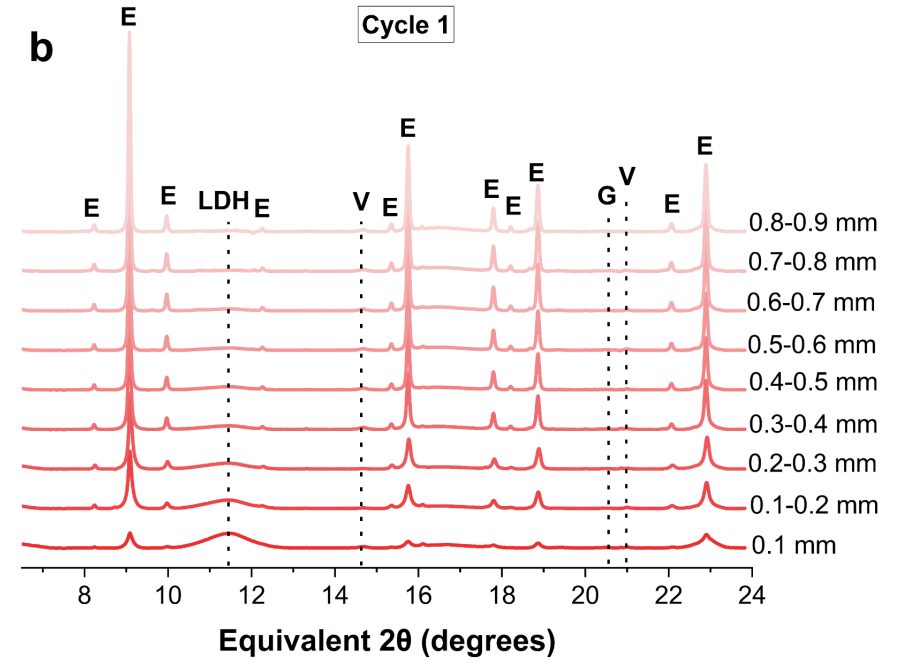
b
Cycle 1
E
E
LDH
E
V
E
E
E
E
G
V
E
E
0.8-0.9 mm
0.7-0.8 mm
0.6-0.7 mm
0.5-0.6 mm
0.4-0.5 mm
0.3-0.4 mm
0.2-0.3 mm
0.1-0.2 mm
0.1 mm
8
10
12
14
16
18
20
22
24
Equivalent 2θ (degrees)

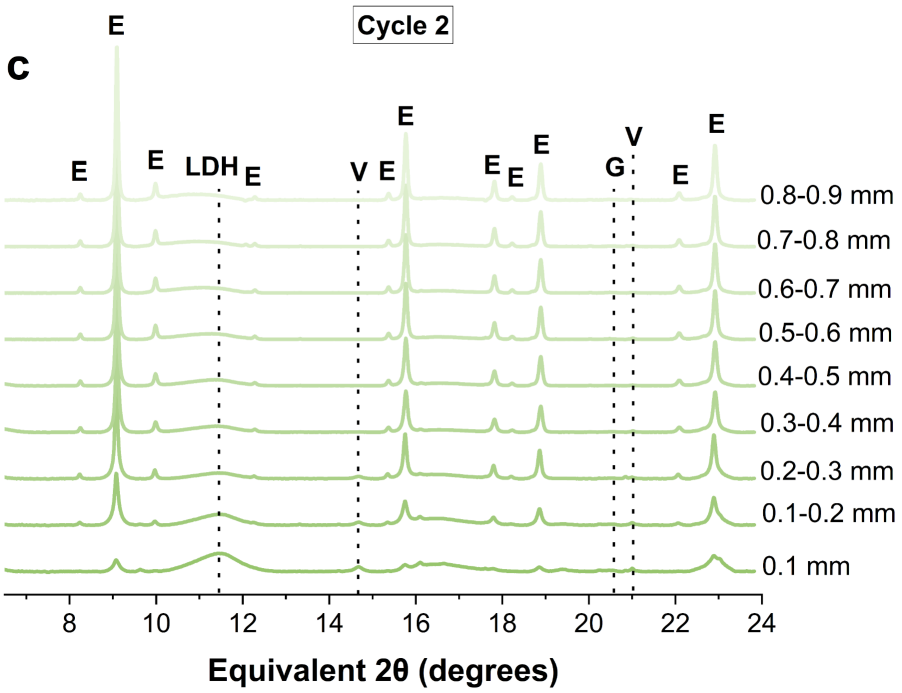
c
Cycle 2
E
E
LDH
E
V
E
E
E
E
G
V
E
E
0.8-0.9 mm
0.7-0.8 mm
0.6-0.7 mm
0.5-0.6 mm
0.4-0.5 mm
0.3-0.4 mm
0.2-0.3 mm
0.1-0.2 mm
0.1 mm
8
10
12
14
16
18
20
22
24
Equivalent 2θ (degrees)

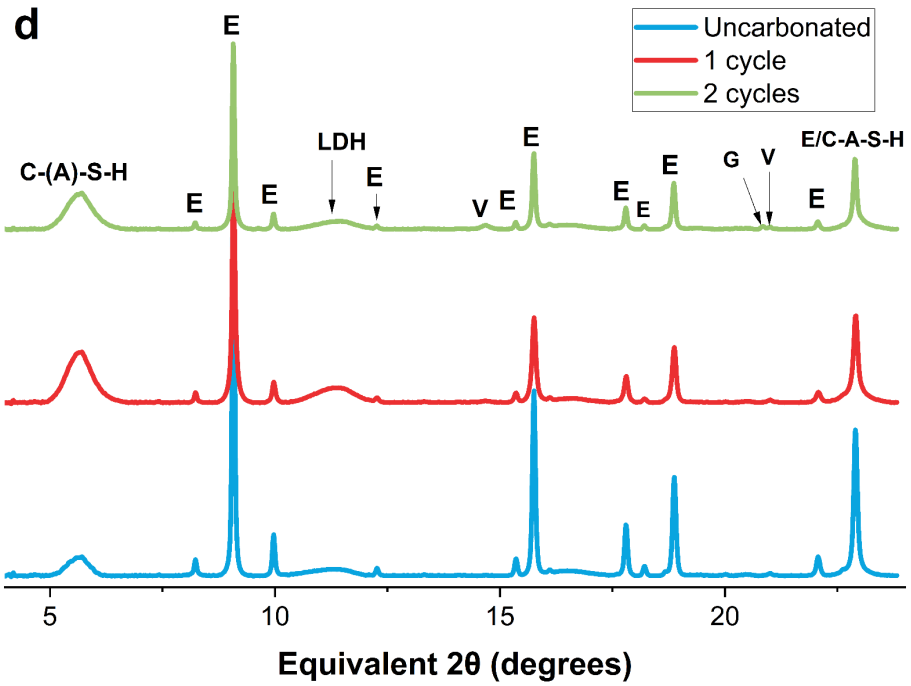

Figure 6-2. Cu-Kα equivalent XRD patterns of each layer (depths as marked) from the surface to the core of the specimen, for (a) uncarbonated; (b) after cycle one (18 mins); and (c) after cycle two (36 mins) of carbonation of sodium sulfate activated S2-slag cements. (d) Cumulation of the XRD patterns for entire specimens before and after carbonation. C-(A)-S-H: aluminium-substituted calcium silicate hydrate; E: ettringite; LDH: Mg-Al-CO_3-LDH; G: gypsum; V: vaterite

As carbonation proceeds from the specimen surface to its core, the amount of ettringite (proportional to the integrated area of the peak at 2θ = 9.138°) diffracted gradually decreases. A subtle decrease was also observed in the gypsum (PDF#00-001-0385) and vaterite (PDF#00-024-0030) phases, consistent with the progress of carbonation of ettringite in the carbonated cements [131]. Figure 6-2d shows the XRD patterns of the entire scanned specimen before and after carbonation. The primary reaction product, tobermorite-type C-(A)-S-H (PDF# 00-019-0052), is evident. During carbonation, the C-(A)-S-H gel exhibits increased crystallinity, as indicated by the shift of the peak position towards a higher diffraction angle, corresponding to a reduced d-spacing. This reduction in d-spacing may be attributed to the removal of interlayer calcium [115], leading to the formation of a more crystalline C-(A)-S-H gel [161], and/or the collapse of gel pores during the drying process, which facilitates polymerisation of -Si-O-Si bonds between C-S-H sheets [382], resulting in a decreased internal surface area of the C-S-H [383]. Figure 6-3 illustrates the spatial distribution of C-(A)-S-H gel before and after carbonation. As carbonation progresses, the C-(A)-S-H gel progressively disappears from the

exterior towards the interior of the specimen, likely due to the decalcification of this primary binding phase [131, 161]. However, the behaviour of C-(A)-S-H gel at the nanostructure scale and their crystallinity under CO_2 conditions in sodium sulfate-activated slag pastes remains largely unknown.

Figure 6-4 shows the 2D (left) and 3D (right) spatial distribution of the ettringite from the surface of the sample to the centre after two cycles of carbonation. In general, this phase is no longer detected in the samples exposed to increasing cycles of carbonation. Locally, a lower amount of ettringite at the sample edges is observed, where there is more CO_2 compared to the core of the specimen. This indicates that ettringite is one of the phases governing the accelerated carbonation of sodium sulfate-activated slag cements. This observation is consistent with bulk lab-based XRD results where it has been identified that carbonation leads to a decreased amount of ettringite and consequent degradation of C-A-S-H gel in sodium sulfate-activated slag cement pastes [131].

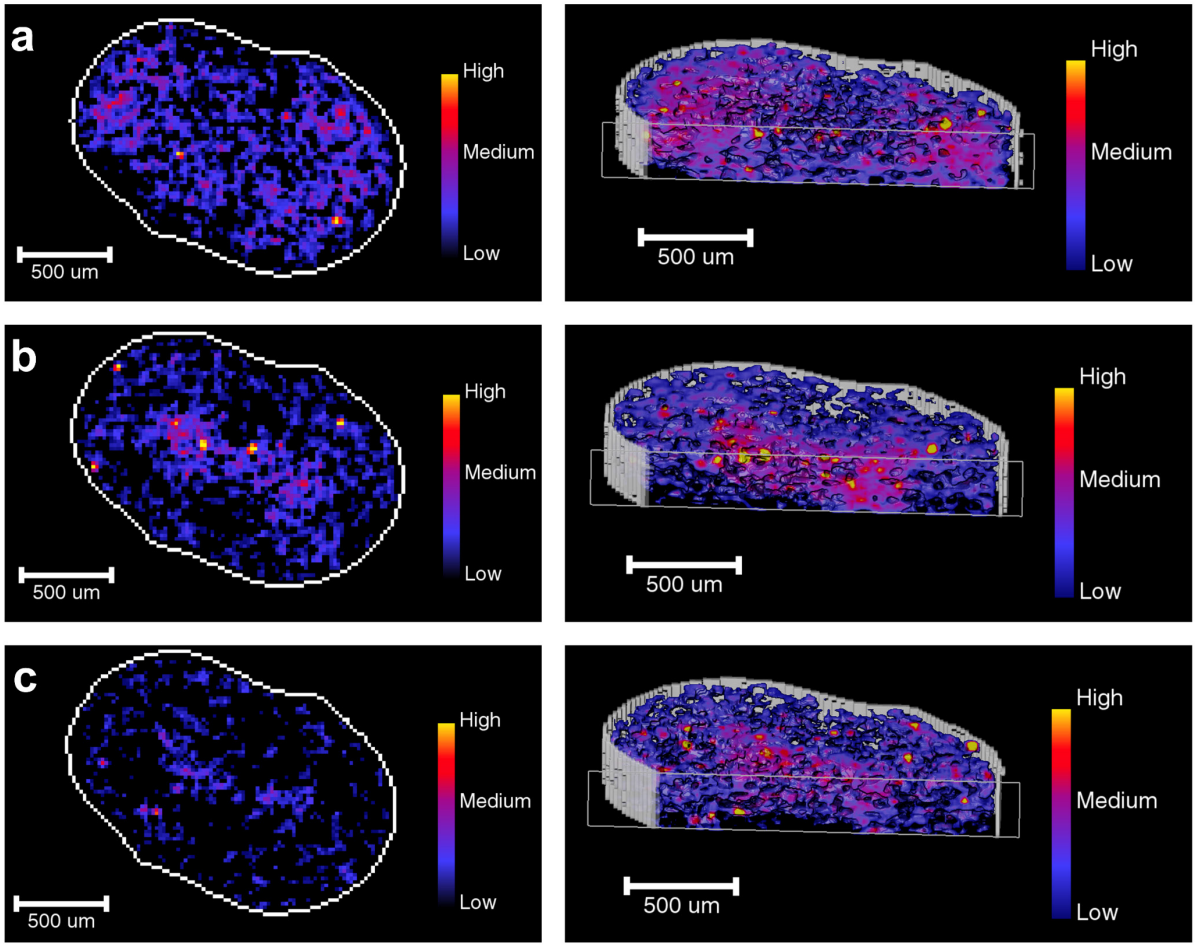

Figure 6-3. Cross-section (left) and corresponding 3D spatial distribution (right) images obtained by XRD-CT showing the distribution of C-(A)-S-H gel in sodium sulfate-activated S2-slag pastes: (a) uncarbonated; (b) after 1 cycle of carbonation (18 mins); (c) after 2 cycles of carbonation (36 mins). The white boundary (1-pixel size) delineates the specimen edge

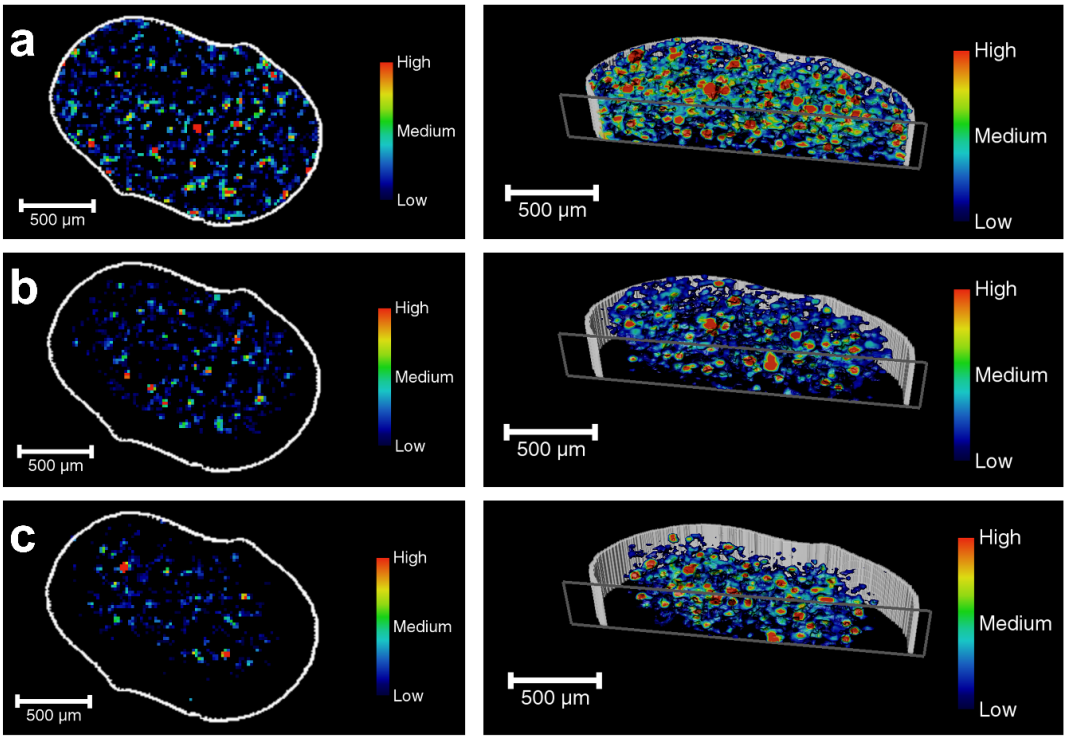

Figure 6-4. Cross-section (left) and corresponding 3D spatial distribution (right) images obtained by XRD-CT showing the distribution of ettringite in sodium sulfate-activated S2-slag pastes: (a) uncarbonated; (b) after 1 cycle of carbonation (18 mins); (c) after 2 cycles of carbonation (36 mins). The white boundary (1-pixel size) delineates the specimen edge

XRD-CT enables the role of secondary reaction products in mitigating carbonation to be investigated further; layered double hydroxides are known to play an important role in defining the durability of alkali-activated slag cements, although the exact mechanisms are not yet fully understood. A crystalline Mg-Al-CO_3-LDH phase was identified in the spectra in Figures 6-2 b and c, especially in the layers close to the surface (0.1 mm) upon carbonation, which forms from Mg-Al-SO_4-LDH. Interlayer anion interchange between sulfate and carbonate ions happens under accelerated carbonation conditions, forming the observed Mg-Al-CO_3-LDH phase. This phase is more crystalline than its sulfate analogue [95]. A similar phenomenon is observed in the carbonation of Na_2CO_3-activated slag cements, where OH^- groups in meixnerite interchange for CO_3^{2-} upon CO_2 exposure [68]. Figure 6-5 shows the spatial distribution of Mg-

Al-CO_3-LDH after one and two cycles of carbonation. This phase preferentially precipitates at the surface of the specimen and increases with increased CO_2 uptake. The formation of an Mg-Al-SO_4-LDH phase was previously hypothesised to take place in Na_2SO_4-activated slag cements based on ^{27}Al MAS NMR results, but this phase has not been detected by lab-based XRD due to its poorly crystalline structure [84, 95], and the spatial heterogeneity of such phases has been unexplored in previous works. The formation of a SO_4^{2-} intercalated Mg-Al-LDH indicates that sulfate anions are consumed in the formation of both ettringite and Mg-Al-SO_4-LDH during sodium sulfate-activation of slags. When the sulfate is consumed from the pore solution, the chemical reaction is likely to proceed similarly to the NaOH-activated slag cement system; a similar reaction mechanism has also been hypothesised for Na_2CO_3-activated slag cements [18, 57, 74].

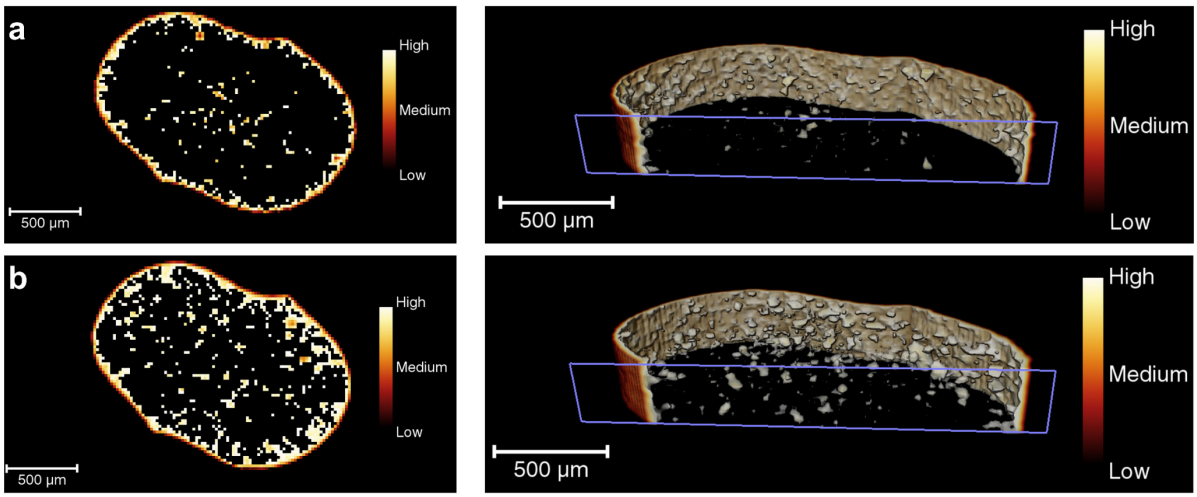

Figure 6-5. 2D virtual cross-sections (left) and 3D renderings (right) obtained by XRD-CT showing the spatial distribution of Mg-Al-CO_3-LDH in Na_2SO_4-activated S2-slag cements after (a) 1 cycle (18 mins) and (b) 2 cycles of carbonation (36 mins)

The variations in the phase assemblage under carbonation, as shown in Figures 6-2b and c at each layer, are expected to modify the pore network. The changes in the porosity as a function of the radial distance from the surface to the core of the specimen are presented in Figure 6-6. As CO_2 penetrates the specimen, the decalcification of C-A-S-H (Fig. 6-3) and ettringite (Fig. 6-4) results in increased porosity, accompanied by the more polymerised Si tetrahedra and formation of gypsum, $CaCO_3$ polymorphs and aluminosilicate [115, 350, 384]. This effect is particularly noticeable in the evaluated cement specimens, especially within the first 0.3 mm from the surface. A decrease in porosity from the CO_2-exposed surface to the core of the sample is consistent with a CO_2 concentration gradient across the specimens, making less CO_2

available to react at its core, consequently preserving its original microstructural features. Interestingly, although ettringite is almost fully consumed on the exposed surface, this has not led to a significant increase in the porosity compared to the values recorded in the uncarbonated sample centre. This may indicate that the formation of Mg-Al-CO_3-LDH, due to the exchange of carbonate for sulfate in the interlayer space of the LDH phase, compensates for some of the volume change associated with ettringite decomposition. It has been reported that the density of Mg-Al-SO_4-LDH (2.21 g/cm^3) is higher than that of Mg-Al-CO_3-LDH (2.02 g/cm^3) [284], so the tetrahedral anion SO_4^{2-} in the interlayer causes an increased *c* lattice constant and unit cell volume compared to the trigonal planar CO_3^{2-} analogue [95, 385]. This finding further confirms the role of Mg-Al-LDH phases in resisting carbonation by acting as a CO_2 sink in alkali-activated slag cements, which delays damage to Ca-bearing phases without significantly affecting the microstructure [18, 68, 75, 76].

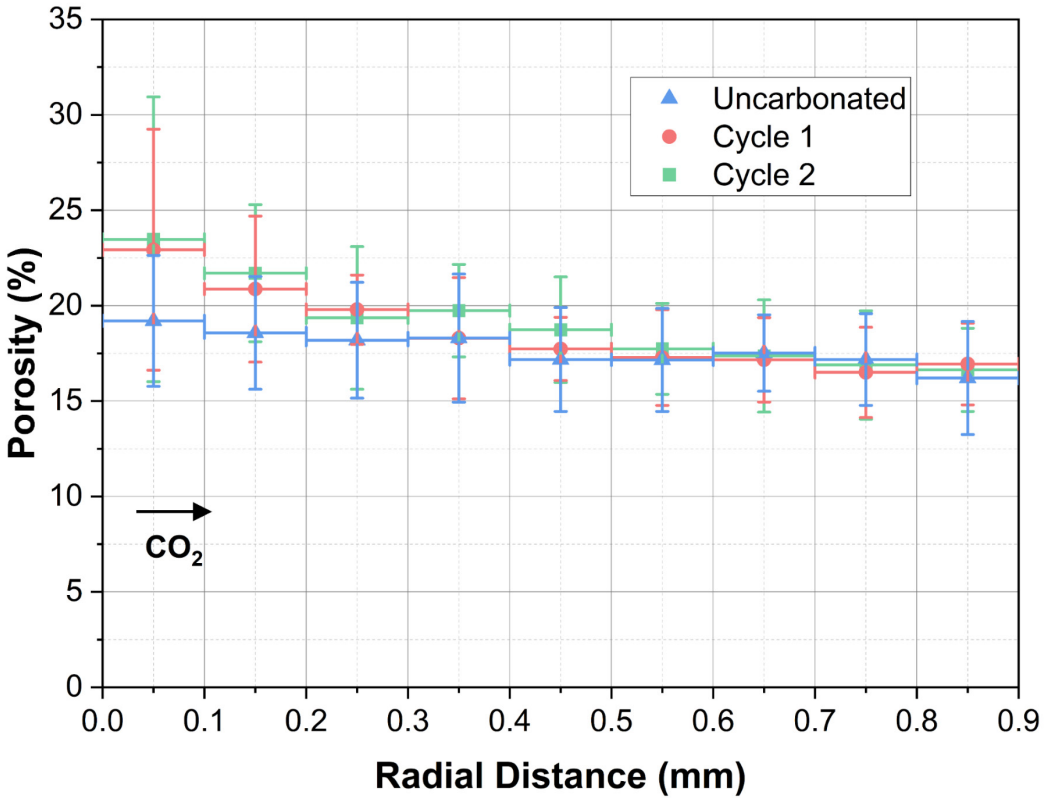

Figure 6-6. Reconstructed porosity in each layer from the surface to the core of the sample, before and after cycle 1 and cycle 2 of carbonation. Porosity values are calculated based on the segmentation of µCT results using the WeKa machine learning method

6.3.2 Tomographic approach to changes in microscale pore structure and predicting transport properties

The precursors and reaction products can be distinguished by their contrast and morphology in μCT images. Figure 6-7 shows representative ortho slices, 3D renderings of reconstructed images, segmented phases and pore size distributions in S2-based pastes before and after 1 and 2 carbonation cycles. The unreacted blast furnace slag has an irregular jagged shape [386]. The presence of tiny bright specks originates from the presence of very small particles of iron that are entrained in the production process of blast furnace slag [387]. During activation with a sodium sulfate solution, the unreacted slag maintains its original geometry and particle shape, exhibiting a relatively higher level of brightness [25, 331], whereas the hydrous (and/or intrinsically porous) reaction products such as C-A-S-H type gel, ettringite and layered double hydroxides (LDH) have lower brightness due to their lower X-ray attenuation coefficient compared to the slag [63, 84, 388]. Ettringite intermixes with C-A-S-H type gel in the outer reaction product regions, where space was originally filled with the activating solution [53]. Simultaneously, LDH intermixes with C-A-S-H gel within the inner reaction product areas, corresponding to the regions where the slag has reacted [312]. All the reaction products are intermixed on the nanoscale and C-A-S-H type gel also has nano-sized pores [84, 155]. Nevertheless, those reaction products appear homogeneous at the moderate spatial resolution achieved in this study.

The black regions correspond to the pores, which have a range of different sizes. Considering the effect of noise in the tomography data, only the pore larger than 2.1 μm was considered, which is 3 times the voxel size. Deleterious ions are mainly transported in macropores (larger than 10 μm) [25, 244], therefore the resolution in this study is deemed sufficient to evaluate the pore network of the sodium sulfate-activated slag cements to infer their effect on the durability performance of these cements. As carbonation progresses, an increased porosity with slightly decreased volume fractions of reaction products and slag was observed in the S2-based pastes.

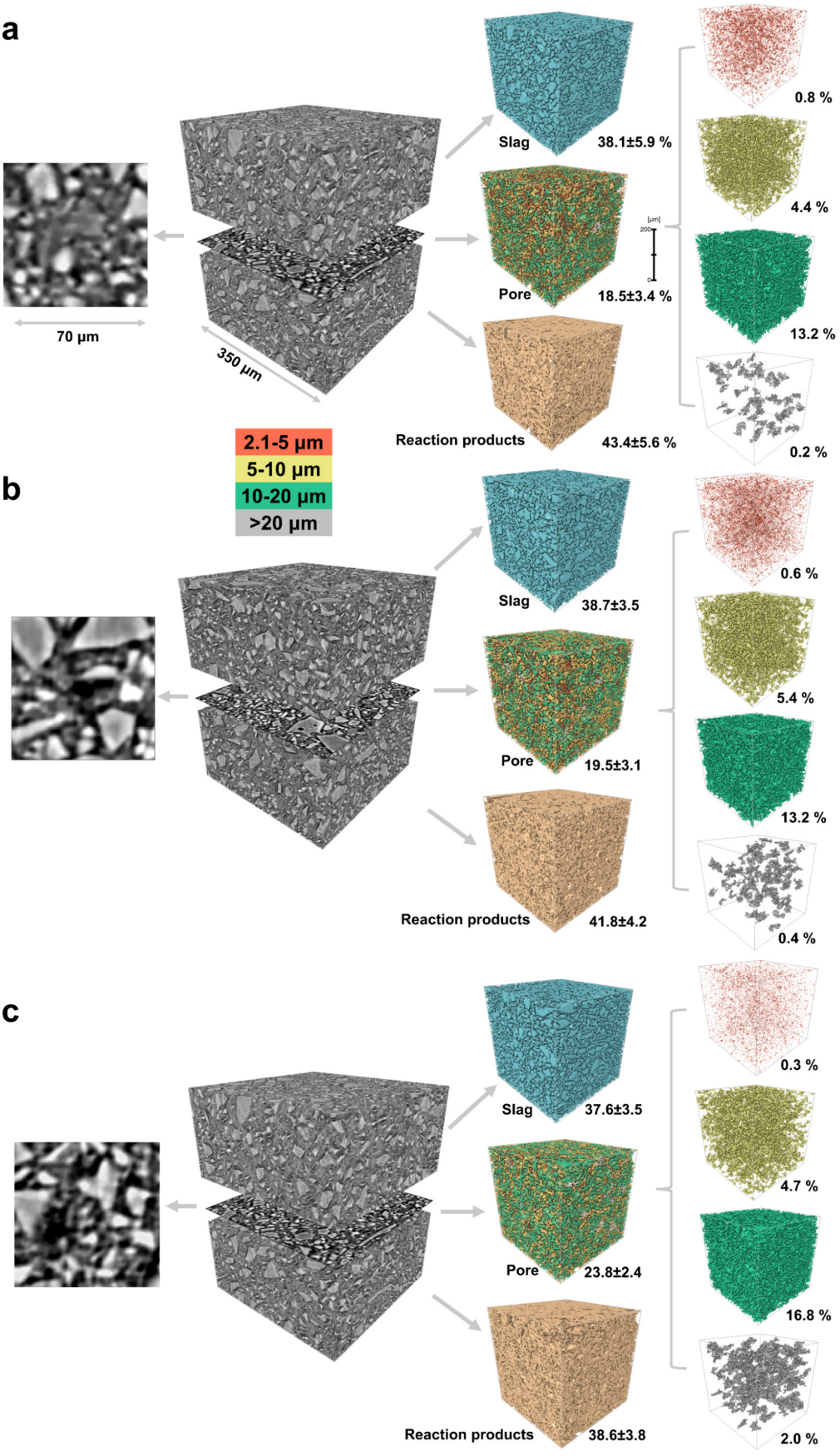
a
70 µm
350 µm
Slag
38.1±5.9 %
Pore
18.5±3.4 %
Reaction products
43.4±5.6 %
0.8 %
4.4 %
13.2 %
0.2 %
2.1-5 µm
5-10 µm
10-20 µm
>20 µm
b
Slag
38.7±3.5
Pore
19.5±3.1
Reaction products
41.8±4.2
0.6 %
5.4 %
13.2 %
0.4 %
c
Slag
37.6±3.5
Pore
23.8±2.4
Reaction products
38.6±3.8
0.3 %
4.7 %
16.8 %
2.0 %

Figure 6-7. From left to right; representative ortho slices, 3D rendering of reconstructed images, segmented phases and pore structure using WeKa machine learning method, uncarbonated (a) and after cycle 1 (b) and cycle 2 (c) of carbonation in S2-based pastes. The uncertainties are calculated from a probability map in the WeKa segmentation, based on the 1σ value of a Gaussian distribution

Figure 6-8 shows the pore size distribution of the 3D segmented pore volume in sodium sulfate-activated slag cements before and after accelerated carbonation for three slags (Fig. 6-8a, 6-8b and 6-8c), as well as a summary of porosity, as determined by 3D μCT (Fig. 6-8d). For all 3 slags, accelerated carbonation led to an increase in overall porosity, which is consistent with previous studies where accelerated carbonated alkali-activated slag cements showed a highly porous microstructure [23, 68, 155]. This is attributed to the fact that exposure to an elevated CO_2 concentration leads directly to the decalcification of C-A-S-H gel and other secondary reaction products forming in these cements [76]. Irrespective of the slag used, carbonation gave a reduced pore volume for the pore size range between 2.1 μm and 10 μm. This is associated with the precipitation of $CaCO_3$ polymorphs in the pore space due to the carbonation of alkali-activated slag cements [68, 135, 155]. For pores larger than 10 μm, the pore volume increases, contributing to increasing the overall porosity of the materials, which is especially pronounced for the pores larger than 20 μm (Fig. 6-7). For cements produced with slag S2, two cycles of accelerated carbonation resulted in further reduction of pore volume for pores of < 10 μm. Extended carbonation leads to the formation of more pores with sizes >10 μm, and a consequent increase in average porosity. The highest porosity values were observed for the S3-based pastes throughout CO_2 exposure. It is related to the lowest Mg/Al ratio (0.5) of S3 slag, with the lowest degree of reaction and amount of reaction products (Chapter 3, Fig. 3-17 and Chapter 4 Fig. 4-15). The 3D pore structures will be used in calculating the diffusion tortuosity and formation factor in the following sections.

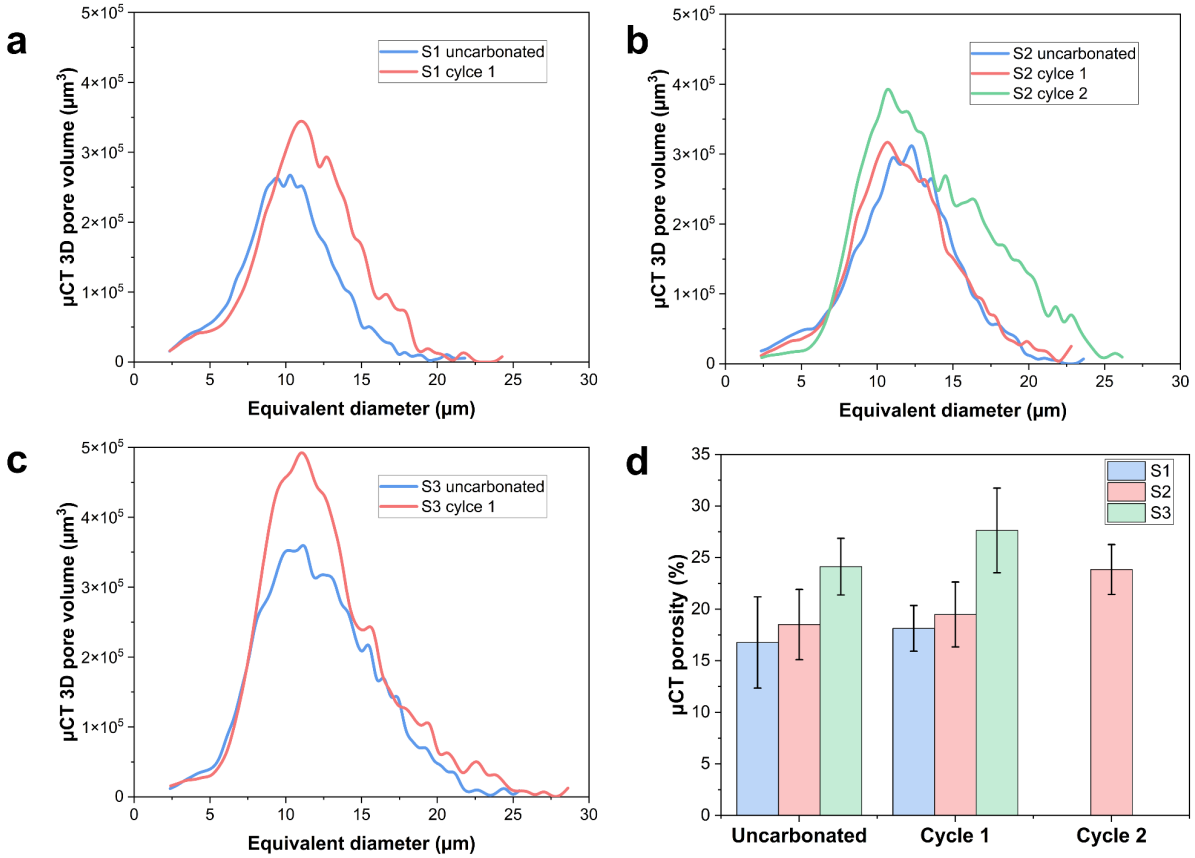

Figure 6-8. The pore size distribution of 3D segmented pore volumes identified in sodium sulfate-activated slag cements produced with (a) slag S1; (b) S2; and (c) S3 before and after carbonation. (d) Summary of µCT porosity before and after carbonation

6.3.2.1 Diffusion tortuosity

Figure 6-9a presents the simulated diffusion tortuosity of sodium sulfate-activated slag cements as a function of the slag type, before and after accelerated carbonation, as calculated using a random walker-based method in the reconstructed pore network. For the three slag cement pastes, accelerated carbonation leads to a decrease in the calculated tortuosity, which means that more connected pores formed in the pore structure resulted in a shorter pathway for the simulated walkers to travel. The alteration in the pore structure is directly related to the chemical reactions occurring between CO_2 and the reaction products, including the decalcification of the C-(A)-S-H gel (Figure 6-3), the decomposition of ettringite (Figure 6-4), and the carbonation of the LDH phase (Figure 6-5). These processes result in an overall increase in pore volume. This is in agreement with previous studies in alkali-activated slag/metakaolin cements carbonated at 3 % CO_2, which showed an increased pore volume after

carbonation [389]. The cement paste produced with slag S1, with the highest Mg/Al ratio (0.8), records the highest tortuosity values at all stages.

Figure 6-9b shows the relationship between segmented porosity from the µCT images and diffusion tortuosity. The dashed (fitted) curve presents an inverse power law relationship, and a horizontal asymptote to a tortuosity at very high porosity, which means walkers travel in free space without any resistance. A similar trend has also been reported in µCT studies of sodium silicate-activated slag cements [23, 25]. The vertical asymptote tends to be infinite when the porosity is 0.15, which generally agrees with the porosity value of the non-percolated pores in Portland cement by modelling of cement hydration (0.18) [390] and sodium hydroxide-activated slag cement characterised by ^{1}H NMR (~0.2) [155]. The similarity of our results with other reported studies further confirms the accuracy of the segmentation approach of the µCT results followed in this study.

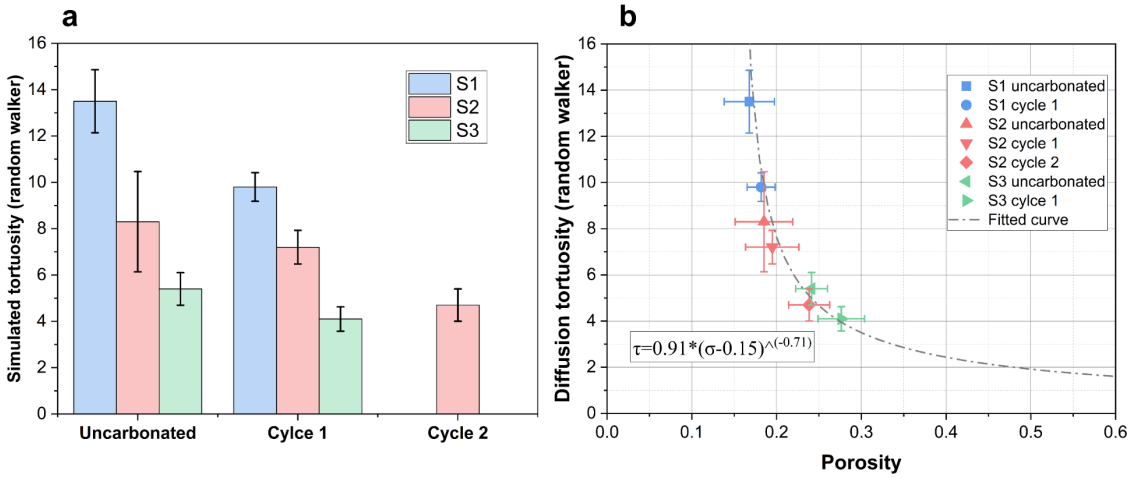

Figure 6-9. (a) Diffusion tortuosity of sodium sulfate-activated slag cements before and after accelerated carbonation using slag S1, S2 and S3. (b) Segmented porosity vs. diffusion tortuosity; σ and τ represent the porosity and diffusion tortuosity in the fitted curve, respectively

6.3.2.2 Formation factor

Figure 6-10 shows the simulated electrical charge transport and formation factor in sodium sulfate-activated slag cements along the X (Fig 6-10a), Y (Fig 6-10b) and Z (Fig 6-10c) axes, before and after carbonation. The formation factor (also called the electrical tortuosity in the field of battery materials research) is the ratio of the material resistivity to its pore solution resistivity, and it is directly related to the electrically resistive effects of porous materials [391,

392]. It is related in principle to transport properties and may also be used to analyse diffusivity within porous cementitious materials [198, 393]. This factor can be estimated by simulating electrical conductivity for the segmented pore 3D reconstruction using a finite volume method [394]. Figure 6-11a shows the formation factor simulations for sodium sulfate-activated slag cements before and after carbonation, as a function of the slag type used. Accelerated carbonation leads to more connected pores, and consequently, more electrical charge can be transported in the pore structure. A higher formation factor indicates a higher electrical resistivity of the material due to a higher amount of non-conductive solid formed compared to the conductive component (pore space), consistent with a more compact and tortuous microstructure. Before inducing carbonation, large deviations of the formation factor along the three axes were observed, irrespective of the slag used. This is consistent with the partial settlement of solids in the direction of the cement casting along the Z axis before it hardens [395]. The deviation in the X and Y axes is possibly related to some streak and ring artefacts during scanning and reconstruction [396], which slightly affect the calculated results of connectivity of the pore network [25]. After CO_2 exposure, the differences in results along the three axes significantly decrease, meaning more connected pores forming in the 3D space.

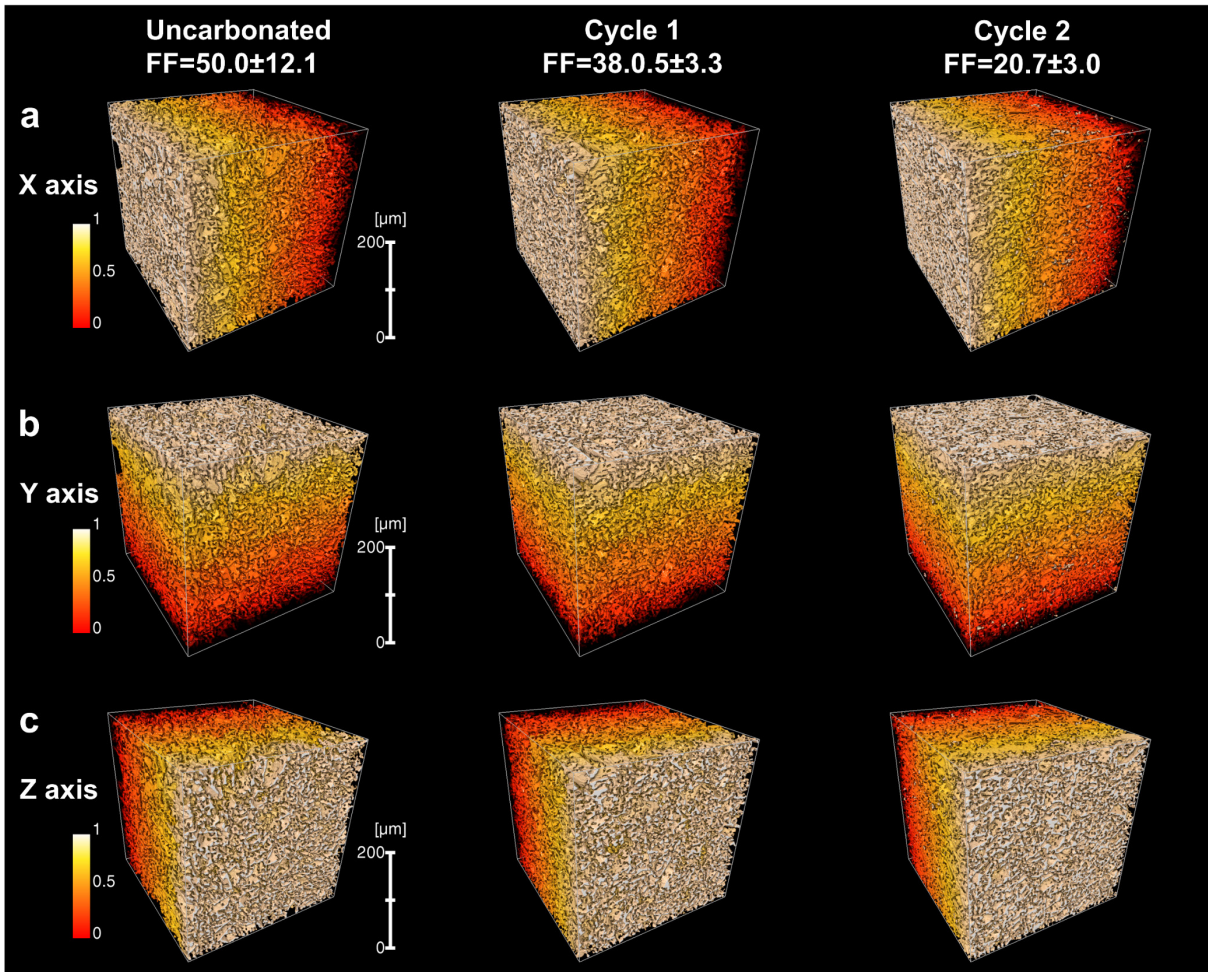

Figure 6-10. Simulated electrical charge transport in sodium sulfate activated S2 slag cements along the a) X, b) Y and c) Z directions, before (left) and after (middle and right) accelerated carbonation. An electrical potential of 1 V is applied along X, Y and Z axis, respectively. FF stands for formation factor, and error estimates are based on the calculated FF in the three directions shown

The paste produced with slag S1, with the highest Mg/Al ratio (0.8), has the highest formation factor (Figure 6-11a), whereas the S3-based cement shows the lowest value. This result agrees well with experimental results when exposing similar cement pastes to a lower CO_2 concentration (1% CO_2), where it was identified that sodium sulfate-activated S1 cements possessed the highest carbonation resistance compared to S2 and S3 [131]. With one and two cycles of accelerated carbonation, increased porosity (Figure 6-8d) and large capillary pores (Figure 6-8b) led to a reduced formation factor. The values of the simulated formation factors here (Figure 6-11a) are in general agreement with the published range of previous experimental results for various cementitious materials, including fresh Portland cement pastes at 90 minutes of curing (FF ranging from ~2.1 to ~3.1) [391], 29-year-old Portland cement pastes with the

same water/solid ratio (FF of ~49.1) [397], sodium silicate-activated slag paste after 28 days of curing using two different water/solid ratios (FF ranging from ~20 to ~60) [393] and Portland cement pastes with the addition of sodium hydroxide using different water/solid ratios from 3 days to 90 days (FF ranging from ~10 to ~60) [398]. It should be noted that the formation factors of mortar and concrete are two orders of magnitude higher than that of pastes due to the addition of sand and aggregate, as the more insulating components increase the resistivity of the bulk specimens [399, 400].

Figure 6-11b presents the segmented porosity vs. formation factor of the cement pastes evaluated here. Increased porosity causes a decrease in formation factor. This trend agrees with experimental observation in other cementitious materials [391, 397, 398]. The fitted curve is based on Archie's law and gives a cementation factor is ~2.4, which agrees well with the published value of ~2.5 for Portland-based materials having a lower porosity [397, 401], the relationship of formation factor and porosity for reservoir rocks [310] and highly cemented rocks (1.3 to 2.2) [391, 402]. The cementation factor is related to the type of porous material and is normally obtained by fitting a large number of datasets from experiments [310, 391]. It seems that independent of the chemical composition of the slag used or exposed CO_2 concentration, there is a fixed relationship between the formation factor and porosity value in sodium sulfate-activated slag cements. However, more data for AASCs are needed to establish an empirical equation for assessing the durability of these materials.

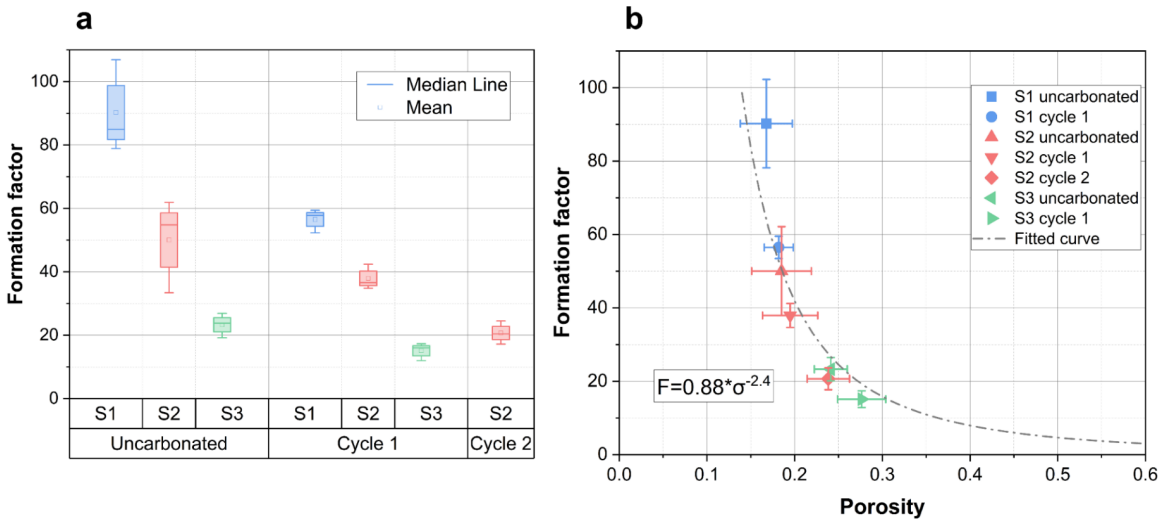

Figure 6-11. (a) Simulated formation factor of sodium sulfate-activated slag cements before and after accelerated carbonation, and (b) relationship between porosity and formation factor; the fitting curve is based on Archie's law. F and σ represent formation and porosity, respectively

6.4 Significance and implications

This study elucidates the distinct microstructural features of sodium sulfate-activated slag cements. Before exposure to CO_2, irrespective of the slag composition, sodium sulfate-activated slag cements exhibit total porosities (above the spatial resolution) of ~20 % after 28 days of curing. This observation agrees with reported porosities reported in sodium hydroxide-activated slag cements (~17% using scanning electron microscopy) [21], sodium silicate-activated slag cements (~18 % using uCT) [23, 25], sodium carbonate-activated slag cements (~16 % using uCT) [68] and sodium sulfate-activated slag cements activated slag cements (~22 % using MIP) [403] after 28 days of curing. Additionally, the porosity of alkali-activated slag cements is comparable, or even lower, compared to metakaolin blended Portland cements cured for 90 days (~30 % to ~35% using MIP) [326], fly ash blended slag cements with 50 % Portland cement substitution for 28 days (~33 % using MIP) [327] and slag blended cements with 70 % clinker replacement after 1 year of curing (~18 % using MIP) [328]. Exposure to an elevated CO_2 concentration causes an increase in percolated porosity in sodium sulfate-activated slag cements, consistent with what has been observed in other alkali-activated slag cements [23, 68, 135, 155]. Similar results have also been found in blended Portland cements with over 50 % of the Portland cement replaced by slag [328], fly ash [328, 404] or calcined clay [405]. This then demonstrates that the behaviour of the porosity developed in alkali sulfate-activated slag cements is comparable to that of other AASCs, and similar to blended Portland cements.

The chemical durability of cementitious materials is strongly dependent on the ability of aggressive ions to ingress the material, which is influenced significantly by the tortuosity of its pore structure and consequently its effect on the diffusivity of ions [196]. Accurate estimation of tortuosity based on non-destructive 3D imaging enables the determination of the diffusivity potential of a given material. This includes considering factors like porosity (the volume available for ionic transport), pore size distribution and pore morphology, which significantly affect tortuosity values, and are listed in approximately decreasing order of impact [392]. There are few studies determining the formation factor values of alkali-activated slag cements in the literature. The simulated formation factors of sodium sulfate-activated slag cements in this study show similar trends, and comparable values, to those reported for commercial blended Portland slag cements [391, 397]. Laboratory-based rapid bulk electrical resistance tests reported in the literature are restricted to testing the specimen for a few hours [406], under non-steady state ionic transport conditions that might lead to an increased formation factor. Modelling the formation factor based on VOI from μCT images enables the calculation of the resistivity in steady-state transport, minimising errors in the calculations. The simulation workflow developed in this study is a significant step forward in developing a rapid and reliable estimation of the formation factor in cementitious materials.

This study demonstrates the capability of Mg-Al-LDH phases in sodium sulfate-activated slag cements in entrapping carbonate ions, acting as in-situ CO_2 sinks. By controlling the mix design, especially the Mg and Al content present in the slag, the amount of Mg-Al-LDH phases can be controlled to optimise the reaction kinetics [18], carbonation [68, 169, 407, 408] and chloride uptake [69, 409, 410] in alkali-activated materials. Lower porosity and higher tortuosity values after carbonation in S1-based pastes compared to S2 and S3 indicate that using slags with higher Mg/Al ratio leads to an increased carbonation resistance. This is mainly because, upon alkali-activation of slags with elevated Mg contents, the formation of more LDH phases is favoured [95]. Intercalation of sulfate ions within the LDH phase causes an increased pH in the pore solution, as in Portland cement-based materials [342]. Further, this study proves the potential of Mg-Al-LDH phases in enhancing carbonation resistance and increasing the CO_2 uptake potential of cementitious materials, and offers insights into tailoring compositions to absorb atmospheric carbon, thereby contributing to sustainable construction practices.

6.5 Conclusions

This study pioneers the application of synchrotron-based X-ray micron scale computed tomography (μCT) and X-ray diffraction computed tomography (XRD-CT) to assess the effects of CO_2 exposure in Na_2SO_4-activated slag cement pastes. The carbonation of Na_2SO_4-

activated slag leads to the decalcification of C-(A)-S-H gel, ettringite decomposition, and the formation of crystalline carbonate-intercalated Mg-Al-LDH phases. The spatially resolved ettringite distribution confirms that the amount of ettringite decreases upon carbonation. Synchrotron XRD in this study has, for the first time, provided irrefutable evidence of the formation of the Mg-Al-SO_4-LDH phase in sodium sulfate-activated slag cements, and its role in CO_2 sink, by anionic exchange sulfate by carbonate in the interlayer space of LDH phase.

Carbonation induced an increase in porosity and a decrease in tortuosity in all of the alkali-activated slag pastes evaluated. Alkali sulfate-activated slag cements achieve comparable pore networks with lower porosity and higher tortuosity compared to blended Portland cements. This was more noticeable when using a slag with the highest Mg/Al ratio (0.8), which also presented the highest carbonation resistance. A correlation between the simulated tortuosity and 3D porosity, approximately following Archie's law was identified. A fitted empirical equation for calculating diffusion tortuosity and formation factor of these cements, as a function of the total porosity of the materials assessed, is proposed.

This study underscores the important role of XRD-CT and μCT in providing comprehensive physicochemical, non-destructive, three-dimensional insights into the carbonation processes of cements. As automated (machine learning) data analysis tools improve, this should simplify and expedite XRD-CT and μCT phase and pore analyses, making it easier to obtain robust quantitative information. Our future research will aim to integrate XRD-CT and μCT data into predictive reactive-transport life service models for the cementitious systems evaluated in this study.

Chapter 7

A REACTIVE-TRANSPORT FRAMEWORK TO MODEL CARBONATION PERFORMANCE OF A HARDENED CEMENT: THE CASE OF ALKALI-SULFATE SLAG CEMENT PASTES

7.1 Introduction

This Chapter introduces a novel reactive transport framework tailored for hardened cementitious materials, applied to a clinker-free sodium sulfate-activated slag cement, as a case study. Figure 1 illustrates the proposed reactive-transport model framework. The reaction kinetics model simulates the degree of slag reaction (DoR) over time and feeds into thermodynamic modelling for phase evolution prediction. Stepwise carbonation simulations explore the relationship between the volume of reaction products and reacted CO_2 at various curing ages. In the transport model section, μCT-scanned pore structures are used to quantify the diffusivity and permeability of the materials, reflecting changes in porosity and saturation degree. The CO_2 transport model considers CO_2 dissolution, transport of dissolved CO_2, and moisture movement between the pore structure and the exposure surface. Pore network evolution (porosity and tortuosity) over time, and reacted CO_2, are imported into this model to define the microstructural evolution.

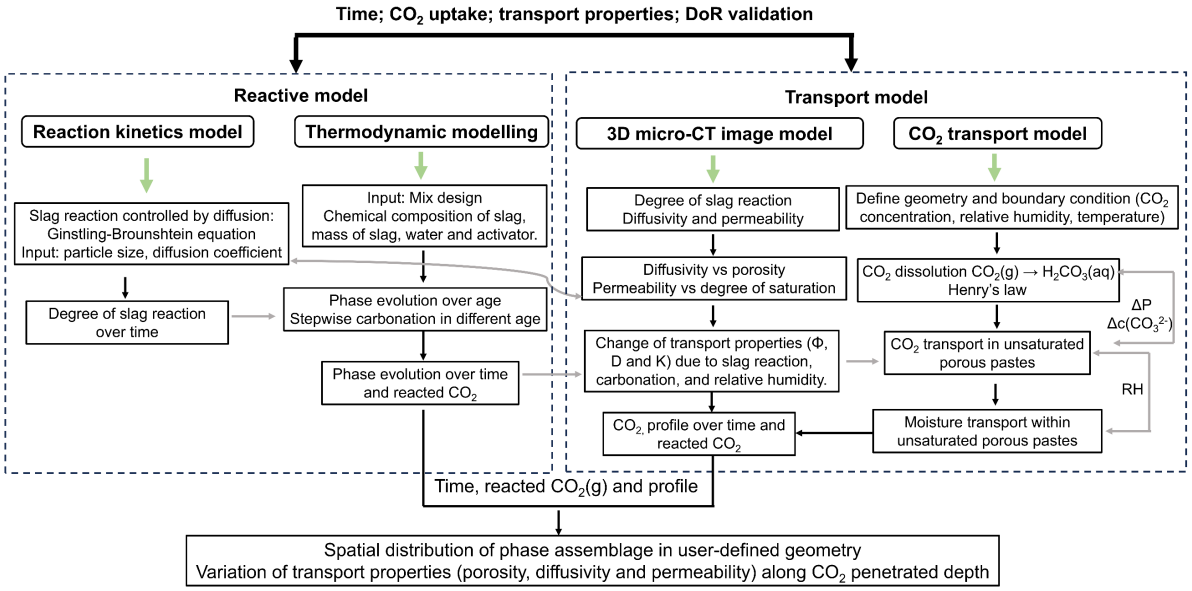

Figure 7-1. Reactive-transport framework for carbonation of sodium sulfate-activated slag cements. *Φ* is the porosity; *D* is diffusivity; *K* is permeability and RH is relative humidity

The framework developed in this study enables the prediction of CO_2-induced alterations in the phase assemblage and transport properties of cementitious materials. These properties include diffusivity, permeability, saturation, liquid volume fraction, and capillary pressure. Additionally, the tool predicts pore solution pH, the composition of aluminium-substituted calcium silicate hydrate gel (C-A-S-H), and CO_2 sequestration profiles at various depths. The framework was applied to simulate one year of accelerated carbonation (1% CO_2 v/v) and ten years of natural carbonation (0.04% CO_2 v/v) under controlled temperature and humidity conditions in the sodium sulfate-activated slag cements system. The simulation results showed strong alignment with experimental data, underscoring the tool's accuracy. This framework represents a significant advancement in predicting the carbonation performance of cementitious materials, facilitating calculations of CO_2 uptake capacity in more complex cement systems, including those with supplementary cementitious materials (SCMs) or based on alkali-activated cements. Given the framework's complexity, each model, as illustrated in Figure 7-1, is individually established, discussed, and validated in subsequent sections.

7.2 Reactive model of chemical reaction in sodium sulfate-activated slag cements

Two types of chemical reactions happen during the carbonation of sodium sulfate-activated slag cements: (a) continuous slag dissolution over time in uncarbonated regions and (b) decalcification of C-(A)-S-H gel and other hydrate products in the carbonated regions of the specimen. In this section, numerical and thermodynamic simulations were utilised and coupled to predict and verify the reaction kinetics model and phase evolution as a function of reacted CO_2.

7.2.1 Reaction kinetics of sodium sulfate-activated slag cements

In the uncarbonated region, slag continues to react throughout the service life of the concrete. An increased degree of reaction (DoR) is expected to cause decreased porosity and increased tortuosity in sodium sulfate-activated slag cements [160]. Considering the lack of an established reaction kinetic model for sodium sulfate-activated slag cements, it is important to find the relationship between DoR and time. The slag reaction rate is defined based on the Ginstling-Brounshtein (G-B) equation 7.1 [411]. This equation has been recommended and used in simulating reaction kinetics in alkali-activated slag cement systems, more correctly considering the surface curvature of spherical particles in a way that the often-used Jander equation does not [174-176]. The differences between using the modified Parrot and Kiloh (MPK) method and the G-B method in modelling the reaction kinetics of cementitious materials has been discussed in detail in Section 2.6.2 of this thesis. It has been emphasised the importance of considering particle surface curvature by using the Ginstling-Brounshtein equation [175]. This equation was then adopted to model heat release from slag dissolution in the first 7 days activated by sodium silicate solution [176]. However, modelling DoR at an extended curing age is needed for service life predictions.

In the sodium sulfate-activated slag cements system, the near-neutral pH value of the activator causes slow dissolution of slag with a gradually increasing degree of reaction [17]. For predicting the life service of such a system, simulating long-term slag reaction is then needed. To achieve this, the empirical coefficient k (in eq.1) is adjusted by considering the OH^- concentration in the pore solution, availability of pore space (porosity) and connectivity of pore structure (tortuosity), as shown in equation 2. This is meant to describe a process controlled by the diffusion of ions released via slag dissolution, influenced also by the precipitation of reaction products around the slag particles.

$$\frac{kt}{R^2} = 3 - 2\alpha - 3(1-\alpha)^{2/3} \quad \text{(Equation 7.1)}$$

$$k = c(OH^-) * \frac{\phi(\alpha)}{\tau(\sigma)} \quad \text{(Equation 7.2)}$$

In equations 1 and 2, α is the degree of slag reaction; c(OH^-) is the molarity of OH^- as a function of the degree of reaction, which is calculated from thermodynamic modelling as discussed in Chapter 4, Figure 4-16. Φ is total porosity as a function of the degree of reaction: $\boldsymbol{\phi = -0.3218\alpha + 0.5154}$; this relationship is determined by thermodynamic modelling, as shown in Chapter 4 for S2-based pastes (Figure 4-15B); it means that the chemical composition of slag and water to binder ratio are also considered implicitly in this model. τ is the tortuosity of the pore structure as a function of percolating pores, which is $\boldsymbol{\tau = 0.91 \times (\Phi - 0.15)^{\wedge(-0.71)}}$, determined from Chapter 6 (Figure 6-8).

R is the mean radius of the slag particle, which is calculated using anhydrous slags using synchrotron X-ray microtomography (uCT). The detailed synchrotron experiment setup is referred to in Chapter 3 section 3.6. The selection of using uCT technique to characterise the slag particle size distribution is to maintain the mathematical consistency in the 3D, because the G-B equation considers the surface curvature of the spherical particle, whereas the conventional laser diffraction method is based on the 2D projection of the particle [412]. Figure 7-2 shows a segmented anhydrous slag rendering and 3D slag particle size distribution. The auto threshold algorithm was used to segment the slag particles from the background to preserve slag boundary information due to similar greyscale between pixels [413].

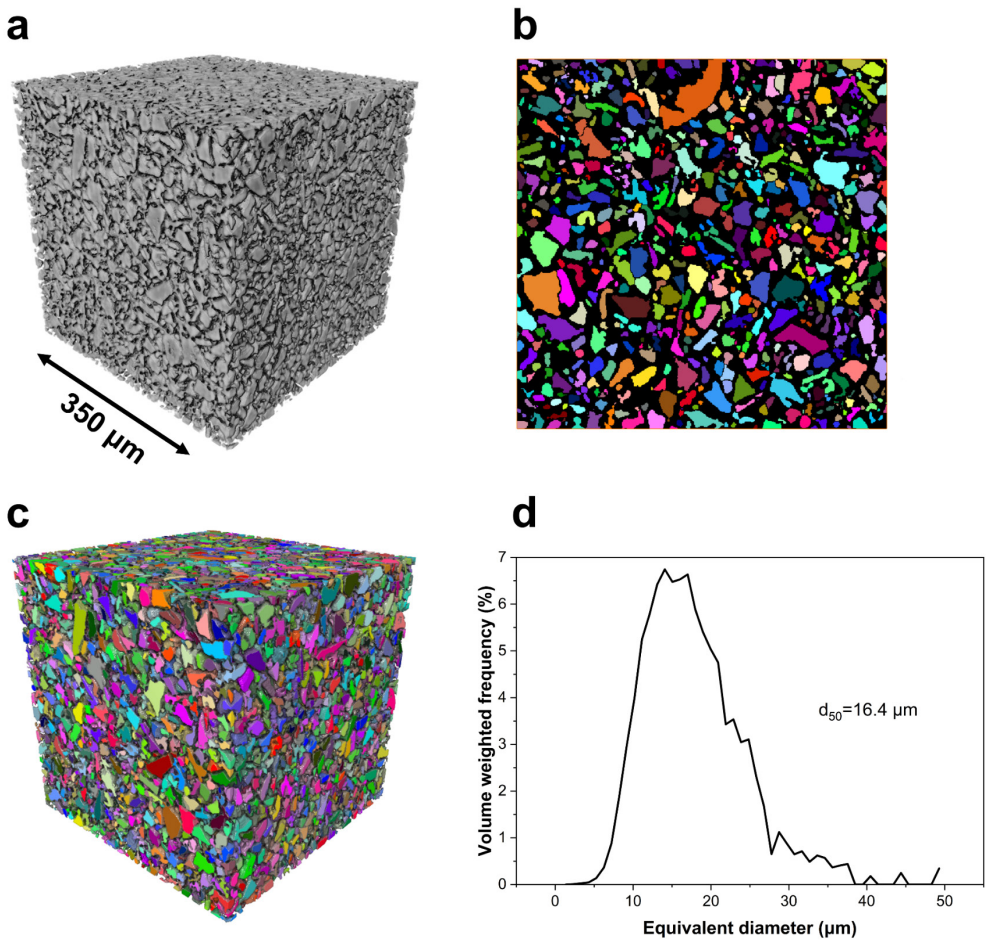

Figure 7-2. Example of the (a) 3D rendering of µCT unreacted slag; (b) segmented ortho slice of µCT images; (c) 3D rendering of segmented raw slag; overall 13985 of slag particles in volume of interest (VOI); (d) unreacted slag S2 particle size distribution using µCT images

7.2.2 Simulated degree of slag reaction in sodium sulfate-activated slag cements

Figure 7-3 illustrates the simulated degree of slag reaction upon sodium sulfate activation, revealing a sharp increase within the first 56 days, including approximately a 20% increase in the DoR between 28 and 56 days. This trend correlates well with the compressive strength development observed in these materials, which shows an increase of approximately 20 MPa during the same period, as detailed in Chapter 4 Figure 4-17. The UK specification BSI PAS 8820:2016 [30] recommends determining the compressive strength of alkali-activated cementitious materials at 56 days, reflecting the latent hydraulic properties of slag. This further supports the validity of this modelling approach adopted.

An indication of a gradual plateau is observed after 360 days of reaction, attributed to decreasing porosity and increasing tortuosity, which slows the diffusion rate of dissolved ions from the slag, leading to the formation of a more compact pore structure. A similar trend has been reported in experimental studies on blended slag-Portland cements, which utilised a selective dissolution method and varied the substitution of slag from 50% to 92%, altering compositions and water-to-binder ratios [414]; DoR values recorded were 30-50 % at 28 days and 45-75 % after 1 year of hydration, using the water/solids ratio between 0.40-0.60 [414].

The simulated DoR curve (Fig. 7-3) aligns well with experimental data, as characterised by various techniques (SEM, μCT, and NMR). Given the lack of data specific to sodium sulfate activation of slag, results for sodium carbonate-activated slag (with a similar activator pH) were also used to validate this curve. It is well known that the composition of the slag significantly influences the phase assemblage and reaction kinetics [18, 20, 84]. Thus, a ±20 % deviation of simulated data is used to cover the experimental results with different slag sources. This reaction kinetic model is subsequently utilised in thermodynamic modelling to predict phase evolution over time.

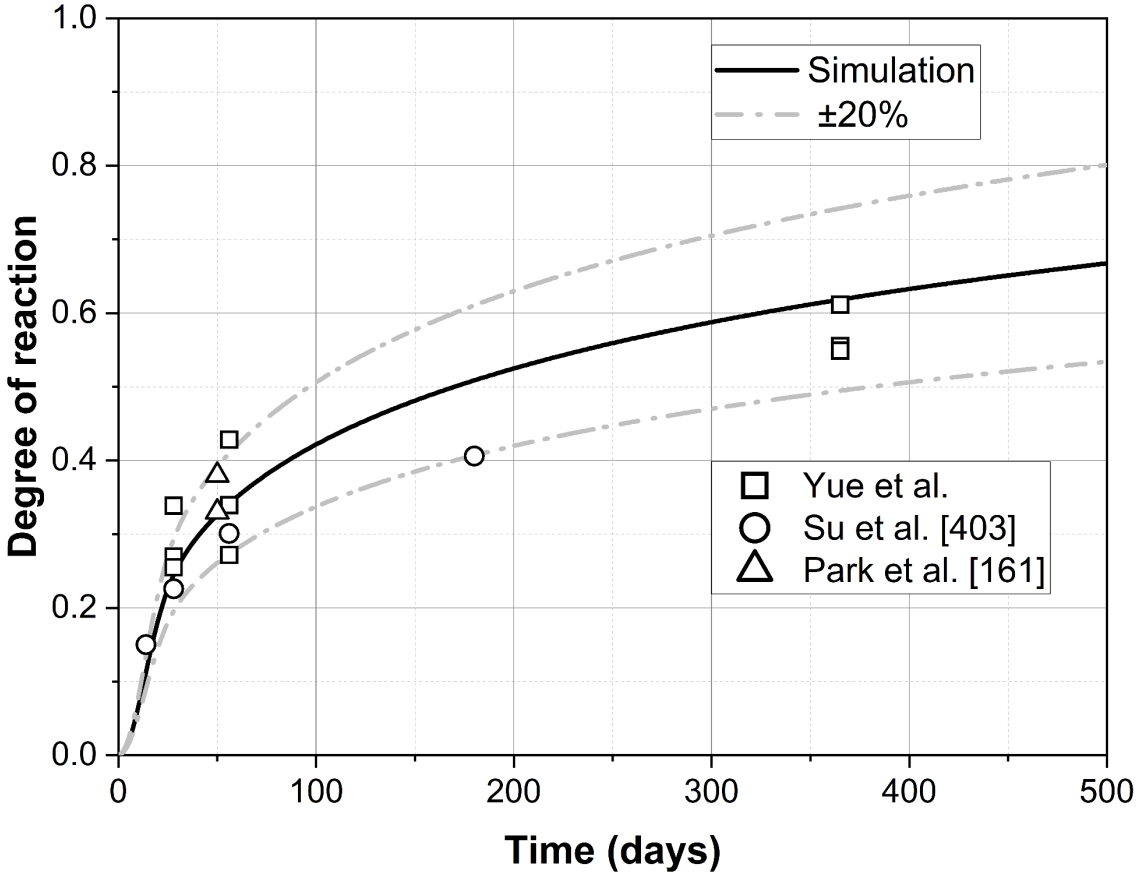

Figure 7-3. Simulated degree of slag reaction over time in sodium sulfate-activated slag cements. Symbol □ is based on DoR in sodium sulfate-activated slag cements at 28, 56 and 365 days of reaction, determined by image analysis of BSE images presented in Chapter 4 Figure 4-8A. ◯ refers to sodium carbonate-activated slag cements at 14, 28, 56 and 180 days of reaction, determined by μCT analysis [403]. △ refers to 50 days reaction of sodium carbonate and sodium sulfate-activated slag, based on the deconvolution of ^{29}Si MAS NMR [161]. Grey dashed lines show ±20 % deviation and can be considered to represent the likely effect of differences in slag composition

7.2.3 Slag reaction and carbonation in sodium sulfate-activated slag cements using thermodynamic modelling

The reaction kinetic model for sodium sulfate-activated slag cements as mentioned in section 7.2.2 was imported into GEM-Selektor, following a similar method to that which is used in modelling hydration of PC [173]. The open-source GEM-Selektor v.3 [195, 281] was used to conduct thermodynamic modelling to simulate phase assemblage [282]. Cemdata18 [108] was used as the primary database to predict phase evolution as a function of time. An extended

Debye-Hückel equation was used to calculate the activity coefficients of aqueous species; this equation has been shown to work successfully in simulating alkali-activated materials [76, 110, 283, 284]. Thermodynamic data for SO_4^{2-}-intercalated Mg-Al-LDH is added to the database based on experimental results [284], to supplement the existing database entries for OH^- and CO_3^{2-} Mg-Al-LDH phases. Detailed model setup and description are referred to in Chapter 3 section 3.5.

7.2.3.1 Predicted phase evolution as a function of time

Figure 7-4 presents the evolution of phase assemblage (e.g. type and amount of reaction products) in sodium surface-activated slag cements over 500 days. The gradual dissolution of slag contributes to the increased formation of primary reaction products: C-(N)-A-S-H gel, ettringite, and Mg-Al-SO_4-LDH phases. Notably, after approximately 200 days of reaction, the decomposition of ettringite into the AFm-structured calcium monosulfoaluminate is predicted, due to the reduced volume of pore solution in the system. This observation is also found in PC-based systems [415]. Similarly, experiments in Chapter 4 also confirm the decreased amount of ettringite after 180 days of reaction. A gradual increase in the Mg-Al-SO_4-LDH phase is related to the supply of Mg content from slag dissolution, the presence of this phase and its increase with curing age have been confirmed by multi-analytical techniques in Chapters 4 and 6. This further validates the accuracy of the modelling approach adopted.

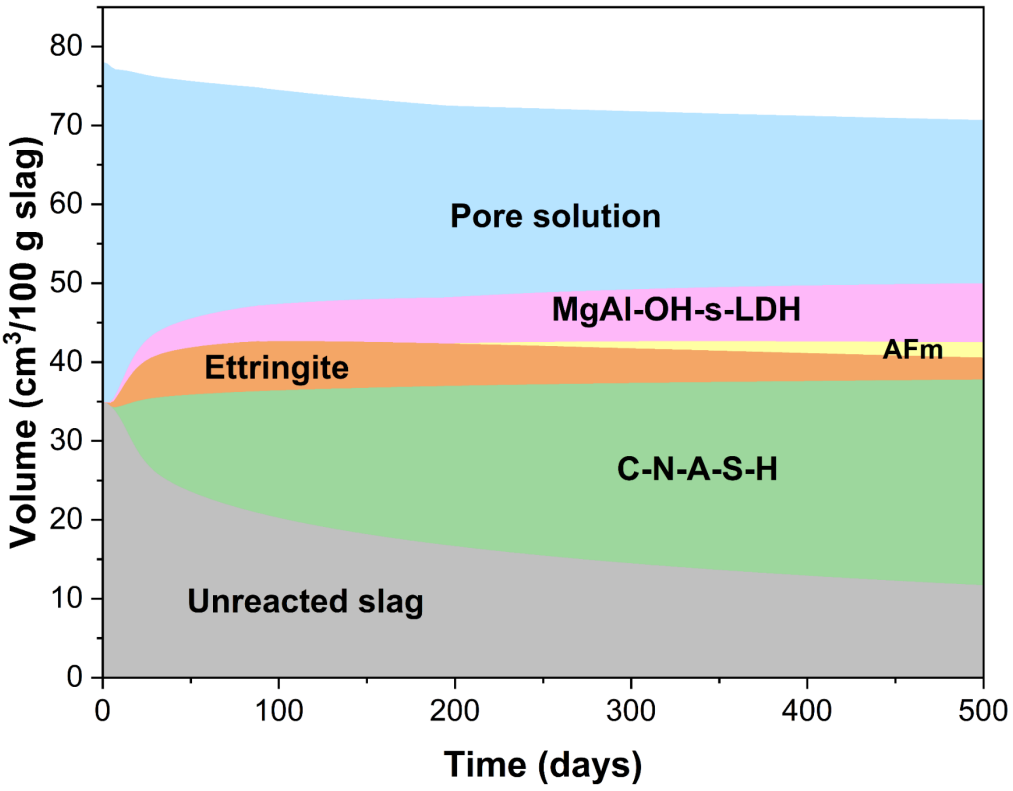

Figure 7-4. Simulated phase evolution in sodium suflate-activated slag cements using slag S2, based on the reaction kinetics model, proposed in this study

7.2.3.2 Stepwise carbonation in sodium sulfate-activated slag cements at different curing ages

Figure 7-5 illustrates the simulation results of stepwise carbonation in sodium sulfate-activated slag cements, where the carbonation was applied to the cement starting at various curing ages from 28 to 365 days. The slag continues to dissolve and form more reaction products in uncarbonated regions over time, leading to decreased porosity. The decomposition of C-(N)-A-S-H, ettringite and Mg-Al-SO_4-LDH occurs directly as carbonation progresses, resulting in the formation of gypsum, calcite, Mg-Al-CO_3-LDH, and aluminosilicate gel, which aligns with experimental observations in sodium sulfate-activated slag cements [131, 257]. This is notably different from the carbonation of the PC-based cements, where the decomposition of $Ca(OH)_2$ is normally used to define the carbonation depth and rate [130]. The formation of gypsum, calcite and aluminosilicate gel was also identified in sodium sulfate-activated slag cements analysed by different analytical techniques, whose results are reported in Chapter 5. Although metastable aragonite and vaterite were observed from experiments, these polymorphs were not predicted to form in these simulations, since thermodynamic modelling only considers the

equilibrium condition of the system and these are metastable phases [416]. The anion exchange between CO_3^{2-} and SO_4^{2-} during the carbonation of sodium sulfate-activated slag cements has been experimentally observed in similar cements to those simulated here, and results are reported in Chapter 6.

In sodium sulfate-activated slag cements, ettringite and C-(N)-A-S-H gel are the primary reaction products, and therefore their decalcification governs the carbonation reaction. An increase in the quantity of these phases over time enhances the CO_2 uptake capacity until their complete decalcification and subsequent decomposition. Therefore, the degree of slag reaction is a key factor influencing the carbonation resistance of the material, as more CO_2 is required to achieve complete decalcification of the C-(N)-A-S-H gel, decomposition of ettringite, and Mg-Al-s-LDH phase, thereby influencing the porosity and transport properties of the material

In the carbonation of C-(N)-A-S-H, loss of charge-balancing Na^+ and Ca^{2+} from the interlayer happens first. Then, bridging site tetrahedral Al is removed, and instead becomes incorporated in tetrahedral $Al(\text{-}OSi)_4$ unit in an aluminosilicate gel carbonation product [115]. Decalcification of the principal layers leads to a significantly decreased Ca/Si ratio in the simulations (right-hand column in Figure 7-5), consistent with experimental observations with the formation of an amorphous silicate phase, as characterised by the observation of Q^3 and Q^4 tetrahedra in ^{29}Si MAS NMR [68, 115], with the calcium instead of $CaCO_3$.

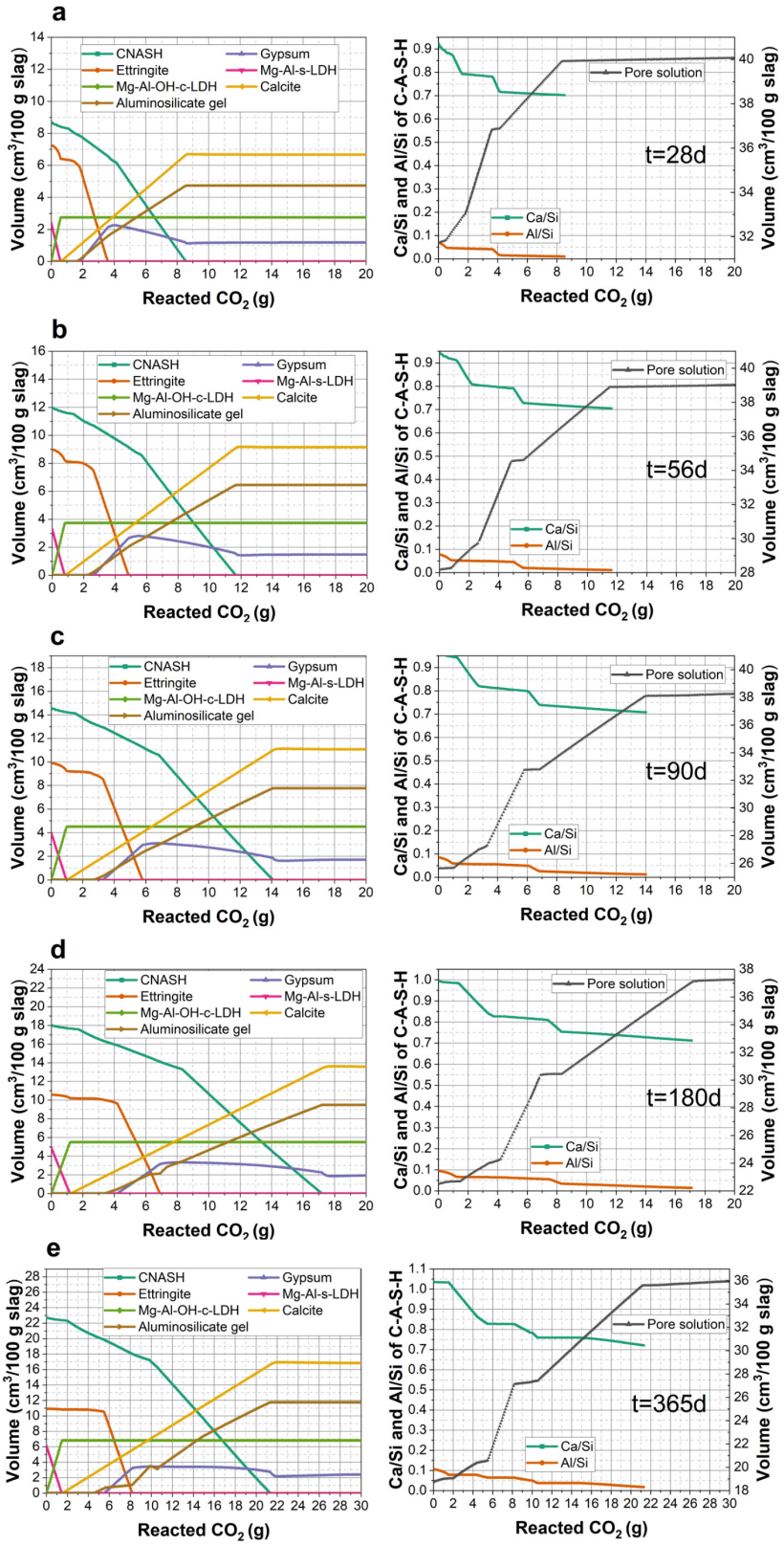
a
CNASH
Ettringite
Mg-Al-OH-c-LDH
Aluminosilicate gel
Gypsum
Mg-Al-s-LDH
Calcite
Volume (cm3/100 g slag)
Reacted CO2 (g)
Pore solution
t=28d
Ca/Si
Al/Si
Ca/Si and Al/Si of C-A-S-H
b
t=56d
c
t=90d
d
t=180d
e
t=365d

Figure 7-5. The volume of reaction products (left) and chemical composition of C-A-S-H gel (right) as a function of reacted CO_2 in sodium sulfate-activated slag cements under, where the carbonation was allowed to commence after (a) 28, (b) 56, (c) 90, (d) 180 and (e) 365 days of curing, shown on rows a, b, c, d and e, respectively. At each step, 0.1 g of pure CO_2 gas (density 1.98 kg/m^3) was added with 6.2 g of dry air (density 1.22 kg/m^3), to mimic 1 vol % CO_2 during carbonation.

7.2.3.3 Integrating reaction kinetics and stepwise carbonation

To integrate the reaction kinetics model, where each reaction product varies as a function of time, with stepwise carbonation through thermodynamic modelling, where each reaction product varies as a function of the reacted CO_2 at five different curing ages, data from Figures 7-4 and 7-5 were input into a matrix in Matlab. A multivariate polynomial regression model was utilised [417], considering both linear and non-linear relationships between variables [418]. Consequently, this model exports the volume of each reaction product as a function of the reacted CO_2 (g) and curing age (days), as shown in Figure 7-6.

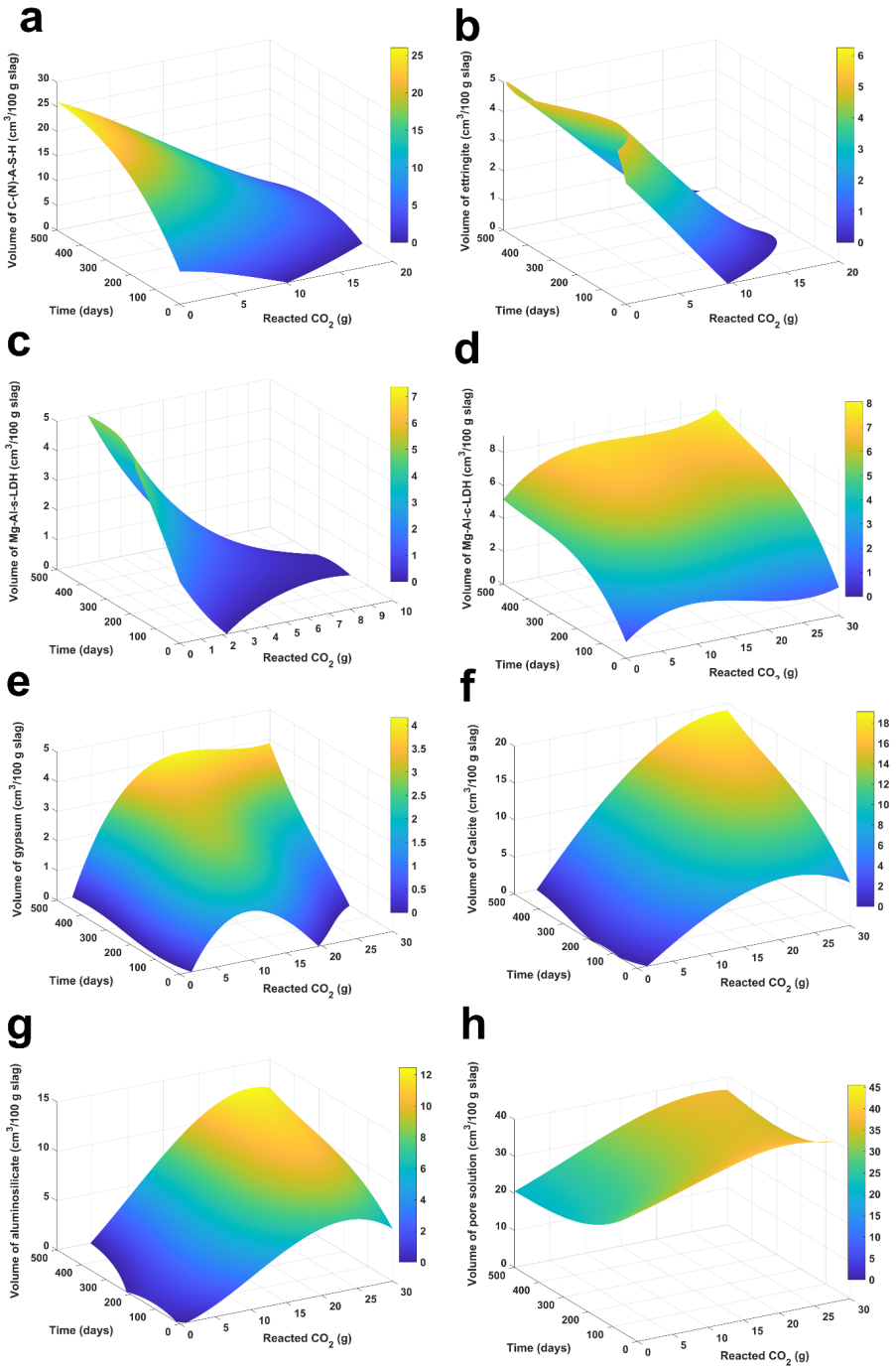

Figure 7-6: Predicted volume (per 100 g of slag) of (a) C-(N)-A-S-H, (b) ettringite, (c) Mg-Al-s-LDH, (d) Mg-Al-c-LDH, (e) gypsum, (f) calcite, (g) aluminosilicate and (h) pore solution in 28 days cured sodium sulfate-activated slag cements (per 100 g slag) as function reacted CO_2 (g) and curing age (days).

7.3 CO_2 transport model for unsaturated sodium sulfate-activated slag cements

In alkali-activated materials, the different chemical compositions in SCMs and the type of activators cause the complexity of the analysed system [121, 149]. In the carbonated regions, as normally determined by spraying 1 % phenolphthalein solution [150], the chemical reaction occurs between dissolved carbonic acid and reaction products. Additionally, a drying process takes place due to the relative humidity gradient between the pore structure and the exposure surface [151]. The release of water during the decomposition of hydrates further alters the saturation within the pore structure [103]. In the uncarbonated region, raw materials proceed with the reaction resulting more compacted microstructure compared to carbonated regions [135, 152]. In these two regions, the CO_2 diffusivity and liquid permeability are significantly different in different regions [153, 154], which is affected by the porosity [155, 156], tortuosity [23, 25], degree of saturation [157, 158] and CO_2 uptake [138, 159]. The complexity of carbonation in alkali-activated materials makes it challenging to isolate a single parameter to fully understand its carbonation mechanism and study the governing parameters controlling the carbonation processes during experiments. Variations in transport properties due to chemical reactions and moisture transport are discussed in the following sections, utilising the proposed modelling method in the studied sodium sulfate-activated slag cements.

7.3.1 CO_2 dissolution and transport

Carbonation of cementitious materials proceeds in two steps: (a) the dissolution of gaseous CO_2 into the pore solution, and (b) the transport of dissolved carbonate and bicarbonate ions (CO_3^{2-} and HCO_3^-) within the pore solution. Although the significance of CO_2 dissolution in the pore solution has been highlighted in a recent review [193], this step is often overlooked in most carbonation modelling studies [203, 419, 420]. In this study, it is assumed that once gaseous CO_2 dissolves in the pore solution, the carbonation reaction happens immediately.

The dissolution of CO_2 is represented by Henry's law, considering that the concentration of dissolved CO_2 in the pore solution is proportional to the partial pressure of CO_2 in the atmosphere at the interface between gas and liquid, as presented in equation 7.3 [197].

$$c_i = HP_{CO_2} \qquad \text{(Equation 7.3)}$$

Here H is the Henry constant for CO_2, 2938.425 (mol /m^3•Pa) [421]. P_{CO2} is the partial pressure of CO_2 (Pa) in the atmosphere. c_i (mol/m^3) is the equilibrium concentration of dissolved CO_2.

The rate of CO_2 dissolution is defined by the following equation 7.4 [197].

$$r_{CO_2} = k(c_i - c) \qquad \text{(Equation 7.4)}$$

Where r_{CO2} is the reaction rate of CO_2 (mol/(m^2·s)), k is the interfacial gas-liquid mass transfer coefficient, which is defined as 2x10^{-6} (m/s) [422], and c (mol/m^3) is the dissolved CO_2 concentration in the liquid, which is a dynamic value with CO_2 transport and is solved in the following section.

Transport of dissolved CO_2 is driven by the concentration gradient between dissolved CO_2 and gas CO_2 and the advection of the liquid phase due to moisture transport, as shown in equation 7.5 [196].

$$\frac{\partial c}{\partial t} + \nabla \cdot (c g_l) = \nabla \cdot \left(D_{eff} \nabla c\right) + r_{CO_2} \qquad \text{(Equation 7.5)}$$

Where g_l is the Darcy velocity of the liquid phase, and D_{eff} is the effective diffusion coefficient of dissolved CO_2, which is discussed in the following section.

7.3.2 Determine the effective diffusion coefficient of dissolved CO_2

Diffusion rate for ionic groups and viscous flow of pore solution within pore structure are fundamental transport properties, as these rates control degradation process properties in cementitious materials [178]. It is important to note that this study does not aim to summarise these values across different cement systems. Diffusivity refers to the capacity for ionic movements—such as sulfate, chloride, and carbonate ions-governed by Fick's law, which states that diffusion through pore solution-filled pores is driven by the concentration gradient between the exposure surface and the interior of the specimen [423]. Permeability, in contrast, is defined according to Darcy's law, which describes fluid velocity driven by a pressure gradient, such as the movement of pore solution and gas in the pore structure of cementitious materials, and is calculated using the Navier-Stokes equations for laminar fluid flow [424]. Effective diffusivity and effective permeability typically incorporate considerations of porosity and saturation within the pore structure [187, 189].

Diffusivity quantifies the movement of ions in a liquid medium (e.g. pore solution in cementitious materials) due to a concentration gradient. In porous hardened cementitious materials, the pore size distribution (as described by tortuosity), porosity and degree of saturation (available liquid volume fraction in the pore structure) are expected to affect this

value, called the effective diffusion coefficient [423], which can be calculated using equations 7.6 and 7.7 [196].

Although it might be true that some studies have used non-linear relationships between diffusivity and saturation, this approach often requires extensive empirical data to determine the appropriate exponent values. Given that sodium sulfate-activated slag cements are a relatively new material with largely unknown chemistry and transport properties, there is currently a lack of comprehensive data to support the selection of a specific non-linear exponent. Therefore, adopting a linear relationship allows for a more straightforward interpretation of how saturation affects diffusivity without introducing additional complexity or requiring extensive input parameters that are not yet well characterised for this material.

$$D_{eff} = \frac{D_0 * \Phi(t,CO_2) * s(t,CO_2)}{\tau} \quad \text{(Equation 7.6)}$$

$$D_0 = \frac{RT\lambda^0}{z^2F^2} \quad \text{(Equation 7.7)}$$

Where Φ is the volume fraction of porosity, which varies as a function of reaction time and reacted CO_2, as determined by the reaction kinetics model and thermodynamic modelling in section 7.2. The value *s* describes the degree of saturation, which also varies with time and is influenced by: a) moisture transport due to the drying process under exposure conditions, outlined in Section 7.3.4; b) ongoing slag reaction in uncarbonated regions; and c) the chemical reaction between carbonic acid and reaction products, also determined by thermodynamic modelling in Section 7.2. The parameter τ is diffusion tortuosity, defined from tomographic reconstruction by the empirical expression: $\boldsymbol{\tau = 0.91 \times (\Phi - 0.15)^{\wedge(-0.71)}}$. This equation is derived from curve-fitting to the results of random walker simulations of seven sodium sulfate-activated slag cements with varying porosity values based on three blast furnace slags with different chemical compositions. The detailed modelling approach is described in Chapter 3 section 3.7.3.

D_0 is the self-diffusion coefficient of an ion at infinite dilution and is determined based on the Nernst-Einstein equation [425-427], in equation 7.7. *R* as the gas constant is 8.314 (J/(mol•K)); *T* (K) is temperature; *z* is the charge of the ion; *F* = 9.6485 x 10^4 C/mol is Faraday constant; λ^0 is the limiting conductivity. In the carbonation of cementitious materials, HCO_3^- and CO_3^{2-} are the ingressing ions. $\boldsymbol{\lambda^0_{HCO3^-}}$ and $\boldsymbol{\lambda^0_{CO3^-}}$ are 4.45 and 13.86 (m^2•mS/mol) [196], so the self-diffusion coefficients HCO_3^- and CO_3^{2-} at 25 °C is 1.19 and 0.92 x 10^{-9} (m^2/s), respectively. Temperature also affects both pore structure and self-diffusion diffusion of ions, and this

change can in principle be captured by the framework here. Nevertheless, an isotherm condition at 25 ℃ was used in this study.

7.3.3 Effective diffusivity of ions at different saturation conditions

During the carbonation of sodium sulfate-activated slag cements, the variation in DoR and reacted CO_2 at each depth from the exposure surface to the interior of the specimen results in different porosity and saturation values. Additionally, moisture transport happens between the pore structure and the exposure surface, essentially a drying process that further impacts the saturation condition of the cementitious materials. Figure 7-7 illustrates the relationship between effective diffusivity and porosity under various saturation conditions. The trend of the simulated curve generally aligns with the diffusivity values reported for blended fly ash mortar [428] and 75% substituted Portland-slag cement pastes [429], where increased porosity leads to higher diffusivity. However, the simulated diffusivity is 2–3 orders of magnitude lower than the reported experimental results. This discrepancy is primarily attributed to the oven-drying process at 105°C and pre-conditioning methods, which causes the decomposition of the C-S-H gel and increases the connectivity of the pore structure. Similar observations have been made using the Lattice Boltzmann method on 3D μCT images [186], the pore size distribution model [187, 188] and image-based diffusivity modelling [189-191], all of which show diffusivity values 2–3 orders of magnitude lower than experimental measurements. This does not necessarily indicate inaccurate validation; rather, it suggests that non-destructive μCT-based image simulations may provide more reliable results.

According to the carbonation standard BSI 1881-210:2013 [348], exposure relative humidity is controlled at ~55 % [347]. Thus, the drying process is expected to commence immediately after placing 28-day cured specimens into the carbonation chamber, causing the diffusivity curve (Fig. 7-7) to shift downward from $s = 1$ to $s = 0.5$. Over time, carbonation increases the porosity in carbonated regions, while ongoing slag reactions decrease the porosity in uncarbonated areas. Notably, when porosity reaches approximately 0.15, the diffusivity approaches zero, reflecting the volume fraction of non-percolating pores and corresponding to nano-sized pores in the C-(A)-S-H gel of alkali-activated materials [155]. Therefore, this model accounts for variations in porosity and saturation, as a function of time and reacted CO_2, to facilitate a more realistic simulation of CO_2 transport.

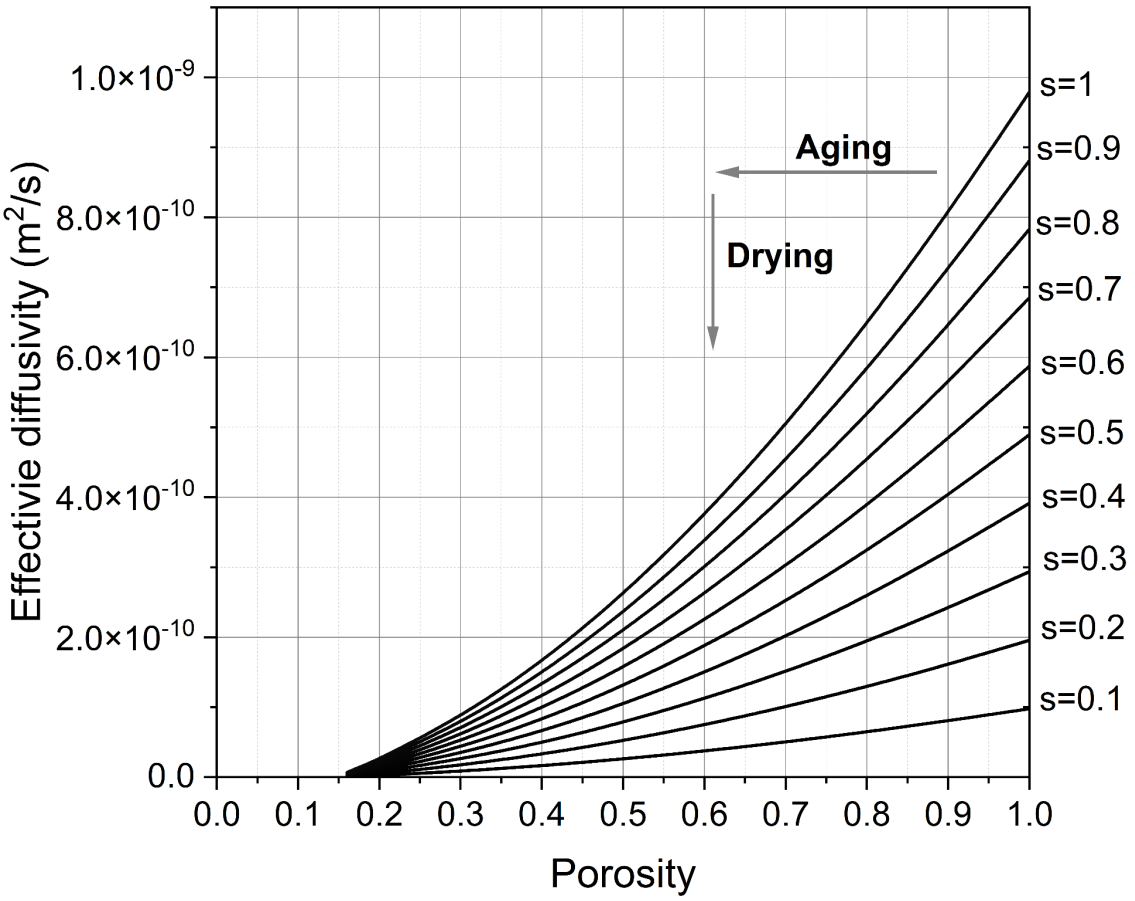

Figure 7-7. Relationship between effective diffusivity and porosity changing from fully saturated conditions (s = 1) to unsaturated conditions (s < 1) in sodium sulfate-activated slag cements, calculating using equation 6

7.3.4. Moisture transport

Moisture transport is also a significant factor influencing the carbonation process. To simply the model, the formation of drying shrinkage microcracks, and recrystallisation of dissolved salts from pore solutions during wet/dry cycles in cementitious materials [430], are not directly described. The fundamental science underlying these phenomena, particularly in alkali-activated materials, remains largely unknown, and therefore any potential assumptions to account for this might be misleading.

The model used to simulate moisture transport considers both liquid water and water vapour; gas pressure is constant and liquid water is incompressible [181]. The moisture mass conservation equations for liquid water and water vapour [431] are listed below in equation 7.8 and 7.9. The transport of liquid water is facilitated by advection, driven by the capillary

movement of free water, and by diffusion, resulting from saturation gradients. Water vapour is a diffusion-based process. D_{eff} is used to describe the influence of tortuosity and porosity of pore networks as resistance factors for the transport of liquid water and water vapour.

$$\frac{\partial w(s)}{\partial t} = -\nabla(g_l + D_{eff\_l}\phi s\rho_l) - \rho_g D_{eff\_g}(1-s)\phi \quad \text{(Equation 7.8)}$$

$$w(s) = \phi s\rho_l + \phi(1-s)\rho_g \quad \text{(Equation 7.9)}$$

where $w(s)$ is water content in the system shown in equation 7.9, which is a function of the degree of saturation; ρ_l and ρ_g (kg/m^3) are gas and liquid water density; g_l (kg/(m^3•s)) is capillary liquid water flux calculated by equation 7.10, which is a function of capillary pressure p_c according to Kelvin's law [432]. The air velocity is set to 0, as the temperature is kept constant at 25 °C. D_{eff_l} and D_{eff_g} are diffusivity of liquid water and water vapour, respectively.

$$g_l = -\rho_l \frac{Kk_l}{\mu}\nabla p_c \quad \text{(Equation 7.10)}$$

$$p_c = -\frac{RT\rho_l}{M_l} ln(RH) \quad \text{(Equation 7.11)}$$

where K is the intrinsic permeability and k_l is the relative liquid permeability of the material, which are discussed in the next section. μ (Pa•s) is the viscosity of the fluid. M_l is the molar mass of water (kg/mol); R is the gas constant (J/(mol•K)), T is the temperature (K) and RH is relative humidity, ranging from 0 to 1.

For converting relative humidity to saturation, previous studies in absorption and desorption isotherms were used [433], shown in Table 7-1, saturation is then calculated based using equations 7.12 and 7.13.

$$\omega_{max} = \frac{\phi\rho_l}{\rho_s} \quad \text{(Equation 7.12)}$$

$$s = \frac{\omega}{\omega_{max}} \quad \text{(Equation 7.13)}$$

Where w_{max} is the maximum water content, ρ_s is the density of the dry sample and w (g/g dry) is the equilibrium water content referred to in Table 7-1. Desorption isotherm is used at the surface where drying is occurring, reflecting moisture loss. Absorption isotherm is applied inside the samples where gained moisture may occur due to water release due to the decomposition of hydrates.

Table 7-1. Absorption and desorption isotherm of alkali-activated slag cements [433]

RH (%)	11.36	32.68	42.85	58.04	74.18	84.17	92.29	96.65	99.46
Absorption (g/ g dry)	0.04	0.06	0.08	0.10	0.14	0.21	0.28	0.33	0.34
RH (%)	10.73	32.49	42.83	57.70	74.43	84.00	99.20		
Desorption (g/ g dry)	0.05	0.12	0.20	0.27	0.34	0.35	0.35		

7.3.4.1 Simulating intrinsic liquid water permeability using 3D μCT images

Intrinsic permeability is the inherent property of materials, only depends on the microstructure and varies due to different fluids viscosity [185]. Thoughtful discussion has been reported in applying the Kozeny-Carman equation [178] and Katz-Thompson model [434] to calculate the intrinsic permeability in cementitious materials. However, those equations were originally used in interconnected pores in rocks with capillary-sized pores [435]. The use of a critical diameter, determined under the assumptions of mercury intrusion porosimetry (MIP) and excluding gel pores, leads to an overestimation of permeability values calculated by these models [181]. This issue primarily arises from neglecting local pore size distribution during fluid transport, which can significantly alter the results.

In this study, the segmented 3D μCT pore structure of sodium sulfate-activated slag cements after 28 days of curing, determined and reported in Chapter 3, for a cubic region of interest with a side length of 350 μm of Section 3.7.2.3, was skeletonised to find the centreline of interconnected regions [436], using Avizo 2022.1® (ThermoFisher Scientific). The simulation of the intrinsic permeability was conducted in the Avizo package Absolute Permeability Experiment Simulation in XLab. Then, a 1000-pressure gradient, which is meant to prevent microstructure damage [183], of liquid water was applied along the z-axis between two opposite faces to direct the flow in a single direction and the remaining four faces were hermetically closed. Intrinsic permeability is determined by Darcy's law (equation 7.14) using the finite volume method. The criterion of this steady state flow is defined by the difference of average velocity in the whole specimen between two consecutive iterations being lower than

1.0×10^{-7} m/s, which is sufficient to give computational accuracy. It was assumed that the pore space is fully saturated, so all segmented pore structure was considered in the simulation.

$$\frac{Q}{S} = -\frac{K}{\mu}\frac{\Delta P}{L} \qquad \text{(Equation 7.14)}$$

Q (m^3/s) is the fluid flow rate along the cross-section; S (m^2) is the cross-section of the sample; K is the intrinsic permeability (m^2); μ (Pa•s) is the dynamic viscosity of the fluid; ΔP (Pa) is the pressure gradient and L (m) is the length of the sample along the flow direction. Figure 7-8a shows the skeletonised interconnected pore structure in a sample of sodium sulfate-activated slag cements; velocity and pressure distribution in the specimen are presented in Figures 7-8b and 7-8c. The intrinsic permeability K is then calculated as 1.4×10^{-14} m^2 using equation 7.12.

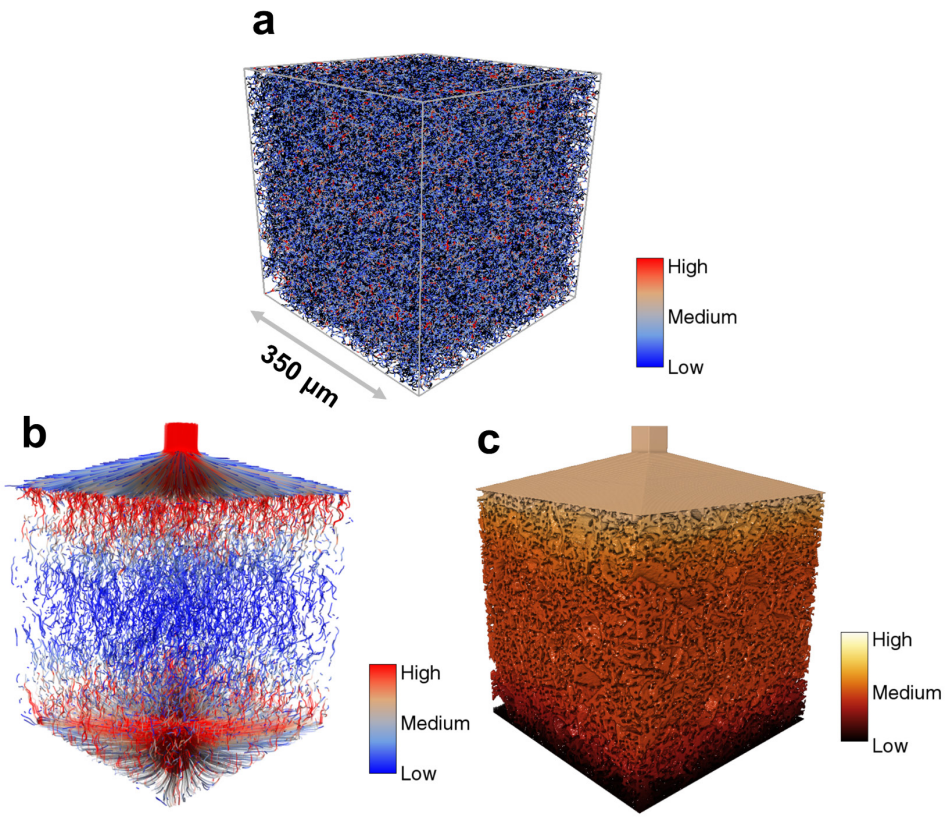

Figure 7-8. (a) Skeletonised pore structure in 28 days cured sodium sulfate-activated slag cement after 28 days of curing. Colourations indicate the thickness of the pore; the mean thickness is 1.6 µm and the highest thickness is 7.2 µm. (b) velocity and pressure (c) distribution by applying a 1000 [Pa] pressure gradient of water along the z-axis

7.3.4.2 Simulating relative liquid and gas permeability as a function of degree of saturation

The degree of saturation within the pore structure influences both water and gas permeability due to moisture transport during carbonation [437]. In a fully saturated pore structure, the liquid permeability equals the intrinsic liquid permeability, and the gas permeability is effectively zero. Conversely, in a completely dried pore structure (s = 0), liquid permeability drops to zero while gas permeability equals the intrinsic gas permeability. Under unsaturated conditions (0 < s < 1), it becomes necessary to determine the relative liquid water permeability and relative gas permeability. The Van Genuchten-Mualem (VGM) model was used to determine the relative liquid permeability, as shown in equation 7.15 [438, 439] and relative gas permeability as a function of water saturation was calculated on the basis of [440], presented in equation 7.16. These equations (equations 7.15 and 7.16) have been successfully applied in cementitious materials to determine the liquid and gas permeability under unsaturated conditions [187].

$$k_l = s_l^n[1-(1-s_l^{1/m})^m]^2 \qquad \text{(Equation 7.15)}$$

$$k_g = (1-s_l)^n[1-(1-s_l^{1/m})^m]^{2m} \qquad \text{(Equation 7.16)}$$

Here *n* and *m* are fitting parameters; n is also regarded as a geometrical tortuosity factor [187]. In the current model, n and m are defined as 1.5 and 0.7. The selection of two values is based on recent experimental results that *n* is in the range of 1 and 2 and *m* ranges from 0.64 to 0.69 for cementitious materials [441].

In the current model, permeability is considered solely as a function of saturation. Although carbonation can alter intrinsic permeability by modifying the pore structure as a result of reacted CO_2, this relationship is not well-defined for sodium sulfate-activated slag cements due to a lack of comprehensive experimental data. Thus, the model assumes permeability is dependent only on saturation, allowing for a more controlled analysis of the influence of moisture transport during the carbonation process. Future research should aim to develop analytical methods that predict permeability changes as a function of pore structure evolution and carbonation in sodium sulfate-activated slag cements. This would enable a more accurate representation of the transport properties in these materials, particularly under conditions where carbonation significantly alters the microstructure.

Figure 7-9 shows the simulated relative liquid permeability and relative gas permeability as a function of water saturation degree. The simulated curves agree well with experimental results for blended cements [441-443] and lattice Boltzmann modelling for PC [186]. This modelling

results reveal that liquid permeability decreases when drying happens during carbonation (decreased water saturation). Relative liquid and gas permeability reach the same value when water saturation reaches around 60 %. Lower than this value, liquid water is more difficult to transport from the pore structure to the outside; gas is easier to transport into the pore structure to proceed with the carbonation. This is consistent with the carbonation exposure condition of ~60 % of relative humidity (RH) generally recommended for accelerated carbonation standards [444], and experimental observations report that the highest carbonation depth in different cement systems when the material is exposed at 60-70 % RH [151, 445, 446]. Additionally, below 20 % water saturation, relative liquid permeability is almost 0, because most of the capillary pores are empty, and the water in the nano-sized gel pores of C-(A)-S-H, cannot be removed by drying. The two simulated curves in Figure 7-8 were then imported into the CO_2 transport model.

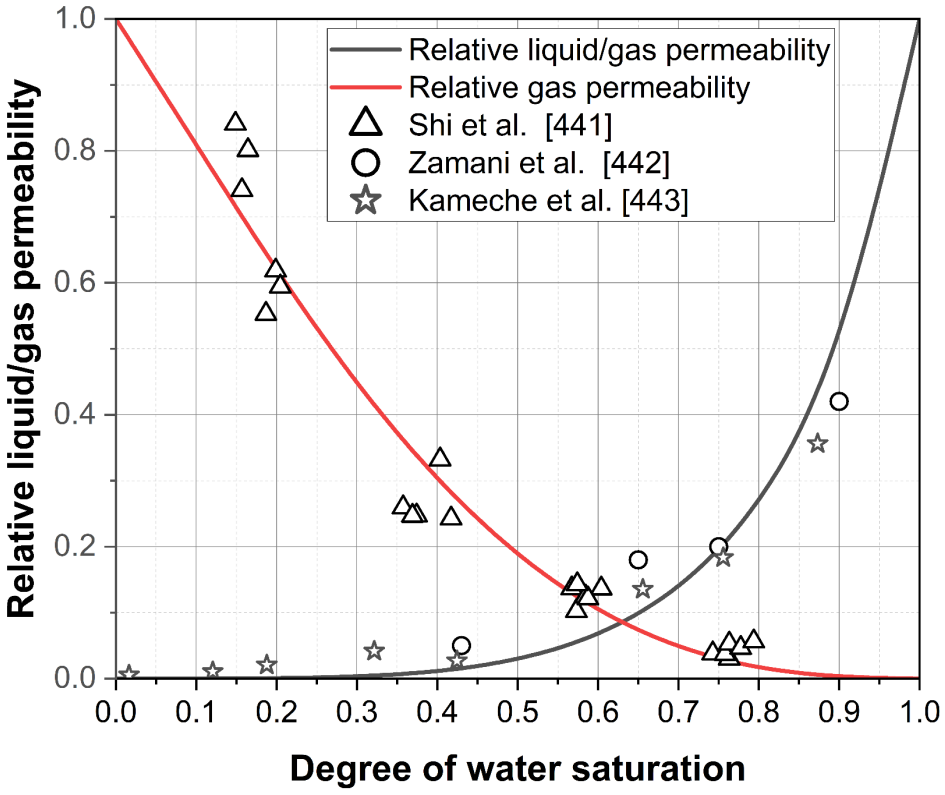

Figure 7-9. Simulated relative liquid permeability and relative gas permeability as a function of the degree of saturation, based on equations 7.15 and 7.16. Experimental results for gas permeability are referred to by Shi et al [441]. Experimental results for relative gas permeability are referred to by Zamani et al. [442] and Kameche et al. [443].

7.3.5 Finite element method model setup and description

In this numerical model, a cylinder with 25 mm of radius and 200 mm of height was built, as shown in Figure 7-10. The curing age of the specimen is 28 days. The exposure conditions 1 % CO_2, 55 % RH and 20 ℃ were specified to induce accelerated carbonation for 1 year. The selection of 1 % CO_2 is based on EN 13295:2004 [347] for evaluating the carbonation of alkali-activated materials; 55 % RH and 20 ℃ are defined in the standard BSI 1881-210:2013 [348]. As natural carbonation conditions 0.04 % CO_2, 55% RH and 20 ℃ were used, and the model ran for 10 years. The use of 1 year of accelerated carbonation and 10 years of natural carbonation aims to demonstrate the model's capabilities and to facilitate comparison and validation against experimental results. This study focuses on understanding the carbonation process under controlled laboratory conditions. Therefore, a Dirichlet boundary condition (constant temperature and relative humidity) was selected to simplify the simulation and ensure consistency with the experimental environment. For future research, particularly studies aiming to simulate the real service life of concrete under variable environmental conditions, implementing Neumann boundary conditions will be necessary to more accurately represent the moisture transport process. In such cases, applying a moisture flux at the boundary would better approximate outdoor conditions.

The degree of reaction, porosity, volume fraction of reaction products, pore solution (as presented in Section 7.2), diffusivity (Figure 7-7), absorption/desorption isotherm (Table 7-1), and permeability (Figure 7-9) were all set as input parameters in the model. The heterogeneity and time evolution of the porous in sodium sulfate-activated slag cements are defined by dynamic values of porosity, tortuosity, diffusivity and permeability which have been discussed in the previous sections. The free triangular mesh method is used in this model. Except for one end of the cylindrical sample is exposed to specific CO_2 and RH conditions (indicated by the arrow), the other surfaces are sealed to isolate moisture and carbon dioxide transport. Partial differential equations for moisture transport, gaseous CO_2 dissolution and dissolved carbonic acid transport, were solved using the COMSOL Multiphysics^{TM} 6.1 FEM software.

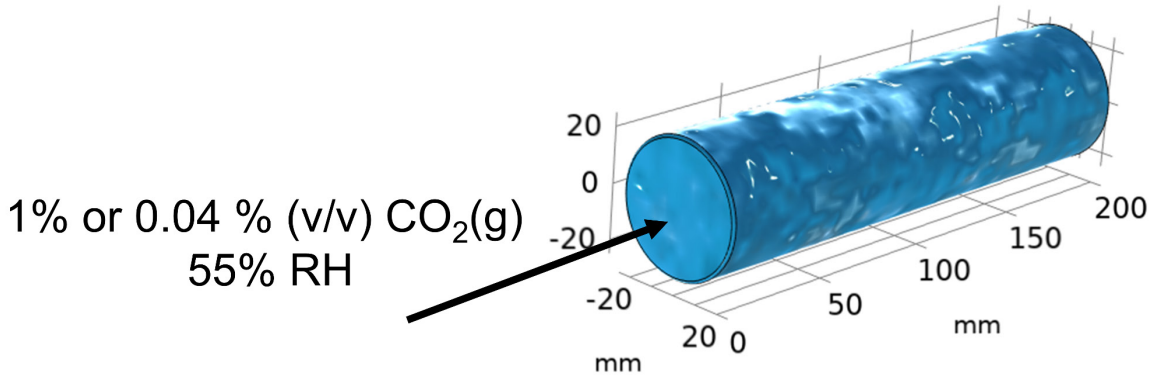

Figure 7-10. The specimen model and initial conditions. All surfaces other than the exposed end are sealed to prevent mass transport.

7.4 Coupled reactive-transport model results

7.4.1 Simulation of 1 year of accelerated carbonation

Under carbonation conditions, the drying process and carbonation in the pore solution happen simultaneously. Figure 7-11 shows the uptake of CO_2 and the degree of saturation profiles in the 3D model after 1 year of accelerated carbonation in sodium sulfate-activated slag pastes. The proposed framework enables the user to export the material properties profiles along the CO_2 transport direction, including the degree of saturation (Fig. 7-12a), liquid volume fraction (Fig. 7-12b), permeability (Fig. 7- 12c), effective diffusion coefficient (Fig. 7-12d), capillary pressure (Fig. 7-12e) and CO_2 uptake (Fig. 7-12f), with the model results shown after 14, 28, 56, 90, 180 and 365 days of accelerated carbonation.

After 14 days of accelerated carbonation, the degree of saturation in the surface regions almost equilibrated with the external exposure environment (RH = 0.55). An inflexion region is observed, when the saturation is around 0.8, and the profile becomes flatter after 1 year of exposure at around 25 mm depth, compared to the first 14 days. From the exposed surface to this inflexion region, there is a sharp increase in saturation. Beyond this region, from 25 mm to 200 mm depth, the rate of increase in saturation slows down. Similar observations are also reported from an experimental study that the moisture loss rate is significantly decreased in longer-cured PC concrete due to a denser pore structure [447] and modelling results for the carbonation of PC pastes [153, 203] show this region reflects the carbonation front between carbonated and uncarbonated regions, assuming the cement hydration is almost complete. The observed inflexion in the current study is related to the increased degree of slag reaction

forming more C-(A)-S-H gel and ettringite, and the carbonation process precipitating $CaCO_3$, gypsum and Mg-Al-CO_3-LDH, as shown in Figure 7-13a. These synergistic effects are reflected in decreased liquid volume fraction (Fig. 7-12b), permeability (Fig. 7-12c) and effective diffusivity (Fig. 7-12d) for longer exposure time.

The liquid permeability and effective diffusion coefficient were affected by changes in microstructure and saturation conditions, as explained in sections 7.3.3 and 7.3.4. These two profiles of transport properties are shown in Figures 7-12c and 7-12d, respectively. For liquid permeability, the drying process from the exposure surface to the interior regions of the specimen causes a significant decrease in liquid permeability due to a drop in saturation. However, ionic diffusivity is more related to the available pore volume (liquid volume fraction) which allows ionic migration to happen. The capillary pressure profile (Fig. 7-12e) shows good agreement with published studies [187, 203] as a function of water saturation.

Figure 7-12f shows the dissolved CO_2 in the pore solution along the CO_2 diffused direction. Maximum CO_2 uptake is around 7.6 g per 100 g slag as shown on the exposure face, which agrees with the power carbonation experiment of sodium sulfate-activated slag cements that maximum CO_2 uptake of this material is between 7.5 g and 10 g per 100 g slag under 1 % CO_2 and 65 % RH conditions [161]. This CO_2 profile will then be coupled with thermodynamic modelling to predict the phase evolution at each point within the specimen in the following section.

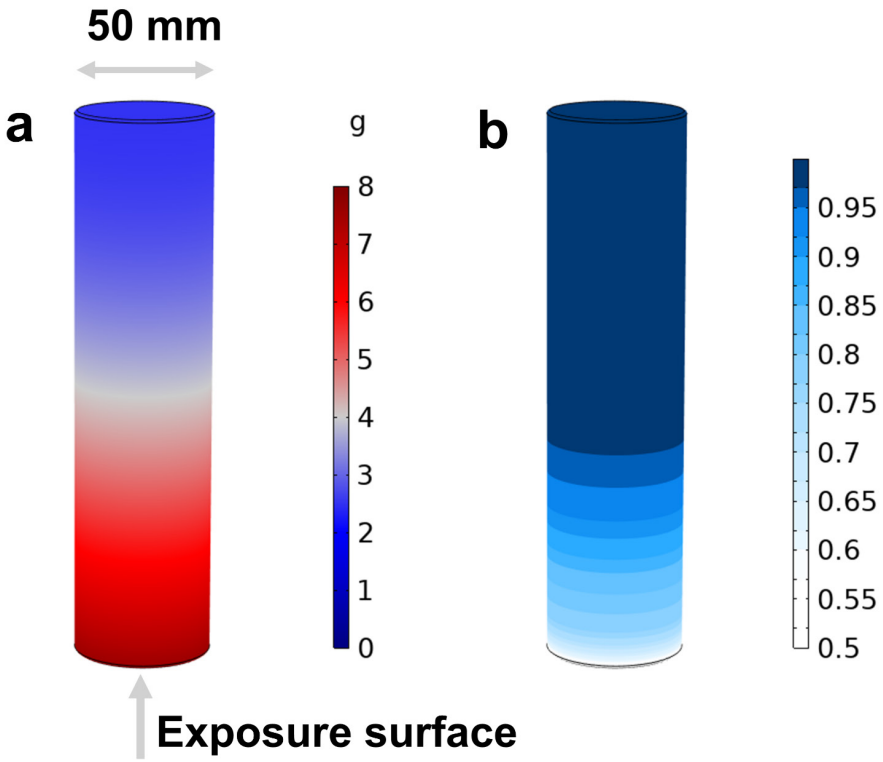

Figure 7-11. CO_2 uptake profile (a) and saturation profile in the generated 3D model in 28 days cured sodium sulfate-activated slag cements after 1 year of accelerated carbonation (55 % RH and 1 % CO_2)

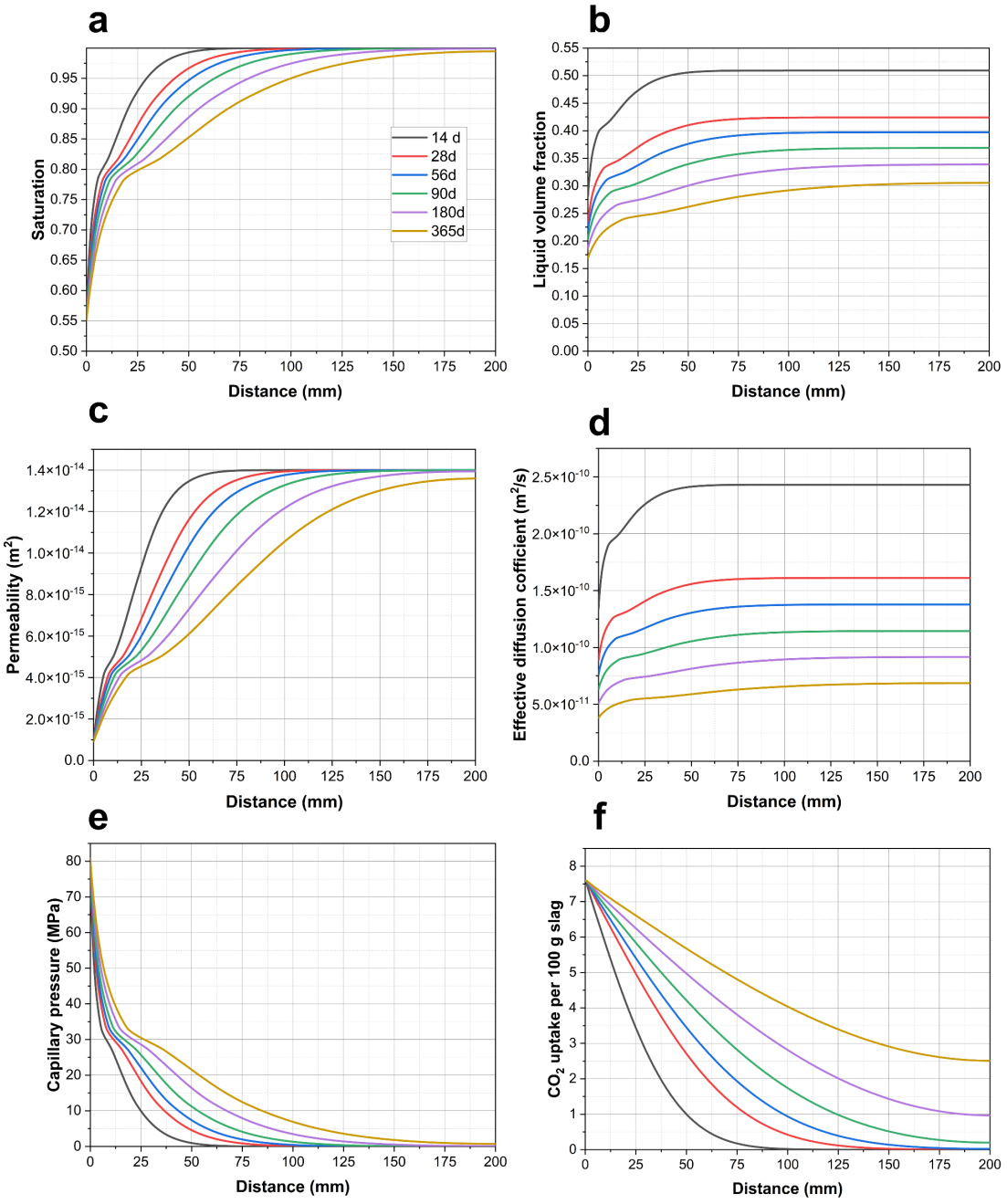

Figure 7-12. Simulated profiles of (a) saturation, (b) liquid volume fraction, (c) permeability, (d) effective diffusion coefficient, (e) capillary pressure and (f) CO_2 uptake from the exposure surface (distance 0) to the interior, in 28 days cured sodium sulfate-activated slag cements after 14, 28, 56, 90 and 365 days of accelerated carbonation under 55 % relative humidity and 1 % CO_2

Figure 7-13a shows the phase evolution along the CO_2 ingress direction. From the inside of the specimen to the exposure surface, decreased C-(A)-S-H gel and ettringite were observed with the formation of $CaCO_3$, gypsum, Mg-Al-CO_3-LDH and aluminosilicate. This observation shows a good agreement with experimental studies in Chapter 5 as characterised by XRD [160], the spatial distribution of ettringite and Mg-Al-CO_3-LDH as characterised by synchrotron XRD-CT in Chapter 6, and other literature reporting experimental data [146, 161]. The decalcification of C-(A)-S-H gel and decomposition of other reaction products happen at the same time, as observed in this study, agreeing with other carbonation modelling results [76] and experimental results in alkali-activated materials [68, 146]. Additionally, increased pore solution content was observed, due to the decomposition of hydrated reaction products that release the bound water. Although increased saturation in the pore structure during carbonation was reported in PC-based cements [103, 152], it has not previously been described in sodium sulfate-activated slag cements.

The precipitated $CaCO_3$ profile is presented in Figure 7-13b. A longer exposure time causes more formation of $CaCO_3$. The trend of the $CaCO_3$ profile agrees well with the experimental study for blended slag cements [328], PC pastes and mortar [152]. The capacity to estimate the amount of $CaCO_3$ as carbonation reaction products in this framework provides potential opportunities for future life cycle assessments (LCA) [448] and CO_2 curing mechanisms [119] of novel cements based on user-defined specimen dimensions. Additionally, as shown in Figures 7-11a and 7-13b, the spatially resolved CO_2 uptake is different at each depth due to variations of microstructure properties and mineralogical properties, so it is important to consider the spatial CO_2 profile in the calculation of bound CO_2 in the cementitious materials.

Figure 7-12b shows the pH profile, Ca/Si ratio and Al/Si ratio of C-(A)-S-H gel within the simulated sample. Two steps of decalcification of C-(A)-S-H gel were observed, corresponding to the removal of Ca^{2+} from the interlayer and main-layer sites, respectively [115]. The Ca/Si ratio in partially carbonated regions between 175 and 200 mm reaches a value of ~1, which agrees well with experimental observations in 1-year sealed cured sodium sulfate-activated slag cements as determined by SEM-EDX in Chapter 4 and deconvolution of ^{29}Si MAS NMR spectra [257]. The Al in the bridging site of silicon tetrahedral chains, characterised as Q^2(1Al) by ^{29}Si MAS NMR [63, 84], is gradually consumed as more CO_2 travels inside from the exposure surface. It is reasonable to define that a Ca/Si ratio lower than 0.7 [115] and a pH value in the pore solution lower than 10.5 [150] reflects the carbonation front. Thus, the carbonation depth in the current framework agrees well with the estimated phenolphthalein carbonation depth [160], which further validates the accuracy of the framework.

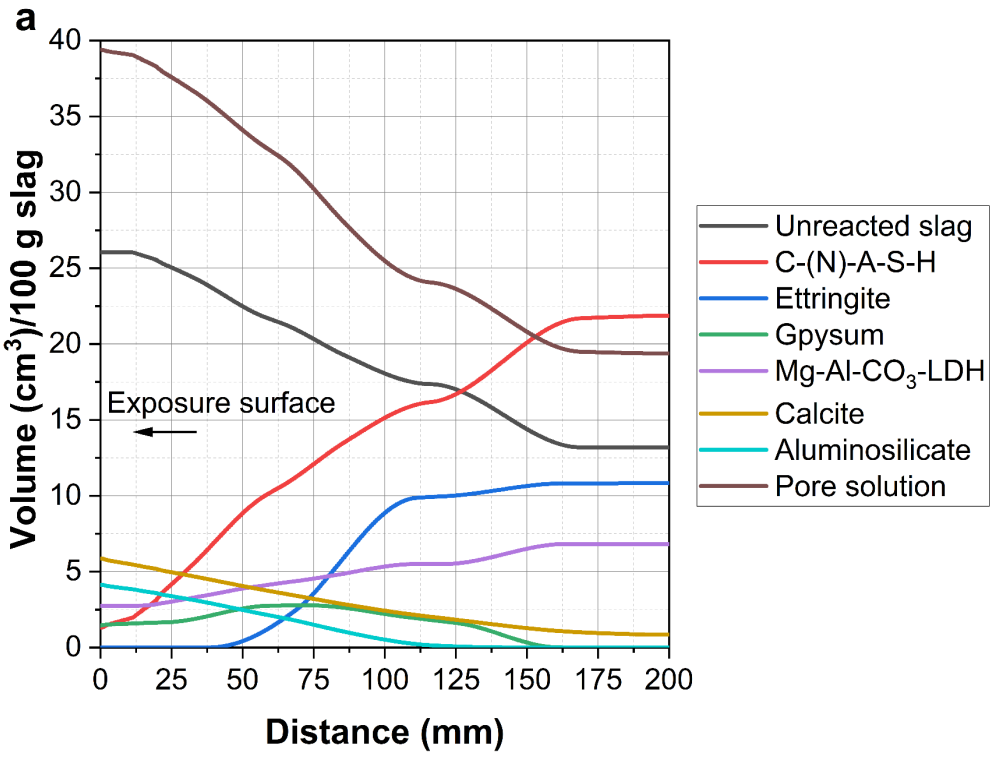
a
Volume (cm3)/100 g slag
Distance (mm)
Exposure surface
Unreacted slag
C-(N)-A-S-H
Ettringite
Gpysum
Mg-Al-CO3-LDH
Calcite
Aluminosilicate
Pore solution

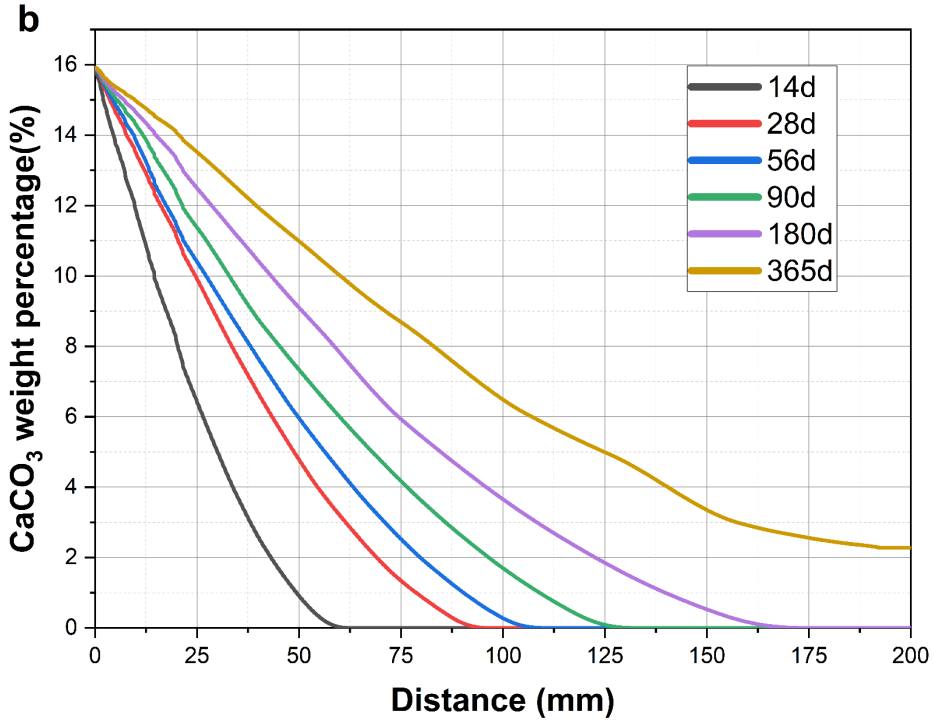
b
CaCO3 weight percentage(%)
Distance (mm)
14d
28d
56d
90d
180d
365d

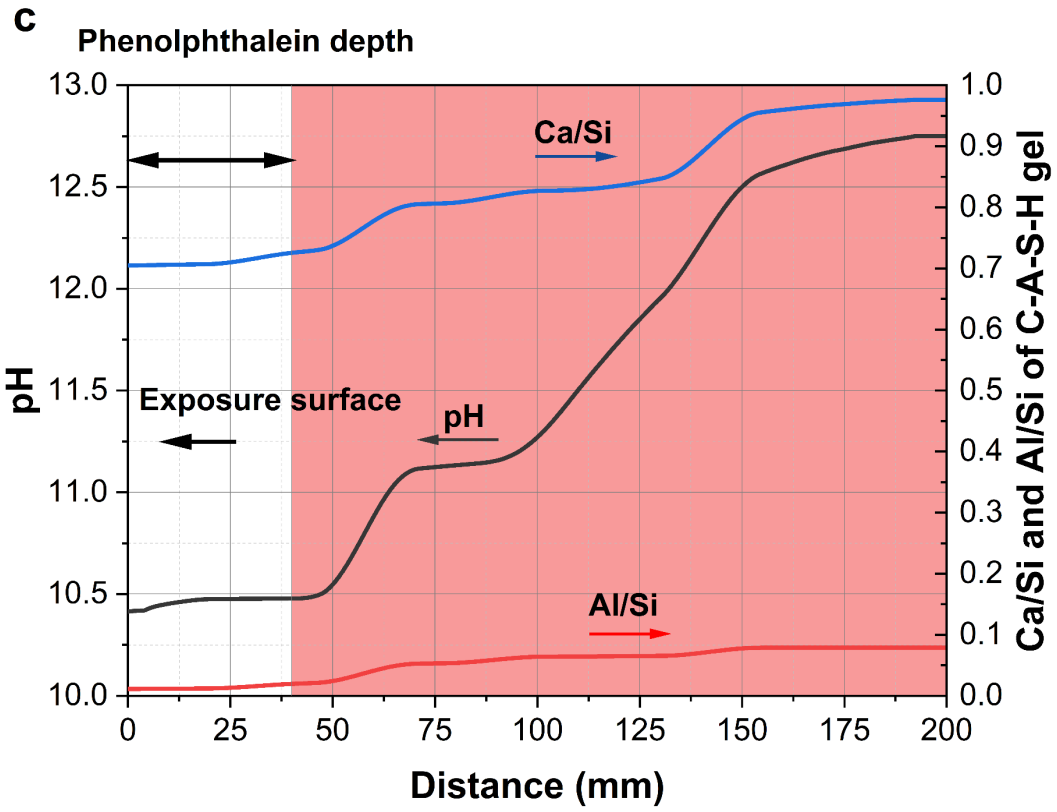

Figure 7-13. (a) Modelled phase evolution in 28 days cured sodium sulfate-activated slag cements from exposure surface to the interior of the specimen after 1 year of accelerated carbonation. (b) Precipitated weight percentage $CaCO_3$ as a function of depth (exposure surface is distance 0), from 14 days to 1 year of accelerated carbonation in 28 days cured samples. (c) Profiles of pH, Ca/Si ratio and Al/Si ratio of C-A-S-H gel. The fuchsia region corresponds to the partially carbonated/uncarbonated region; the colourless region represents the phenolphthalein carbonated region, which is estimated as a function of the square root of the time [163]; $x = 2.09\sqrt{t}$ based on the experimental results of this material [131], where x (mm) is the carbonation depth and t is the exposure time (days).

7.4.2 Simulation of 10 years natural carbonation

To simulate a decade of natural carbonation, the hydration simulation was adjusted so that the maximum DoR in the uncarbonated regions was set to 80%. This approach is grounded in experimental findings indicating that the highest DoR for blast furnace slag tends to stabilise at approximately 80% in alkali-activated slag cements after both 8 years [449] and 18 years of reaction [53], as determined by deconvolution of ^{29}Si MAS NMR spectra [450].

Figure 7-14 illustrates the changes in transport properties and CO_2 profiles from 1 to 10 years of natural carbonation. Before 3 years of natural exposure, both the slag reaction (in uncarbonated regions), carbonation and moisture transport influence the transport properties. After 3 years, the liquid volume fraction (Fig. 7-14b) and the effective diffusion coefficient (Fig. 7-14d) remain relatively unchanged over time, attributed to the completion of the slag reaction at 80%, which stabilises the porosity and tortuosity. Subsequently, moisture transport becomes the predominant factor affecting CO_2 transport, as evidenced by the alterations in saturation within the pore structure (Fig. 7-14a), pore solution permeability (Fig. 7-14c), and capillary pressure (Fig. 7-14e). A more pronounced inflexion region is observed in Figure 7-14 (Fig. 7-14a, 7-14c, and 7-14e) after 10 years of natural exposure compared to 1 year of accelerated carbonation at approximately 25 mm from the exposure surface. This variation can be attributed to the accumulation of ettringite, C-(A)-S-H, and Mg-Al-CO_3-LDH, Figure 7-15a, which contribute to a more complex and compact microstructure. Additionally, due to the lower extent of carbonation and extended drying period, the volume of pore solution in specimens exposed for 10 years naturally (Fig. 7-14a) is significantly lower throughout the specimen, compared to 1 year of accelerated carbonation (Fig. 7-12a).

After 10 years of natural exposure, the dissolved CO_2 penetrates through the specimen. Nevertheless, the maximum dissolved CO_2 (~7.6g per 100g of slag) under natural carbonation (Fig. 7-14f) is similar to accelerated carbonation (Fig. 7-12f). This observation is corroborated by experimental findings that the amount of bound $CaCO_3$ is comparable to the natural carbonation of a powder for 120 days [105], and accelerated carbonation for 28 days in sodium sulfate-activated slag cements [257]. Additionally, the maximum bound CO_2 content observed in this study under natural carbonation aligns with the experimental results indicating uptake of ~7g CO_2 per 100 g of cement (slag+clinker) at the exposure surface in 75 % substituted slag concrete after 10 years of natural exposure [451]. Figure 7-15b presents the precipitated mass percentage $CaCO_3$ profile from 1 year to 10 years of natural carbonation. For extended natural exposure (after 3 years), the DoR at each layer and the bound CO_2 are the main factors determining the precipitated mass amount of $CaCO_3$.

Figure 7-15c depicts changes in the Ca/Si and Al/Si ratios of C-(A)-S-H gel, as well as the pH values in the pore solution, after 10 years of natural carbonation. The decalcification process of C-(A)-S-H gel is discussed in Sections 7.2.3.2 and 7.4.1. The Ca/Si and Al/Si ratio profiles after 10 years of natural exposure are higher than those after 1 year of accelerated carbonation under controlled environmental conditions (Fig. 7-13c). Notably, both ratios tend to stabilise at around 1 and 0.1, respectively, from 100 mm to 200 mm of cover depth, closely associated with achieving 80% of the maximum DoR in blast furnace slag (Fig. 7-15c). This finding

explains a more polymerised silicate structure in C-(A)-S-H under 1% CO_2 concentration, evidenced by the formation of Q^3 and Q^4 tetrahedral silicates [257], in contrast to natural carbonation for 10 years. The latter predominantly features Q^2 and Q^2(1Al) structures [84, 131] in sodium sulfate-activated slag cements, where the foil-like C-(A)-S-H morphology may contribute to a more impermeable microstructure [312, 329].

Although the phenolphthalein indicator shows the colour change for the solution at ~7.3 [452], on-site experiments show pH value of ~10.5 corresponds to fully carbonated regions with colouration change and does not necessarily drop below this value in fully carbonated sodium carbonate-activated slag mortar [453], sodium silicate-activated slag mortar [453], sodium silicate-activated fly ash/slag blended concrete [454, 455]. Only ~5.6 mm carbonation depth was observed after simulated 10 years of natural carbonation. The simulated results align with experimental data based on the square-root-of-time model, specifically in the colourless region depicted in Figure 7-14c [131]. Few studies have reported on carbonation depth for long-term natural carbonation of alkali-activated slag cements. The estimated carbonation depth in this simulation generally agrees with experimental observations of ~3.2 mm in 70% substituted slag blended concrete after 12 years of natural exposure with a water/binder (w/b) ratio of 0.4 [456], ~1.7 mm depth in sodium silicate-activated slag concrete after 8 years of exposure using 0.42 of w/b ratio [41] and ~12 mm depth in blended 75 %fly ash-25% slag geopolymer concrete with 0.3 of w/b ratio [455]. These findings suggest that although 1 year of 1% CO_2 exposure leads to significant phase alterations (Fig. 7-13a), a decreased pH value in the pore solution (Fig. 7-13c), and ~40 mm of carbonation depth (Fig. 7-13c), such accelerated carbonation only partially reflects the actual carbonation that sodium sulfate-activated slag cements might undergo during their service life. This assertion further supports the recommendation of the RILEM TC 247-DTA of using atmospheric levels of CO_2 concentration to realistically evaluate the carbonation performance of alkali-activated concrete over its service life [133]. This further validates the accuracy of the framework for natural service life estimation and underscores its potential engineering significance. To achieve good carbonation resistance in SCMs-based cement systems during their service life, it is crucial not only to enhance early reaction kinetics, but also to ensure that the cementitious components can still react over extended periods of curing and exposure.

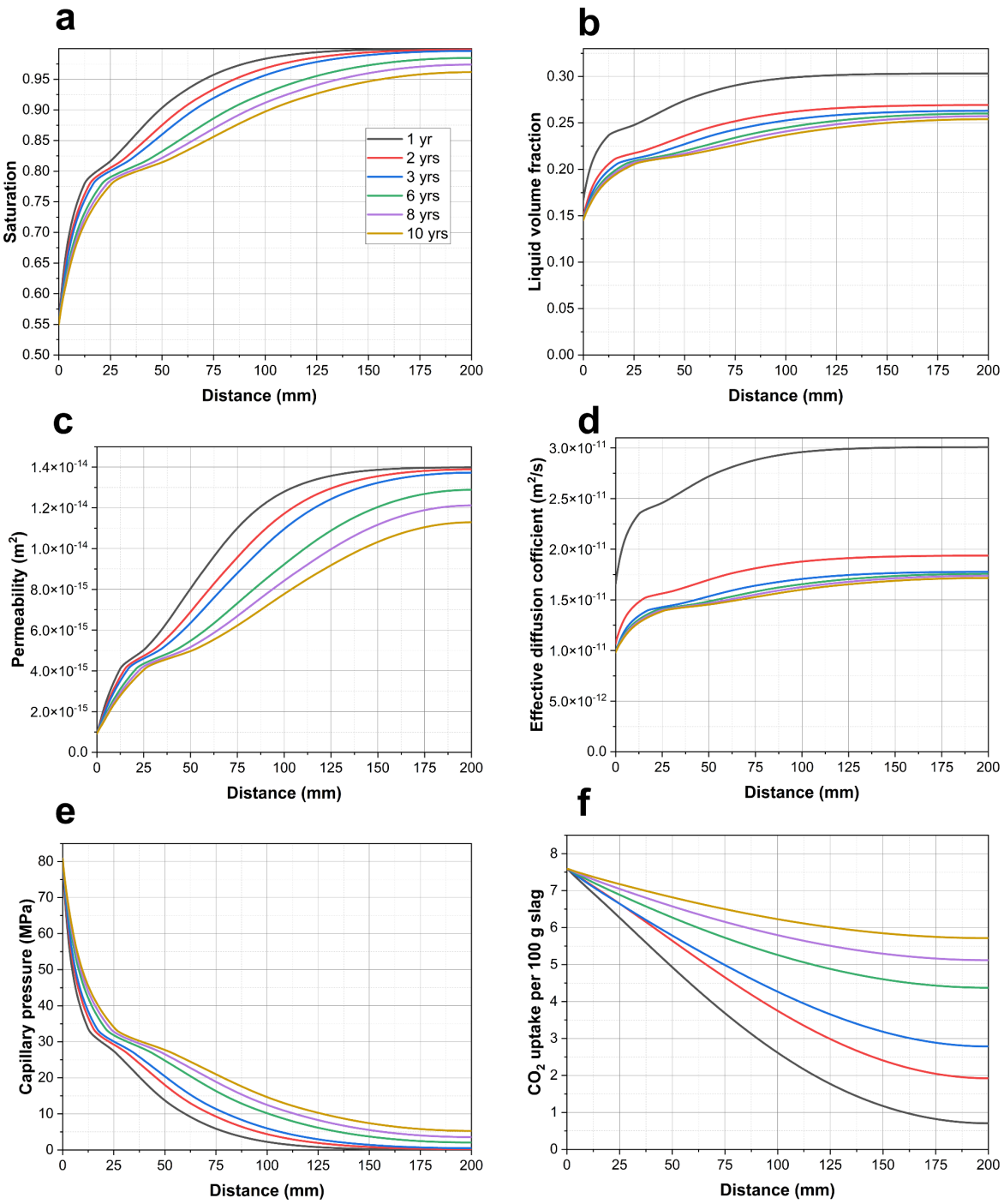

Figure 7-14. Simulated profiles of (a) saturation, (b) liquid volume fraction, (c) permeability, (d) effective diffusion coefficient, (e) capillary pressure and (f) CO_2 uptake from exposure surface to the interior in 28 days cured sodium sulfate-activated slag cements after 1, 2, 3, 6, 8 and 10 years of natural carbonation under 55 % relative humidity and 1 % CO_2 condition.

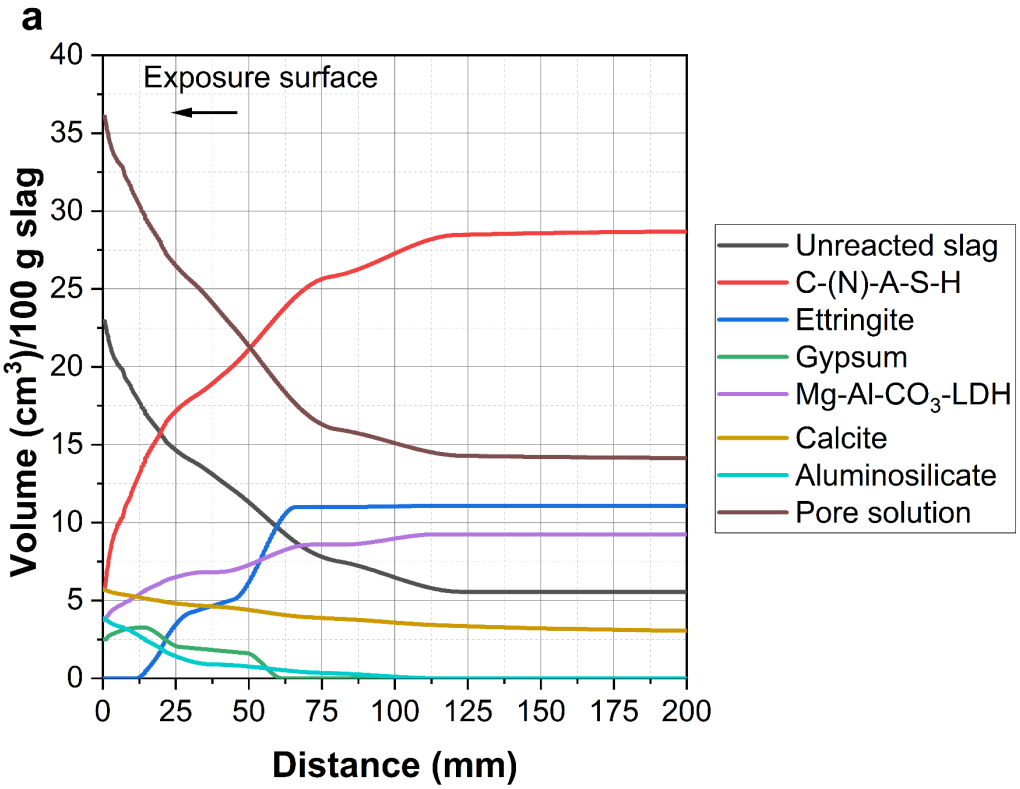
a
Exposure surface
Volume (cm³)/100 g slag
Distance (mm)
Unreacted slag
C-(N)-A-S-H
Ettringite
Gypsum
Mg-Al-CO3-LDH
Calcite
Aluminosilicate
Pore solution

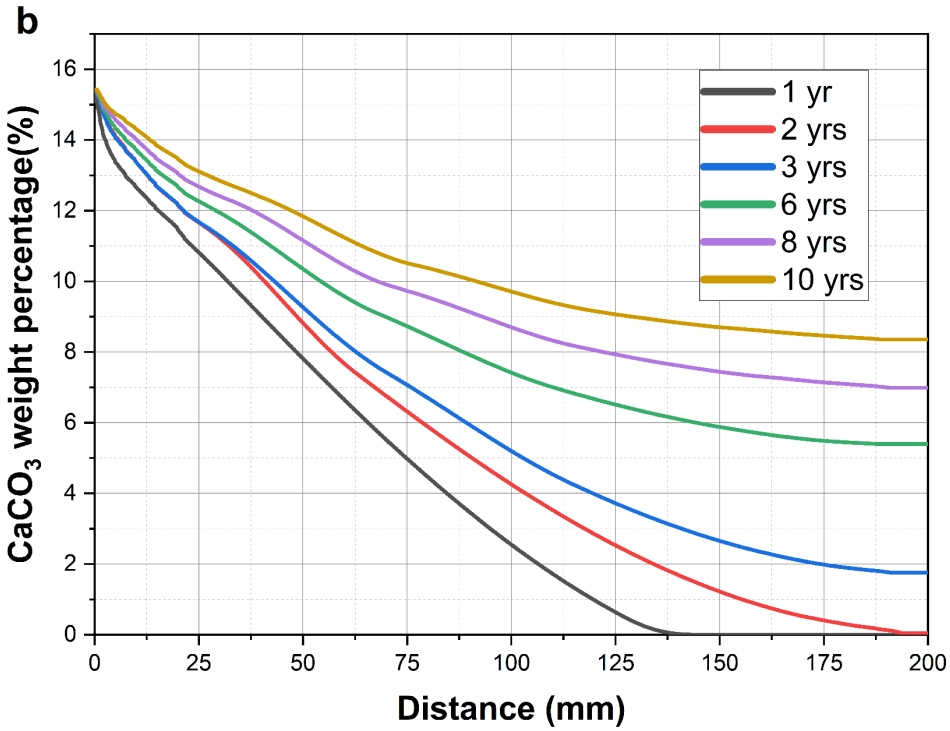
b
CaCO3 weight percentage(%)
Distance (mm)
1 yr
2 yrs
3 yrs
6 yrs
8 yrs
10 yrs

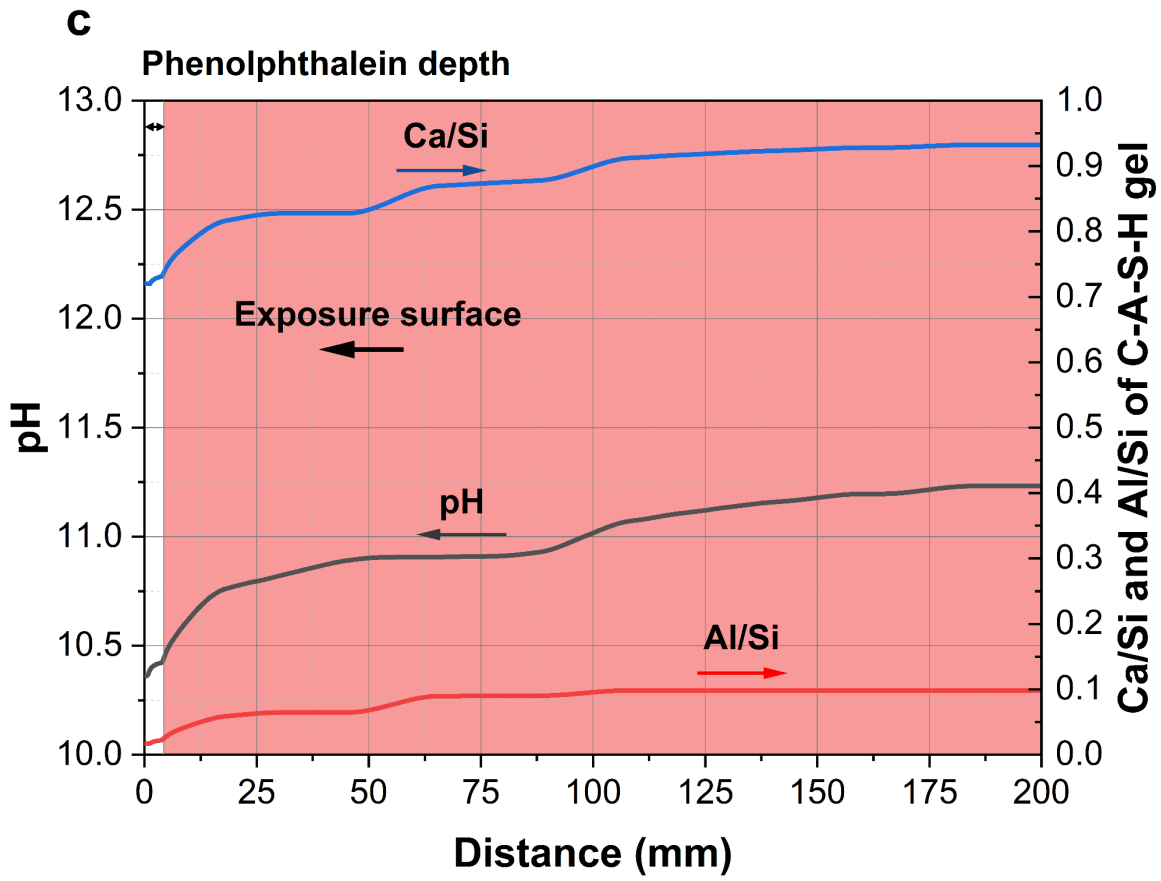

Figure 7-15. (a) Modelled phase evolution in 28 days cured sodium sulfate-activated slag cements from exposure surface to the interior of the specimen after 10 years of natural carbonation. (b) Precipitated weight percentage $CaCO_3$ as a function of depth (exposure surface is distance 0), from 1 year to 10 years of natural carbonation in 28 days cured samples. (c) Profiles of pH, Ca/Si ratio and Al/Si ratio of C-A-S-H gel. The fuchsia region corresponds to the partially carbonated/uncarbonated region; the colourless region represents the phenolphthalein carbonated region, which is estimated as a function of the square root of the time [163]; $x = 0.07\sqrt{t}$ is based on experimental results [131], where x is the carbonation depth and t is the exposure time (days).

7.5 Further validation by reported experimental results

To further validate the proposed reactive-transport model presented in this chapter, experimental results from the carbonation of 70% blended slag cements reported in the literature [328] were used as a benchmark. The literature describes specimens cured for one year prior to carbonation, which is assumed to have produced mature pastes [328], ensuring that the degree of reaction of both Portland cement and slag remains relatively stable over time. Tables 7-2 and 7-3 detail the chemical compositions of the Portland cement and slag, respectively. The degree of Portland cement reaction (DoR) is assumed to be 80%, based on the MPK model [173]; while the slag's DoR is taken as 50%, following Kolani et al. [457]. The basic information and exposure conditions are summarised in Table 7-5.

Figure 7-16a illustrates the modelled phase evolution across the depth of the specimen, from the exposure surface to the interior. Prior to carbonation (at a depth of 40 mm), the primary hydration products in the 70% slag blend include C-S-H gel, ettringite, siliceous hydrogarnet, strätlingite and Mg-Al-LDH, which aligns well with previously reported experimental and modelling findings [159]. Portlandite is not predicted suggesting the completed pozzolanic reaction between $Ca(OH)_2$ and slag [458]. Notably, iron-siliceous hydrogarnet, typically associated with elevated temperatures and long-term hydration [459, 460], has been identified at room temperature in Portland cement pastes by synchrotron X-ray absorption spectroscopy (XAS) after only one day of hydration [461]. This suggests that its formation may not be limited to specific extreme conditions. Strätlingite is unstable in the presence of Portlandite [462], which has been reported to form in high-alumina cements [463] and calcium sulphoaluminate cements [464].

In the depth range from the interior to the exposure surface, a distinct increase in the formation of $CaCO_3$, aluminosilicates, and pore solution is observed, which can be attributed to the decalcification of hydration products. The formation of aluminosilicates is closely related to the decalcification of C-S-H gel, leading to increased silicate chain polymerisation and a higher mean chain length (MCL) [357]. Although thermodynamic modelling predicts only the formation of C-S-H gel due to the current limitations in the thermodynamic database, experimental studies have demonstrated that aluminium content from slag tends to replace bridging sites in silicon tetrahedra, forming $Q^2(1Al)$ units, and resulting in the production of aluminium-substituted calcium silicate hydrate (C-(A)-S-H) in blended slag cement systems [302, 357]. Future work should prioritise the development of thermodynamic databases that can accurately represent the behaviour of C-(A)-S-H gel in blended slag cements.

Figure 7-16b presents a comparison between the simulated weight percentage of the $CaCO_3$ profile and experimental data from the literature [328] as a function of distance from the exposure surface. The modelled carbonation profiles exhibit good agreement with the experimental results, particularly in terms of the exposure distance and the distribution of $CaCO_3$. This provides strong evidence that the reactive-transport model can reliably predict the carbonation behaviour of blended slag cements under the given conditions.

Overall, these validation results highlight the capability of the model to predict both the qualitative and quantitative aspects of carbonation in high-volume blended slag cements. The agreement between the modelled phase distributions and the experimental data underscores the robustness of the model assumptions, particularly regarding hydration product stability and carbonation mechanisms. Nonetheless, further refinements, such as the inclusion of a more comprehensive thermodynamic database for C-(A)-S-H gel in the blended cements system, would enhance the predictive accuracy of the model and support its applicability across a broader range of slag compositions and exposure scenarios.

Table 7-2. Input chemical composition of Portland cement as inputs from the literature [328]

Crystalline composition (wt. %)	Alite	Belite	Aluminate	Ferrite	Anhydrite	Lime
Portland cement	54.6	29.0	6.16	6.83	0.56	2.35
DoR (%) [173]	85	55	83	63	100	100

Table 7-4. Input chemical composition of slag as inputs from the literature [328]

Chemical composition (wt. %)	CaO	SiO_2	Al_2O_3	MgO	Fe_2O_3	K_20	SO_3
slag	39.86	34.85	11.90	9.78	0.47	0.29	1.69
DoR (%) [457]				50			

Table 7-5. Basic information as inputs collected from the literature [328]

Information	values
Water/binder ratio by weight	0.5
Mass of Portland cement	450 g
Mass of slag	1050 g
Curing age	12 months
CO_2 concentration	3 % (v/v)
Temperature	20 ℃
Relative humidity	75 %
Exposure time	84 days
Specimen dimension	Width: 50 mm Height: 40 mm

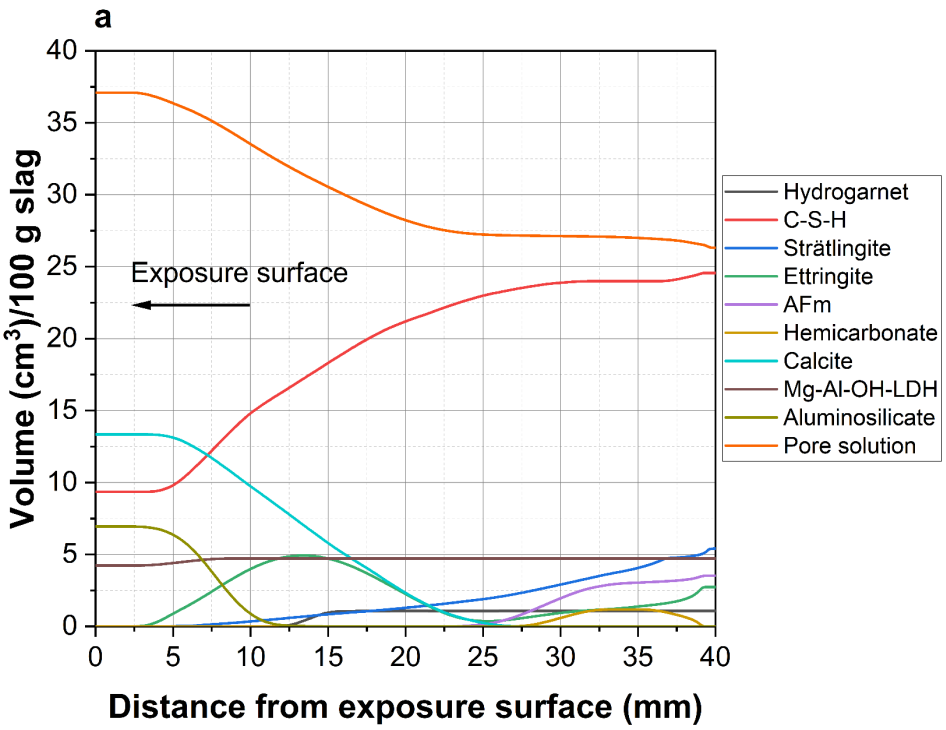

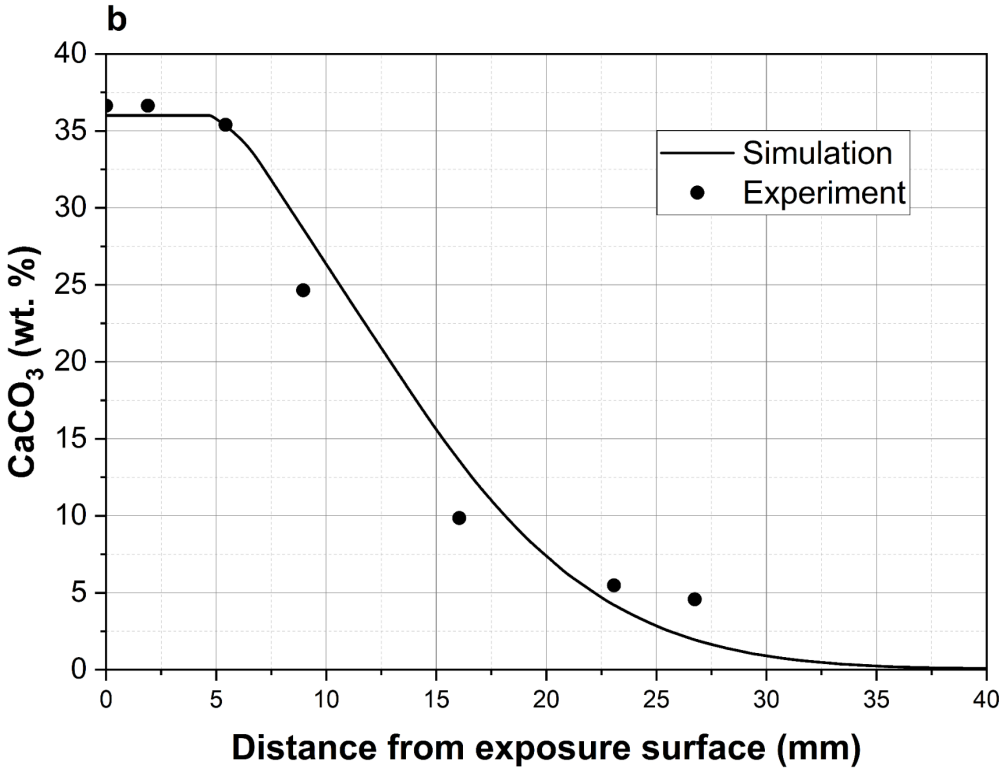

Figure 7-16. (a) Modelled phase evolution in 12 months cured blended slag cements with 70 % substitution from exposure surface to the interior of the specimen after 84 days of accelerated carbonation. (b) Simulated weight percentage $CaCO_3$ and experimental data, as a function of depth (exposure surface is distance 0). The experimental data is based on the literature [328]

7.6 Conclusion

This study introduces a novel reactive-transport framework that integrates thermodynamic modelling with the finite element method to predict chemical and physical alterations in cementitious materials exposed to CO_2. Unlike previous models, which often focus on isolated processes, this framework comprehensively considers multiple interacting factors, including cement hydration, carbonation, CO_2 dissolution, ionic diffusion, and moisture transport, along with their evolving transport properties such as porosity, saturation, diffusivity, and permeability. As a case study, the framework is applied to assess the carbonation performance of clinker-free alkali sulfate-activated slag cements and high-volume blended slag cements, but its flexible design allows for adaptation to virtually any cementitious system.

What sets this framework apart is its holistic approach to analysing carbonation, offering a clear step-by-step methodology for understanding and validating each physicochemical process involved. This is a significant departure from conventional models that often present mathematical equations as a final coupled result without sufficient guidance on individual processes. This detailed process-by-process analysis makes the framework particularly valuable in studying new cementitious systems, where reaction kinetics, phase assemblage, transport properties, and degradation processes are not well understood.

Given the increasing demand for sustainable cements using diverse local supplementary cementitious materials, whose physicochemical properties are largely unknown, this framework provides a pioneering tool for predicting microstructural evolution, transport properties, and durability performance. By offering a robust method for estimating the long-term performance and potential longevity of novel cementitious materials under various scenarios, this framework represents a critical step forward in sustainable cement development. The key findings of this study are listed below:

- μCT scanned anhydrous slag and sodium sulfate-activated slag cements 3D images can be used in determining 3D anhydrous slag particle distribution, tortuosity, diffusivity, intrinsic permeability and degree of slag reaction in hardened sodium sulfate-activated slag cements.

- The Ginstling-Brounshtein (G-B) equation is applied in sodium sulfate-activated slag cements in predicting the degree of slag reaction. The simplicity of this equation only requires the average radius of anhydrous particles and transport properties of ionic species, which can be obtained from the analysis of μCT data.

- Carbonation of sodium sulfate-activated slag cements causes an increase in pore solution. The drying process causes a rapid change of saturation in the pore structure. The combined effect of continued slag reaction and carbonation between dissolved carbonic acid and cements pastes is significant in the region of the carbonation front. An inflexion region is observed due to forming a denser pore structure at a higher DoR in the interior of the sample. Before this region, the drying process caused increased capillary pressure and reduced saturation at the exposure surface, leading to sharp variation of permeability and diffusivity. After this region, the slag reaction and less bound CO_2 produce a more compact microstructure, slowing down the moisture loss via a reduction of permeability and diffusivity. This phenomenon becomes more pronounced at prolonged exposure times.

- Different CO_2 uptake and $CaCO_3$ profiles were observed for using 0.04 % and 1 % CO_2 concentrations at the same 55 % and 20 ℃ for 10 years and 1 year of exposure, which is fundamentally related to the variation of transport properties at each cover depth with different DoR, as well as differences in pore fluid chemistry as a function of CO_2 partial pressure. Simulated carbonation depth agrees well with experimental results, showing that testing at 1 % CO_2 can only partially reflect the service life-defined performance of sodium sulfate-activated slag cements.

This framework only requires a high-resolution μCT scan of the specimen to model the transport properties of the material and particle size distribution of anhydrous raw materials to define reaction kinetics, minimising the use of other or input data. This framework could be extended to simulate other durability stresses, such as chloride and sulfate ingress, in alkali-activated materials, high-volume blended supplementary cementitious materials, or other novel SCMs-based cementitious systems, whose reaction mechanism is unknown. The presentation of this framework undoubtedly required comparison with experimental data and further optimisation; however, this framework does provide a quick estimation of phase evolution, CO_2 uptake and transport properties under the service life of the concrete.

Considering the rapid development of adapting different types of local SCMs for producing sustainable cements, where the physicochemical properties are largely unknown, this framework could provide a first estimation of microstructure evolution, transport properties and durability performance of studied novel cements and estimate the potential longevity in different scenarios.

Chapter 8.

CONCLUSIONS AND FUTURE WORK

8.1 Conclusion

In summary, this thesis presents fundamental studies including the development, optimisation, and life service prediction of sustainable, near-neutral salt sodium sulfate-activated slag cements, addressing many current barriers to their widespread adoption. In Chapter 4, the materials developed herein achieve mechanical properties, microstructure, and pore structure comparable to, or even surpass, those of blended Portland cements. Contrary to general observations and expectations, the amount of Al_2O_3 content in the slag does not reliably predict cement performance. While pastes made with higher Al_2O_3 content slag exhibit faster reaction kinetics, those using slag with a higher Mg/Al ratio demonstrate superior compressive strength and reduced porosity over extended curing periods. Notably, Chapter 4 provides experimental and modelling evidence of the long-term stability of hardened cements, with over 600 days of characterisation, considering the effect of the slag composition.

In Chapter 5, significant differences in the phase assemblages were identified when pastes were exposed to accelerated or natural carbonation, indicating that exposure to low CO_2 concentrations (1%) does not induce comparable mineralogical or microstructural alterations to those observed under natural carbonation conditions (500 days). No correlation between the natural and accelerated carbonation rates was identified, suggesting that accelerated carbonation exposure is unsuitable for determining the carbonation potential of sodium sulfate-activated slag cement pastes. Furthermore, Na_2SO_4-activated slag mortar exhibited compressive strength gain and excellent carbonation resistance under natural carbonation conditions, demonstrating that the use of this near-neutral salt is beneficial for producing alkali-activated binders with enhanced carbonation resistance. This is in contrast to the performance observed when using silicate or hydroxide solutions as primary activators. This chapter provides novel insights into the physicochemical CO_2 interaction mechanisms with the studied materials and underscores the importance of selecting appropriate methodologies for studying

the carbonation of sodium sulfate-activated slag cements and establishing realistic long-term carbonation models based on experimental fundamentals.

Furthermore, Chapter 6 has made significant advancements in understanding these systems through the pioneer application of time-resolved synchrotron techniques. Specifically, it couples X-ray diffraction computed tomography (XRD-CT) and X-ray microcomputed tomography (μCT) to study sodium sulfate-activated slag cements. This chapter also includes the development of machine-learning approaches for processing and interpreting imaging data. The analysis provides the first irrefutable evidence of Mg-Al-SO_4-layered double hydroxide (LDH) phase formation and its spatial distribution in studied materials, underscoring its critical role in CO_2 sequestration. The integration of μCT and XRD-CT with the developed research methodologies and trajectories in this thesis represents a significant step forward, enabling rapid and reliable estimation of the carbonation resistance and CO_2 binding capacity of alkali-activated slag cements.

The accumulated experimental fundamentals in chapters 4, 5 and 6 help to validate and optimise both thermodynamic and transport models in the development of a 3D realistic service life prediction framework in chapter 7. This tool not only simulates the evolving chemistry of cements under CO_2 exposure and the corresponding changes in pore structure but also aids in designing materials resilient to climate change. The developed framework allows users to customise mix designs, chemical compositions, dimensions of specimens and carbonation conditions for sodium sulfate-activated slag cements with the capacity to export the CO_2 uptake, transport properties and phase assemblage evolution along the cements cover depth. The modelling approach spans multiple length scales of cementitious materials to simulate deterioration processes in cementitious materials and aids in designing slag cements tailored to local slag chemistries available globally. This comprehensive modelling framework, unique to complex physicochemical changes like those studied here, offers insights into selecting slags that are highly compatible with specific activators, enhancing the sustainability and durability of alkali-activated slag cements.

This framework can be adapted and extended to other low-carbon cements due to its fundamental-driven approach, particularly for predicting the performance of supplementary cementitious materials-based concrete under various service conditions, thus enhancing the safety and durability of future concrete infrastructure. This research represents a substantial advancement in understanding the long-term durability of concrete infrastructure. It provides valuable tools for predicting and planning necessary repairs in ageing infrastructure, such as

reinforced autoclaved aerated concrete (RAAC), which has posed significant challenges in vital UK infrastructure.

8.2 Directions for future work

The work presented in this thesis has provided irrefutable evidence that near-neutral salts sodium sulfate-activated slag cements exhibit satisfactory mechanical properties, microstructure stability, and carbonation resistance, with potential for application in various industrial settings. The research methodology and trajectory employed in the analysis and interpretation of 3D and 4D tomography data provide a workflow for applying advanced tomographic techniques to other SCM-based systems. The reactive-transport frameworks developed using 3D μCT images offer realistic service-life models and templates for predicting the performance of SCM-based concrete infrastructure. To further enhance and bolster confidence in using near-neutral salts-activated slag cements and the associated service-life model, the following research questions and tentative resolutions are listed below:

1. The primary reaction products, C-(A)-S-H gel, contribute to over 50% of the volume percentage of pastes and are the main strength-giving phase in concrete. While some studies have synthesised C-(A)-S-H gel with varying Ca/Si and Al/Si ratios to understand their chemistry in alkali-activated slag cements, systematic studies suggest that hardened cement pastes provide a more representative understanding of the morphology, Ca/Si and Al/Si ratios of C-(A)-S-H gel, and the Mg/Al ratio of LDH phases, supported by TEM-EDX analysis. To enhance understanding of the C-(A)-S-H nanostructure and validate TEM-EDX results, quantification through ^{29}Si MAS NMR is needed. This method would offer detailed insights into the volume percentages of each silicate species, the degree of reaction, the Al/Si ratio, and the Ca/(Al+Si) ratio, supported by the universal relationship, mean chain length, and site occupancy factor. Despite challenges in deconvolving ^{29}Si MAS NMR data due to the incongruent dissolution of blast furnace slag at the neutral pH values typically seen in sodium sulfate-activated slag cements, recent experiments indicate that the pH value in fresh pastes and pore solutions can exceed 12.5 [465-467], aligning with promising compressive strength and degree of reaction comparable to that of blended cements found in this study. Therefore, the deconvolution of ^{29}Si MAS NMR in sodium sulfate-activated slag cements is not supposed to be problematic for advancing understanding of the nanostructure of C-(A)-S-H in this system, by carefully following the well-documented data processing steps. It is reasonable to hypothesise that there are certain principles beyond all sulfate-activated cement systems.

2. The durability of cementitious materials is fundamentally contingent upon mass transport within porous media. The remarkable aspect of these materials is that their pore sizes range from nanometres to millimetres, with each scale offering unique scientific insights. Developing a full-scale 3D pore structure model for alkali-activated slag cements presents an interesting research topic, supported by laboratory-based techniques and machine learning technology. Although laboratory methods such as mercury intrusion porosimetry (MIP) are destructive and carry inherent assumptions, they still provide a valuable engineering perspective with certain accuracy using more accessible techniques. Utilising these 3D full-scale models could significantly enhance predictions of mass transport in alkali-activated slag cements across a wide range of life service applications.

3. The formation of microcracking is expected to happen during carbonation processes. Autogenous shrinkage, drying shrinkage, and carbonation shrinkage occur concurrently and contribute to the observed cracking [468]. Different exposures (CO_2 concentration, temperature and relative humidity) can affect the stress distribution and the type of cracks [227]. Stress distribution is not considered in the current framework due to a lack of fundamental understanding of this research topic. Future experimental studies in near-neutral salt slag cements are needed to establish numerical modelling in shrinkage and crack development, which can then be coupled into the current framework based on the finite element method.

4. In the current framework, microstructure and transport properties of geometrical specimens were characterised based on thermodynamic modelling, including the degree of slag reaction, phase evolution, and porosity, while transport properties such as tortuosity, diffusivity, and permeability were determined through modelling of μCT images. This approach is designed to simulate the transport of CO_2 and moisture on the millimetre-centimetre scale within the specimen. Ideally, CO_2 transport modelling should incorporate the actual CT-scanned pore structure. Currently, even synchrotron X-ray tomography, limited to small sample size (diameter: 2 mm) for observing pores as small as 2.1 μm, challenges the accurate simulation of real-life infrastructure service. With advancements in GPU technology, machine learning-based scaling algorithms have the potential to accurately simulate the pore structure of cementitious materials across scales from nanometres to metres. This is achieved by processing a large dataset of μCT images from the same samples [469-471].

5. The presentation of the reactive-transport model is limited to paste specimens in this thesis, due to computational limitations of the desktop workstation with 128 GB RAM (random access memory) used in this study. For modelling concrete service life, the random seeding algorithm can help to define the spatial distribution of fine and coarse aggregate and μCT scans of those

raw materials are needed to define the sphericity of those particles, which can affect the transport properties by orders of magnitudes [392]. Seeding fine and coarse aggregates in machine learning generated full-scale pore structure for real service concrete infrastructure and running the entire framework proposed in this study would be an interesting follow-up study, with the support of a supercomputing cluster.

References

1. Uratani, J.M. and S. Griffiths, *A forward looking perspective on the cement and concrete industry: Implications of growth and development in the Global South.* Energy Research & Social Science, 2023. **97**: p. 102972.
2. Provis, J.L. and S.A. Bernal, *Geopolymers and related alkali-activated materials.* Annual Review of Materials Research, 2014. **44**: p. 299-327.
3. Olivier, J.G., J.A. Peters, and G. Janssens-Maenhout, *Trends in global CO_2 emissions. 2012 report.* 2012.
4. Allwood, J.M., et al., *Sustainable materials: with both eyes open*. Vol. 2012. 2012: UIT Cambridge Limited Cambridge, UK.
5. Lolli, F. and K.E. Kurtis, *Life Cycle Assessment of alkali activated materials: preliminary investigation for pavement applications.* RILEM Technical Letters, 2021. **6**: p. 124-130.
6. Awoyera, P. and A. Adesina, *A critical review on application of alkali activated slag as a sustainable composite binder.* Case Studies in Construction Materials, 2019. **11**: p. e00268.
7. Juenger, M., et al., *Advances in alternative cementitious binders.* Cement and concrete research, 2011. **41**(12): p. 1232-1243.
8. Yuksel, I., *12 - Blast-furnace slag*, in *Waste and Supplementary Cementitious Materials in Concrete*, R. Siddique and P. Cachim, Editors. 2018, Woodhead Publishing. p. 361-415.
9. Yuksel, I.S., Rafat; Cachim, Paulo, *Chapter12 -Blast-furnace slag*, in *Waste and Supplementary Cementitious Materials in Concrete*. 2018, Woodhead Publishing. p. 361-415.
10. Guo, J., Y. Bao, and M. Wang, *Steel slag in China: Treatment, recycling, and management.* Waste management, 2018. **78**: p. 318-330.
11. Matsuura, H., et al., *Recycling of ironmaking and steelmaking slags in Japan and China.* International Journal of Minerals, Metallurgy and Materials, 2022. **29**(4): p. 739-749.

12. Dippenaar, R., *Industrial uses of slag (the use and re-use of iron and steelmaking slags).* Ironmaking & steelmaking, 2005. **32**(1): p. 35-46.
13. Pacheco-Torgal, F., et al., *Handbook of alkali-activated cements, mortars and concretes*. 2014: Elsevier.
14. Blotevogel, S., et al., *Glass structure of industrial ground granulated blast furnace slags (GGBS) investigated by time-resolved Raman and NMR spectroscopies.* Journal of Materials Science, 2021. **56**(31): p. 17490-17504.
15. Arvaniti, E.C., et al., *Determination of particle size, surface area, and shape of supplementary cementitious materials by different techniques.* Materials and Structures, 2015. **48**(11): p. 3687-3701.
16. Zhu, X., et al., *Setting behaviours and early-age microstructures of alkali-activated ground granulated blast furnace slag (GGBS) from different regions in China.* Cement and Concrete Composites, 2020. **114**: p. 103782.
17. Zhu, X., et al., *Understanding the setting behaviours of alkali-activated slag from the dissolution-precipitation point of view.* Cement and Concrete Composites, 2024. **148**: p. 105474.
18. Ke, X., S.A. Bernal, and J.L. Provis, *Controlling the reaction kinetics of sodium carbonate-activated slag cements using calcined layered double hydroxides.* Cement and Concrete Research, 2016. **81**: p. 24-37.
19. Blotevogel, S., et al., *Ability of the R3 test to evaluate differences in early age reactivity of 16 industrial ground granulated blast furnace slags (GGBS).* Cement and Concrete Research, 2020. **130**: p. 105998.
20. Haha, M.B., et al., *Influence of slag chemistry on the hydration of alkali-activated blast-furnace slag—Part I: Effect of MgO.* Cement and Concrete Research, 2011. **41**(9): p. 955-963.
21. Haha, M.B., et al., *Influence of slag chemistry on the hydration of alkali-activated blast-furnace slag—Part II: Effect of Al_2O_3.* Cement and Concrete Research, 2012. **42**(1): p. 74-83.
22. Winnefeld, F., et al., *Influence of slag composition on the hydration of alkali-activated slags.* Journal of Sustainable Cement-Based Materials, 2015. **4**(2): p. 85-100.

23. Wang, S.Y., E. McCaslin, and C.E. White, *Effects of magnesium content and carbonation on the multiscale pore structure of alkali-activated slags.* Cement and Concrete Research, 2020. **130**: p. 105979.
24. Zhu, X., et al., *Characterisation of pore structure development of alkali-activated slag cement during early hydration using electrical responses.* Cement and Concrete Composites, 2018. **89**: p. 139-149.
25. Provis, J.L., et al., *X-ray microtomography shows pore structure and tortuosity in alkali-activated binders.* Cement and Concrete Research, 2012. **42**(6): p. 855-864.
26. Whiting, J., *Manufacture of Cement*, U.S.P.O. US544706A, 1895, Samuel E. Hibben, E. Nemett: United States.
27. Provis, J.L., et al., *Demonstration projects and applications in building and civil infrastructure.* Alkali Activated Materials: State-of-the-Art Report, RILEM TC 224-AAM, 2014: p. 309-338.
28. Yang, K., et al., *First structural use of site-cast, alkali-activated slag concrete in China.* Proceedings of the Institution of Civil Engineers - Structures and Buildings, 2018. **171**(10): p. 800-809.
29. Buchwald, A., et al., *Purdocement: application of alkali-activated slag cement in Belgium in the 1950s.* Materials and Structures, 2015. **48**: p. 501-511.
30. PAS, B., *8820.(2016). Construction Materials. Alkali-activated Cementitious Material and Concrete Specification.* British Standards Institution.
31. Chi, M., *Effects of dosage of alkali-activated solution and curing conditions on the properties and durability of alkali-activated slag concrete.* Construction and Building Materials, 2012. **35**: p. 240-245.
32. Fernández-Jiménez, A., J.G. Palomo, and F. Puertas, *Alkali-activated slag mortars: Mechanical strength behaviour.* Cement and Concrete Research, 1999. **29**(8): p. 1313-1321.
33. Taghvayi, H., K. Behfarnia, and M. Khalili, *The effect of alkali concentration and sodium silicate modulus on the properties of alkali-activated slag concrete.* Journal of Advanced Concrete Technology, 2018. **16**(7): p. 293-305.
34. Collins, F.G. and J.G. Sanjayan, *Workability and mechanical properties of alkali activated slag concrete.* Cement and Concrete Research, 1999. **29**(3): p. 455-458.

35. Kong, Y. and K. Kurumisawa, *Fresh properties and characteristic testing methods for alkali-activated materials: A review.* Journal of Building Engineering, 2023: p. 106830.
36. Alonso, M., et al., *Alkali-activated mortars: Workability and rheological behaviour.* Construction and Building Materials, 2017. **145**: p. 576-587.
37. Bernal, S.A. and J.L. Provis, *Durability of alkali-activated materials: progress and perspectives.* Journal of the American Ceramic Society, 2014. **97**(4): p. 997-1008.
38. Zhang, J., et al., *Durability of alkali-activated materials in aggressive environments: A review on recent studies.* Construction and Building Materials, 2017. **152**: p. 598-613.
39. Wang, A., et al., *The durability of alkali-activated materials in comparison with ordinary Portland cements and concretes: a review.* Engineering, 2020. **6**(6): p. 695-706.
40. Gluth, G.J., et al., *Carbonation rate of alkali-activated concrete and high-volume SCM concrete: a literature data analysis by RILEM TC 281-CCC.* Materials and Structures, 2022. **55**(8): p. 1-15.
41. Bernal, S.A., et al., *Natural carbonation of aged alkali-activated slag concretes.* Materials and Structures, 2014. **47**: p. 693-707.
42. Bernal, S.A., et al., *Accelerated carbonation testing of alkali-activated binders significantly underestimates service life: The role of pore solution chemistry.* Cement and Concrete Research, 2012. **42**(10): p. 1317-1326.
43. Babaee, M. and A. Castel, *Chloride diffusivity, chloride threshold, and corrosion initiation in reinforced alkali-activated mortars: Role of calcium, alkali, and silicate content.* Cement and Concrete Research, 2018. **111**: p. 56-71.
44. Bondar, D., et al., *Alkali activated slag concretes designed for a desired slump, strength and chloride diffusivity.* Construction and Building Materials, 2018. **190**: p. 191-199.
45. Zhang, J., et al., *Review on chloride transport in alkali-activated materials: Role of precursors, activators and admixtures.* Construction and Building Materials, 2022. **328**: p. 127081.
46. Thomas, R.J., et al., *Comparison of chloride permeability methods for Alkali-Activated concrete.* Construction and Building Materials, 2018. **165**: p. 104-111.
47. Komljenović, M., et al., *External sulfate attack on alkali-activated slag.* Construction and Building Materials, 2013. **49**: p. 31-39.

48. Ye, H., Z. Chen, and L. Huang, *Mechanism of sulfate attack on alkali-activated slag: The role of activator composition.* Cement and Concrete Research, 2019. **125**: p. 105868.

49. Gong, K. and C.E. White, *Nanoscale Chemical Degradation Mechanisms of Sulfate Attack in Alkali-activated Slag.* The Journal of Physical Chemistry C, 2018. **122**(11): p. 5992-6004.

50. Myers, R.J., et al., *Generalized structural description of calcium–sodium aluminosilicate hydrate gels: the cross-linked substituted tobermorite model.* Langmuir, 2013. **29**(17): p. 5294-5306.

51. Richardson, I.G., *The nature of C-S-H in hardened cements.* Cement and Concrete Research, 1999. **29**(8): p. 1131-1147.

52. Richardson, I.G., *Model structures for C-(A)-S-H (I).* Acta Crystallographica Section B: Structural Science, Crystal Engineering and Materials, 2014. **70**(6): p. 903-923.

53. Richardson, I. and S. Li, *Composition and structure of an 18-year-old 5M KOH-activated ground granulated blast-furnace slag paste.* Construction and Building Materials, 2018. **168**: p. 404-411.

54. Zhu, X. and I.G. Richardson, *Morphology-structural change of C-A-S-H gel in blended cements.* Cement and Concrete Research, 2023. **168**: p. 107156.

55. Richardson, I., et al., *Hydration of water-and alkali-activated white Portland cement pastes and blends with low-calcium pulverized fuel ash.* Cement and Concrete Research, 2016. **83**: p. 1-18.

56. Luukkonen, T., et al., *One-part alkali-activated materials: A review.* Cement and Concrete Research, 2018. **103**: p. 21-34.

57. Bernal, S.A., *Advances in near-neutral salts activation of blast furnace slags.* RILEM Technical Letters, 2016. **1**: p. 39-44.

58. Shi, C., D. Roy, and P. Krivenko, *Alkali-activated cements and concretes*. 2003: CRC press.

59. Richards, T., C. Pavletic, and J. Pettersson, *Efficiencies of NaOH production methods in a Kraft pulp mill.* International journal of energy research, 2009. **33**(15): p. 1341-1351.

60. Heath, A., K. Paine, and M. McManus, *Minimising the global warming potential of clay based geopolymers.* Journal of Cleaner Production, 2014. **78**: p. 75-83.

61. Habert, G., J.D.E. De Lacaillerie, and N. Roussel, *An environmental evaluation of geopolymer based concrete production: reviewing current research trends.* Journal of cleaner production, 2011. **19**(11): p. 1229-1238.

62. Mobasher, N., et al., *Characterisation of Ba (OH)$_2$–Na$_2$SO$_4$–blast furnace slag cement-like composites for the immobilisation of sulfate bearing nuclear wastes.* Cement and Concrete Research, 2014. **66**: p. 64-74.

63. Mobasher, N., S.A. Bernal, and J.L. Provis, *Structural evolution of an alkali sulfate activated slag cement.* Journal of Nuclear Materials, 2016. **468**: p. 97-104.

64. Akturk, B., et al., *Microstructure and Strength Development of Sodium Carbonate–Activated Blast Furnace Slags.* Journal of Materials in Civil Engineering, 2019. **31**(11): p. 04019283.

65. Steinhauser, G., *Cleaner production in the Solvay Process: general strategies and recent developments.* Journal of Cleaner Production, 2008. **16**(7): p. 833-841.

66. Rashad, A., et al., *Hydration and properties of sodium sulfate activated slag.* Cement and concrete composites, 2013. **37**: p. 20-29.

67. Clark, B. and P. Brown, *The formation of calcium sulfoaluminate hydrate compounds: Part II.* Cement and Concrete Research, 2000. **30**(2): p. 233-240.

68. Ke, X., et al., *Slag-based cements that resist damage induced by carbon dioxide.* ACS Sustainable Chemistry & Engineering, 2018. **6**(4): p. 5067-5075.

69. Ke, X., et al., *Chloride binding and mobility in sodium carbonate-activated slag pastes and mortars.* Materials and Structures, 2017. **50**(6): p. 252.

70. Gao, X., et al., *Calcium carbide residue as auxiliary activator for one-part sodium carbonate-activated slag cements: compressive strength, phase assemblage and environmental benefits.* Construction and Building Materials, 2021. **308**: p. 125015.

71. Abdalqader, A.F., F. Jin, and A. Al-Tabbaa, *Development of greener alkali-activated cement: utilisation of sodium carbonate for activating slag and fly ash mixtures.* Journal of Cleaner Production, 2016. **113**: p. 66-75.

72. Bernal, S.A., et al., *Role of carbonates in the chemical evolution of sodium carbonate-activated slag binders.* Materials and Structures, 2015. **48**: p. 517-529.

73. Yuan, B., Q. Yu, and H. Brouwers, *Assessing the chemical involvement of limestone powder in sodium carbonate activated slag.* Materials and Structures, 2017. **50**: p. 1-14.

74. Bernal, S.A., et al., *Role of carbonates in the chemical evolution of sodium carbonate-activated slag binders.* Materials and Structures, 2015. **48**(3): p. 517-529.

75. Ke, X., et al., *Chloride binding and mobility in sodium carbonate-activated slag pastes and mortars.* Materials and Structures, 2017. **50**(6): p. 1-13.

76. Ke, X., et al., *Thermodynamic modelling of phase evolution in alkali-activated slag cements exposed to carbon dioxide.* Cement and Concrete Research, 2020. **136**: p. 106158.

77. Mobasher, N., et al., *Characterisation of $Ba(OH)_2$–Na_2SO_4–blast furnace slag cement-like composites for the immobilisation of sulfate bearing nuclear wastes.* Cement and Concrete Research, 2014. **66**: p. 64-74.

78. Bai, Y., et al., *The potential for using slags activated with near neutral salts as immobilisation matrices for nuclear wastes containing reactive metals.* Journal of Nuclear Materials, 2011. **413**(3): p. 183-192.

79. Shi, C. and A. Fernández-Jiménez, *Stabilization/solidification of hazardous and radioactive wastes with alkali-activated cements.* Journal of Hazardous Materials, 2006. **137**(3): p. 1656-1663.

80. Douglas, E. and J. Brandstetr, *A preliminary study on the alkali activation of ground granulated blast-furnace slag.* Cement and concrete research, 1990. **20**(5): p. 746-756.

81. Wang, S.-D., K.L. Scrivener, and P. Pratt, *Factors affecting the strength of alkali-activated slag.* Cement and concrete research, 1994. **24**(6): p. 1033-1043.

82. Xu, H., et al., *Characterization of aged slag concretes.* ACI Materials Journal, 2008. **105**(2): p. 131.

83. Provis, J.L., et al., *Historical aspects and overview*, in *Alkali activated materials*. 2014, Springer. p. 11-57.

84. Marsh, A.T., et al., *Influence of limestone addition on sodium sulphate activated blast furnace slag cements.* Construction and Building Materials, 2022. **360**: p. 129527.

85. Rashad, A., et al., *Chemical and mechanical stability of sodium sulfate activated slag after exposure to elevated temperature.* Cement and Concrete Research, 2012. **42**(2): p. 333-343.

86. Tan, H., et al., *Compressive strength and hydration process of wet-grinded granulated blast-furnace slag activated by sodium sulfate and sodium carbonate.* Cement and Concrete Composites, 2019. **97**: p. 387-398.

87. Rashad, A.M., *Influence of different additives on the properties of sodium sulfate activated slag.* Construction and Building Materials, 2015. **79**: p. 379-389.

88. Oey, T., et al., *The filler effect: the influence of filler content and surface area on cementitious reaction rates.* Journal of the American Ceramic Society, 2013. **96**(6): p. 1978-1990.

89. Dhandapani, Y., et al., *Towards ternary binders involving limestone additions—A review.* Cement and Concrete Research, 2021. **143**: p. 106396.

90. Gruskovnjak, A., et al., *Hydration mechanisms of super sulphated slag cement.* Cement and Concrete Research, 2008. **38**(7): p. 983-992.

91. Avet, F., et al., *Development of a new rapid, relevant and reliable (R^3) test method to evaluate the pozzolanic reactivity of calcined kaolinitic clays.* Cement and Concrete Research, 2016. **85**: p. 1-11.

92. C1897-20, A., *Standard Test Methods for Measuring the Reactivity of Supplementary Cementitious Materials by Isothermal Calorimetry and Bound Water Measurements*. 2020, ASTM C. p. 5.

93. Adesina, A. and C.R. Kaze, *Physico-mechanical and microstructural properties of sodium sulfate activated materials: A review.* Construction and Building Materials, 2021. **295**: p. 123668.

94. Kucharczyk, S., et al., *Structure and reactivity of synthetic CaO-Al_2O_3-SiO_2 glasses.* Cement and Concrete Research, 2019. **120**: p. 77-91.

95. Bernard, E., et al., *Stability of hydrotalcite (Mg-Al layered double hydroxide) in presence of different anions.* Cement and Concrete Research, 2022. **152**: p. 106674.

96. He, J., et al., *Effect of reactive MgO on hydration and properties of alkali-activated slag pastes with different activators.* Construction and Building Materials, 2021. **271**: p. 121608.

97. Zheng, W., et al., *Investigation of effects of reactive MgO on autogenous and drying shrinkage of near-neutral salt activated slag cement.* Ceramics International, 2022. **48**(4): p. 5518-5526.

98. Yuan, B., Q. Yu, and H. Brouwers, *Phase modification induced drying shrinkage reduction on Na_2CO_3 activated slag by incorporating Na_2SO_4.* Materials and Structures, 2017. **50**: p. 1-11.

99. Etcheverry, J.M., et al., *Phase Evolution of Hybrid Alkali Sulfate-Activated Ground-Granulated Blast Furnace Slag Cements.* ACS Sustainable Chemistry & Engineering, 2023. **11**(49): p. 17519-17531.

100. Wu, M., et al., *Effects of sodium sulfate on the hydration and properties of lime-based low carbon cementitious materials.* Journal of Cleaner Production, 2019. **220**: p. 677-687.

101. Joseph, S., R. Snellings, and Ö. Cizer, *Activation of Portland cement blended with high volume of fly ash using Na2SO4.* Cement and Concrete Composites, 2019. **104**: p. 103417.

102. Valencia-Saavedra, W., R. Robayo-Salazar, and R. Mejía de Gutiérrez, *Alkali-Activated Hybrid Cements Based on Fly Ash and Construction and Demolition Wastes Using Sodium Sulfate and Sodium Carbonate.* Molecules, 2021. **26**(24): p. 7572.

103. von Greve-Dierfeld, S., et al., *Understanding the carbonation of concrete with supplementary cementitious materials: a critical review by RILEM TC 281-CCC.* Materials and Structures, 2020. **53**(6): p. 1-34.

104. Qiu, Q., *A state-of-the-art review on the carbonation process in cementitious materials: Fundamentals and characterization techniques.* Construction and Building Materials, 2020. **247**: p. 118503.

105. Ye, H., R. Cai, and Z. Tian, *Natural carbonation-induced phase and molecular evolution of alkali-activated slag: Effect of activator composition and curing temperature.* Construction and Building Materials, 2020. **248**: p. 118726.

106. Shi, Z., et al., *Experimental studies and thermodynamic modeling of the carbonation of Portland cement, metakaolin and limestone mortars.* Cement and Concrete Research, 2016. **88**: p. 60-72.

107. Hargis, C.W., et al., *Carbonation of calcium sulfoaluminate mortars.* Cement and Concrete Composites, 2017. **80**: p. 123-134.

108. Lothenbach, B., et al., *Cemdata18: A chemical thermodynamic database for hydrated Portland cements and alkali-activated materials.* Cement and Concrete Research, 2019. **115**: p. 472-506.

109. Navrotsky, A. and Z.R. Tian, *Systematics in the enthalpies of formation of anhydrous aluminosilicate zeolites, glasses, and dense phases.* Chemistry - A European Journal, 2001. **7**(4): p. 769-774.

110. Ke, X. and Y. Duan, *Coupling machine learning with thermodynamic modelling to develop a composition-property model for alkali-activated materials.* Composites Part B: Engineering, 2021. **216**: p. 108801.

111. Ma, B. and B. Lothenbach, *Synthesis, characterization, and thermodynamic study of selected K-based zeolites.* Cement and Concrete Research, 2021. **148**: p. 106537.

112. Ma, B. and B. Lothenbach, *Synthesis, characterization, and thermodynamic study of selected Na-based zeolites.* Cement and Concrete Research, 2020. **135**: p. 106111.

113. Cundy, C.S. and P.A. Cox, *The hydrothermal synthesis of zeolites: Precursors, intermediates and reaction mechanism.* Microporous and mesoporous materials, 2005. **82**(1-2): p. 1-78.

114. Shah, V., et al., *Changes in microstructure characteristics of cement paste on carbonation.* Cement and Concrete Research, 2018. **109**: p. 184-197.

115. Sevelsted, T.F. and J. Skibsted, *Carbonation of C–S–H and C–A–S–H samples studied by ^{13}C, ^{27}Al and ^{29}Si MAS NMR spectroscopy.* Cement and Concrete Research, 2015. **71**: p. 56-65.

116. Groves, G., D. Rodway, and I. Richardson, *The carbonation of hardened cement pastes.* Advances in Cement Research, 1990. **3**(11): p. 117-125.

117. Chen, J.J., J.J. Thomas, and H.M. Jennings, *Decalcification shrinkage of cement paste.* Cement and concrete research, 2006. **36**(5): p. 801-809.

118. Swenson, E.G. and P.J. Sereda, *Mechanism of the carbonatation shrinkage of lime and hydrated cement.* Journal of Applied Chemistry, 1968. **18**(4): p. 111-117.

119. Zhang, D., Z. Ghouleh, and Y. Shao, *Review on carbonation curing of cement-based materials.* Journal of CO2 Utilization, 2017. **21**: p. 119-131.

120. Provis, J.L. and J.S. Van Deventer, *Alkali activated materials: state-of-the-art report, RILEM TC 224-AAM*. Vol. 13. 2013: Springer Science & Business Media.

121. Myers, R.J., et al., *Thermodynamic modelling of alkali-activated slag cements.* Applied Geochemistry, 2015. **61**: p. 233-247.

122. Myers, R.J., S.A. Bernal, and J.L. Provis, *Phase diagrams for alkali-activated slag binders.* Cement and Concrete Research, 2017. **95**: p. 30-38.

123. Ben Haha, M., et al., *Influence of activator type on hydration kinetics, hydrate assemblage and microstructural development of alkali activated blast-furnace slags.* Cement and Concrete Research, 2011. **41**(3): p. 301-310.

124. Walkley, B., et al., *Activator anion influences the nanostructure of alkali-activated slag cements.* The Journal of Physical Chemistry C, 2021. **125**(37): p. 20727-20739.

125. Bernal, S.A., *Effect of the activator dose on the compressive strength and accelerated carbonation resistance of alkali silicate-activated slag/metakaolin blended materials.* Construction and building materials, 2015. **98**: p. 217-226.

126. Puertas, F., M. Palacios, and T. Vázquez, *Carbonation process of alkali-activated slag mortars.* Journal of materials science, 2006. **41**(10): p. 3071-3082.

127. Law, D.W., et al., *Durability assessment of alkali activated slag (AAS) concrete.* Materials and Structures, 2012. **45**(9): p. 1425-1437.

128. Bakharev, T., J. Sanjayan, and Y.-B. Cheng, *Resistance of alkali-activated slag concrete to carbonation.* Cement and Concrete Research, 2001. **31**(9): p. 1277-1283.

129. Papadakis, V.G., C.G. Vayenas, and M.N. Fardis, *Experimental investigation and mathematical modeling of the concrete carbonation problem.* Chemical Engineering Science, 1991. **46**(5): p. 1333-1338.

130. Papadakis, V.G., C.G. Vayenas, and M.N. Fardis, *Fundamental modeling and experimental investigation of concrete carbonation.* Materials Journal, 1991. **88**(4): p. 363-373.

131. Yue, Z., et al. *Influence of Slag Chemistry on the Carbonation of Sodium Sulfate-Activated Slag Cements*. in *International RILEM Conference on Synergising Expertise towards Sustainability and Robustness of Cement-based Materials and Concrete Structure*. 2023. International RILEM Conference on Synergising Expertise towards Sustainability and Robustness of Cement-based Materials and Concrete Structure, Milos, Greece Springer Nature Switzerland.

132. Auroy, M., et al., *Comparison between natural and accelerated carbonation (3% CO_2): Impact on mineralogy, microstructure, water retention and cracking.* Cement and Concrete Research, 2018. **109**: p. 64-80.

133. Gluth, G.J., et al., *RILEM TC 247-DTA round robin test: carbonation and chloride penetration testing of alkali-activated concretes.* Materials and Structures, 2020. **53**: p. 1-17.

134. Palacios, M. and F. Puertas, *Effect of carbonation on alkali‐activated slag paste.* Journal of the American Ceramic Society, 2006. **89**(10): p. 3211-3221.

135. Shi, Z., et al., *Effect of alkali dosage and silicate modulus on carbonation of alkali-activated slag mortars.* Cement and Concrete Research, 2018. **113**: p. 55-64.

136. Bernal, S.A., et al., *MgO content of slag controls phase evolution and structural changes induced by accelerated carbonation in alkali-activated binders.* Cement and Concrete Research, 2014. **57**: p. 33-43.

137. Bernal, S.A., et al., *Gel nanostructure in alkali-activated binders based on slag and fly ash, and effects of accelerated carbonation.* Cement and Concrete Research, 2013. **53**: p. 127-144.

138. Bernal, S.A., et al., *Accelerated carbonation testing of alkali-activated binders significantly underestimates service life: The role of pore solution chemistry.* Cement and Concrete Research, 2012. **42**(10): p. 1317-1326.

139. Ye, H. and A. Radlińska, *Carbonation-induced volume change in alkali-activated slag.* Construction and building materials, 2017. **144**: p. 635-644.

140. Ma, J., et al., *Effects of layered double hydroxides incorporation on carbonation resistance of cementitious materials.* Journal of Materials Research and Technology, 2019. **8**(1): p. 292-298.

141. Shui, Z.H., et al., *Improvement of concrete carbonation resistance based on a structure modified Layered Double Hydroxides (LDHs): Experiments and mechanism analysis.* Construction and Building Materials, 2018. **176**: p. 228-240.

142. Duan, P., C. Yan, and W. Zhou, *Effects of calcined layered double hydroxides on carbonation of concrete containing fly ash.* Construction and Building Materials, 2018. **160**: p. 725-732.

143. Duan, P., et al., *Influence of layered double hydroxides on microstructure and carbonation resistance of sulphoaluminate cement concrete.* Construction and Building Materials, 2013. **48**: p. 601-609.

144. Shi, P., H. He, and G.C. Marano, *Improving the carbonation performance of sulfate-activated material cured waste sediments by calcined Mg-Al hydrotalcite: Influence of CLDH dosages, carbonation concentrations and cycles.* Construction and Building Materials, 2024. **421**: p. 135604.

145. Nedeljković, M., et al., *Carbonation resistance of alkali-activated slag under natural and accelerated conditions.* Journal of Sustainable Metallurgy, 2018. **4**(1): p. 33-49.

146. Rashad, A.M., *Additives to Increase Carbonation Resistance of Slag Activated with Sodium Sulfate.* ACI Materials Journal, 2022. **119**(2).

147. Rashad, A.M. and Y. Bai, *Effect of Slag Fineness and Na_2SO_4 Concentration on Carbonation of Na 2 SO 4-Activated Slag.* ACI Materials Journal, 2023. **120**(1).

148. Burkan Isgor, O. and A.G. Razaqpur, *Finite element modeling of coupled heat transfer, moisture transport and carbonation processes in concrete structures.* Cement and Concrete Composites, 2004. **26**(1): p. 57-73.

149. Xiao, R., et al., *Analytical investigation of phase assemblages of alkali-activated materials in CaO-SiO2-Al2O3 systems: The management of reaction products and designing of precursors.* Materials & Design, 2020. **194**: p. 108975.

150. Chang, C.-F. and J.-W. Chen, *The experimental investigation of concrete carbonation depth.* Cement and Concrete research, 2006. **36**(9): p. 1760-1767.

151. Papadakis, V.G., M. Fardis, and C.G. Vayenas, *Effect of composition, environmental factors and cement-lime mortar coating on concrete carbonation.* Materials and structures, 1992. **25**: p. 293-304.

152. Morandeau, A., M. Thiéry, and P. Dangla, *Investigation of the carbonation mechanism of CH and C-S-H in terms of kinetics, microstructure changes and moisture properties.* Cement and Concrete Research, 2014. **56**: p. 153-170.

153. Phung, Q.T., et al., *Modelling the carbonation of cement pastes under a CO_2 pressure gradient considering both diffusive and convective transport.* Construction and Building Materials, 2016. **114**: p. 333-351.

154. Boumaaza, M., et al., *Influence of carbonation on the microstructure and the gas diffusivity of hardened cement pastes.* Construction and Building Materials, 2020. **253**: p. 119227.

155. Li, N., N. Farzadnia, and C. Shi, *Microstructural changes in alkali-activated slag mortars induced by accelerated carbonation.* Cement and Concrete Research, 2017. **100**: p. 214-226.

156. Dewaele, P., E. Reardon, and R. Dayal, *Permeability and porosity changes associated with cement grout carbonation.* Cement and concrete research, 1991. **21**(4): p. 441-454.

157. Leemann, A. and F. Moro, *Carbonation of concrete: the role of CO 2 concentration, relative humidity and CO 2 buffer capacity.* Materials and Structures, 2017. **50**: p. 1-14.

158. Steiner, S., et al., *Effect of relative humidity on the carbonation rate of portlandite, calcium silicate hydrates and ettringite.* Cement and Concrete Research, 2020. **135**: p. 106116.

159. Liu, Z., et al., *Carbonation of blast furnace slag concrete at different CO2 concentrations: Carbonation rate, phase assemblage, microstructure and thermodynamic modelling.* Cement and Concrete Research, 2023. **169**: p. 107161.

160. Yue, Z., et al. *Influence of Slag Chemistry on the Carbonation of Sodium Sulfate-Activated Slag Cements*. in *International RILEM Conference on Synergising expertise towards sustainability and robustness of CBMs and concrete structures*. 2023. Springer.

161. Park, S., et al., *Thermodynamic Modeling and Experimental Study of Carbonation of Alkali-Activated Slag Cements.* ACS Sustainable Chemistry & Engineering, 2023. **11**(10): p. 4049-4063.

162. Ekolu, S., *A review on effects of curing, sheltering, and CO_2 concentration upon natural carbonation of concrete.* Construction and Building Materials, 2016. **127**: p. 306-320.

163. Sisomphon, K. and L. Franke, *Carbonation rates of concretes containing high volume of pozzolanic materials.* Cement and Concrete Research, 2007. **37**(12): p. 1647-1653.

164. Papadakis, V.G., C.G. Vayenas, and M.N. Fardis, *Experimental investigation and mathematical modeling of the concrete carbonation problem.* Chemical Engineering Science, 1991. **46**(5-6): p. 1333-1338.

165. Vanoutrive, H., et al., *Carbonation of cement paste with GGBFS: Effect of curing duration, replacement level and CO_2 concentration on the reaction products and CO_2 buffer capacity.* Cement and Concrete Composites, 2022. **129**: p. 104449.

166. Van den Heede, P., M. De Schepper, and N. De Belie, *Accelerated and natural carbonation of concrete with high volumes of fly ash: chemical, mineralogical and microstructural effects.* Royal Society open science, 2019. **6**(1): p. 181665.

167. Pouhet, R. and M. Cyr, *Carbonation in the pore solution of metakaolin-based geopolymer.* Cement and Concrete Research, 2016. **88**: p. 227-235.

168. Gluth, G.J., et al., *Carbonation rate of alkali-activated concretes and high-volume SCM concretes: a literature data analysis by RILEM TC 281-CCC.* Materials and structures, 2022. **55**(8): p. 225.

169. McCaslin, E.R. and C.E. White, *A parametric study of accelerated carbonation in alkali-activated slag.* Cement and Concrete Research, 2021. **145**: p. 106454.

170. Nedeljković, M., et al., *Carbonation resistance of alkali-activated slag under natural and accelerated conditions.* Journal of Sustainable Metallurgy, 2018. **4**: p. 33-49.

171. Thomas, J.J., et al., *Modeling and simulation of cement hydration kinetics and microstructure development.* Cement and concrete research, 2011. **41**(12): p. 1257-1278.

172. Xie, T. and J.J. Biernacki, *The origins and evolution of cement hydration models.* Computers and Concrete, 2011. **8**(6): p. 647-675.

173. Lothenbach, B. and F. Winnefeld, *Thermodynamic modelling of the hydration of Portland cement.* Cement and Concrete Research, 2006. **36**(2): p. 209-226.

174. Fernández-Jiménez, A. and F. Puertas, *Alkali-activated slag cements: kinetic studies.* Cement and concrete research, 1997. **27**(3): p. 359-368.

175. Provis, J.L., *On the use of the Jander equation in cement hydration modelling.* RILEM Technical Letters, 2016. **1**: p. 62-66.

176. Caron, R., R.A. Patel, and F. Dehn, *Activation kinetic model and mechanisms for alkali-activated slag cements.* Construction and Building Materials, 2022. **323**: p. 126577.

177. Bernal, S., X. Ke, and J. Provis. *Activation of slags using near-neutral salts: The importance of slag chemistry*. in *The 14th International Congress on Chemistry of Cement. Beijing, China*. 2015.

178. Garboczi, E.J., *Permeability, diffusivity, and microstructural parameters: a critical review.* Cement and concrete research, 1990. **20**(4): p. 591-601.

179. Konecny, L. and S. Naqvi, *The effect of different drying techniques on the pore size distribution of blended cement mortars.* Cement and concrete research, 1993. **23**(5): p. 1223-1228.

180. Zhang, J. and G.W. Scherer, *Comparison of methods for arresting hydration of cement.* Cement and Concrete Research, 2011. **41**(10): p. 1024-1036.

181. Zhang, Z. and G. Scherer, *Determination of water permeability for a moisture transport model with minimized batch effect.* Construction and Building Materials, 2018. **191**: p. 193-205.

182. Phung, Q.T., et al., *Determination of water permeability of cementitious materials using a controlled constant flow method.* Construction and Building Materials, 2013. **47**: p. 1488-1496.

183. Nguyen, T.N., et al., *Microstructure, water permeability and micromechanical properties of alkali activated slag subjected to accelerated leaching.* Materials & Design, 2024. **238**: p. 112706.

184. Xie, J., et al., *Estimation of chloride diffusion coefficient from water permeability test of cementitious materials.* Construction and Building Materials, 2022. **340**: p. 127816.

185. Zhang, Z., M. Thiery, and V. Baroghel-Bouny, *Investigation of moisture transport properties of cementitious materials.* Cement and Concrete Research, 2016. **89**: p. 257-268.

186. Zhang, M., *Pore-scale modelling of relative permeability of cementitious materials using X-ray computed microtomography images.* Cement and Concrete Research, 2017. **95**: p. 18-29.

187. Xiong, Q.X., et al., *A new analytical method to predict permeability properties of cementitious mortars: the impacts of pore structure evolutions and relative humidity variations.* Cement and Concrete Composites, 2023. **137**: p. 104912.

188. Wong, H., N. Buenfeld, and M. Head, *Estimating transport properties of mortars using image analysis on backscattered electron images.* Cement and Concrete Research, 2006. **36**(8): p. 1556-1566.

189. Garboczi, E. and D. Bentz, *Computer simulation of the diffusivity of cement-based materials.* Journal of materials science, 1992. **27**: p. 2083-2092.

190. Zhang, M., G. Ye, and K. van Breugel, *Multiscale lattice Boltzmann-finite element modelling of chloride diffusivity in cementitious materials. Part I: Algorithms and implementation.* Mechanics Research Communications, 2014. **58**: p. 53-63.

191. Zhang, M., G. Ye, and K. van Breugel, *Multiscale lattice Boltzmann-finite element modelling of chloride diffusivity in cementitious materials. Part II: Simulation results and validation.* Mechanics Research Communications, 2014. **58**: p. 64-72.

192. Sleiman, H.C., et al., *From tomographic imaging to numerical simulations: an open-source workflow for true morphology mesoscale FE meshes.* RILEM Technical Letters, 2023. **8**: p. 158-164.

193. You, X., et al., *A review on the modelling of carbonation of hardened and fresh cement-based materials.* Cement and Concrete Composites, 2022. **125**: p. 104315.

194. Tongaria, K., S. Mandal, and D. Mohan, *A Review on Carbonation of Concrete and its Predictive Modelling.* J. Environ. Nanotechnol, 2018. **7**(4): p. 75-90.

195. Kulik, D.A., et al., *GEM-Selektor geochemical modeling package: revised algorithm and GEMS3K numerical kernel for coupled simulation codes.* Computational Geosciences, 2013. **17**: p. 1-24.

196. Samson, E. and J. Marchand, *Modeling the transport of ions in unsaturated cement-based materials.* Computers & Structures, 2007. **85**(23-24): p. 1740-1756.

197. Sander, R., *Compilation of Henry's law constants (version 4.0) for water as solvent.* Atmospheric Chemistry and Physics, 2015. **15**(8): p. 4399-4981.

198. Isgor, O.B. and W.J. Weiss, *A nearly self-sufficient framework for modelling reactive-transport processes in concrete.* Materials and Structures, 2019. **52**(1): p. 1-17.

199. Azad, V.J., et al., *A COMSOL–GEMS interface for modeling coupled reactive-transport geochemical processes.* Computers & Geosciences, 2016. **92**: p. 79-89.

200. Skibsted, J. and R. Snellings, *Reactivity of supplementary cementitious materials (SCMs) in cement blends.* Cement and Concrete Research, 2019. **124**: p. 105799.

201. Scrivener, K.L., et al., *TC 238-SCM: hydration and microstructure of concrete with SCMs: State of the art on methods to determine degree of reaction of SCMs.* Materials and Structures, 2015. **48**: p. 835-862.

202. Georget, F., J.H. Prévost, and B. Huet, *A reactive transport simulator for variable porosity problems.* Computational Geosciences, 2017. **21**: p. 95-116.

203. Georget, F., J.H. Prévost, and B. Huet, *Impact of the microstructure model on coupled simulation of drying and accelerated carbonation.* Cement and concrete research, 2018. **104**: p. 1-12.

204. Huet, B.M., J.H. Prevost, and G.W. Scherer, *Quantitative reactive transport modeling of Portland cement in CO_2-saturated water.* International Journal of Greenhouse Gas Control, 2010. **4**(3): p. 561-574.

205. Ichikawa, T., K. Haga, and K. Yamada, *Extraction of Carbonation Rate from Depth Profile of Concrete Carbonation by using Pseudo-analytical Solution of Two-component Reaction-diffusion Equation.* Journal of Advanced Concrete Technology, 2024. **22**(3): p. 139-148.

206. Jeong, J., H. Ramézani, and E. Chuta, *Reactive transport numerical modeling of mortar carbonation: atmospheric and accelerated carbonation.* Journal of Building Engineering, 2019. **23**: p. 351-368.

207. Seigneur, N., et al., *Predicting the atmospheric carbonation of cementitious materials using fully coupled two-phase reactive transport modelling.* Cement and Concrete Research, 2020. **130**: p. 105966.

208. Seigneur, N., et al., *Recoupling flow and chemistry in variably saturated reactive transport modelling - An algorithm to accurately couple the feedback of chemistry on water consumption, variable porosity and flow.* Advances in Water Resources, 2018. **122**: p. 355-366.

209. Xie, M., P. Dangla, and K. Li, *Reactive transport modelling of concurrent chloride ingress and carbonation in concrete.* Materials and Structures, 2021. **54**(5): p. 177.

210. Shen, J., P. Dangla, and M. Thiery, *Reactive transport modeling of CO_2 through cementitious materials under CO2 geological storage conditions.* International Journal of Greenhouse Gas Control, 2013. **18**: p. 75-87.

211. Kari, O.-P., J. Puttonen, and E. Skantz, *Reactive transport modelling of long-term carbonation.* Cement and Concrete Composites, 2014. **52**: p. 42-53.

212. Patel, R.A., S.V. Churakov, and N.I. Prasianakis, *A multi-level pore scale reactive transport model for the investigation of combined leaching and carbonation of cement paste.* Cement and Concrete Composites, 2021. **115**: p. 103831.

213. Michel, A., et al., *Microstructural changes and mass transport in cement-based materials: A modeling approach.* Cement and Concrete Research, 2021. **139**: p. 106285.

214. Herman, G.T., *X-ray-computed tomography—basic principles*, in *Three-dimensional biomedical imaging*. 2017, CRC Press. p. 61-80.

215. Withers, P.J., et al., *X-ray computed tomography.* Nature Reviews Methods Primers, 2021. **1**(1): p. 18.

216. Rockett, P. and G. Wang, *The principles of X-ray computed tomography.* ABOUT THE EDITOR, 2009: p. 267.

217. Kak, A.C. and M. Slaney, *Principles of computerized tomographic imaging*. 2001: SIAM.

218. Schofield, R., et al., *Image reconstruction: Part 1–understanding filtered back projection, noise and image acquisition.* Journal of cardiovascular computed tomography, 2020. **14**(3): p. 219-225.

219. Gordon, R., R. Bender, and G.T. Herman, *Algebraic reconstruction techniques (ART) for three-dimensional electron microscopy and X-ray photography.* Journal of theoretical Biology, 1970. **29**(3): p. 471-481.

220. Willemink, M.J. and P.B. Noël, *The evolution of image reconstruction for CT—from filtered back projection to artificial intelligence.* European radiology, 2019. **29**: p. 2185-2195.

221. Pan, X., E.Y. Sidky, and M. Vannier, *Why do commercial CT scanners still employ traditional, filtered back-projection for image reconstruction?* Inverse problems, 2009. **25**(12): p. 123009.

222. Koetzier, L.R., et al., *Deep learning image reconstruction for CT: technical principles and clinical prospects.* Radiology, 2023. **306**(3): p. e221257.

223. Song, Y., et al., *Characterizing porous volume of cement-based concrete by multiscale image analysis.* Journal of Materials in Civil Engineering, 2020. **32**(9): p. 04020267.

224. Liu, C. and M. Zhang, *Multiscale modelling of ionic diffusivity in unsaturated concrete accounting for its hierarchical microstructure.* Cement and Concrete Research, 2022. **156**: p. 106766.

225. McDonald, P.J., et al., *Sorption, anomalous water transport and dynamic porosity in cement paste: A spatially localised 1H NMR relaxation study and a proposed mechanism.* Cement and Concrete Research, 2020. **133**: p. 106045.

226. Samson, E., et al., *Modeling ion and fluid transport in unsaturated cement systems in isothermal conditions.* Cement and Concrete Research, 2005. **35**(1): p. 141-153.

227. Auroy, M., et al., *Impact of carbonation on unsaturated water transport properties of cement-based materials.* Cement and concrete research, 2015. **74**: p. 44-58.

228. Bakharev, T., J.G. Sanjayan, and Y.-B. Cheng, *Sulfate attack on alkali-activated slag concrete.* Cement and Concrete Research, 2002. **32**(2): p. 211-216.

229. Chen, Z. and H. Ye, *Understanding the impact of main seawater ions and leaching on the chloride transport in alkali-activated slag and Portland cement.* Cement and Concrete Research, 2023. **164**: p. 107063.

230. Shi, J., M. Wu, and J. Ming, *Long-term corrosion resistance of reinforcing steel in alkali-activated slag mortar after exposure to marine environments.* Corrosion Science, 2021. **179**: p. 109175.

231. Juenger, M.C.G. and H.M. Jennings, *The use of nitrogen adsorption to assess the microstructure of cement paste.* Cement and Concrete Research, 2001. **31**(6): p. 883-892.

232. Kumar, R. and B. Bhattacharjee, *Study on some factors affecting the results in the use of MIP method in concrete research.* Cement and Concrete Research, 2003. **33**(3): p. 417-424.

233. Muller, A.C.A., *Characterization of porosity & CSH in cement pastes by ^{1}H NMR*. 2014, Epfl.

234. Baral, A., et al., *Characterisation of iron-rich cementitious materials.* Cement and Concrete Research, 2024. **177**: p. 107419.

235. Brisard, S., M. Serdar, and P.J. Monteiro, *Multiscale X-ray tomography of cementitious materials: A review.* Cement and Concrete Research, 2020. **128**: p. 105824.

236. Xu, K., et al., *Microstructure and water absorption of ancient concrete from Pompeii: An integrated synchrotron microtomography and neutron radiography characterization.* Cement and Concrete Research, 2021. **139**: p. 106282.

237. Chae, S.R., et al., *Advanced nanoscale characterization of cement based materials using X-ray synchrotron radiation: a review.* International Journal of Concrete Structures and Materials, 2013. **7**: p. 95-110.

238. Fang, G., Q. Wang, and M. Zhang, *In-situ X-ray tomographic imaging of microstructure evolution of fly ash and slag particles in alkali-activated fly ash-slag paste.* Composites Part B: Engineering, 2021. **224**: p. 109221.

239. Promentilla, M.A.B., et al., *Quantification of tortuosity in hardened cement pastes using synchrotron-based X-ray computed microtomography.* Cement and Concrete Research, 2009. **39**(6): p. 548-557.

240. Bushberg, J.T. and J.M. Boone, *The essential physics of medical imaging*. 2011: Lippincott Williams & Wilkins.

241. Gervaise, A., et al., *CT image quality improvement using adaptive iterative dose reduction with wide-volume acquisition on 320-detector CT.* European radiology, 2012. **22**: p. 295-301.

242. Seo, D., et al., *Spatial resolution of synchrotron X-ray microtomography in high energy range: Effect of X-ray energy and sample-to-detector distance.* Applied physics letters, 2012. **101**(26).

243. Mindess, S., F. Young, and D. Darwin, *Concrete 2nd Edition.* Technical Documents, 2003. **585**.

244. Lloyd, R.R., et al., *Spatial distribution of pores in fly ash-based inorganic polymer gels visualised by Wood's metal intrusion.* Microporous and Mesoporous Materials, 2009. **126**(1-2): p. 32-39.

245. Wenzel, O., et al., *Investigating the pore structure of the calcium silicate hydrate phase.* Materials Characterization, 2017. **133**: p. 133-137.

246. Kjellsen, K., et al., *Preparation of flat-polished specimens for SEM-backscattered electron imaging and X-ray microanalysis—importance of epoxy impregnation.* Cement and Concrete Research, 2003. **33**(4): p. 611-616.

247. Mayo, S.C., A.W. Stevenson, and S.W. Wilkins, *In-line phase-contrast X-ray imaging and tomography for materials science.* Materials, 2012. **5**(5): p. 937-965.

248. Shirani, S., et al., *4D nanoimaging of early age cement hydration.* Nature Communications, 2023. **14**(1): p. 2652.

249. Provis, J.L., et al., *Hard X-ray nanotomography of amorphous aluminosilicate cements.* Scripta Materialia, 2011. **65**(4): p. 316-319.

250. Harding, G., J. Kosanetzky, and U. Neitzel, *X-ray diffraction computed tomography.* Medical physics, 1987. **14**(4): p. 515-525.

251. Vamvakeros, A., et al., *5D operando tomographic diffraction imaging of a catalyst bed.* Nature Communications, 2018. **9**(1): p. 4751.

252. Artioli, G., et al., *Direct imaging of nucleation mechanisms by synchrotron diffraction micro-tomography: superplasticizer-induced change of C–S–H nucleation in cement.* Crystal Growth & Design, 2015. **15**(1): p. 20-23.

253. Voltolini, M., et al., *Understanding cement hydration at the microscale: new opportunities frompencil-beam'synchrotron X-ray diffraction tomography.* Journal of Applied Crystallography, 2013. **46**(1): p. 142-152.

254. Artioli, G., et al., *X-ray diffraction microtomography (XRD-CT), a novel tool for non-invasive mapping of phase development in cement materials.* Analytical and Bioanalytical Chemistry, 2010. **397**: p. 2131-2136.

255. Claret, F., et al., *Deciphering mineralogical changes and carbonation development during hydration and ageing of a consolidated ternary blended cement paste.* IUCrJ, 2018. **5**(2): p. 150-157.

256. Bernal, S.A., et al. *Factors controlling carbonation resistance of alkali-activated materials*. in *Special Publication 320: Proceedings of the 10th ACI/RILEM International Conference on Cementitious Materials and Alternative Binders for Sustainable Concrete*. 2017. American Concrete Institute.

257. Park, S., et al., *Thermodynamic Modeling and Experimental Study of Carbonation of Alkali-Activated Slag Cements.* ACS Sustainable Chemistry & Engineering, 2022.

258. Bernal, S.A., et al., *Characterization of supplementary cementitious materials by thermal analysis.* Materials and Structures, 2017. **50**(1): p. 1-13.

259. Zhu, X., et al., *Using GGBS: Clarification of the Importance of Relative Humidity at Storage on Reactivity of GGBS.* Journal of Advanced Concrete Technology, 2022. **20**(11): p. 663-675.

260. Montes-Morán, M.A., et al., *Linz-Donawitz steel slag for the removal of hydrogen sulfide at room temperature.* Environmental science & technology, 2012. **46**(16): p. 8992-8997.

261. Krumgalz, B., *Temperature dependence of mineral solubility in water. Part 3. Alkaline and alkaline earth sulfates.* Journal of Physical and Chemical Reference Data, 2018. **47**(2).

262. EN, B., *196-1: 2005.* Methods of testing cement-Part, 2005. **1**: p. 196-1.

263. Londono-Zuluaga, D., et al., *Report of RILEM TC 267-TRM phase 3: validation of the R3 reactivity test across a wide range of materials.* Materials and structures, 2022. **55**(5): p. 142.

264. Zogg, A., et al., *Isothermal reaction calorimetry as a tool for kinetic analysis.* Thermochimica acta, 2004. **419**(1-2): p. 1-17.

265. Khoshnazar, R., et al., *Solvent exchange in sulphoaluminate phases. Part I: ettringite.* Advances in Cement Research, 2013. **25**(6): p. 314-321.

266. Zhang, Z. and G.W. Scherer, *Physical and chemical effects of isopropanol exchange in cement-based materials.* Cement and Concrete Research, 2021. **145**: p. 106461.

267. Jauncey, G., *The scattering of x-rays and Bragg's law.* Proceedings of the national academy of sciences, 1924. **10**(2): p. 57-60.

268. Materazzi, S., *Mass Spectrometry Coupled to Thermogravimetry (TG-MS) for Evolved Gas Characterization: A Review.* Applied Spectroscopy Reviews, 1998. **33**(3): p. 189-218.

269. Bernal Lopez, S., et al. *Effect of testing condition on the loss on ignition results of anhydrous granulated blast furnace slags determined via thermogravimetry*. in *Segment on Concrete with Supplementary Cementitious Materials*. 2016. RILEM Publications SARL.

270. Günther, H., *NMR spectroscopy: basic principles, concepts and applications in chemistry*. 2013: John Wiley & Sons.

271. Giraudeau, P., et al., *Reference and normalization methods: Essential tools for the intercomparison of NMR spectra.* Journal of pharmaceutical and biomedical analysis, 2014. **93**: p. 3-16.

272. Kannan, M., *Scanning electron microscopy: Principle, components and applications.* A textbook on fundamentals and applications of nanotechnology, 2018: p. 81-92.

273. Scrivener, K., et al., *A practical guide to microstructural analysis of cementitious materials*. Vol. 540. 2016: Crc Press Boca Raton, FL, USA:.

274. Abd Mutalib, M., et al., *Scanning electron microscopy (SEM) and energy-dispersive X-ray (EDX) spectroscopy*, in *Membrane characterization*. 2017, Elsevier. p. 161-179.

275. Promentilla, M.A.B., et al., *Characterizing the 3D pore structure of hardened cement paste with synchrotron microtomography.* Journal of Advanced Concrete Technology, 2008. **6**(2): p. 273-286.

276. Schindelin, J., et al., *Fiji: an open-source platform for biological-image analysis.* Nature methods, 2012. **9**(7): p. 676-682.

277. Surdo, A.L., E.M. Alzola, and F.J. Millero, *The (p, V, T) properties of concentrated aqueous electrolytes I. Densities and apparent molar volumes of NaCl, Na_2SO_4, $MgCl_2$, and $MgSO_4$ solutions from 0.1 mol· kg− 1 to saturation and from 273.15 to 323.15 K.* The Journal of Chemical Thermodynamics, 1982. **14**(7): p. 649-662.

278. Berthomieu, C. and R. Hienerwadel, *Fourier transform infrared (FTIR) spectroscopy.* Photosynthesis research, 2009. **101**: p. 157-170.

279. Grdadolnik, J., *ATR-FTIR spectroscopy: Its advantage and limitations.* Acta Chimica Slovenica, 2002. **49**(3): p. 631-642.

280. Higl, J., et al., *Detailed in situ ATR-FTIR spectroscopy study of the early stages of CSH formation during hydration of monoclinic C3S.* Cement and Concrete Research, 2021. **142**: p. 106367.

281. Wagner, T., et al., *GEM-Selektor geochemical modeling package: TSolMod library and data interface for multicomponent phase models.* The Canadian Mineralogist, 2012. **50**(5): p. 1173-1195.

282. Lothenbach, B., *Thermodynamic equilibrium calculations in cementitious systems.* Materials and Structures, 2010. **43**(10): p. 1413-1433.

283. Mundra, S., et al., *Modelling chloride transport in alkali-activated slags.* Cement and Concrete Research, 2020. **130**: p. 106011.

284. Prentice, D.P., et al., *The effects of (di-, tri-valent)-cation partitioning and intercalant anion-type on the solubility of hydrotalcites.* Journal of the American Ceramic Society, 2020. **103**(10): p. 6025-6039.

285. Myers, R.J., S.A. Bernal, and J.L. Provis, *A thermodynamic model for C-(N-)A-S-H gel: CNASH_ss. Derivation and validation.* Cement and Concrete Research, 2014. **66**: p. 27-47.

286. Ma, B. and B. Lothenbach, *Thermodynamic study of cement/rock interactions using experimentally generated solubility data of zeolites.* Cement and Concrete Research, 2020. **135**: p. 106149.

287. Hansen, P.F. and O.M. Jensen, *The science of construction materials*. 2009: Springer.

288. Vaughan, G.B.M., et al., *ID15A at the ESRF - a beamline for high speed operando X-ray diffraction, diffraction tomography and total scattering.* Journal of Synchrotron Radiation, 2020. **27**(2): p. 515-528.

289. Erb, M.P., et al., *Reconstructing Holocene temperatures in time and space using paleoclimate data assimilation.* Climate of the Past, 2022. **18**(12): p. 2599-2629.

290. Kieffer, J. and D. Karkoulis, *PyFAI, a versatile library for azimuthal regrouping.* Journal of Physics: Conference Series, 2013. **425**(20): p. 202012.

291. Valentini, L., et al., *Towards three-dimensional quantitative reconstruction of cement microstructure by X-ray diffraction microtomography.* Journal of Applied Crystallography, 2011. **44**(2): p. 272-280.

292. Garboczi, E.J. and D.P. Bentz, *The effect of statistical fluctuation, finite size error, and digital resolution on the phase percolation and transport properties of the NIST cement hydration model.* Cement and Concrete Research, 2001. **31**(10): p. 1501-1514.

293. Yang, Z., et al., *In-situ X-ray computed tomography characterisation of 3D fracture evolution and image-based numerical homogenisation of concrete.* Cement and Concrete Composites, 2017. **75**: p. 74-83.

294. Zelelew, H. and A. Papagiannakis, *A volumetrics thresholding algorithm for processing asphalt concrete X-ray CT images.* International Journal of Pavement Engineering, 2011. **12**(6): p. 543-551.

295. Van Eijnatten, M., et al., *CT image segmentation methods for bone used in medical additive manufacturing.* Medical Engineering & Physics, 2018. **51**: p. 6-16.

296. Carlson, W.D., *Three-dimensional imaging of earth and planetary materials.* Earth and Planetary Science Letters, 2006. **249**(3-4): p. 133-147.

297. Arganda-Carreras, I., et al., *Trainable Weka Segmentation: a machine learning tool for microscopy pixel classification.* Bioinformatics, 2017. **33**(15): p. 2424-2426.

298. Bulgarevich, D.S., et al., *Pattern recognition with machine learning on optical microscopy images of typical metallurgical microstructures.* Scientific Reports, 2018. **8**(1): p. 2078.

299. Villagrán-Zaccardi, Y.A., et al., *Recommendation of RILEM TC 238-SCM: determination of the degree of reaction of siliceous fly ash and slag in hydrated cement paste by the selective dissolution method.* Materials and Structures, 2018. **51**: p. 1-5.

300. Kocaba, V., E. Gallucci, and K.L. Scrivener, *Methods for determination of degree of reaction of slag in blended cement pastes.* Cement and Concrete Research, 2012. **42**(3): p. 511-525.

301. Richardson, I., et al., *The characterization of hardened alkali-activated blast-furnace slag pastes and the nature of the calcium silicate hydrate (CSH) phase.* Cement and Concrete Research, 1994. **24**(5): p. 813-829.

302. Taylor, R., I. Richardson, and R. Brydson, *Composition and microstructure of 20-year-old ordinary Portland cement–ground granulated blast-furnace slag blends containing 0 to 100% slag.* Cement and Concrete Research, 2010. **40**(7): p. 971-983.

303. Münch, B. and L. Holzer, *Contradicting geometrical concepts in pore size analysis attained with electron microscopy and mercury intrusion.* Journal of the American Ceramic Society, 2008. **91**(12): p. 4059-4067.

304. Shen, L. and Z. Chen, *Critical review of the impact of tortuosity on diffusion.* Chemical Engineering Science, 2007. **62**(14): p. 3748-3755.

305. Nakashima, Y. and S. Kamiya, *Mathematica programs for the analysis of three-dimensional pore connectivity and anisotropic tortuosity of porous rocks using X-ray computed tomography image data.* Journal of Nuclear Science and Technology, 2007. **44**(9): p. 1233-1247.

306. Tjaden, B., D.J. Brett, and P.R. Shearing, *Tortuosity in electrochemical devices: a review of calculation approaches.* International Materials Reviews, 2018. **63**(2): p. 47-67.

307. Tranter, T.G., et al., *pytrax: A simple and efficient random walk implementation for calculating the directional tortuosity of images.* SoftwareX, 2019. **10**: p. 100277.

308. WATANABE, Y. and Y. NAKASHIMA, *Two-dimensional random walk program for the calculation of the tortuosity of porous media.* Journal of Groundwater Hydrology, 2001. **43**(1): p. 13-22.

309. Glover, P.W., M.J. Hole, and J. Pous, *A modified Archie's law for two conducting phases.* Earth and Planetary Science Letters, 2000. **180**(3-4): p. 369-383.

310. Worthington, P.F., *The uses and abuses of the Archie equations, 1: The formation factor-porosity relationship.* Journal of Applied Geophysics, 1993. **30**(3): p. 215-228.

311. Chen, M., et al., *Effective pressure law for the intrinsic formation factor in low permeability sandstones.* Journal of Geophysical Research: Solid Earth, 2017. **122**(11): p. 8709-8723.

312. Richardson, I. and G. Groves, *Microstructure and microanalysis of hardened cement pastes involving ground granulated blast-furnace slag.* Journal of Materials Science, 1992. **27**: p. 6204-6212.

313. Taylor, H.F., *Cement chemistry*. Vol. 2. 1997: Thomas Telford London.

314. Damidot, D. and F. Glasser, *Thermodynamic investigation of the CaO-Al_2O_3-$CaSO_4$-H_2O system at 25 ℃ and the influence of Na_2O.* Cement and concrete research, 1993. **23**(1): p. 221-238.

315. Schilling, P.J., et al., *^{29}Si and ^{27}Al MAS-NMR of NaOH-activated blast-furnace slag.* Journal of the American Ceramic Society, 1994. **77**(9): p. 2363-2368.

316. Walkley, B. and J.L. Provis, *Solid-state nuclear magnetic resonance spectroscopy of cements.* Materials Today Advances, 2019. **1**: p. 100007.

317. Skibsted, J., E. Henderson, and H. Jakobsen, *Characterization of calcium aluminate phases in cements by aluminum-27 MAS NMR spectroscopy.* Inorganic Chemistry, 1993. **32**(6): p. 1013-1027.

318. MacKenzie, K.J., et al., *^{27}Al and ^{25}Mg solid-state magic-angle spinning nuclear magnetic resonance study of hydrotalcite and its thermal decomposition sequence.* Journal of Materials Chemistry, 1993. **3**(12): p. 1263-1269.

319. Rocha, J., et al., *Reconstruction of layered double hydroxides from calcined precursors: a powder XRD and ^{27}Al MAS NMR study.* Journal of Materials Chemistry, 1999. **9**(10): p. 2499-2503.

320. Dai, Z., T.T. Tran, and J. Skibsted, *Aluminum Incorporation in the C–S–H phase of white Portland cement–metakaolin blends studied by ^{27}Al and ^{29}Si MAS NMR spectroscopy.* Journal of the American Ceramic Society, 2014. **97**(8): p. 2662-2671.

321. Andersen, M.D., H.J. Jakobsen, and J. Skibsted, *Incorporation of aluminum in the calcium silicate hydrate (C−S-H) of hydrated Portland cements: A high-field ^{27}Al and ^{29}Si MAS NMR investigation.* Inorganic Chemistry, 2003. **42**(7): p. 2280-2287.

322. Kunhi Mohamed, A., et al., *The atomic-level structure of cementitious calcium aluminate silicate hydrate.* Journal of the American Chemical Society, 2020. **142**(25): p. 11060-11071.

323. L'Hôpital, E., et al., *Alkali uptake in calcium alumina silicate hydrate (C-A-S-H).* Cement and Concrete Research, 2016. **85**: p. 122-136.

324. Hall, C., et al., *Thermal decomposition of ettringite $Ca_6[Al(OH)_6]_2(SO_4)_3 \cdot 26H_2O$.* Journal of the Chemical Society, Faraday Transactions, 1996. **92**(12): p. 2125-2129.

325. Scrivener, K.L., *Backscattered electron imaging of cementitious microstructures: understanding and quantification.* Cement and concrete Composites, 2004. **26**(8): p. 935-945.

326. Zunino, F. and K. Scrivener, *Microstructural developments of limestone calcined clay cement (LC3) pastes after long-term (3 years) hydration.* Cement and Concrete Research, 2022. **153**: p. 106693.

327. Yu, Z. and G. Ye, *The pore structure of cement paste blended with fly ash.* Construction and Building Materials, 2013. **45**: p. 30-35.

328. Wu, B. and G. Ye, *Development of porosity of cement paste blended with supplementary cementitious materials after carbonation.* Construction and Building Materials, 2017. **145**: p. 52-61.

329. Zhu, X. and I.G. Richardson, *Morphology-structural change of CASH gel in blended cements.* Cement and Concrete Research, 2023. **168**: p. 107156.

330. Reuter, W. *The ionization function and its application to the electron probe analysis of thin films*. in *Proceedings of the sixth International Conference on X-ray Optics and Microanalysis*. 1972. University of Tokyo Press.

331. San Nicolas, R., et al., *Distinctive microstructural features of aged sodium silicate-activated slag concretes.* Cement and Concrete Research, 2014. **65**: p. 41-51.

332. Jia, Z., et al., *The characteristics and formation mechanism of the dark rim in alkali-activated slag.* Cement and Concrete Composites, 2020. **112**: p. 103682.

333. Xu, Z., et al., *Insight into ion exchange behavior of LDHs: Asynchronous chloride adsorption and intercalated ions release processes.* Cement and Concrete Composites, 2024. **147**: p. 105433.

334. Bharadwaj, K., et al., *Predicting pore volume, compressive strength, pore connectivity, and formation factor in cementitious pastes containing fly ash.* Cement and Concrete Composites, 2021. **122**: p. 104113.

335. Matschei, T., B. Lothenbach, and F.P. Glasser, *Thermodynamic properties of Portland cement hydrates in the system $CaO–Al_2O_3–SiO_2–CaSO_4–CaCO_3–H_2O$.* Cement and Concrete Research, 2007. **37**(10): p. 1379-1410.

336. Roy, A., et al., *Activation of ground blast-furnace slag by alkali-metal and alkaline-Earth hydroxides.* Journal of the American Ceramic Society, 1992. **75**(12): p. 3233-3240.

337. Walkley, B. and J. Provis, *Solid-state nuclear magnetic resonance spectroscopy of cements.* Materials Today Advances, 2019. **1**: p. 100007.

338. Rinaldi, R., M. Sacerdoti, and E. Passaglia, *Strätlingite: Crystal structure, chemistry, and a reexamination of its polytpye vertumnite.* European Journal of Mineralogy, 1990: p. 841-850.

339. Myers, R.J., J.L. Provis, and B. Lothenbach, *Composition–solubility–structure relationships in calcium (alkali) aluminosilicate hydrate (C-(N, K-) ASH).* Dalton Transactions, 2015. **44**(30): p. 13530-13544.

340. Walkley, B., et al., *Nanostructure of CaO-(Na_2O)-Al_2O_3-SiO_2-H_2O gels revealed by multinuclear solid-state magic angle spinning and multiple quantum magic angle spinning nuclear magnetic resonance spectroscopy.* The Journal of Physical Chemistry C, 2019. **124**(2): p. 1681-1694.

341. Lothenbach, B. and A. Gruskovnjak, *Hydration of alkali-activated slag: thermodynamic modelling.* Advances in cement research, 2007. **19**(2): p. 81-92.

342. Fu, J., et al., *Mechanisms of enhancement in early hydration by sodium sulfate in a slag-cement blend–Insights from pore solution chemistry.* Cement and Concrete Research, 2020. **135**: p. 106110.

343. Le Cornec, D., et al., *Structural role of titanium on slag properties.* Journal of the American Ceramic Society, 2021. **104**(1): p. 105-113.

344. Wang, P., et al., *Influence of the TiO_2 content on the reactivity of granulated blastfurnace slags.* Cem Int, 2002. **1**(1): p. 120-128.

345. Blotevogel, S., et al., *Effect of TiO_2 and 11 minor elements on the reactivity of ground-granulated blast-furnace slag in blended cements.* Journal of the American Ceramic Society, 2021. **104**(1): p. 128-139.

346. Stumm, W., *Aquatic chemistry.* Introduction Emphasizing Chemical Equilibria in Natural Waters, 1981.

347. EN13295, B., *Products and systems for the protection and repair of concrete structures—Test methods—Determination of resistance to carbonation.* National Standards Authority of Ireland, Dublin, 2004.

348. Institute., T.B.S., *BSI 1881-210:2013 Testing hardened concrete. Determination of the potential 1042 carbonation resistance of concrete. Accelerated carbonation method.* 2013.

349. Cui, D., W. Sun, and N. Banthia, *Use of tomography to understand the influence of preconditioning on carbonation tests in cement-based materials.* Cement and Concrete Composites, 2018. **88**: p. 52-63.

350. Nishikawa, T., et al., *Decomposition of synthesized ettringite by carbonation.* Cement and Concrete Research, 1992. **22**(1): p. 6-14.

351. Zhang, Y., et al., *The influence of relative humidity on the heterogeneous oxidation of sulfur dioxide by ozone on calcium carbonate particles.* Science of the Total Environment, 2018. **633**: p. 1253-1262.

352. Galan, I., C. Andrade, and M. Castellote, *Natural and accelerated CO2 binding kinetics in cement paste at different relative humidities.* Cement and Concrete Research, 2013. **49**: p. 21-28.

353. Fernández-Díaz, L., Á. Fernández-González, and M. Prieto, *The role of sulfate groups in controlling CaCO3 polymorphism.* Geochimica et Cosmochimica Acta, 2010. **74**(21): p. 6064-6076.

354. Sato, M. and S. Matsuda, *Structure of vaterite and infrared spectra.* Zeitschrift für Kristallographie, 1969. **129**(5-6): p. 405-410.

355. Zhang, Z., et al., *Transformation of amorphous calcium carbonate into aragonite.* Journal of Crystal Growth, 2012. **343**(1): p. 62-67.

356. Andersen, F.A., et al., *Infrared spectra of amorphous and crystalline calcium carbonate.* Acta Chem. Scand, 1991. **45**(10): p. 1018-1024.

357. Herterich, J., et al., *Microstructure and phase assemblage of low-clinker cements during the early stages of carbonation.* Cement and Concrete Research, 2022. **152**: p. 106643.

358. García-Lodeiro, I., et al., *Effect of alkalis on fresh C–S–H gels. FTIR analysis.* Cement and Concrete Research, 2009. **39**: p. 147-153.

359. Yu, P., et al., *Structure of calcium silicate hydrate (C-S-H): Near-, Mid-, and Far-infrared spectroscopy.* Journal of the American Ceramic Society, 1999. **82**(3): p. 742-748.

360. Durdziński, P.T., *Hydration of multi-component cements containing cement clinker, slag, calcareous fly ash and limestone*. 2016, EPFL.

361. Scrivener, K., R. Snellings, and B. Lothenbach, *A practical guide to microstructural analysis of cementitious materials*. 2018: Crc Press.

362. Di Bella, C., M. Wyrzykowski, and P. Lura, *Evaluation of the ultimate drying shrinkage of cement-based mortars with poroelastic models.* Materials and Structures, 2017. **50**: p. 1-13.

363. Ye, H. and A. Radlińska, *Shrinkage mechanisms of alkali-activated slag.* Cement and Concrete Research, 2016. **88**: p. 126-135.

364. De Weerdt, K., et al., *Effect of carbonation on the pore solution of mortar.* Cement and Concrete Research, 2019. **118**: p. 38-56.

365. Dhandapani, Y., et al. *Elucidating the carbonation front in blended calcined kaolinite clays binders using different analytical techniques*. 2023. ICCC.

366. Hossain, M.S. and S. Ahmed, *Synthesis of nano-crystallite gypsum and bassanite from waste Pila globosa shells: crystallographic characterization.* RSC advances, 2022. **12**(38): p. 25096-25105.

367. Association, P.C., *Ettringite formation and the performance of concrete*. 2001: Portland Cement Association.

368. Georget, F., W. Soja, and K.L. Scrivener, *Characteristic lengths of the carbonation front in naturally carbonated cement pastes: Implications for reactive transport models.* Cement and Concrete Research, 2020. **134**: p. 106080.

369. Åhs, M., *Redistribution of moisture and ions in cement based materials*. Vol. 1028. 2011: Lund University.

370. Le Cornec, D., et al., *Greening effect in slag cement materials.* Cement and Concrete Composites, 2017. **84**: p. 93-98.

371. Park, S., *Simulating the carbonation of calcium sulfoaluminate cement blended with supplementary cementitious materials.* Journal of CO_2 Utilization, 2020. **41**: p. 101286.

372. Raiswell, R., *Woods, TL and Garrels, RM Thermodynamic Values at Low Temperature for Natural Inorganic Materials: an uncritical summary. New York and Oxford (Oxford University Press), 1987, xvi+ 266 pp. Price s.*

373. Lothenbach, B., *Thermodynamic equilibrium calculations in cementitious systems.* Materials and Structures, 2010. **43**: p. 1413-1433.

374. Chermak, J.A. and J.D. Rimstidt, *Estimating the thermodynamic properties (ΔGf_0 and ΔHf_0) of silicate minerals at 298 K from the sum of polyhedral contributions.* American Mineralogist, 1989. **74**(9-10): p. 1023-1031.

375. Cundy, C.S. and P.A. Cox, *The hydrothermal synthesis of zeolites: Precursors, intermediates and reaction mechanism.* Microporous and Mesoporous Materials, 2005. **82**(1): p. 1-78.

376. Tasevski, D., M.F. Ruiz, and A. Muttoni, *Compressive strength and deformation capacity of concrete under sustained loading and low stress rates.* Journal of Advanced Concrete Technology, 2018. **16**(8): p. 396-415.

377. Chi, M.-c., J.-j. Chang, and R. Huang, *Strength and drying shrinkage of alkali-activated slag paste and mortar.* Advances in Civil Engineering, 2012. **2012**.

378. Li, Z., J. Liu, and G. Ye, *Drying shrinkage of alkali-activated slag and fly ash concrete; A comparative study with ordinary Portland cement concrete.* Heron, 2019. **64**(1/2): p. 01-15.

379. Snellings, R., *Surface chemistry of calcium aluminosilicate glasses.* Journal of the American Ceramic Society, 2015. **98**(1): p. 303-314.

380. Addis, B.J. and M.G. Alexander, *Cement-Saturation and its effects on the compressive strength and stiffness of concrete.* Cement and concrete research, 1994. **24**(5): p. 975-986.

381. Yu, B., et al., *Carbonation of supersulfated cement concrete after 8 years of natural exposure.* Cement and Concrete Composites, 2023: p. 105165.

382. Yin, J., et al., *Irreversible microstructural changes of calcium silicate hydrate during the first drying-resaturation cycle.* Cement and Concrete Research, 2023. **163**: p. 107032.

383. Thomas, J.J., A.J. Allen, and H.M. Jennings, *Structural changes to the calcium–silicate–hydrate gel phase of hydrated cement with age, drying, and resaturation.* Journal of the American Ceramic Society, 2008. **91**(10): p. 3362-3369.

384. Grounds, T., H. Midgley, and D. Novell, *Carbonation of ettringite by atmospheric carbon dioxide.* Thermochimica Acta, 1988. **135**: p. 347-352.

385. Fahami, A. and G.W. Beall, *Mechanosynthesis and characterization of Hydrotalcite like Mg–Al–SO_4-LDH.* Materials Letters, 2016. **165**: p. 192-195.

386. Duxson, P. and J.L. Provis, *Designing Precursors for Geopolymer Cements.* Journal of the American Ceramic Society, 2008. **91**(12): p. 3864-3869.

387. Ahmad, J., et al., *A comprehensive review on the ground granulated blast furnace slag (GGBS) in concrete production.* Sustainability, 2022. **14**(14): p. 8783.

388. Lloyd, R.R., J.L. Provis, and J.S. Van Deventer, *Microscopy and microanalysis of inorganic polymer cements. 2: The gel binder.* Journal of Materials Science, 2009. **44**: p. 620-631.

389. Bernal, S.A., R.M. de Gutiérrez, and J.L. Provis, *Engineering and durability properties of concretes based on alkali-activated granulated blast furnace slag/metakaolin blends.* Construction and Building Materials, 2012. **33**: p. 99-108.

390. Bentz, D.P. and E.J. Garboczi, *Percolation of phases in a three-dimensional cement paste microstructural model.* Cement and Concrete Research, 1991. **21**(2-3): p. 325-344.

391. Sallehi, H., P. Ghods, and O.B. Isgor, *Formation factor of fresh cementitious pastes.* Cement and Concrete Composites, 2018. **91**: p. 174-188.

392. Holzer, L., et al., *Tortuosity and microstructure effects in porous media: classical theories, empirical data and modern methods*. 2023: Springer Nature.

393. Zhu, X., et al., *Characterisation of temporal variations of alkali-activated slag cement property using microstructure features and electrical responses.* Construction and Building Materials, 2020. **261**: p. 119884.

394. Darwish, M. and F. Moukalled, *The finite volume method in computational fluid dynamics: an advanced introduction with OpenFOAM® and Matlab®*. 2016: Springer.

395. Vigor, J.E., et al., *Automated correction for the movement of suspended particulate in microtomographic data.* Chemical Engineering Science, 2020. **223**: p. 115736.

396. Davis, G.R. and J.C. Elliott, *Artefacts in X-ray microtomography of materials.* Materials Science and Technology, 2006. **22**(9): p. 1011-1018.

397. Tumidajski, P., et al., *On the relationship between porosity and electrical resistivity in cementitious systems.* Cement and Concrete Research, 1996. **26**(4): p. 539-544.

398. Bu, Y. and J. Weiss, *The influence of alkali content on the electrical resistivity and transport properties of cementitious materials.* Cement and Concrete Composites, 2014. **51**: p. 49-58.

399. Bajja, Z., et al., *The validity of the formation factor concept from through-out diffusion tests on Portland cement mortars.* Cement and Concrete Composites, 2015. **63**: p. 76-83.

400. Ma, H., D. Hou, and Z. Li, *Two-scale modeling of transport properties of cement paste: Formation factor, electrical conductivity and chloride diffusivity.* Computational Materials Science, 2015. **110**: p. 270-280.

401. Christensen, B.J., et al., *Impedance spectroscopy of hydrating cement -based materials: measurement, interpretation, and application.* Journal of the American Ceramic Society, 1994. **77**(11): p. 2789-2804.

402. Atkins Jr, E. and G.H. Smith, *The significance of particle shape in formation resistivity factor-porosity relationships.* Journal of Petroleum Technology, 1961. **13**(03): p. 285-291.

403. Zixian Su, Z.Y., Alastair T.M. Marsh, Timothy L. Burnett, Susan A. Bernal, Philip J. Withers *Characterization of Pore Structure Evolutions in Alkali Activated Slag Cements Using Time-lapsed In-situ X-ray Computed Tomography and Scanning Electron Microscopy*. in *42nd Annual Cement & Concrete Science Conference*. 11-12 September, 2023. Civil and Environmental Engineering Department, Imperial College London: Institute of Materials, Minerals & Mining.

404. Morandeau, A., M. Thiéry, and P. Dangla, *Impact of accelerated carbonation on OPC cement paste blended with fly ash.* Cement and Concrete Research, 2015. **67**: p. 226-236.

405. Shah, V. and S. Bishnoi, *Analysis of pore structure characteristics of carbonated low-clinker cements.* Transport in Porous Media, 2018. **124**: p. 861-881.

406. Spragg, R., et al., *Factors that Influence Electrical Resistivity Measurements in Cementitious Systems.* Transportation Research Record, 2013. **2342**(1): p. 90-98.

407. Zhang, M., et al., *Improving the carbonation resistance of alkali-activated slag mortars by calcined Mg/Al layered double hydroxides.* Applied Clay Science, 2022. **216**: p. 106379.

408. Xu, R., et al., *Improving the carbonation resistance of alkali-activated slag mortars with different additives: experimental evaluations.* Construction and Building Materials, 2023. **366**: p. 130197.

409. Zuo, Y., *Effect of chloride salt on the phase evolution in alkali-activated slag cements through thermodynamic modelling.* Applied Geochemistry, 2022. **136**: p. 105169.

410. Liu, T., Q. Yu, and H. Brouwers, *In-situ formation of layered double hydroxides (LDHs) in sodium aluminate activated slag: The role of Al-O tetrahedra.* Cement and Concrete Research, 2022. **153**: p. 106697.

411. Ginstling, A. and B. Brounshtein, *Concerning the diffusion kinetics of reactions in spherical particles.* J. appl. chem. USSR, 1950. **23**(12): p. 1327-1338.

412. Gajjar, P., et al., *3D characterisation of dry powder inhaler formulations: Developing X-ray micro computed tomography approaches.* European Journal of Pharmaceutics and Biopharmaceutics, 2020. **151**: p. 32-44.

413. Luo, S., et al. *An improved moment-preserving auto threshold image segmentation algorithm*. in *International Conference on Information Acquisition, 2004. Proceedings.* 2004. IEEE.

414. Lumley, J., et al., *Degrees of reaction of the slag in some blends with Portland cements.* Cement and concrete research, 1996. **26**(1): p. 139-151.

415. Christensen, A.N., T.R. Jensen, and J.C. Hanson, *Formation of ettringite, $Ca_6Al_2(SO_4)_3(OH)_{12}\cdot 26H_2O$, AFt, and monosulfate, $Ca_4Al_2O_6(SO_4)\cdot 14H_2O$, AFm-14, in hydrothermal hydration of Portland cement and of calcium aluminum oxide—calcium sulfate dihydrate mixtures studied by in situ synchrotron X-ray powder diffraction.* Journal of solid state chemistry, 2004. **177**(6): p. 1944-1951.

416. Gavryushkin, P.N., et al., *Metastable structures of $CaCO_3$ and their role in transformation of calcite to aragonite and postaragonite.* Crystal Growth & Design, 2020. **21**(1): p. 65-74.

417. Sinha, P., *Multivariate polynomial regression in data mining: methodology, problems and solutions.* Int. J. Sci. Eng. Res, 2013. **4**(12): p. 962-965.

418. Xu, J., et al., *Prediction of triaxial behavior of recycled aggregate concrete using multivariable regression and artificial neural network techniques.* Construction and Building Materials, 2019. **226**: p. 534-554.

419. He, T., et al., *Carbonation modeling analysis on carbonation behavior of sand autoclaved aerated concrete.* Construction and Building Materials, 2018. **189**: p. 102-108.

420. Ta, V.-L., et al., *A new meta-model to calculate carbonation front depth within concrete structures.* Construction and Building Materials, 2016. **129**: p. 172-181.

421. Enick, R.M. and S.M. Klara, *CO_2 solubility in water and brine under reservoir conditions.* Chemical Engineering Communications, 1990. **90**(1): p. 23-33.

422. Teng, H. and A. Yamasaki, *Mass transfer of CO_2 through liquid CO_2–water interface.* International journal of heat and mass transfer, 1998. **41**(24): p. 4315-4325.

423. Weissberg, H.L., *Effective diffusion coefficient in porous media.* Journal of Applied Physics, 1963. **34**(9): p. 2636-2639.

424. Millington, R. and J. Quirk, *Permeability of porous media.* Nature, 1959. **183**(4658): p. 387-388.

425. Li, T., et al., *Measurement of the instantaneous velocity of a Brownian particle.* Science, 2010. **328**(5986): p. 1673-1675.

426. Robinson, R.A. and R.H. Stokes, *Electrolyte solutions*. 2002: Courier Corporation.

427. Zeebe, R.E., *On the molecular diffusion coefficients of dissolved CO_2, HCO_3^-, and $CO3^{2-}$and their dependence on isotopic mass.* Geochimica et Cosmochimica Acta, 2011. **75**(9): p. 2483-2498.

428. Nielsen, E.P. and M.R. Geiker, *Chloride diffusion in partially saturated cementitious material.* Cement and Concrete Research, 2003. **33**(1): p. 133-138.

429. Namoulniara, K., P. Turcry, and A. Aït-Mokhtar, *Measurement of CO_2 effective diffusion coefficient of cementitious materials.* European Journal of Environmental and Civil Engineering, 2016. **20**(10): p. 1183-1196.

430. Kumarappa, D.B., S. Peethamparan, and M. Ngami, *Autogenous shrinkage of alkali activated slag mortars: Basic mechanisms and mitigation methods.* Cement and Concrete Research, 2018. **109**: p. 1-9.

431. Carmeliet, J. and S. Roels, *Determination of the isothermal moisture transport properties of porous building materials.* Journal of Thermal Envelope and Building Science, 2001. **24**(3): p. 183-210.

432. Fisher, L. and J. Israelachvili, *Direct experimental verification of the Kelvin equation for capillary condensation.* Nature, 1979. **277**(5697): p. 548-549.

433. Babaee, M. and A. Castel, *Water vapor sorption isotherms, pore structure, and moisture transport characteristics of alkali-activated and Portland cement-based binders.* Cement and Concrete Research, 2018. **113**: p. 99-120.

434. El-Dieb, A. and R. Hooton, *Evaluation of the Katz-Thompson model for estimating the water permeability of cement-based materials from mercury intrusion porosimetry data.* Cement and Concrete Research, 1994. **24**(3): p. 443-455.

435. Johnson, D.L., J. Koplik, and L.M. Schwartz, *New pore-size parameter characterizing transport in porous media.* Physical review letters, 1986. **57**(20): p. 2564.

436. Ma, J., et al., *Real-time skeletonization for sketch-based modeling.* Computers & Graphics, 2022. **102**: p. 56-66.

437. Li, K., et al., *Water permeability of unsaturated cementitious materials: A review.* Construction and Building Materials, 2021. **302**: p. 124168.

438. Mualem, Y., *A new model for predicting the hydraulic conductivity of unsaturated porous media.* Water resources research, 1976. **12**(3): p. 513-522.

439. Van Genuchten, M.T., *A closed - form equation for predicting the hydraulic conductivity of unsaturated soils.* Soil science society of America journal, 1980. **44**(5): p. 892-898.

440. Lenhard, R. and J. Parker, *A model for hysteretic constitutive relations governing multiphase flow: 2. Permeability - saturation relations.* Water Resources Research, 1987. **23**(12): p. 2197-2206.

441. Shi, J., et al., *Experimental study on gas permeability of cement-based materials.* Cement and Concrete Composites, 2022. **129**: p. 104491.

442. Zamani, S., R. Kowalczyk, and P. McDonald, *The relative humidity dependence of the permeability of cement paste measured using GARField NMR profiling.* Cement and concrete research, 2014. **57**: p. 88-94.

443. Kameche, Z., et al., *Assessment of liquid water and gas permeabilities of partially saturated ordinary concrete.* Construction and Building Materials, 2014. **65**: p. 551-565.

444. Bernal S.A., D.Y., Elakneswaran Y., Gluth G.J.G., Gruyaert E., Juenger M.C.G., Lothenbach B., Olonade K.A., Sakoparnig M., Shi Z., Thiel C., Van den Heede P., Vanoutrive H., von Greve-Dierfeld S., De Belie N., Provis J.L. , *Report of RILEM TC 281-CCC - A critical review of the standardised testing methods to determine carbonation resistance of concrete (submitted).* Materials and Structures, 2024.

445. Elsalamawy, M., A.R. Mohamed, and E.M. Kamal, *The role of relative humidity and cement type on carbonation resistance of concrete.* Alexandria Engineering Journal, 2019. **58**(4): p. 1257-1264.

446. Liu, P., Z. Yu, and Y. Chen, *Carbonation depth model and carbonated acceleration rate of concrete under different environment.* Cement and Concrete Composites, 2020. **114**: p. 103736.

447. Ishida, T., K. Maekawa, and T. Kishi, *Enhanced modeling of moisture equilibrium and transport in cementitious materials under arbitrary temperature and relative humidity history.* Cement and concrete research, 2007. **37**(4): p. 565-578.

448. Van den Heede, P. and N. De Belie, *Environmental impact and life cycle assessment (LCA) of traditional and 'green'concretes: Literature review and theoretical calculations.* Cement and concrete composites, 2012. **34**(4): p. 431-442.

449. Richardson, I.G., et al., *The characterization of hardened alkali-activated blast-furnace slag pastes and the nature of the calcium silicate hydrate (C-S-H) phase.* Cement and Concrete Research, 1994. **24**(5): p. 813-829.

450. Dyson, H.M., I.G. Richardson, and A.R. Brough, *A Combined 29Si MAS NMR and Selective Dissolution Technique for the Quantitative Evaluation of Hydrated Blast Furnace Slag Cement Blends.* Journal of the American Ceramic Society, 2007. **90**(2): p. 598-602.

451. Younsi, A., P. Turcry, and A. Aït-Mokhtar, *Quantification of CO_2 uptake of concretes with mineral additions after 10-year natural carbonation.* Journal of Cleaner Production, 2022. **349**: p. 131362.

452. McBain, J.W., *LXXXV.—The use of phenolphthalein as an indicator. The slow rate of neutralisation of carbonic acid.* Journal of the Chemical Society, Transactions, 1912. **101**: p. 814-820.

453. Tian, Z., C. Fu, and H. Ye, *How does carbonation of alkali-activated slag and Portland cement systems impact steel corrosion differently?* Cement and Concrete Research, 2024. **181**: p. 107528.

454. Khan, M., A. Castel, and A. Noushini, *Carbonation of a low-calcium fly ash geopolymer concrete.* Magazine of Concrete Research, 2017. **69**(1): p. 24-34.

455. Pasupathy, K., et al., *Carbonation of a blended slag-fly ash geopolymer concrete in field conditions after 8years.* Construction and Building Materials, 2016. **125**: p. 661-669.

456. Lollini, F. and E. Redaelli, *Carbonation of blended cement concretes after 12 years of natural exposure.* Construction and Building Materials, 2021. **276**: p. 122122.

457. Kolani, B., et al., *Hydration of slag-blended cements.* Cement and concrete composites, 2012. **34**(9): p. 1009-1018.

458. Dodson, V.H., *Pozzolans and the pozzolanic reaction*, in *Concrete admixtures*. 1990, Springer. p. 159-201.

459. Paul, M. and F. Glasser, *Impact of prolonged warm (85 °C) moist cure on Portland cement paste.* Cement and Concrete Research, 2000. **30**(12): p. 1869-1877.

460. Le Saout, G., et al., *Chemical structure of cement aged at normal and elevated temperatures and pressures: Part I. Class G oilwell cement.* Cement and concrete research, 2006. **36**(1): p. 71-78.

461. Dilnesa, B., et al., *Fe-containing phases in hydrated cements.* Cement and Concrete Research, 2014. **58**: p. 45-55.

462. Damidot, D. and F. Glasser, *Investigation of the CaO-Al_2O_3-SiO_2-H_2O system at 25 °C by thermodynamic calculations.* Cement and Concrete Research, 1995. **25**(1): p. 22-28.

463. Ding, J., Y. Fu, and J. Beaudoin, *Strätlingite formation in high alumina cement-silica fume systems: significance of sodium ions.* Cement and Concrete Research, 1995. **25**(6): p. 1311-1319.

464. Winnefeld, F. and B. Lothenbach, *Hydration of calcium sulfoaluminate cements—Experimental findings and thermodynamic modelling.* Cement and Concrete Research, 2010. **40**(8): p. 1239-1247.

465. Dai, X., et al., *Fresh and hardened state properties, reaction kinetics and microstructure of sodium sulfate/sodium hydroxide – Activated slag mixtures.* Construction and Building Materials, 2023. **401**: p. 132943.

466. Fu, J., et al., *A microstructural investigation of a Na_2SO_4 activated cement-slag blend.* Cement and Concrete Research, 2021. **150**: p. 106609.

467. Yu, S., et al., *Study on hydration process of alkali-activated slag cement activated by weakly alkaline components.* Construction and Building Materials, 2024. **413**: p. 134716.

468. Benboudjema, F., F. Meftah, and J.-M. Torrenti, *Interaction between drying, shrinkage, creep and cracking phenomena in concrete.* Engineering structures, 2005. **27**(2): p. 239-250.

469. Lubbers, N., et al., *Modeling and scale-bridging using machine learning: Nanoconfinement effects in porous media.* Scientific reports, 2020. **10**(1): p. 13312.

470. Karra, S., et al., *Predictive scale-bridging simulations through active learning.* Scientific Reports, 2023. **13**(1): p. 16262.

471. Viswanathan, H., et al. *Scale-bridging using machine-learning: nanoconfinement effects in porous media*. in *AGU Fall Meeting Abstracts*. 2021.

Publication and awards from the thesis

Journal publication (3)

1. **Zengliang Yue**, Yuvaraj Dhandapani, Samuel Adu-Amankwah, Susan A. Bernal. Phase evolution and performance of sodium sulfate-activated slag cement pastes**.** CEMENT (2024): 100117.

2. **Zengliang Yue**, Yuvaraj Dhandapani, Susan A. Bernal. Structural alterations in alkali-sulfate-activated slag cement pastes induced by natural and accelerated carbonation. Cement and Concrete Research. (accepted).

3. **Zengliang Yue**, Zixian Su, Partha P. Paul, Alastair T.M. Marsh, Alice Macente, Marco DiMichiel, John L. Provis, Philip J. Withers, Susan A. Bernal. 3D crystalline phase and pore structure evolution upon CO_2 exposure in sodium sulfate-activated cement pastes. Cement and Concrete Research (accepted).

Conference publications (peer-reviewed) (10)

1. **Zengliang Yue**, Yuvaraj Dhandapani, John L. Provis, Susan A. Bernal. 'A reactive-transport framework to model carbonation behaviours of a hardened cement'. 76th RILEM Annual Week and International Conference on Regeneration and Conservation of Structures, Kyoto, Japan, September 2022. (extended abstract and oral presentation)

2. **Zengliang Yue**, Zixian Su, Partha P. Paul, Alastair T.M. Marsh, Alice Macente, Marco DiMichiel, John L. Provis, Philip J. Withers, Susan A. Bernal. 'Synchrotron based X-ray diffraction computed tomography analysis of alkali-activated slag cements'. The Bragg Exchange 2023, Leeds, United Kingdom, January 2023. (extended abstract and poster)

3. **Zengliang Yue**, Yuvaraj Dhandapani, Xinyuan Ke, Samuel Adu-Amankwah, Susan A. Bernal. 'Influence of slag chemistry on the properties of near neutral salt sodium sulfate-activated slag cements'. 41st Cement & Concrete Science Conference, Leeds, United Kingdom, September 2022. (extended abstract and oral presentation)

4. **Zengliang Yue**, Yuvaraj Dhandapani, Samuel Adu-Amankwah, Susan A. Bernal. 'Influence of slag chemistry on the carbonation of sodium sulfate-activated slag cements'. The International RILEM Conference on Synergising expertise towards sustainability and robustness of cement-based materials and concrete structures (SynerCrete'23), Milos Island, Greece, June 2023. (extended abstract and oral presentation)

5. **Zengliang Yue**, Zixian Su, Partha P. Paul, Alastair T.M. Marsh, Alice Macente, Marco DiMichiel, John L. Provis, Philip J. Withers, Susan A. Bernal. 'Carbonation of Na_2SO_4-activated slag cement: new insights into reaction mechanism, phase evolution and pore structure'. 16th International Congress on the Chemistry of Cement (ICCC) 2023, Bangkok, Thailand, 2023. (extended abstract and oral presentation)

6. **Zengliang Yue**, Zixian Su, Partha P. Paul, Alastair T.M. Marsh, Alice Macente, Marco DiMichiel, John L. Provis, Philip J. Withers, Susan A. Bernal. 'The effect of slag chemistry on the pore structure of Na2SO4-activated slag cements under accelerated carbonation'. 42nd Cement & Concrete Science Conference, London, United Kingdom, September 2023. (extended abstract and poster)

7. **Zengliang Yue**, Zixian Su, Partha P. Paul, Alastair T.M. Marsh, Alice Macente, Marco DiMichiel, John L. Provis, Philip J. Withers, Susan A. Bernal. 'Synchrotron X-Ray Diffraction Computed Tomography (XRD-CT) investigation of sodium sulfate-activated slag cements under accelerated carbonation'. Tomography for Scientific Advancement, Glasgow, September 2023. (extended abstract and oral presentation)

8. Yuvaraj Dhandapani, **Zenglaing Yue**, Moro Sabtiwu, Susan A. Bernal, Advances in characterising carbonation in low clinker and alternative cements, The 3rd International Workshop on Technologies for low carbon and lean construction, Chennai, 28-31 Jan 2024. At: Chennai, India. (abstract and oral presentation)

9. Yuvaraj Dhandapani, Moro Sabtiwu, Savan Kumar, **Zengliang Yue**, Susan A. Bernal, Challenges in characterising carbonation in hardened and end-of-life concrete: Implications on performance, Gordon Research Conference on Accelerating Sustainable Concrete Construction, Advanced Materials for Sustainable Infrastructure series, February 25-March 1, 2024. Ventura, California, USA. (abstract and oral presentation)

10. **Zengliang Yue**, Yuvaraj Dhandapani, Susan A. Bernal. Influence of slag chemistry and CO_2 concentration on the carbonation performance of sodium sulfate-activated slag cements. 10th International Conference on Concrete Under Severe Conditions-Environment & Loading, September 25-27, 2024, Chennai, Indi. (extended abstract and poster)

Awards

1. **Postgraduate Researcher Travel award**, School of Civil Engineering, University of Leeds, June 2022.

2. **Postgraduate Researcher Travel award**, School of Civil Engineering, University of Leeds, January 2023.

3. **Outstanding Student Award**, Faculty of Engineering and Physical Science, University of Leeds, May 2023.

4. **The 2023 Adam Neville Prize for the best national PhD in the field of cement and concrete**, Neville Centre of Excellence in Cement and Concrete Engineering; UK Concrete Society, December 2023.

5. **Outstanding Student Award**, Faculty of Engineering and Physical Science, University of Leeds, May 2024.

6. **Academic performance**, School of Civil Engineering, University of Leeds, April 2024.

Additional publications during the period of doctoral studies

Book chapter (1)

1. Sreejith Krishnan, Elijah D. Adesanya, Boyu Chen, Jean Noel Yankwa Djobo, Yuyan Huang, Alastair T.M. Marsh, Marija Nedeljkovic, Guang Ye, Juho Yliniemi, **Zengliang Yue**, Susan A. Bernal. Mechanical Properties of Alkali Activated Concrete, State-of-the-Art Report, RILEM TC 294 MPA. Chapter 4: Non-conventional Precursors and Activators. Springer (submitted).

Journal publications (3)

1. Alastair T.M. Marsh, **Zengliang Yue**, Yuvaraj Dhandapani, Katharine Button, Samuel Adu-Amankwah, Susan A. Bernal. Influence of limestone addition on sodium sulphate activated blast furnace slag cements. Construction and Building Materials. 2022; 360:129527.

2. Juan Manuel Etcheverry, **Zengliang Yue**, Sreejith Krishnan, Yury Andres Villagran-Zaccardi, Philip Van den Heede, Yuvaraj Dhandapani, Susan Andrea Bernal, and Nele De Belie. Phase Evolution of Hybrid Alkali Sulfate-Activated Ground-Granulated Blast Furnace Slag Cements. ACS Sustainable Chemistry & Engineering. 2023, 11 (9): 17519-17531.

3. Huang, Yuyan, Alastair TM Marsh, **Zengliang Yue**, Sreejith Krishnan, Samuel Adu-Amankwah, and Susan A. Bernal. "Hybrid Organic–Inorganic Blast Furnace Slag Binders Activated with Alkali Acetates." ACS omega (2024).

Conference publications (2)

1. Zixian Su, **Zengliang Yue**, Alastair T.M. Marsh, Susan A. Bernal, Philip J. Withers 'Characterization of pore structure evolution in alkali activated slag cements using time-lapsed in-situ X-ray computed tomography and scanning electron microscopy'. IOM3 42rd Cement and Concrete Science Conference. London, UK, 11-12 September 2023.

2. Zixian Su, **Zengliang Yue**, Partha P. Paul, Alastair T.M. Marsh, Marco DiMichiel, Timothy L. Burnett, John L. Provis, Susan A. Bernal, Philip J. Withers. Impact of CO_2 exposure in the microstructure of alkali-activated slag cement – A time-resolved 3D synchrotron XRD-CT/μXCT Analysis. FEMS Junior EUROMAT 2024: 15-18 July 2024, Manchester, UK